Master's thesis

2020

Pieter Jaime Matthijs

NTNU
Norwegian University of
Science and Technology
Faculty of Engineering
Department of Marine Technology

Master's thesis

Pieter Jaime Matthijs

Validation of aero-hydro-servo-elastic load and motion simulations in BHawC/OrcaFlex for the Hywind Scotland floating offshore wind farm

July 2020

NTNU
Norwegian University of
Science and Technology

NTNU
Norwegian University of
Science and Technology

NTNU

Norwegian University of
Science and Technology

Validation of aero-hydro-servo-elastic load and motion simulations in BHawC/OrcaFlex for the Hywind Scotland floating offshore wind farm

Pieter Jaime Matthijs

European Wind Energy Master - Offshore engineering track

Submission date: July 2020

Supervisor: E. E. Bachynski

Co-supervisor: A. V. Metrikine
A. C. Vire
N. Maljaars

Norwegian University of Science and Technology
Department of Marine Technology

Validation of aero-hydro-servo-elastic load and motion simulations in BHawC/OrcaFlex for the Hywind Scotland floating offshore wind farm

Pieter Jaime Matthijs Bussemakers

TU Delft Delft University of Technology
SIEMENS Gamesa RENEWABLE ENERGY
NTNU – Trondheim Norwegian University of Science and Technology

Cover photo: Hywind Scotland floating offshore wind farm
Credit: Equinor [31]

Model validation

of aero-hydro-servo-elastic load and motion simulations in BHawC/OrcaFlex for the Hywind Scotland floating offshore wind farm

by

P. J. M. Bussemakers

to obtain the degrees

Master of Science
in Offshore and Dredging Engineering
at Delft University of Technology

&

Master of Science
in Technology - Wind Energy
at Norwegian University of Science and Technology

to be defended on July 30th, 2020

Thesis committee:	Prof. Dr. Ir. A. V. Metrikine	TU Delft – Chairman
	Dr. Ir. A. C. Viré	TU Delft
	Prof. Dr. Ir. E. E. Bachynski	NTNU
	Prof. Dr. Ir. Z. Gao	NTNU
	Ir. N. Maljaars	Siemens Gamesa Renewable Energy
Thesis work duration:	September 23rd, 2020	July 30th, 2020
Student number:	TU Delft - 4322167	NTNU - 499936

An electronic version of this thesis is available at `http://repository.tudelft.nl/`.

SIEMENS Gamesa RENEWABLE ENERGY DTU EWEM TU Delft NTNU

Preface

"If you want to model nature you must copy nature,
if you want to copy nature you must understand nature." [98]

This MSc. thesis project is one of the requirements to obtain a Master of Science degree in Offshore and Dredging Engineering at Delft University of Technology (TU Delft) and in Wind Energy Technology at the Norwegian University of Science and Technology (NTNU), as part of the European Wind Energy Master - Offshore Engineering track, an international joint education program hosted by four leading Universities in the field of wind energy research and education.

The project was executed in collaboration with Siemens Gamesa Renewable Energy (SGRE). The topic was proposed by SGRE and further defined with supervisors at TU Delft and NTNU. Hywind Scotland measurement data was made available through a data sharing agreement between ORE Catapult and Equinor ASA, which were involved only as supplier of and consultant on these data. The work was carried out during the academic year 2019/2020 at the SGRE office in The Hague, the Netherlands.

Delft, July 25^{th}, 2020

P. J. M. Bussemakers

Acknowledgements

Professional

First and foremost, I would like to express my sincere gratitude to all committee members. Andrei, thank you very much for guiding this project. Your positive involvement and sincere feedback on vital moments have been very helpful to me. Axelle, thank you for your supervision during the project and sharing your broad experience to the world of research. Your help on this project is much appreciated. Nico, thank you for everything. Your great experience in the field of (floating) offshore wind turbine engineering have proven an inexhaustible resource for the many questions that popped up over the course of these ten months. Your never-ending positive attitude helped me complete this thesis not only in a structured, but also in a fun way. I enjoyed our weekly meetings, including our way too long introduction chats and the occasional political discussions. Thank you for making me feel welcome to the SGRE office from the very start. Erin, "The more you learn, the more you realise how much you don't know". To me, you have been the living proof of that. Your knowledge in the field of floating offshore wind validation and far beyond is ever astonishing. Thank you for all our challenging discussions and your committed supervision.

Furthermore, I would like to thank Pim Versteijlen for his bi-weekly support and occasional wisdom of life. My fellow SGRE graduate students, in particular Tobias, Dion, Rameen, Nelson and Jason for both deep-going discussion, welcome off-topic distractions and way too many potjes. It was a pleasure to get to know all of you. Thank you Col for the many great chats we've had during the year and your engaging welcome from the start. And thanks to all the other SGRE colleagues I have met during these months. Thank you for the open, welcoming environment and many fruitful conversations. It has been an amazing opportunity to work with you. And finally, I would like to thank Bjorn Skaare from Equinor ASA for his advice on the Hywind measurement data and Alan Ross from Orcina for his consultation OrcaFlex.

Personal

I wouldn't know where to start in my expression of gratitude to my parents, Henk Bussemakers and Claudine van Lith and my brother Roel for their support and encouragement during my thesis and my study time as a whole. We are and always will be a great team. Thanks, Saskia, for everything. Our shared study time has been an amazing adventure and I look forward to whatever our next chapter will bring. A big thanks to Laurens, Joris, Mees, Bas, Rogier and Jaap for your support and for making my study time and this thesis year as good as has been. In one word: 'nice!'. The many travels, parties, surfing sessions and more will never be forgotten. Furthermore I would like to thank my EWEM cohort, Wichert, Sara, Sanne, Jelle and Johan for being my home away from home during the past years. Times were fun, intense and inspiring with each and everyone of you and I look forward to working together in the wind industry. As your student time is more than acquiring a set of engineering skills, I would like to thank the groups that helped me develop to who I am today: The 7^{th} board of Boardsports Association DROP Delft and my co-founders of Green-mE. And, finally, the guys from Koestig, who were always there to remind me that life is more fun when it's less serious.

I feel blessed and privileged with such a wonderful group of people to thank.

Abstract

Climate change, as a result from global warming, requires an energy transition: the reduction of greenhouse gas emissions from fossil fuels and a radical innovation of the global energy system to proceed apace. Offshore wind is an important source of clean, renewable energy, and it plays a key role in the transition. 80% of the worldwide offshore wind is to be produced on locations in deep waters; here floating foundations are required, that to date are far more expensive than their bottom-fixed counterparts. To reduce costs of floating wind energy, reliable, detailed predictions of the system's loads and motion response are crucial. Floating foundations are designed using 'aero-hydro-servo-elastic' software codes that simulate the dynamic response of a floating offshore wind turbine system to the offshore environment. Predictive accuracy can be improved by comparing simulation results from a model of a known system against measurements taken from the real-world system, a so-called model validation. One promising state-of-the-art aero-hydro-servo-elastic software code is BHawC/OrcaFlex, developed by Siemens Gamesa Renewable Energy (SGRE). Due to its novelty, however, validation of the code has only been carried out to a limited extend, giving rise to uncertainty about the interpretation of simulation results. The purpose of this MSc. thesis project is to validate the performance of BHawC/OrcaFlex by comparing its simulated load and motion results to measurements on a real-world floating turbine from the Hywind Scotland floating offshore wind farm (Hywind). Measurement data and a description of the 'as-built' system were made available by the wind farm owner Equinor ASA. In order to establish an achievable level of modelling accuracy and predictive value of BHawC/OrcaFlex, the code was verified against another aero-hydro-servo-elatic software code: OrcaFlex, by setting up a similar model of the Hywind system in both codes. Limited information is available on the performance of OrcaFlex in floating wind load and motion predictions. Therefore, it was in turn verified against a wide range of industry-standard aero-servo-hydro-elastic software codes, using a modeled system that closely resembled the Hywind turbine and load cases that step-by-step increased in complexity, to further isolate causes of discrepancies between the models. OrcaFlex predictions matched very well across all load cases. The main differences were attributed to differently modeled additional linear hydrodynamic damping, as the official damping prescription resulted in prediction errors. In the BHawC/OrcaFlex verification against OrcaFlex, both models were subjected to multiple load cases that step-by-step increased in complexity, to further isolate causes of discrepancies between the models. Simulation results from running both models appeared to be nearly identical, though some discrepancy was observed from due to the simplified aero-servo-elastic OrcaFlex code. Examples are lower rotor efficiency due to simplified blade profiles, underprediction of tower bending moments due to simplified structural damping and lower wind-induced excitation due to simplified idling blade pitch control. The final validation of BHawC/OrcaFlex to full-scale Hywind measurements is performed at below-rated, rated and above cut-out wind speeds with a wind-wave and swell components and currents each with different directions. In general, BHawC/OrcaFlex motion frequency domain predictions appeared to correspond well to the actual Hywind measurements. Most phenomena in the low-frequency, wave-frequency and high-frequency region were captured by the simulations. However, large errors were observed in the mean surge, sway and bridle line tensions predictions. Discrepancies were found originating from errors in the model set-up, e.g. lack of hydrodynamic damping, simplifications in the wave model or errors in the mooring system set-up. Tuning of the mooring system showed improvement of the results, but further improvements could be made. Several sensitivity studies were added on parameters, such as hydrodynamic drag, tower damping and mooring drag. This showed overprediction of the surge/sway and roll/pitch frequency responses can be mitigated by both additional linear and viscous hydrodynamic damping. The main recommendations for further research are to further analyse errors identified in the model set-up. In addition, some yet unexplained phenomena that are not captured by BHawC/OrcaFlex in the current model, are to be addressed. Finally, a the development of a standardized approach to relate model validation studies in the field of floating wind to cost improvements could further quantify the value of future comparison studies.

Contents

Preface iii

Acknowledgements v

Abstract vii

List of abbreviations xi

List of Figures xii

List of Tables xv

1 Introduction 2
- 1.1 Research motivation 2
- 1.2 Preliminary research objectives and approach 4

2 Theory, methods and research objectives 5
- 2.1 Structural Dynamics 5
- 2.2 Hydrodynamics 8
- 2.3 Aerodynamics 21
- 2.4 Restoring forces 23
- 2.5 Model validation methodology 27
- 2.6 Final research objective and questions 30
- 2.7 Final research approach 30

3 OrcaFlex verification to industry-standard codes 32
- 3.1 Introduction to the OC3-project 32
- 3.2 Set-up of the general OC3-Hywind model in OrcaFlex 33
- 3.3 Load case table 33
- 3.4 Specific model set-up per load case 34
- 3.5 OrcaFlex verification results 37
- 3.6 Conclusions: OrcaFlex verification against industry-standard codes 45

4 BHawC/OrcaFlex verification to OrcaFlex 47
- 4.1 Set-up of the Hywind support structure model in OrcaFlex 48
- 4.2 Set-up of the Hywind turbine and aerodynamic model in OrcaFlex 49
- 4.3 BHawC/OrcaFlex general Hywind model set-up 50
- 4.4 Load case table 51
- 4.5 Specific model set-up per load case 51
- 4.6 OrcaFlex vs BHawC/OrcaFlex verification results 53
- 4.7 Conclusions: BHawC/OrcaFlex verification against OrcaFlex 59

5 BHawC/OrcaFlex validation with full-scale measurements 60
- 5.1 Set-up of the Hywind Scotland model in BHawC/OrcaFlex 60
- 5.2 Overview of environmental conditions measurements 61
- 5.3 Overview of full-scale load and motion measurements 65
- 5.4 Load case table 66
- 5.5 Hywind Scotland validation results 68
- 5.6 Detailed analysis of selected errors 79
- 5.7 Conclusions: Hywind Scotland validation 84

6 Conclusions **86**

7 Discussion and recommendations **89**

Appendices **91**

A Literature survey compact overview **92**

B Discussion of types of physical models **96**

C Additional information on OrcaFlex Hywind turbine model set-up **98**
C.1 Method structural parameters from BHawC to OrcaFlex 98
C.2 Method blade profile from BHawC to OrcaFlex 99

D Hydrodynamic analysis of full-scale measurements **101**
D.1 Diffraction significance 101
D.2 Dominant hydrodynamic loading 102
D.3 Wave steepness 103
D.4 Turbulence 104

E Measurements and simulation results post-processing **105**

Bibliography **108**

List of abbreviations

1P	rotational speed frequency
3P	blade-passing frequency
ADAMS	Automatic Dynamic Analysis of Mechanical Systems
BHawC	Bonus Horizontal Axis Wind turbine simulation Code
BH/OF	BHawC/OrcaFlex
BLT	bridle line tension
CFD	computational fluid dynamics
DLL	dynamic link library
DOF	degree of freedom
ETM	extreme turbulence model
F-A	fore-aft
FAST	Fatigue, Aerodynamics, Structures and Turbulence
FD	frequency domain
FEM	finite element method
FFT	fast Fourier Transform
FOWT	floating offshore wind turbine
HAWC2	Horizontal Axis Wind turbine simulation Code 2nd generation
Hywind	Hywind Scotland floating offshore wind farm
IEC	International Electrotechnical Commission
KC	Keulegan-Carpenter number
LC	load case
ME	Morison equation
ml1b1	main line 1, bridle line 1
ml1b2	main line 1, bridle line 2
ml2b1	main line 2, bridle line 1
ml2b2	main line 2, bridle line 2
ml3b1	main line 3, bridle line 1
ml3b2	main line 3, bridle line 2
MLT	mooring line tension
MSL	mean sea level
NREL	National Renewable Energy Laboratory
NSS	normal sea state
NTM	normal turbulence model
NTNU	Norwegian University of Science and Technology
OC3	Offshore Code Comparison Collaboration
OC5	Offshore Code Comparison Collaboration, Continued, with Correlation
OC6	Offshore Code Comparison Collaboration, Continued, with Correlation and unCertainty
OF	OrcaFlex
PCHIP	piecewise cubic hermite interpolating polynomial
PF	potential flow theory
PSD	power spectral density
QTF	quadratic transfer function
RAO	response amplitude operator
RNA	rotor-nacelle-assembly
Re	Reynolds number
RPM	rotations per minute
S-S	side-side
SCADA	Supervisory control and data acquisition
SGRE	Siemens Gamesa Renewable Energy
SWL	still water line
SWT-6.0-154	Siemens wind turbine, 6.0MW output, 154m rotor diameter
TU Delft	Delft University of Technology
TI	turbulence intensity
VIM	vortex-induced motions
VIV	vortex-induced vibrations

List of Figures

1 A schematic overview of the definitions of the subsystems of a spar-type floating offshore wind turbine used throughout the report. Figure adapted from Equinor [33] 1
2 A schematic overview of the definitions of rigid body motions of a floating offshore wind turbine. Figure adapted from Equinor [33]. 1

1.1 An outline of the preliminary research approach. 4

2.1 An intuitive representation of the potential flow problem. The middle figure represents the radiation problem, whereas the right figure represents the diffraction problem. Note here only heave motion is depicted, while the problem is in fact determined for six DOF. Adapted from [51]. 9
2.2 An intuitive explanation of the generation of a wave spectrum from a 'real-world' sea. 11
2.3 A comparison between linear and non-linear wave theory and 'real-world' waves. 13
2.4 A theoretical overview of the applicable (non-linear) wave models for a certain range of dimensionless wave height and water depth [58]. 14
2.5 Ranges of expected wake behaviour for a flow in a cylinder of increasing Reynolds number [38]. 16
2.6 An intuitive representation of the pressure difference caused from vortex shedding [51]..... 16
2.7 An overview of the expected inertia and drag contribution for a certain range of waveheight over structure length and structure length over wavelength [8]. 18
2.8 Radial cut in a wind turbine rotor and definition of the velocity triangle for a blade section. Adapted from [40]..... 23
2.9 The stability triangle as defined by Borg and Collu [11]. 24
2.10 A schematic representation of the stability of a freely floating body [11]. 24
2.11 A schematic representation of a catenary mooring line [51]..... 26
2.12 An intuitive representation of the mooring line tensions due to higher-order wave elevations [39]. 26
2.13 Model validation methodology. Adapted from [101]..... 27
2.14 An outline of the research approach conducted in this report. 31

3.1 The effect of using the OC3 wave-spectrum instead of an OrcaFlex-generated wave-spectrum. . 35
3.2 A comparison of the TurbSim-generated wind spectrum, compared to the prescribed OC3 wind velocity, a theoretical API spectrum and the OrcaFlex-generated API spectrum..... 36
3.3 Full-system hydro-elastic prediction of first 19 natural frequencies from OC3 LC 1.2, comparison between OrcaFlex and selected participants..... 37
3.4 Free decay in platform surge, heave and pitch from OC3 LC 1.4, rigid body motion comparison between OrcaFlex and selected participants..... 38
3.5 Hydro-elastic response to regular waves from OC3 LC 4.1, comparison between OrcaFlex and selected participants. 39
3.6 Hydro-elastic response to irregular waves from OC3 LC 4.2, comparison between OrcaFlex and selected participants. 40
3.7 Aero-hydro-servo-elastic response to steady wind + regular waves from OC3 LC 5.1, motion comparison between OrcaFlex and selected participants..... 41
3.8 Aero-hydro-servo-elastic response to steady wind + regular waves from OC3 LC 5.1, system behaviour comparison between OrcaFlex and selected participants. 42
3.9 Aero-hydro-servo-elastic response to irregular waves + turbulent (rated) wind, from OC3 LC 5.2, comparison between OrcaFlex and selected participants..... 44

4.1 An impression of the OrcaFlex aero-hydro-servo-elastic model of the Hywind Scotland floating offshore wind turbine used for this verification step..... 47

4.2 Overview of the blade section coordinate systems used in BHawC and in OrcaFlex. The steps for rewriting BHawC coordinates to OrcaFlex coordinates can be found in C.1 50
4.3 An impression of the BHawC/OrcaFlex aero-hydro-servo-elastic model of the Hywind Scotland floating offshore wind turbine used for this verification step. An interface vessel (with dummy shape) is used in the coupling between BHawC and OrcaFlex. No user interface is available for the wind turbine in BHawC. 50
4.4 A schematic representation of the different software components of BHawC/OrcaFlex used in coupled dynamic analysis. Adapted from [62]. 51
4.5 Wind field comparison of the spectrum used in OrcaFlex the spectrum used in BHawC/OrcaFlex. 52
4.6 Aero-hydro-elastic response to load case 3.1 comparison between OF and BH/OF. 55
4.7 Aero-hydro-elastic response to load case 3.2 comparison between OF and BH/OF. 56
4.8 Hydro-elastic response to load case 4 comparison between OF and BH/OF. 57
4.9 Aero-hydro-elastic response to load case 5.1 comparison between OF and BH/OF. 58
4.10 Aero-hydro-elastic response to load case 5.2 comparison between OF and BH/OF. 58

5.1 An overview of the location and lay-out of the Hywind Scotland floating offshore wind farm. Adapted from [33]. 61
5.2 An overview wind and wave conditions per load case. 62
5.3 An overview of the wind and wave conditions per load case. Ordered with respect to increasing wind speed. 63
5.4 An overview of the current conditions per load case. 63
5.5 An overview of the directions of environmental conditions per load case. 64
5.6 Schematic overview of the floater and bridle lines lay-out. 68
5.7 Comparison of tower roll response of load case 1 predicted by BH/OF and full-scale measurements. 69
5.8 Wind conditions per load case according to different sources. 69
5.9 A schematic overview of the wind, swell, wind-wave and current conditions of load case 3. 70
5.10 Statistical comparison of motion and bridle line response of load case 3. The layout of the bridle lines is found in figure 5.6. 70
5.11 Comparison of tower pitch response of load case 3 predicted by BH/OF and full-scale measurements. 72
5.12 Comparison of platform surge response of load case 3 predicted by BH/OF and full-scale measurements. 72
5.13 Comparison of platform sway response of load case 3 predicted by BH/OF and full-scale measurements. 72
5.14 Comparison of platform yaw response of load case 3 predicted by BH/OF and full-scale measurements. 73
5.15 Comparison of main line 1, bridle line 1 response of load case 3 predicted by BH/OF and full-scale measurements. 73
5.16 Comparison of main line 2, bridle line 2 response of load case 3 predicted by BH/OF and full-scale measurements. 73
5.17 A schematic overview of the wind, swell, wind-wave and current conditions of load case 2. 74
5.18 Statistical comparison of motion and bridle line response of load case 2. The layout of the bridle lines is found in figure 5.6. 75
5.19 Comparison of tower pitch response of load case 2 predicted by BH/OF and full-scale measurements. 75
5.20 Comparison of platform surge response of load case 2 predicted by BH/OF and full-scale measurements. 75
5.21 A schematic overview of the wind, swell, wind-wave and current conditions of load cases 10 and 11. 76
5.22 Statistical comparison of system dynamics and bridle tension response of load case 10. For load case 11, equivalent values are observed. 76
5.23 Comparison of platform surge response of load case 10 predicted by BH/OF and full-scale measurements. 77
5.24 Comparison of platform yaw response of load case 10 predicted by BH/OF and full-scale measurements. 77

5.25 Comparison of main line 1, bridle line 1 response of load case 10 predicted by BH/OF and full-scale measurements. 78
5.26 Comparison of restoring properties of the tuned and un-tuned mooring system. 79
5.27 Statistical variation of simulations with stochastic environmental input for different seed realisations. 80
5.28 A visual impression of mooring line eigenmodes. 81
5.29 A demonstration of the improvement of tower-bending frequency response predictions for an increased structural tower damping percentage from different sources. 81
5.30 A demonstration of the effect of varying linear hydrodynamic damping. 82
5.31 A demonstration of the improvement of surge/sway and roll/pitch frequency response predictions for increased drag coefficients. 83

D.1 Basic properties of the Hywind Scotland system used in the hydrodynamic analysis. 101
D.2 Analysis of the diffraction significance per load case. 102
D.3 Analysis of the dominant type of hydrodynamic loading per load case. 103
D.4 Analysis of the dominant type of hydrodynamic loading per load case. 103
D.5 Analysis of the wave steepness per load case. 104
D.6 Analysis of the flow regime per load case. 104

E.1 An example of the effect of interpolation on the Hywind measurement signals. 106
E.2 An example of the effect of windowing on the Hywind Scotland measurement signals. 107

List of Tables

2.1 An overview of the measure of preference of different type of physical models for different requirements. 28

3.1 Load-case table used in the OC3 Phase IV project. 34

4.1 An overview of selected parameters of the floater-mooring system of the OrcaFlex Hywind model. 48
4.2 Load-case table used in the comparison of BHawC/OrcaFlex to OrcaFlex. 51
4.3 A comparison of the static analysis results of OrcaFlex, BHawC/OrcaFlex and Equinor provided values. 53
4.4 Comparison of rigid body motions natural periods of the Hywind Scotland system predicted by OF and BH/OF. 53

5.1 Mooring line tensions and their corresponding relative error to prescribed values from Equinor [32], before and after tuning. 61
5.2 Load-case table used in the comparison of BHawC/OrcaFlex to full-scale Hywind measurements. 67
5.3 Comparison of rigid body motions natural periods of the Hywind Scotland system predicted by BH/OF and values provided by Equinor. 70
5.4 An overview of the occurring eigenmodes of the mooring system and its natural frequency per component. 81

A.1 A compact overview of recent numerical model validation studies in the field of (floating) offshore wind energy. For the full legend explaining abbreviations see 'Legend'. 94

Definitions

Floating wind turbine system

An overview of the important definitions used to describe a floating offshore wind turbine system (figure 1) and its six degree of freedom rigid body motions (figure 2). From theory, the surge and sway motion refer to the turbine motion compared to the wind, i.e. by including its yaw motion. In the full-scale measurements, OrcaFlex and BHawC/OrcaFlex aero-hydro-servo-elastic codes used for verification and validation, the surge and sway motion are provided in cardinal coordinates. This was adopted in this project to minimize comparison errors caused by differences between definitions of local coordinate system in different results. Therefore, in results presented in Chapter 3 through 6 of this report, positive 'surge' and 'sway' motions refer to positive 'North' and 'East' motions of the system, respectively.

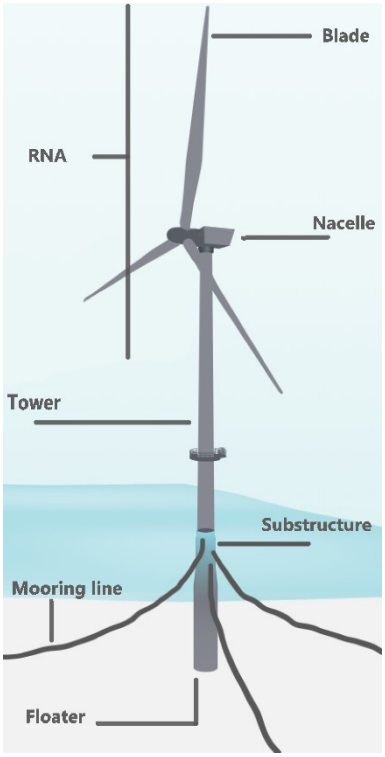

Figure 1: A schematic overview of the definitions of the subsystems of a spar-type floating offshore wind turbine used throughout the report. Figure adapted from Equinor [33]

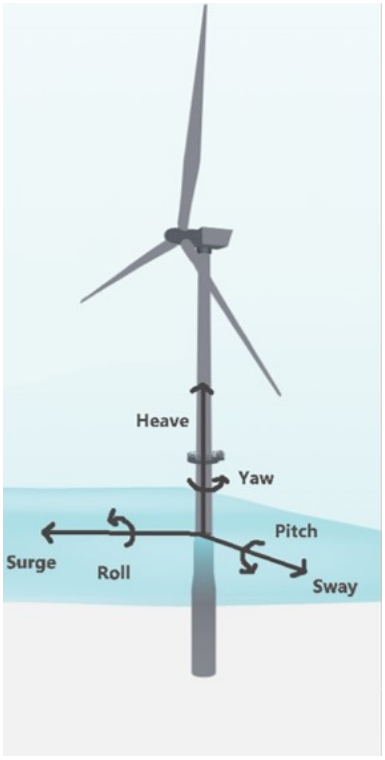

Figure 2: A schematic overview of the definitions of rigid body motions of a floating offshore wind turbine. Figure adapted from Equinor [33].

1 Introduction

This report aims at providing an overview of the process and results of my MSc. thesis project: the validation of a simulation model that predicts the dynamic behaviour of- and loads exerted on a floating offshore wind turbine, by comparing its simulation results to the results of measurements of a real-world system. This introduction contains the motivation to start this study, leading to preliminary research objectives and questions. The definitive, concept-based research objectives and questions are to be found in chapter 2 after preliminary research was completed.

1.1 Research motivation

For the past millennia, humans roamed the surface of this planet. In the early days, population numbers were small and an equilibrium between nature and mankind could easily be maintained or restored: what was taken from nature would regrow, whatever polluted nature would be broken down. Over the past centuries human population has rapidly expanded and its consuming needs have risen accordingly. At the beginning of the first industrial revolution, the use of fossil fuels was introduced to generate efficient energy on a large scale. This resulted in a boost in welfare and technological development. However, nature's capacity to deal with human species' consumption and pollution level did no longer suffice. Increased consumption resulted in significant loss of biodiversity, whereas with a growing use of fossil fuels, a large amount of greenhouse gasses has been emitted. The latter was discovered in the early 20^{th} century to cause global warming, leading to climate change. In the late 20^{th} century it was stated that when the consumption and pollution levels would not decrease in the upcoming century, nature could no longer support economic and population growth in the long term [68]. Today, scientists agree that climate-related risks to health, livelihoods, food security, water supply, human security, and economic growth are projected to increase with global warming of 1.5°C and increase further with 2°C [65].

The discovery of the human-caused climate change started a slow but steady transition from using traditional fossil fuels to new forms of energy. Greenhouse gas emissions largely result from using fossil fuels for energy production. In the European Union, the energy sector is responsible for over 75% of the total greenhouse gas emissions [18]. New sources of energy generation are required that neither contribute to pollution nor require nonrenewable consumption. Some of the most prominent forms of renewable energy are wind energy, solar energy, bio-energy, geothermal energy, and wave energy. Offshore wind energy is expected to have taken the lead in energy generation in 2040, having a share of 20% percent of the total power production compared to 0.3% today [2]. According to the European Commission, 450GW of offshore wind energy is required in 2050, compared to 20GW today [19].

From a technological as well as an economic viewpoint, wind turbines with floating support structures have multiple advantages over conventional bottom-founded foundations in offshore wind energy. Consequently, floating structures are expected to acquire an important role in energy production for decades to come, mainly for the following reasons. Wind energy is deployed in locations known for high and consistent wind speeds. 75% of these locations in Europe can be found in waters at least 60 metres deep; worldwide, 80% of the offshore wind production potential is in waters beyond this depth [34]. Here, conventional

bottom-founded foundations are no longer economically viable [111].

Traditional monopile foundations, as well as installation technology, currently are struggling to keep up with the increasing size of wind turbine generators. Assembling a floating wind system can take place onshore, after which the turbine can be towed to its final location, rendering expensive equipment for offshore installation obsolete [13]. Moreover, floating turbines have less environmental impact, as damaging piling noises and visual pollution will be avoided, due to the remoteness of deep waters.

For a short period after their introduction, new kinds of technology in general are expensive, for knowledge about their manufacturing, installation, maintenance and decommissioning is lacking, leading to inefficient processes. For technologies that are bound by conformity with strict health, safety and environmental protection standards, a conservative design approach will be chosen from the start. This means that new structures are over-dimensioned to account for possible design flaws and unknown types of excitation. Several sources of increased uncertainty when designing floating wind turbines instead of bottom-founded structures are [48]:

- Floating systems can move and rotate in six degrees of freedom, which introduces new types of loading and response and limits the applicability of existing load prediction methods [22];
- The introduction of low-frequency eigenmodes changes the overall response of the system;
- The mooring system introduce a new component that impacts the overall dynamic analysis;
- The support structure no longer needs to be slender and cylindrical, such that hydrodynamic radiation, diffraction and other wave effects can become important.

Generally, along with an increase in product development, an increase in knowledge of a system's behaviour becomes apparent. Floating wind turbines still are in an early stage of development, but their costs are expected to fall by 50% in 2050 [111] due to increased efficiency in their design and deployment processes.

A floating wind turbine is placed in an offshore environment where it is constantly subjected to varying wind, waves, currents and other types of environmental conditions, which cause a dynamic response. To minimise costs, whilst maximising energy production and meeting health-, safety- and environmental requirements, it is necessary to accurately predict the dynamic response caused by placing a floating wind turbine structure in its planned environment. Higher loads require a stronger structure design, that in turn requires more or stronger material to cope with these loads. Confidence in response predictions provides designers with the information necessary for making decisions that influence the time, cost and risk associated with product development, without necessarily building and rebuilding full-scale prototypes. Detailed dynamic analysis of the above mentioned behaviour and environmental conditions of floating offshore wind turbines is executed by mathematical modelling using simulation software, so-called 'aero-hydro-servo-elastic' codes. The validation of these codes with measurements on real-life systems is a frequently appearing topic in offshore wind literature. Describing, explaining, demonstrating and mitigating errors helps to better interpret results from simulations, as well as prevents errors from recurring in future validation studies.

One promising aero-hydro-servo-elastic simulation software is called BHawC/OrcaFlex, developed by Siemens Gamesa Renewable Energy (SGRE). It is well-equipped for the detailed predictions, as it combines thoroughly validated aero-servo-elastic software BHawC and industry-leading hydro-elastic software code OrcaFlex. Due its novelty, extensive validation against full-scale measurements was not yet performed. At SGRE I was given the opportunity to work on the validation of BHawC/OrcaFlex software, as a MSc. thesis project. The validation process mainly entailed comparison of the code's performance to full-scale measurements of Hywind Scotland: the world's first floating offshore wind farm. In an initial phase of the project, the performance of the code was compared to a variety of other aero-hydro-servo-elastic codes for verification purposes. This report aims at providing a clear overview of the process, decisions and results of my MSc. thesis project.

1.2 Preliminary research objectives and approach

At the start of the project the following preliminary research objective has been established:
The purpose of this MSc. thesis project is to contribute to the validation of the performance of BHawC/OrcaFlex aero-hydro-servo-elastic software, by comparing its simulating capacity to measurements of the Hywind Scotland floating offshore wind farm.

The following preliminary research question has been established:
How can the performance of BHawC/OrcaFlex aero-hydro-servo-elastic software be validated by using measurements of the Hywind Scotland floating offshore wind farm?

Figure 1.1 shows the an outline of the structure of the report. Chapter 2 supports the formulation of a final research question by means of a literature survey of theoretical background, recent model validation studies and validation methodology. This results in final research questions, which are answered by means of the final research methodology.

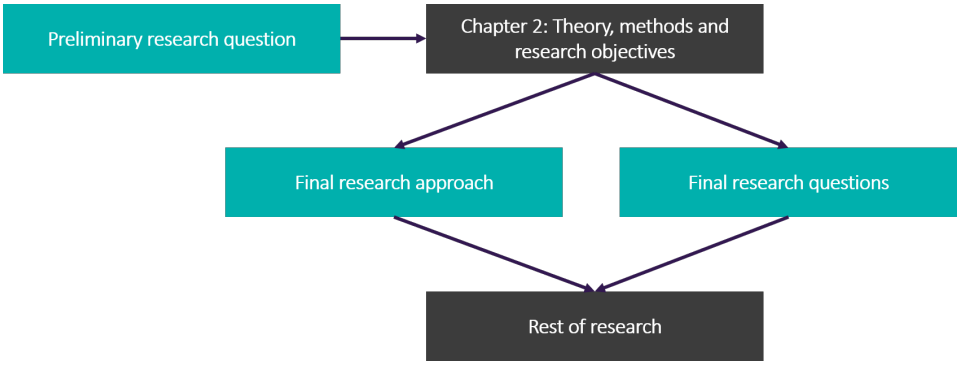

Figure 1.1: An outline of the preliminary research approach.

2

Theory, methods and research objectives

Environmental conditions and operational conditions to which a real-world floating offshore wind turbine (FOWT) structure is subjected determine the way it behaves over time. By simulation models using aero-hydro-servo-elastic code software, a numerical model of a real-world system is set up, in which environmental conditions and predictions of the system dynamic response can be simulated. The accuracy of these predictions depends on the accuracy with which the model simulates behaviour of the system subjected to operational and environmental conditions, as well as these conditions themselves.

For dynamic simulations, information is derived from prediction theories, which model the real-world simulation system input and output as accurately as possible. In reverse, information gathered from application of these theory-based models improves the theoretical validity and provides deepened insight in their range of application, thereby raising the accuracy level of the simulation models.

Many real-world phenomena can be described with great accuracy by prediction theories. However, given limited computing power, simplification of theories is inherent in a workable code set up. Knowing which simplifications are made under which assumptions gives insight in the simulated results and origin of occurring errors. Moreover, increased knowledge about ranges of application minimizes potential errors made in the model set-up.

The validation of simulation codes with measurements of a real-world system is a frequently appearing topic in offshore wind literature. In this study, the system's dynamic response is modelled by assumptions made in structural dynamics- and mooring theory, which relate loads induced by the hydrodynamic and aerodynamic environment to body motions and resisting forces, from a theoretical point of view. Other types of response-inducing conditions can be distinguished, e.g. soil conditions, ice conditions, vessel impact, seismic conditions, precipitation and lightning, but those are considered beyond the scope of this report.

This chapter starts with an overview of prediction theories used for modelling the relation between loads and motions of a system to its environmental conditions in aero-hydro-servo-elastic codes, which contributs to explaining and predicting this relation from a theoretical and methodological point of view. When trade-offs between different types of modelling occur, a discussion on trade-offs made in recent published model validation studies. A compact overview of model validation studies considered can be found in Appendix A.

Subsequently, the methodology of validation processes is described, in general and from an applicability viewpoint to this study. Some concepts and measures are defined that are important to establish any level of conformity to requirements or progress regarding BHawC/OrcaFlex' modelling capacity, as a result from the validation process. The chapter continues with describing the main research objective and main research questions, and ends by outlining the chosen final research methodology.

2.1 Structural Dynamics

Structural dynamics describes the behaviour of a structure when it is subjected to different types of dynamic loading, which are explained in later sections. In this section, a distinction is made between rigid body dynamics and flexible body dynamics, where the first proves useful for the prediction of overall system be-

haviour and the latter gives a more detailed description of reality.

2.1.1 Rigid body dynamics

The equations of motion provide a mathematical relationship between the external loading and the structures response based on its inertia, damping and restoring term. Here, the structure is assumed to be rigid, meaning it will not deform under the action of applied forces. It can still translate and rotate freely in six degrees of freedom (DOFs), as shown in figure 2. The time-domain equations of motion for a floating body are:

$$(\mathbf{M}+\mathbf{A})\ddot{\underline{\mathbf{x}}}+\mathbf{B}\dot{\underline{\mathbf{x}}}+\mathbf{C}\underline{\mathbf{x}}=\mathbf{F}_{ext}(t) \tag{2.1}$$

Here, the $\underline{\mathbf{x}}$ vector and its time derivatives represent each of the six DOF accelerations, velocities and displacement. **M, A, B** and **C** are the mass, added mass, damping and restoring force coefficient matrices, respectively, which relate the external force to the body motion $\underline{\mathbf{x}}$. Loads in one DOF can result in motions in another DOF, which is referred to as coupling of terms. In a 6 DOF analysis, these matrices are 6x6, where non-diagonal terms provide information about coupling.

External loads can be decomposed as a superposition of different types of loading a body floating wind turbine is subjected to (2.2). This comprises a combination of loads caused by environmental conditions and restoring loads. Waves and current loads are combined here under 'hydrodynamic loading'. Wind loads are referred to as the 'aerodynamic loading' and the mooring and hydrostatic loads are combined under 'restoring loads'. Note that (hydro)static restoring loads are independent of time. One could argue that each of these loads depends on the position, velocity or acceleration of the body, e.g. the restoring loads where the hydrostatic and mooring stiffness depend on the position. These dependencies are considered to be included in the external load timeseries, showing a purely time-dependent representation of the equations of motion.

$$\mathbf{F}_{ext}(t)=\underbrace{\mathbf{F}_{static}+\mathbf{F}_{mooring}(t)}_{Restoring\ loads}+\underbrace{\mathbf{F}_{waves}(t)+\mathbf{F}_{current}(t)}_{Hydrodynamic\ loads}+\underbrace{\mathbf{F}_{wind}(t)}_{Aerodynamic\ loads} \tag{2.2}$$

External loads often consist of a constant and an oscillating part. It is of interest to analyse these oscillations in terms of their frequencies and amplitudes. In case the system can be fully linearised, a frequency domain solution can be found by rewriting time-dependent equations of motion (2.1) into frequency dependent equations of motion. The oscillations of a linearised system have a similar frequency as the oscillating excitation. We can then assume resulting motions to be harmonic (2.3). Substituting this into the equations of motion and rewriting gives the motion amplitude for a certain excitation frequency (2.4). In frequency domain (FD) analysis, the system response of to excitation of a wide range of frequencies is considered.

$$\underline{\mathbf{x}}=\underline{\tilde{\mathbf{X}}}e^{i\omega t} \tag{2.3}$$

$$\underline{\tilde{\mathbf{X}}}(\omega)=\frac{\mathbf{F}_{ext}(\omega)}{\left[\omega^2(\mathbf{M}+\mathbf{A}(\omega))+i\omega\mathbf{B}(\omega)+\mathbf{C}\right]} \tag{2.4}$$

A special case is excitation of a linearised system due to regular waves only. The excitation reduces to $F_{ext}(\omega)=|F_{ext}(\omega)|\zeta(\omega)$, where ζ is the surface elevation. Equation (2.4) can now be rewritten to the transfer function H(ω) (2.6), which gives a compact description of the input/output relation of a linear system [112]. From the transfer function, the response amplitude operator (RAO) can be derived by taking its absolute value (2.5).

$$H(\omega)=\frac{\underline{\tilde{\mathbf{X}}}(\omega)}{\zeta(\omega)} \tag{2.5}$$

$$RAO=|H(\omega)|=\frac{|F_{ext}(\omega)|}{\left[\omega^2(\mathbf{M}+\mathbf{A}(\omega))+i\omega\mathbf{B}(\omega)+\mathbf{C}\right]} \tag{2.6}$$

The RAO relates the response amplitude to the incoming wave amplitude. In general, a transfer function for each linear relation between input and output can be found. FD analysis reveals the system natural frequencies, by showing at which frequencies the system gives starts to resonate. The natural frequencies in each motion degree of freedom can also be determined mathematically as:

$$\det\left[-\omega_i^2(\mathbf{M}+\mathbf{A})+i\omega\mathbf{B}+\mathbf{C}\right]=0 \tag{2.7}$$

In the case of an impulse to the system, the an undamped system would oscillate indefinitely at its natural frequency, as opposed to an under-damped system, at which the system would go back to its equilibrium position after several oscillations. In the case of critically damped system, the system would go back to its

equilibrium position without oscillating. The damping ratio provides the level of damping compared to critical damping and can be determined from (2.8). In a single degree of freedom, the damping ratio can be determined from the logarithmic decrement, using equations (2.9) and (2.10) for a decaying vibration. Here, $x(t)$ is the overshoot at a given time and n is the number of successive positive peaks.

$$\xi = \mathbf{B}(\omega)\,[2\omega_n(\mathbf{M}+\mathbf{A}(\omega))]^{-1} \quad (2.8)$$

$$\xi = \frac{1}{\sqrt{1+(\frac{2\pi}{\delta})^2}} \quad (2.9)$$

$$\delta = \frac{1}{n}\ln\frac{x(t)}{x(t+nT)} \quad (2.10)$$

2.1.2 Flexible body dynamics

In the equations of motion presented in (2.1), the body is assumed rigid. However, all real-world systems are flexible, no matter how high their material stiffness. In order to accurately describe the behaviour of a floating wind turbine subjected to external loading, one should include elastic behaviour of structure itself. This makes is harder to linearise the system and requires a solution in time domain.

The system can be extended to contain a finite number of elements (referred to as the finite element method (FEM)), where each element represents a part of the structure. One way of doing this is by using beam elements with the appropriate mass, stiffness and damping. Bending deformation in a beam found from an external bending moment is known from structural mechanics to relate as:

$$M(x,t) = EI(x)\frac{\partial^2 w(x,t)}{\partial x^2} \quad (2.11)$$

Where E is the Young modulus and I(x) the moment of inertia of the cross-section. Note here, that both the moment and deflection are time-varying.

The Euler-Bernoulli beam formulation is considered, which assumes the cross-sections of the beam remain perpendicular to the neutral axis during bending. Therefore, it is limited to small slopes of the beam: $\left(\frac{\partial w}{\partial x}\right)^2 \ll 1$. The dynamic equation of motion of the beam is then found from equation (2.12), where A is the cross-sectional area and f the external force per unit length. This equation was derived from the balance of forces of an infinitesimal element of a beam in bending (see [69] for a full derivation).

$$\rho A(x)\frac{\partial^2 w(x,t)}{\partial t^2} + \frac{\partial^2}{\partial x^2}\left[EI(x)\frac{\partial^2 w(x,t)}{\partial x^2}\right] = f(x,t) \quad (2.12)$$

This a special case of the Timoshenko beam theory [22], which also accounts for deformation due to shear and rotational inertia. The equations of motion are then extended to include the shear coefficient, shear modulus and shear rotation.

Flexible beam elements can separately be excited by harmonic oscillations, which will introduce new natural frequencies in the system. An example is given by Spijkers et al. [93] for a simply supported bending beam under synchronous harmonic motion. By solving the equations of motion with its corresponding boundary conditions, the natural frequencies are found by equation (2.13). Each beam natural frequency has its own eigenfunction, which for this example can be found from equation (2.14), where $w_n(x)$ is the mode shape corresponding to each eigenfunction n.

$$\omega_n = n^2\left(\frac{\pi}{l}\right)\sqrt{\frac{EI}{\rho A}} \qquad (n = 1,2,...,\infty) \quad (2.13)$$

$$w(x,t) = \sum_{n=1}^{\infty} w_n(x)\sin(\omega_n t + \phi_n) \quad (2.14)$$

This beam type appears to have infinite natural frequencies. According to [93], this simplified solution is reliable only for low values of n and Timoshenko beam theory approach may be desired for calculation of higher natural frequencies of a beam element.

In this example, only the solution to simplified bending beam problems are provided. In a more detailed FEM solution, this may be extended by considering torsional-, longitudinal- motion and shear deformation of the beam element. Each of these deformations will introduce new degrees of freedom to the system and, consequently, new natural frequencies.

2.2 Hydrodynamics

Hydrodynamics describes the motion of fluids and the forces exerted to floating bodies by relative motion to these fluids. A floating offshore wind turbine structure is partly submerged in dynamic water. This exerts time-varying loads on the floating structure that causes motion of the structure, which in turn causes additional fluid motion (so-called fluid-structure interaction). The hydrodynamic environment consists of waves and currents. In this section, these en types of loading it induces on a floating structure are explained and augmented by results from a literature survey.

2.2.1 Wave loads

In the description of wave loads, first a description of regular wave behaviour is provided based on assumptions made in first-order potential flow theory. Later, first- and second-order potential flow theory is explained in terms of its waveload predicting capacities to regular waves. Then, the hydrodynamic environment description is extended to include irregular wave, non-linear wave kinematics and viscosity. This is used to explain flow separation effects and current loads. The Morison equation is explained to allow prediction of viscous hydrodynamic loads. Finally, an overview of different sources of hydrodynamic damping and its effect on the dynamic response is provided.

Trade-offs in the model set-up that arise from different descriptions of the hydrodynamic environment and their effect on load predictions are augmented with insights from comparable validation studies found from literature.

First-order potential flow theory

All types of fluid motion under any condition can be described using the Navier-Stokes equations. However, due to limitations in computing power, assumptions from this theory has to be made to come to a workable aero-hydro-servo-elastic code. A full derivation of Navier-Stokes equations to the first order potential flow solution for a single regular wave propagating in finite water can be found in [6].

$$\phi_0(x,y,z,t) = \frac{\zeta_a g}{\omega}\frac{\cosh[k(h+z)]}{\cosh[kh]}\cdot\cos(\omega t - \mathbf{k}\cdot\mathbf{r}+\gamma) \tag{2.15}$$

This derivation is based on the assumptions of an irrotational flow comprising an inviscid, incompressible fluid of constant density. From the velocity potential solution, the wave surface elevation, vertical and horizontal velocity and acceleration can be obtained directly. Inserting it into the Bernoulli equation [51], one can find the pressure variation in the wave. Inserting the velocity potential into the free surface kinematic boundary condition [36] results in the dispersion relation, which provides a widely used relationship between the wave number and the frequency for a given water depth:

$$\omega^2 = g\,k\tanh kh \tag{2.16}$$

From this combination, several wave properties such as its wavelength, wave number and celerity can be determined.

The wave velocity from potential flow theory is calculated up to the still water line (SWL). However, by definition the wave velocity has maximum at the free-surface thus this solution needs to be extrapolated.The most popular way of taking this into account is Wheeler stretching [110]:

$$z' = \frac{z-\zeta}{h+\zeta}\cdot h \tag{2.17}$$

Using this method, the wave velocity profile is stretched vertically to give the same velocity still water level at the instantaneous surface elevation instead.

From basic mechanics, it is known that the force acting on any body is the pressure integrated along the surface on which the pressure is applied. In case of a floating body, the hydrodynamic pressure is applied only on the wetted surface of the body. In the case of a fluid-structure interaction problem, full velocity potential solution should be extended to include waves generated by the body as well:

$$\phi(x,y,z,t) = \underbrace{\underbrace{\phi_0(x,y,z,t)}_{incident wave} + \underbrace{\phi_D(x,y,z,t)}_{scattering}}_{diffraction} + \underbrace{\phi_R(x,y,z,t)}_{radiation} = \mathbb{R}e\left[\phi(x,y,z)e^{i\omega t}\right] \tag{2.18}$$

The physical meaning of radiation is the potential caused by oscillatory motion of the body in still water. The physical meaning of diffraction is the potential caused by the waves on a fixed body as can be observed from figures (2.1).

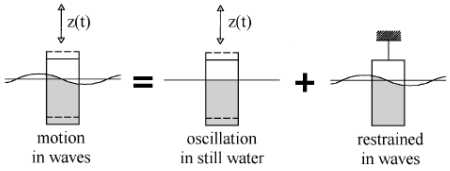

Figure 2.1: An intuitive representation of the potential flow problem. The middle figure represents the radiation problem, whereas the right figure represents the diffraction problem. Note here only heave motion is depicted, while the problem is in fact determined for six DOF. Adapted from [51].

Due to linearity and steady state conditions, one can solve the problem assuming a separation of time and space variables. From structural dynamics, it is known that the response of a linear system to an oscillatory motion in steady state conditions follows the same frequency [69].

This yields a more general description of the wave loads and moments according to potential flow theory, provided here in generalized force notation:

$$F_k(t) = -\rho \iint_{S_{Body}} \left(\frac{\partial \phi_0}{\partial t} + \frac{\partial \phi_S}{\partial t} + \frac{\partial \phi_R}{\partial t} \right) \cdot n_k \cdot dS, \qquad k = 1..6 \tag{2.19}$$

$$\begin{cases} n_k & k = 1,2,3 \\ (\mathbf{r} \times \mathbf{n}_k)_{k-3} & k = 4,5,6 \end{cases} \tag{2.20}$$

The radiation problem can be solved when the body is forced to oscillate in six degrees of freedom with a certain frequency ω and an amplitude $\eta_{j,a}$. The solution to the radiation problem is a definition of the added mass and damping matrices of the floating body, knowing that the added mass loads are in phase with the acceleration and the damping loads are in phase with the velocity.:

$$A_{k,j}(\omega) = \mathbb{R}e\left[\rho \iint_{S_{Body}} \phi_j n_k dS \right] \tag{2.21}$$

$$B_{k,j}(\omega) = -\omega \mathbb{I}m\left[\rho \iint_{S_{Body}} \phi_j n_k dS \right] \tag{2.22}$$

Steady state conditions and linear motions are assumed. Notice that the added mass and damping terms are in fact dependent on the frequency of incoming waves.

The diffraction problem is solved by finding the incident wave velocity potential and the diffraction (scattering) velocity potential. Invoking Green's second theorem [51] and rewriting using the Haskind relation [36], the problem can be made dependent only on the radiation and incident wave potentials as

$$F_{D,k}(t) = \mathbb{R}e\left[-i\rho e^{i\omega t} \iint_{S_{Body}} \left(\phi_w \frac{\partial \phi_k}{\partial n} + \phi_k \frac{\partial \phi_w}{\partial n} \right) \cdot dS \right] \tag{2.23}$$

A more detailed derivation of the radiation and diffraction problem is found in [12].

Second-order potential flow theory

When extending the problem from a single wave to two regular incoming waves with different amplitude and a different frequency, the velocity potential solution accurate to the second order is found as

$$\phi_2(x,t) = \mathbb{R}e \sum_i \sum_j \left[\phi^+_{i,j}(x) \exp^{i(\omega_i+\omega_j)t} + \phi^-_{i,j}(x) \exp^{i(\omega_i-\omega_j)t} \right] \tag{2.24}$$

The pressure can be obtained from substituting the definition of the second-order velocity potential into the Bernoulli equation [39] and crossing out all terms higher than second order, resulting in equation 2.25.

$$p(x,y,z,t) = -\rho g z - \rho \frac{\partial \phi_1}{\partial t} - \frac{\partial \phi_2}{\partial t} - \rho \frac{1}{2} \nabla \phi_1 \nabla \phi_1 - \rho \frac{1}{2} \cancelto{0}{\nabla \phi_1 \nabla \phi_2} - \frac{1}{2} \cancelto{0}{\nabla \phi_2 \nabla \phi_2} \tag{2.25}$$

Focusing only on the horizontal velocity of the products of the two first-order potentials and assuming the position to be x = 0 yields: 2.25:

$$\left(\left.\frac{\partial\phi_0}{\partial x}\right|_{x=0}\right)^2 = \underbrace{(A_1^2+A_2^2)/2+}_{meandrift}$$
$$\underbrace{A_1^2\cos[2(\omega_1 t+\epsilon_1]/2+A_2^2\cos[2(\omega_2 t+\gamma_2)]/2+A_1A_2\cos[(\omega_1+\omega_2)t+(\gamma_1-\gamma_2)]+}_{sum-frequency}$$
$$\underbrace{A_1A_2\cos[(\omega_1-\omega_2)t+(\gamma_1-\gamma_2)]}_{difference-frequency} \quad (2.26)$$

Several trigonometric properties have been used to obtain the final form of this solution. One can distinguish the following in the solution:

- Several terms are independent of any of the frequencies of ϕ_1 or ϕ_2. These will result in a mean load acting on the floating body, independent of time and are therefore called the **mean-drift term**.
- Several terms consist of a summation of both frequencies of ϕ_1 and ϕ_1. These will result in a load of high frequency and are therefore called the **sum-frequency terms**.
- Several terms consist of a difference in the frecuencies of ϕ_1 and ϕ_1. These result in loads with a lower frequency than loads of both independent waves and are therefore called the **difference-frequency terms**.

As described above, the two regular incoming waves are able to cause excitation at frequencies different from the incoming wave frequencies. The contribution of these components can be relevant in the hydrodynamic analysis of an offshore (floating) structure.

Mean drift loads due to multiple regular waves of different frequencies and amplitudes can be found from

$$\overline{F}_i = \sum_{j=1}^{N}\left(\frac{\overline{F}_i(\omega_j,\beta)}{\zeta_a^2}\right)\cdot A_j^2 \qquad i = 1..6 \qquad (2.27)$$

$$A_j = \sqrt{2S(\omega_j)\triangle\omega_j} \qquad (2.28)$$

Here, a transfer function is created describing the mean wave loads caused by an irregular wave spectrum. The transfer function should be created by determining the mean wave loads separately for a regular wave of each frequency and each direction. From potential flow theory, the mean wave loads are important for wavelengths similar to those of the structure. However, for very low wave frequencies and high wave amplitudes, the viscous effects become apparent. According to [39], these viscous mean order wave loads are in the order ζ_a^3. Therefore, the mean wave drift loads caused on a cylinder are given from (2.45). The same holds for mean wave loads due to a current.

Slow drift loads are caused by differences in the mean wave pressure over time when a body is subjected to irregular incident waves [36]. The loads from an irregular wave spectrum can be found from equation (2.29). The terms 'T's are slow-drift Quadratic Transfrer Functions (QTFs) describing the in-phase and out-of-phase slow drift loads per unit incident-wave amplitude.

$$F_{i,slow} = \sum_{j=1}^{N}\sum_{k=1}^{N} A_jA_k\left(T_{j,k}^{i,c}\cos[(\omega_k-\omega_j)t+(\epsilon_k-\epsilon_j)]+T_{j,k}^{i,s}\cos[(\omega_k-\omega_j)t+(\epsilon_k-\epsilon_j)]\right) \qquad (2.29)$$

The expression can be made dependent on the mean-drift transfer function 2.27 using Newman's approximation [36], meaning only the first-order velocity potential has to be determined. Conditions for this are that the difference-frequency values are small and the transfer functions from equation (2.29) do not change much with the frequency.

Modeling trade-off: Second-order hydrodynamic loads

As explained in section 2.2.1.2, exposing a floating body to multiple waves with different frequencies can cause responses outside of the wave frequency region. In load and motion analysis, these effects will show a response in the low frequency part of horizontal motions and mooring line tensions. The following on prediction of these effects in aero-hydro-servo-elastic codes is found from literature:

- In early versions of numerical tools like FAST, second-order difference frequency responses were not included. As highlighted by Couling et al. [21], most low frequency responses and loads are underpredicted. This is most evident in the case of the surge response and mooring line tensions.
- Li et al. [59] later developed a numerical code which incorporated mean drift and slow drift loads. The new model (WINDSKLOE) was tested against wave basin experiments and (first order PF in) FAST. A significant decrease in error is found in the low-frequency motion response in the new model.
- Later, Bayati et al. [7] developed a method to incorporate second-order hydrodynamics effects in FAST simulations and compared the results to a first-order analysis and model experiments. The comparison showed the importance of including difference-frequency effects in floating wind simulations and states the effects can no longer be neglected in dynamic analysis.
- Duarte et al. [25] implemented a second-order difference-frequency approach in FAST and compared the results of hydrodynamic simulations against OrcaFlex. In OrcaFlex, both the Newman approximation approach and the full QTF solution were implemented and compared as well. A significant reduction of computational time was observed for the new FAST model and the OrcaFlex Newman approximation compared to the full QTF OrcaFlex solution.
- Duarte et al. [25] also showed that second-order hydrodynamic effects play a role mainly in wave-dominated load cases, i.e. with an idling or parked wind turbine.
- In [82], codes using potential flow theory underpredict tower base ultimate- and fatigue loads and codes using Morison equation overpredict them, in the case of a wave-only excitation. One of the reasons for underprediction is errors in modelling pitch response, which could be due to modelling non-linear loads. Reasons of excitation of non-linear loads are second-order difference-frequency effects, non-linear wave kinematics, wave stretching effects and the calculation of hydrodynamic loads at the instantaneous position of the floater.

Irregular waves

In the previous sections, potential flow theory was used to find an expression for a regular wave. Later, this is extended to an expression for two incident regular waves of different frequency and amplitude. In reality, a large water body usually consists of an irregular pattern of waves coming from many directions, with many frequencies and of many heights. One important assumption to make in the following is that all waves are considered linear, which makes superposition principle valid [36]. Due to this assumption, an irregular surface pattern can be decomposed as a summation of different regular waves with constant frequency and amplitude as shown in figure 2.2a. The frequency and amplitude of each wave component can be plotted in frequency domain to obtain a wave spectrum representing a given sea state. An important disadvantage is that individual phase shifts of the original surface elevation are discarded in this approach.

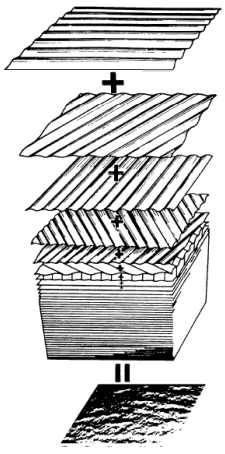

(a) An intuitive representation of the construction of an irregular surface profile from superposition multiple regular wave surface profiles [51].

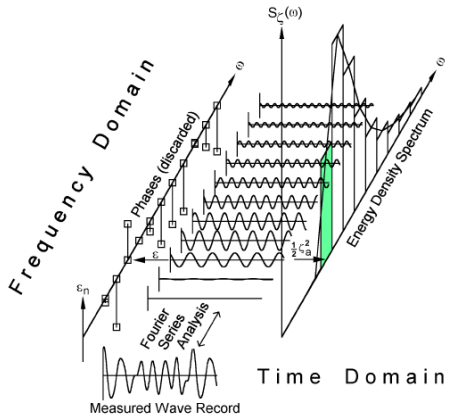

(b) An intuitive representation of the construction of an energy density spectrum form a measured wave record in time domain [51].

Figure 2.2: An intuitive explanation of the generation of a wave spectrum from a 'real-world' sea.

When no wave timeseries measurements are available, one can use a pre-defined spectrum to represent a sea state. One example for this is the JONSWAP (Joint North Sea Wave Project)-spectrum, which is commonly

used to describe waves in the North Sea. This spectrum was obtained empirically by considerable efforts of a wide range of projects [41]. Before development of the JONSWAP spectrum, the Pierson-Moskowitz (PM) spectrum was the predominatly used to describe sea states. The main difference is that the PM spectrum assumes a fully-developed sea [36], whereas JONSWAP is mostly used for seas with limited fetch. The equation describing this spectrum are given as:

$$S(\omega) = \frac{320 H_s^2}{T_p^4} \cdot \omega^{-5} \cdot \exp\left(\frac{-1950}{T_p^4} \cdot \omega^{-4}\right) \cdot \gamma^{\exp\left[-\left(\frac{\frac{\omega}{\omega p}-1}{\sigma\sqrt{2}}\right)^2\right]} \tag{2.30}$$

Where γ is the peakedness factor, which is usuallyt taken as 3.3 (when $\gamma = 1$ it equals the Pierson-Moskowitz spectrum). $\sigma = 0.07$ for $\omega < \omega_p$ and $\sigma = 0.09$ for $\omega > \omega_p$. In some cases, low-frequent swell which is generated far from the location of measurements can result in an additional energy peak at lower frequencies [42]. If one is interested in generating a wave field from a given spectrum, equation 2.31 can be used to obtain this surface elevation. Recall that when creating the spectrum, the phase shift has been discarded. That means that it is impossible to obtain the same surface elevation timeseries from a spectrum as the one used to create the spectrum. One can create a surface elevation with the same statistical properties, by assigning random phases following a uniform distribution to each wave component.

$$\zeta = \sum_{j=1}^{N} A_j(\sin\omega_j t - k_j x + \gamma_j) \tag{2.31}$$

$$A_j = 2\sqrt{S(\omega_j) \cdot \triangle\omega_j} \tag{2.32}$$

$$\gamma_j = Randn \in [0; 2\pi] \tag{2.33}$$

An important consequence of the linearised superposition principle explained in section 2.2.1.4 is that the loads and responses on a floating structure to an irregular sea state can be given by superposition of its response to each individual regular wave [36]. An approach for the latter has been described in the previous sections.

As shown previously, the relation between the incoming regular waves and the response of a floating structure are given by the linear transfer function (2.5). This can be used to create a response spectrum for a given incoming linear wave spectrum, assuming the response to be harmonic. The wave spectrum is given marked by the symbol ζ for clarity. The approach for this is given in equation (2.34).

$$S_j(\omega) = \left|H_{j\zeta}(\omega)\right|^2 S_\zeta(\omega) \qquad j = 1..6 \tag{2.34}$$

This gives a rather straightforward approach for a stochastic calculation of the response of a linearised system to a given linear sea state.

Wave spreading

These equations can be extended by creating a directional wave spectrum depending on the wave angle θ of each wave component. The directional spectrum is often represented using a spreading function [61]:

$$S(\omega, \theta) = S(\theta) \cdot S(\omega) \tag{2.35}$$

An example of a spreading function is the cosine distribution [74]:

$$S_d(\theta) = K(n)\cos^n(\theta - \theta_p) \tag{2.36}$$

$$K(n) = \frac{\gamma(\frac{n}{2}+1)}{\sqrt{\pi}\gamma(\frac{n}{2}+\frac{1}{2})} \tag{2.37}$$

Here, n is spreading exponent, θ is the wave direction and θ_p is the principal wave direction and K(n) is a normalizing constant. The form of this directional spectrum along each direction is the same and only its intensity varies as a function of direction.

If one is interested in representing a real-world sea state, the distribution is not equal. Its shape depends on the local weather situation at that moment for wind-wave components as well as on the weather in the whole water body in the recent past for any swell component [51].

Non-linear wave kinematics

Waves so far have been described by means of linear wave theory, which assumes low wave steepness. However, as the steepness increases, the description of a wave surface elevation as a simple sine function becomes inaccurate. In this section, a selection of higher-order wave models is provided. Each of the following theories is limited to the fact that only a steady, regular wave is considered in which all (linear and non-linear) components travel with the same celerity.

Stokes ([97], [96]) solved the potential flow theory problem while including higher-order terms. In Stokes theory, the measure of the steepness is small, H/L « 1, which means non-linear terms exist but are much smaller than linear terms. As a result, different solutions for the surface elevation can be provided. For the second order, this can be found as:

$$\zeta^{(2)}(x,y,t) = \frac{H}{2}\cos(kx-\omega t+\gamma) + \frac{H^2}{2L}\frac{\cosh(kh)(2+\cosh(2kh))}{\sinh^3(kh)}\cos(2(kx-\omega t+\gamma)) \tag{2.38}$$

Here, the $^{(2)}$ implies the solution is found up to the second order. The results are that the wave elevation has sharper peaks and shallower troughs, which gives a better representation of reality for waves of increasing steepness (see figure 2.3a and 2.3b). New phenomena are introduced by this solution. The wave celerity is now dependent on the amplitude and the particles in the wave slowly displace, which is called Stokes drift. Multiple Stokes 5th order solutions to the problem have been found, for example by [89] and [37]. Differences between provided solutions depend on the expansion variables used in the Taylor expansion.

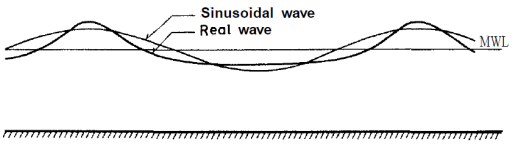

(a) A schematic overview of the differences observed between the surface profile of a linear (sinusoidal) and a non-linear (real) wave [98].

(b) An example of the real waves where a characteristic non-linear surface profile can clearly be observed [4].

Figure 2.3: A comparison between linear and non-linear wave theory and 'real-world' waves.

Dean Stream function

Next to the Stokes wave solutions, the Stream Function method is a way of describing non-linear wave kinematics [23]. The stream function fulfilled the need to find a method of uniform validity. It was first described by Dean by expanding stream and surface elevations into Fourier series. In derivation of the wave kinematics, the fluid flow is considered incompressible and irrotational. The difference from the solutions found before is that the streamlines of a flow are analyzed instead of the velocity potentials. The total streamline function ψ is then found as:

$$\psi(x_1,z) = B_0(z+h) + \sum_{j=1}^{N} B_j \frac{\sinh(jk[z+h])}{\cosh(jkD)}\cos(jkx_1) \tag{2.39}$$

Here, k is the wave number, B_j the undetermined coefficients and N the order to which the equation is solved. The goal is to find all wave parameters and at the same time determine the coefficients that satisfy the boundary conditions. By differentiation of the stream function, the velocity field is determined.

Applicability

Two important non-linear wave kinematic theories are described. Both give slightly different results in the wave velocity. The most important feature of the Dean Stream function is that the solution can be solved to a very high order without becoming incredibly complex. Therefore, it can be considered more accurate than Stokes theory for some applications, in particular at very steep waves. According to [99], solutions up to the

64th order are able to describe the steepest of waves. At values of h/L smaller than 0.1, Stokes theory fails to give accurate solutions of the velocity profile.

A graphic describing the applicability of different wave theories is provided in figure 2.4. Here, a suggestion of the wave model that gives the most accurate solution theory can be found depending on the dimensionless parameters $\frac{H}{gT^2}$ and $\frac{d}{gT^2}$.

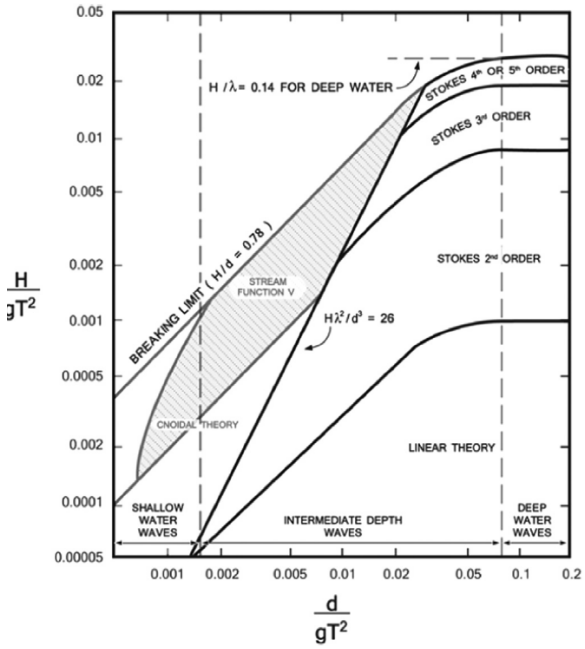

Figure 2.4: A theoretical overview of the applicable (non-linear) wave models for a certain range of dimensionless wave height and water depth [58].

Modeling trade-off: Non-linear wave kinematics

As explained in chapter 2.2.1.6, regular waves can be represented by linear or non-linear wave kinematics. The importance of using non-linear wave kinematics is highlighted by some studies.

- Robertson et al. [79] found that for the case of a bottom-founded rigid cylinder in regular waves, response peaks are found outside of the wave frequency excitation region. All participants using linear (Airy) wave theory were not able to capture these peaks in their simulations. The response in these frequencies is found to be caused by higher-order harmonics that are due to non-linearity in wave kinematics.
- Robertson et al. [81] found that for a bottom-founded flexible cylinder in regular waves, similar effects occur. A fully flexible cylinder introduces many extra degrees of freedom in the total system and therefore additional natural frequencies can be identified. Some of these natural frequencies were excited by non-linear wave kinematics and were therefore not captured by participants using linear wave theory. Also, the maximum loads occurring in the flexible cylinder were underpredicted by all participants using linear wave theory, as the sharper crests of non-linear waves result in higher wave particle velocities in the free surface and therefore larger peak loads. In the case a steep sloping section, all participants underpredicted hydrodynamic peak loads. In this case, wave breaking occurred causing extra peak loads, which was not included in any of the participants. Due to the deep water considered in the case of Hywind Scotland, wave breaking is considered beyond the scope of this thesis.
- Li et al. [59] confirm that for extreme wave events where the wave steepness increases, the use of linear wave theory breaks down. This resulted in underprediction of all motions outside of the wave-frequency region.
- Robertson et al. [82] found a significant underprediction in the tower base loads and mooring line tensions for many participants in the OC5 phase 2 project using a semi-submersible floating wind turbine. An explanation for this was the found in significant underprediction of the pitch response at natural fre-

quencies by all participants. These underpredicitons are possibly due to the fact that the natural pitch frequency is excited by some non-linear phenomenon in the system, such as non-linear wave kinematics, non-linear wave stretching methods or higher-order load effects. Another possible explanation could be due to the fact that loads are calculated at the instantaneous position of the floater.

2.2.2 Currents description

A current is described by a steady flow of sea water. According to [51], current is caused by ocean circulation, cyclic change in lunar and solar gravity (tides), wind at the free surface level and differences in sea water density (internal waves). [24] also includes long-shore currents and eddy currents. In general, a distinction is made between wind-generated current and the other types of currents [24].

Different current types can follow different vertical velocity profiles. The profile can be found from a summation of the different current contributions. Wind-generated current has its maximum velocity near the free surface, where wind shear stress is applied. It is likely to follow a linear profile (2.40) and disappear at a certain depth. Wind generated current at sea level is usually a small percentage of the mean wind speed at 10 meters height (2.41). Vertical velocity profiles from other current contributions are more likely to follow a (root)power law (2.42) and apply on the full water depth.

$$U_{c,w}(z) = U_{c,w}(0)\left(\frac{d_0+z}{d_0}\right) \quad (2.40) \qquad U_{c,w}(0) = k\cdot\overline{V}(10m) \quad (2.41) \qquad U_c(z) = U_c(0)\left(\frac{d+z}{d}\right)^{\alpha} \quad (2.42)$$

Similar to waves, current velocities apply up to SWL. They can therefore be stretched to the instantaneous surface elevation using Wheeler stretching (2.17). Currents can be described by means of a site-specific probability density function, created by a histogram of measurements. A probability density function that is proposed by [105] is a Gumbel distribution. The cumulative distribution can then be used to find the extreme current velocities for a given probability. For a given site, the current velocity may change direction over time. Consequently, a current rose can be created showing the probability of certain direction to occur or the tuning parameters of the Gumbel function for each direction.

2.2.3 Viscous hydrodynamic loads

Two important assumptions made in the derivation of potential flow theory are that the flow is irrotational and inviscid. The hydrodynamic model is extended in this section to include viscosity. Vorticity is included in the analysis of vortex shedding and its consequences. Then, viscous wave loads and regions of application are provided. In the explanation of viscous loads from a constant flow in this section, the cross-flow principle is assumed valid. The relative velocity of a flow past a cylinder is divided into its normal and axial components, which determine the normal and axial components of the drag force.

Viscous loads from a constant flow

As shown in [39], using potential flow theory to describe the loads of a steady flow on a cylinder result in a net zero force. This is referred to as D'Alembert's paradox. A more accurate response is found after including viscosity. The main difference between a viscid and inviscid fluid is that the fluid will be subject to a friction force when it flows past an object. As a result, part of the fluid velocity is reduced near the object, which is called the boundary layer [38]. The introduction of viscosity is accompanied by the introduction of several parameters:

$$Re = \frac{U_\infty \delta}{\nu} \quad (2.43) \qquad C_p = \frac{\triangle p}{\frac{1}{2}\rho U_\infty^2} \quad (2.44) \qquad C_D = \frac{F_D}{\frac{1}{2}\rho U_\infty^2 D} \quad (2.45) \qquad U_{turb} = \overline{U} + u' \quad (2.46)$$

Reynolds number (Re) gives the dimensionless ratio of kinetic energy to viscous damping in a fluid flow, and is used to quantify the level of turbulence. ν is the kinematic viscosity of a fluid. δ is the boundary layer thickness. In the case of a cylinder in a flow it can be replaced by the cylinder diameter D. The flow velocity is described by (2.46), where $\overline{U}$ is the mean flow speed and u' are the turbulent flow fluctuations. These fluctuations can take any frequency. C_p is the pressure coefficient, which is gives a dimensionless indication of the pressure difference between the body and the incoming flow. C_D is the drag coefficient, which gives the dimensionless drag load on a cylinder.

Turbulence is a result of small vortices which form when a flow is disturbed and is characterized as irregular changes in pressure and velocity [51]. The introduction of turbulence to a flow can lead to instability of

a boundary layer. The difference in velocity between the flow near an object and the flow further away from an object causes a pressure difference tangential to it [36]. When the flow is slowed down enough, a negative pressure gradient between incoming flow and flow at the body surface arises. This causes flow separation. The flow stream will no longer follow the body, but return to continue with the ambient incoming flow before the end of the cylinder.

The region behind the cylinder after separation point is called the wake. After separation, a flux of vorticity is shed from the body in the form of vortices [36]. Therefore, the wake can not be considered irrotational and potential flow theory does not hold. The way in which vortices leave the cylinder depends on the Re number. This flow of vortices can be both laminar or turbulent. If the boundary layer is laminar before separation, the flow will still become turbulent at some distance behind the cylinder. Figure 2.5 provides a general overview of the possible separation regimes. As the Re number increases, e.g. by increasing the flow velocity, the boundary layer can become turbulent as well. Usually, the instability point at which a boundary layer becomes turbulent is located upstream of the separation point on the cylinder. Therefore, the flow is likely to first become turbulent and later separate. For very low Re-numbers, the flow will remain laminar until it separates. As the number increases, the instability point moves upstream along the body until the flow becomes turbulent before it reaches the separation point. Disturbance on the incoming viscous flow causes a drag force, which is in line with the flow direction [51].

Equation (2.45) provides a dimensionless parameter called the drag coefficient. Once this is known, the drag force can be found for a given incoming flow velocity.

The frequency at which the alternate vortices are released from the cylinder is called the shedding frequency. Assuming the separation point is at the top and bottom of the cylinder so the distance between vortices equals the cylinder diameter the vortices travel with the same velocity as the incoming flow, one can then find the shedding frequency from equation (2.47). The shedding frequency can be made non-dimensional to obtain the Strouhal number (2.48). This number gives the ratio between the cylinder diameter and the distance covered by the inflow current during a shedding period [36].

$$f_v = \frac{0.28D}{U_\infty} \qquad (2.47) \qquad St = \frac{f_v D}{U_\infty} \qquad (2.48)$$

$$C_L = \frac{|F_L|}{\frac{1}{2}\rho U_\infty^2 D} \qquad (2.50)$$

$$F_L(t) = |F_L|\cos(2\pi f_v t + \alpha) \qquad (2.49)$$

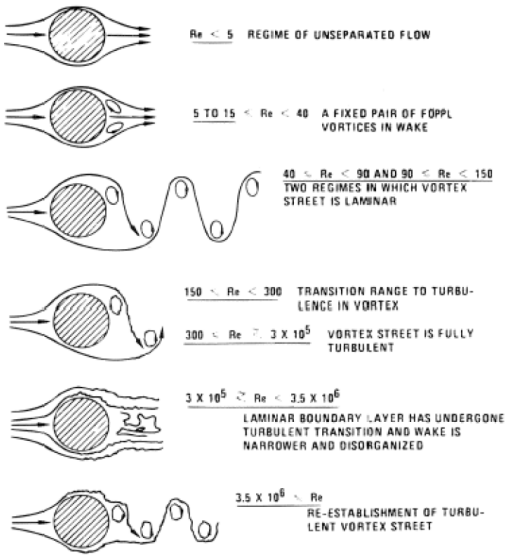

Figure 2.5: Ranges of expected wake behaviour for a flow in a cylinder of increasing Reynolds number [38].

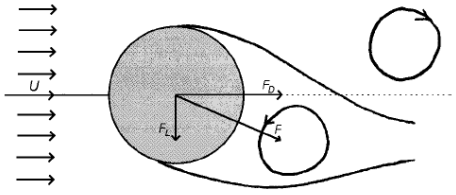

Figure 2.6: An intuitive representation of the pressure difference caused from vortex shedding [51].

A cylinder is symmetric for any incoming flow direction and will not cause any load components perpendicular to the drag force. An exception, arises when vortices shed from the cylinder. The pressure near a vortex behind a cylinder is lower than the ambient pressure due to an increase of the local flow velocity

[51]. The load component perpendicular to the incoming flow is called the lift force. An equation for calculating the lift force from vortex shedding is given by (2.49). This force can be made dimensionless by means of (2.50). Due to shedding, the lift component alternates with the shedding frequency and an initial phase shift, as depicted in figure 2.6.

As described by Journée and Massie [51], the moment in between the shedding of two vortices, a minor alternating drag force occurs. Therefore, a small pressure difference due to increased distance between a vortex and a cylinder causes a small drag force parallel to the flow direction. This cycle repeats itself for each vortex, so the frequency is twice that of the lift force: $f_d = 2f_v$.

$$F_D(t) = A_D \cos(4\pi f_v t + \beta) \tag{2.51}$$

As explained in section 2.1.1, a floating structure has a wide range of rigid and elastic natural frequencies. When the frequency of vortex shedding interferes with a natural frequency of the structure, resonance can occur [51]. These are referred to as Vortex Induced Motions in the case of (rigid) motion oscillations or Vortex Induced Vibrations (VIV) in the case of structural (elastic) oscillations. More on the effects of VIM and VIV on a structure can be found in [12].

Modeling trade-off: Flow separation

From literature it is found that only very few studies include the effects of currents in their validation. This can be due to absence of full-scale current measurements or difficulties of generating currents in certain wave basins. From studies that include current, the following can be concluded:

- In the case potential flow theory is used for simulations of an object in a steady flow, it will give zero loads if no Morison drag term is added (see section 2.2.3.1). As shown by Benitz et al. [8], using a Morison model to calculate the loads on a floater in uniform currents results in only a mean constant force. No transverse forces are captured by default. When comparing the results to a CFD model, one can observe that the latter does include flow separation effects. The mean inline force calculated by the Morison model is found to match the mean CFD force of the model.
- Dunbar et al. [26] found that the absence of flow separation in a numerical model caused errors in the natural period of a free decay event compared to CFD simulations. This error increases when the initial positions are made larger.
- During model validation of tools used to design the Hywind Demo project, mooring line tensions at low-frequency motions are found to be underpredicted [88]. One of the reasons given for this discrepancy is the absence of flow separation (and VIM) prediction capabilities in the numerical model. At low-frequency waves, flow separation could physically occur. However, other possible reasons given are the fact that the load case is wind-dominated and there could be a discrepancy between the simulated and measured wind field.

Viscous Wave Loads

So far, only the phenomena caused by a steady viscous flow are taken into account. As swell and wind waves are by definition varying in time, they can not be described as a steady flow. The importance of viscous forces from waves is classified in figure 2.7. As can be derived from this figure, for a high ratio of $\frac{\lambda}{D}$ and $\frac{H}{D}$, viscous forces become important. Several parameters are introduced.

$$KC = \frac{U_M T}{D} \tag{2.52}$$

$$U_M = \omega \cdot A_{wave} \tag{2.53}$$

The Keulegan-Carpenter number (KC) represents ratio of wave height to the structure characteristic dimensions [55], with U_M the maximum wave velocity. (2.53) provides a rule of thumb based on linear wave theory for the maximum occurring wave velocity. Alternatively, one can calculate a full timeseries of the wave velocity profile and isolate the maximum occurring velocity.

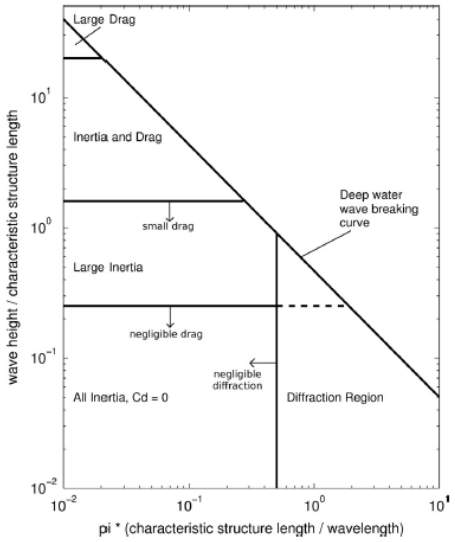

Figure 2.7: An overview of the expected inertia and drag contribution for a certain range of waveheight over structure length and structure length over wavelength [8].

A prominent way of calculating wave loads on cylindrical structures including viscosity is given by the Morison equation [70]. The equation is constructed by superimposing the inertia force obtained from potential flow theory and the the drag force obtained from viscous flows on a cylindrical structure [51]:

$$dF = \underbrace{A\rho C_M \frac{\partial u_1}{\partial t} dz - A\rho(C_M - 1)\ddot{\eta}_1 dz}_{Inertia\ component} + \underbrace{\frac{1}{2}\rho C_D D|u_1 - \dot{\eta}_1|(u_1 - \dot{\eta}_1)dz}_{Drag\ component} \tag{2.54}$$

Morison equation for a moving object is provided here, where the inertia component partially depends on the body acceleration and the drag component depends on the relative velocity between the flow and the body. The load is determined on a strip along a slender cylinder, as the inertia component originates from strip theory and long-wave approximation applied to the potential flow solution for a cylinder. However, using the appropriate drag and inertia coefficients and equivalent diameters, Morison equation is extended to other cross-sectional shapes as well.

The inertia component is not purely dependent on the relative acceleration because the potential flow Froude-Kriloff contribution does not depend on the body acceleration. A single added mass coefficient is used, therefore Morison equation is not able to account for hydrodynamic coupling effects that are obtained from the potential flow theory added mass matrix. Moreover, both the drag and added mass components are no longer frequency-dependent. On the other hand, potential flow theory does not account for water particle acceleration above SWL [56].

To obtain the time-dependent force, one should integrate the separate forces on strips over the entire length of the cylinder. The horizontal velocity and acceleration of the wave particles at the height of each strip along the cylinder can be determined from any wave model. It can be observed that the loads in the inertia component includes a term that is independent of the inertia coefficient. This is due to the fact that radiation loads are included for a moving body in water.

Modeling trade-off: Morison coefficient determination

One advantage of Morison models compared to potential flow models is that tuning of these coefficients allows to calibrate the model to measurements and therefore achieve a better match. As described in Kvittem et al. [56], each type of Morison calculation (i.e. load integration up to different levels) can be tuned to match potential flow theory in the wave-excitation region. On the other hand, determining Morison coefficients purely based on a theoretical approach often results in discrepancies. Several ways of determining the drag and added mass coefficients are found in literature. The following overview presents some frequently occurring methods.

- **Measurements**. As explained in section 2.2.3.3, coefficients can be tuned using measurements timeseries either by means of Morisons approach or a (weighted) least squares method. he idea behind this approach is that the inertia component and drag component are 90^o out of phase due to their dependence on the wave acceleration and wave velocity, respectively. Here, the fact that the added mass force contribution is in line with the acceleration and the drag contribution is in phase with the velocity is used. [79] uses 4 out of 20 measurement timeseries of different sea states for coefficient calibration. Also, C_D and C_M can be calculated using a Fourier transform approach. The advantage of this method is that the entire loads timeseries is considered in the analysis and therefore it can be considered more accurate. However, it is still accurate up to linear terms only.
- **Look up tables.** Publicly available empirical/semi-empirical relationships between certain hydrodynamic conditions like Reynolds number, KC-number, surface roughness and coefficients are available. Most relationships are based on experiments in which an infinitely long' cylinder is placed in a constant flow of varying speed and the drag terms are measured. These are referred to as look-up tables. In [79], some participants chose to use these to determine coefficients for each simulated sea state. Limited data is available for very low KC or very high Re numbers cases, which do often occur in the case of floating offshore wind turbines. Benitz et al. [9] showed discrepancies between look-up tables for a floating body, The main difference noted were floater bottom flow patter effects, as a spar buoy is not infinitely long.
- **Constant values.** Standards prescribe constant coefficient values for coefficients for certain wave conditions. In Robertson et al. [79], some participants use this approach to determine the drag coefficient. A frequently used value for C_d is 1.0. Utsunomiya et al. [103] uses multiple API standard prescribed values for both coefficients. It is found that certain values from standards yield better results than others.
- **Potential flow theory.** The solution to the radiation problem from first order potential flow theory (see section 2.2.1.1) can be used to determine added mass coefficients for Morison's equation. Kvittem et al. [56] state after thorough comparison that this does not necessarily yield the best agreement between Morison's equation and potential flow theory.
- **Computational Fluid Dynamics.** Benitz et al. [9] use OpenFOAM CFD software to predict the drag coefficients on a floating structure. This can prove useful as CFD includes 3D streamline effects, free surface, free end effects and vortex shedding to result in a more accurate flow representation.

As stated by Robertson et al. [79], the preferred method when comparing the results of different OC5 participants is either the least-squares approach or a look-up table. However, no unambiguous outcome to this matter is found from the current literature survey.

Modeling trade-off: Morison equation vs. Potential Flow theory

In this section, two main theories used in offshore wind hydrodynamic load calculations are explained. Both theories are widely applied and suitable for numerical simulations. Modern-day aero-hydro-servo-elastic software codes often support both hydrodynamic models. However, differences between theories can lead to differences in simulation accuracy.

In general, it can be observed that both theories are equally popular in the field of offshore wind energy. In some validation cases where potential flow theory is obviously not applicable, like current-only loads on a cylinder, Morison's equation is the preferred theory (see section 2.2.3.3). In large code comparison projects, differences between the two become apparent. In later studies, methods have been developed to use a combination of both theories. Researchers then add the drag term of Morison's equation to the general (2nd order) potential flow theory solution to account for viscous effects. In other cases [8], each component of a multi-member structure is evaluated separately in terms of applicable theory, which is then incorporated in numerical simulations. Most studies performed by a single research group, however, adhere to the use of one theory over the other. Kvittem et al. [56] explained methods of including non-linear drag coefficients to potential and Morison solutions.

- Neither one of the theories is capable of capturing vortex-shedding effects and resulting VIV events. One difference found by Benitz et al. [8], is the occurrence of shadowing effects. In many applications, Morison's equation assumes all components of multi-member structures to be subject to an undisturbed incoming flow field, whereas potential flow theory does take into account shadowing effects. In the same study, it is found that for small members, Morison's equation is the preferred theory, due to the dominance of viscous effects.
- In [79], it is found that a 3rd order harmonic response peak is not captured by models using potential

flow theory. This is explained by the fact that a model needs a non-linear drag term found in Morison's equation to properly capture this phenomenon. On the other hand, in cases where non-slender diffraction loads become more important, second-order response peaks are found to be overpredicted by models using Morison's equation.

- In [82], it is found that when simulating braced structures, it is important to include dynamic pressure on the top and bottom of horizontal columns. This is automatically included for potential flow theory models, whereas for Morison's equation this is not the case. The differences become apparent mainly when calculating heave motions. Kvittem et al. [56] also studied this effect, and found that this improves calculations.
- According to [56], the same results in wave-frequency region between Morison and potential flow solutions can be obtained, when Morison forces are integrated to the instantaneous surface elevation. The main difference occurs due to diffraction effects at small periods and faulty Morison coefficients selection.
- The most significant difference in the use of both theories is found from the OC5 project [82], where large differences in load prediction arise between the use of either potential flow theory or Morison's equation. Disparity is attributed to prediction non-linear wave excitation forces, which may be due to second-order potential-flow theory, higher order wave kinematics and application of wave-excitation at the instantaneous position of the body.

2.2.4 Hydrodynamic damping

Hydrodynamic damping gives the decrease of amplitude of oscillation of a body from cycle to cycle by forces in anti-phase with its velocity due to fluid-structure interaction. It is an extremely complex phenomenon in hydrodynamics that is not yet fully understood [85]. Several sources of hydrodynamic damping are identified and are explained in this section.

Solutions to linear potential flow theory radiation problem are an added mass and damping matrix that are frequency-dependent and are related to the dynamic pressure caused by the body motions. This damping term is referred to as linear wave-radiation damping, and goes to zero at infinitely low and high frequencies. It originates from energy radiated from the body in the form of waves as it moves. Given the linearity of the first-order radiation problem, this form of damping is often referred to as 'linear damping'. In practice, frequency domain numerical-panel method software like WAMIT is used to determine the solution to the determine $\mathbf{A}(\omega)$ and $\mathbf{B}(\omega)$. Ook gezien in OC3.

Wave-drift damping, provides damping of low-frequency motion in the horizontal plane due to interaction of the body with irregular waves. The incoming wave spectrum causes a mean drift-force in correspondence with second-order potential flow theory that dampens the slowly varying oscillations. The damping term itself also shows a slowly varying behaviour as it is dependent on the body velocity, which has limited effect on the response standard deviation but is relevant for calculating extremes [39].

The Morison equation for a moving body shows that the (viscous) drag component is dependent on the relative body velocity Therefore, it is considered a damping term in the solution. The viscous-drag contribution depends on the squared relative velocity between the fluid particles and the body, therefore it is often referred to as 'quadratic' or 'non-linear' damping [50]. It depends on the drag coefficient, making this damping term subject of theoretical investigation and tuning.

Next to the floater, mooring lines experiences hydrodynamic damping as well, which may give a significant contribution to the total system damping for floating offshore wind turbines. As the mooring system is designed to be fully submerged at all times, no wave-making capacity is expected here. Moreover, from potential flow theory it is known that the wave velocity decreases exponentially with the water depth. Therefore, mainly viscous drag damping related to the relative velocity between the line and steady currents (or still water) are expected to contribute to the total system damping. Here, again, the drag component from relative Morison equation is often used in practice.

Viscous damping from the floater and mooring lines depend mainly on slowly-varying body motion and therefore show mostly on the low-frequency part of the solution. Radiation damping, on the other hand, depends on the body oscillation period and consequently apply mostly in the wave-frequency and high frequency parts of the solution.

Modeling trade-off: hydrodynamic damping

Several studies point out the relative importance of viscous drag effects for the prediction of motions of a spar ([54], [47]). Due to the assumption of inviscid fluid and irrotational flow, potential flow theory models lack any viscous damping term. In some aero-hydro-servo-elastic software codes, the potential flow term is augmented with the Morison drag component to account for viscous effects. Similarly, it is found that Morison models do not account for radiation damping.

It is found that summation of radiation damping from linear potential flow theory and viscous damping from Morison equation often not sufficient to capture all real-world damping effects. One example is the comparison of decay-tests from the Hywind Demo system to aero-hydro-servo-elastic simulations, where additional linear hydrodynamic damping had to be added to the system to match decay amplitudes [47]. For a spar-type floating offshore wind turbine in this study, it comprised damping in the surge, sway, heave and yaw degrees of freedom. Additional linear hydrodynamic damping to the floater motions directly and not to the relative motion between the platform and wave particle velocities.

Another source of hydrodynamic damping is due to attached boundary layer flow, found from the 2D quadratic damping coefficient (see equation 2.55). This is used by [5] to explain a part of the difference between measured and the summation of radiation and viscous damping. Here, a viscous term may in fact have a linear contribution to the damping.

$$C_D^F = 4\pi\sqrt{\frac{\pi}{ReKc}} \tag{2.55}$$

2.3 Aerodynamics

The main purpose of a floating wind turbine is to harvest energy of the winds and convert it to active power. Wind loads cause a thrust force on the rotor, which results in an overturning moment of the total system. This thrust force and overturning moment make aerodynamic loading dominant in many cases. In this section, first several ways of describing wind are explained. Then, ways of calculating aerodynamic loading from these wind descriptions are provided.

2.3.1 Wind environment description

The wind environment describes the way air moves across the simulated spatial domain. Similar to viscous hydrodynamic effects, turbulent flows exists in the aerodynamic environment. It is more easily achieved than in hydrodynamics given the low flow viscosity, giving high Re-numbers at low flow velocities. In simulations, simplifications are made mainly in terms of turbulence description. Three ways of modeling turbulence are provided in this section: steady wind (no turbulence in the incoming wind flow), 2D varying turbulence and 3D varying turbulence.

Steady wind

Wind can be considered as a constant air flow with a mean velocity. As discussed before in section (2.2.2), a velocity of constant viscous flow is influenced the bottom friction. The velocity profile can therefore not be considered constant over the height of the flow. A widely accepted way of defining the mean wind speed over the height is given by the logarithmic profile (2.56). Here, z_0 is defined as the bottom roughness length which depends on the environment at which the wind turbine is placed. A wind turbine in rural environments can experience a roughness length up to 1 meter, whereas for an offshore turbine typically 0.0001 meter is assumed [24]. The height at which the mean wind speed is measured, h_{ref} is often different from the turbine hub height.

$$V(h) = V(h_{ref}) \cdot \frac{\ln\left(\frac{h}{z_0}\right)}{\ln\left(\frac{h_{ref}}{z_0}\right)} \tag{2.56}$$

The mean wind speed is subject to long-term time variation. Usually, probability density functions are derived for a certain location, based on a histogram with measurements of the mean wind speed in the past. A probability density function which is found to fit long term measurements is the Weibull distribution from equation (2.57) [24]. In order to include the wind direction, often a wind rose is created, this can indicate the probability of a given wind speed, but it can also define the shape parameters (a and K) of a Weibull function for each wind direction [10].

$$f(V) = \frac{k}{V}\left(\frac{V}{a}\right)^k \exp[-(V/a)^k] \tag{2.57}$$

Unsteady wind

Wind does in general not behave as a steady fluid flow. Due to the low density and viscosity of air, the smallest disturbances in the flow field can cause turbulence. This is measured as a random variance around the mean wind speed. Turbulence can be defined in terms of a certain turbulence intensity (TI) (2.59). Similar to the superposition of regular waves to determine a certain irregular wave pattern, the turbulence consists of a superposition of harmonic wind speed variations. Consequently, it can be defined by a spectrum as well. A widely accepted spectrum describing turbulence is the Kaimal spectrum from equation (2.58) [53].

$$S_{Kaimal}(f) = \frac{4(TI)^2 \overline{V} \cdot l_k}{1+6\frac{f \cdot l_k}{\overline{V}}} \qquad l_k = \begin{cases} 5.67h & h < 60m \\ 340.2 & h > 60m \end{cases} \tag{2.58}$$

$$TI = \frac{\sigma}{\overline{V}} \tag{2.59}$$

Combining the expressions for the mean wind speed and the turbulence intensity, a wind speed time-series can be generated. The set of equations is listed in (2.60). Note a random phase shift is applied to each turbulence oscillation frequency obtained from the spectrum to account for lost phase shifts.

$$\begin{aligned} V(t) &= \overline{V} + \sum_{p=1}^{M} b_p \cos(\omega_p t + \gamma_p) \\ b_p &= \sqrt{2 S_W(f_p) \triangle f} \\ \gamma_p &= randn \in [0; 2\pi] \end{aligned} \tag{2.60}$$

Spatially varying wind fields

A way of describing wind conditions is by creating spatially varying wind field. The wind field then varies both in space and time. Consequently, the wind velocity that the turbine encounters is no longer constant over the entire rotor. This gives a better representation of reality and therefore more accurate predictions.

A velocity spectrum describes a fluctuating velocity. This can be used to create a force spectrum. However, here, the cross-spectra for a 3D wind field play an important role as well. Spectral-tensor models can be used to model spectra and cross-spectra, and can therefore be used to predict loads on a wind turbine. These spectral-models should be accurately defined to represent the atmospheric boundary layer and the corresponding turbulence of the incoming wind flow. According to [17], most used models in the wind energy community are the Kaimal et al. [52], Veers [107] and Mann models. Here, the Mann model is recommended by the IEC to estimate loads on a wind turbine [20].

The Mann model can be used to determine the flow structure L in a turbulent incoming wind field. The Mann model [63] uses a frozen-Taylor assumption to represent a wind timeseries asa spatial wind field (equation 2.61. This means the advection caused by turbulent circulations is small and therefore the advection on a mean point can be assumed to be entirely due to the mean wind inflow. The flow is now coherent, meaning that properties like temperature and pressure will be advective with the mean wind speed.

$$\tilde{\mathbf{u}}(x, y, z, t) = \tilde{\mathbf{u}}(x - Ut, y, z, 0) \tag{2.61}$$

The same turbulence will be expected in another point in space and is therefore preserved at different spatial positions. Next, an isotropic flow is assumed, meaning that the same properties apply in the x-plane. The flow is considered incompressible and can therefore be described by linearized Navier-Stokes equations to estimate the effect of the shear on the turbulence [64]. The shear is considered linear. Large scale anisotropy applies, meaning:

$$\sigma_u^2 > \sigma_v^2 > \sigma_w^2 \qquad , \qquad \langle uw \rangle < 0 \tag{2.62}$$

The final Mann wind field can now be specified by three parameters: L, $\lceil$ and $\alpha\epsilon^{2/3}$. The result is a varying output of u, v and w with different variance.

2.3.2 Aerodynamic loads

Wind turbine blades generate a lift force from the wind flow. As seen before for objects in steady flow in section 2.2.3, this inevitably results in a drag force as well. In order to accurately determine the lift and drag force on the blades from simulations and in turbine design, several aerodynamic load prediction models can be used. For the scope of this thesis, the steady BEM-code is described.

The Blade Element Momentum (BEM) is proposed by [40]. Here, the distribution of the thrust (resulting in tower loads) and torque (resulting in power) loads over the length of the blade are obtained. The blade is divided into elements of a single size dN. Here, each element is considered as a constant airfoil with a given chord (c), pitch angle (θ_p), twist angle (β), lift coefficient (C_l)and drag coefficient (C_d). Many parameters vary as a function of the radius (r) of the blade, as the blade geometry is not constant to optimize the turbine power output. The lift and drag force of an airfoil are given as:

$$F_L = \frac{1}{2}\rho V_{rel}^2 C_l(\alpha) c \qquad (2.63) \qquad F_d = \frac{1}{2}\rho V_{rel}^2 C_d(\alpha) c \qquad (2.64) \qquad \alpha = \phi - (\beta(r) + \theta_p) \qquad (2.65)$$

α equals the local angle of attack, which depends on the blade pitch and local blade twist, as well as on the angle between the rotor plane of rotation and the relative velocity ϕ (equation 2.65). The velocity triangle is used to determine these angles and the relative velocity, which can then be used to calculate the loads on each section (see figure 2.8). Here V_a is the axial velocity through the rotor, given by the incoming wind speed wind speed V_0 and axial induction factor a as $V_a = (1-a)V_0$, where a gives a relationship between the wind speed before and after passing the rotor.

The set of equations used is given in (2.66). The normal force on the blade F_N is integrated to obtain the thrust on the blade, which is multiplied by the blade number (B) to obtain the total thrust. Similarly, the tangential force on the blade F_T is integrated to obtain the total power generated by the rotor. The process is iterative, an induction factor is assumed, after which angle of attack, lift and drag coefficients and aerodynamic loads are determined, which give a new induction factor until it converges to below a certain tolerance.

$$\begin{aligned} F_N(r) &= F_L(r)\cos\phi(r) + F_d(r)\sin\phi(r) \qquad (2.66)\\ T &= B\int_r F_N(r)\,dr \\ F_T(r) &= F_L(r)\sin\phi(r) - F_d(r)\cos\phi(r) \\ P &= \omega B\int_r r F_T(r)\,dr \end{aligned}$$

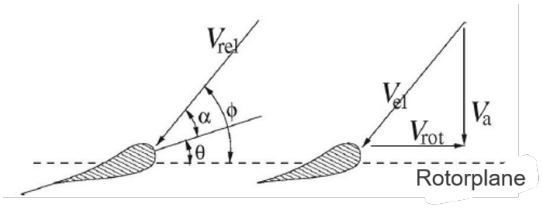

Figure 2.8: Radial cut in a wind turbine rotor and definition of the velocity triangle for a blade section. Adapted from [40].

2.4 Restoring forces

When a dynamic excitation force cause a displacement of the floating structure, restoring forces act to bring it back to its equilibrium position. Two types of restoring forces are distinguished: hydrostatics and mooring tensions. Here, hydrostatic restoring forces describe the stability of the body. Both are explained in this section.

2.4.1 Hydrostatics

The most basic load acting on a floating body is the buoyant force. This phenomenon was discovered by Archimedes a long time ago. Unfortunately, his work is not citable, but the physical law still carries his name: the Archimedes law (2.67). For a freely floating body in still water the buoyant force should equal the gravitational force.

$$F_B = \rho g \nabla = F_g \qquad (2.67)$$

Here, ρ and ∇ are the density and displaced volume of the fluid in which the body is floating. For complex structure geometries, volume integrals are required to obtain the buoyant forces. The buoyant force can change over time when the body is subjected to waves, as the submerged volume of the body will consequently.

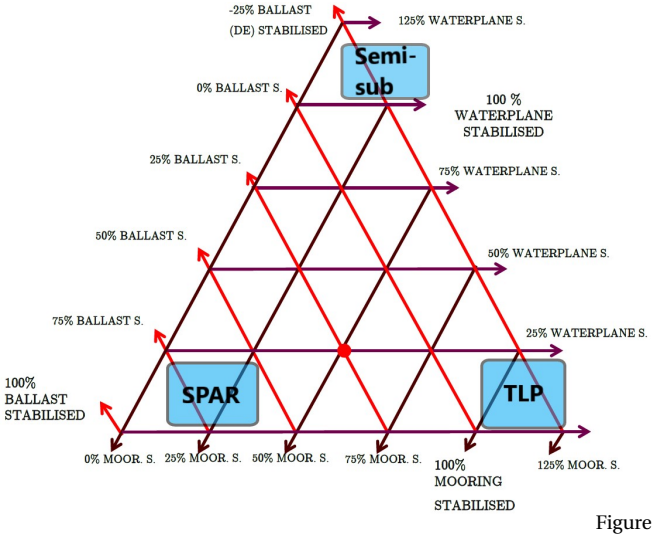

Figure 2.9: The stability triangle as defined by Borg and Collu [11].

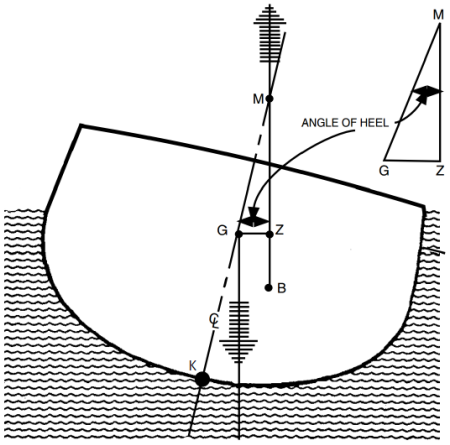

Figure 2.10: A schematic representation of the stability of a freely floating body [11].

Hydrodynamic stability for floating structures can be provided either by ballast, water plane stability or mooring systems [11]. This is depicted in figure 2.9, where ways of stability for different types of floaters are categorized accordingly. As can be observed, a spar buoy is mainly of the 'ballast stabilised' type with a slight contribution of stability from the mooring system.

The hydrostatic stability of a floating body of any shape is depicted in figure 2.10. Here, the geometric properties of the body are illustrative. K refers to the keel depth, G refers to the centre of gravity and B refers to the centre of buoyancy. Stability of the system is given by the value of GM_x. If GM_x is positive, the system is stable. If GM_x is zero, the system is meta-stable. The physical interpretation of stability is that the buoyant force counteracts the gravitational force thus the body is forced to return to equilibrium position. BM_x is calculated from (2.69).

$$GM_x = KB + BM_x - KG \tag{2.68}$$

$$BM_x = \frac{I_x}{\nabla} \tag{2.69}$$

When the body rotates, the change in the submerged body geometry causes a restoring moment, which is calculated from equation (2.70). All of these equations assume small rotations. Due to ballasting of a spar, the centre of gravity is made low compared to its centre of buoyancy hereby increasing stability.

$$\tau = GM_x \cdot F_B \tag{2.70}$$

In order to construct a restoring coefficient matrix **C** (see equation 2.1), the increase in buoyant force or restoring moment due to displacement of the structure is determined. Contribution to the hydrostatic restoring moment are in the heave, roll and pitch directions only for a freely floating body. The generalized restoring loads are then given from equation 2.71 [39].

$$\mathbf{F}_{k,restore}(t) = -\sum_{j=1}^{6} C_{kj}\eta_j \qquad k = 1..6 \tag{2.71}$$

2.4.2 Mooring Loads

According to [51], any mooring system is made of a number of lines (chain, wire or synthetic rope) with their upper ends attached to different points of the floating structure and their lower ends anchored at the sea bed. Pre-tension is applied to lines to ensure the system exerts a load on the floating body for all displacements, i.e. to prevent slack of the lines under all conditions. As the mooring system is connected to the floating body throughout its lifetime and the loads are mostly due to to rigid body motions, it is also possible to 'internalize' the loads as additional coefficients in the restoring matrix **C**. Here, the mooring restoring matrix can be obtained from a change in mooring stiffness due to body motions. Note that the presence of a catenary

mooring system also changes the static equilibrium position.

$$\mathbf{F}_{k,restore}(t) = -\sum_{j=1}^{6}(C_{hydrostatic} + C_{mooring})\eta_j \qquad k = 1..6 \tag{2.72}$$

Catenary mooring loads are due to the fact that for system displacements the position of the mooring end connected to it changes. This changes the lines weight in water, as a part of it will be lifted from the seabed or placed on the seabed [16]. Each of these are used throughout varying concepts of floating wind energy.

Static loading provided by catenary mooring systems can be divided into three parts: a displacement part which describes the loads caused by displacement of the centre of gravity of the mooring lines, a deformation part caused by (elastic) deformation of the mooring lines due to body motions and a friction part, which is caused by the part of the mooring system laying on the seabed [51]. Firstly, due to the tightening of the mooring line when the body moves away from the anchor, the bottom part is lifted from the seabed and its gravitational forces increases. Secondly, the angle between the mooring line and the floating body increase and its load component becomes more horizontal. The combined loads from these phenomena results in strongly non-linear behaviour of the mooring system for horizontal displacements of the floating body [16]. Usually, restoring forces from mooring systems are low and are mainly used to withstand mean loads acting on the system. Due to the non-linearity, however, large mooring peak loads can be found [16].

Additionally, dynamic effects can play an important role in the loads exerted by a mooring system. These are mainly caused by the fact that a full-scale mooring line can be seen as a large submerged structure itself. Diameters of a catenary mooring line can be significant, with up to 0.5 meters in the case of Hywind Scotland [35]. Segments of mooring lines can be considered as submerged cylinders, which are subject to loads as explained in 2.2.3. When the body is moving from its equilibrium position, mooring lines move through water, causing drag forces on the line itself. Moreover, waves and currents can cause drag forces on non-moving mooring lines. In unfavourable conditions, mooring lines could therefore be subject to VIV. Due to their geometry this is very unlikely to occur [16] on catenary mooring lines.

A popular way of calculating the behaviour and loads of a dynamic mooring line is the lumped mass method, as described by Van den Boom [104]. In this method, a mooring line is divided in a finite number of segments. The properties of each segment, such as added mass, damping, length and material properties, are 'lumped' into the nodes between each segment. Consequently, a set of equations of motion can be constructed describing each node and its behaviour due to motions of the body and external (hydrodynamic) excitation of each node. This set can be solved using a numerical solver. The nodes are connected by linear springs. Here, frequency-independent coefficient can be used for normal mooring chains and wires [51]. Torsional springs can be applied between nodes to give a more detailed representation of the mooring line system including bending stiffness [74].

Additionally, sea bed friction can be modeled by adding dampers to the nodal connections at sea bed. Moreover, the spring stiffness can be increased to account for soil friction [51].

Mooring response due to act mostly in the horizontal plane, i.e. in surge, sway and yaw motions. The stiffness in these degrees of freedom generally low and result in large natural periods, in the order of 1 minute or larger [39]. Wave spectra are often of higher frequency than this. Difference-frequency loads, however, may cause excitation of the horizontal motion. A visual representation of the mooring line excitation by slow drift is given in figure 2.12. As the hydrodynamic damping at these frequencies is usually low, they could result in severe resonance conditions of the floating body. Mooring chain structural damping due to internal friction between chain links could provide up to 80% of the total damping of horizontal motions of the moored system [43]. Given the long oscillation periods, the response resembles that of a body in steady flow. Therefore, hydrodynamic drag provides a second source of damping for mooring resonance.

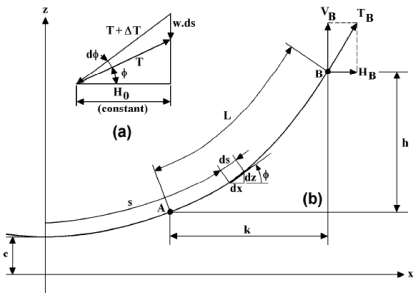

Figure 2.11: A schematic representation of a catenary mooring line [51].

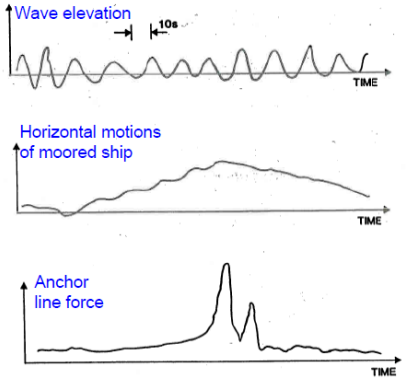

Figure 2.12: An intuitive representation of the mooring line tensions due to higher-order wave elevations [39].

In order to simplify computational efforts for simulations, a quasi-static approach can be chosen. Here, mooring line response is modeled by its static restoring terms at each timestep. This is correct when mainly the floating body loads and motions are of importance or when the mooring loads are small compared to the overall body loads [74]. According to [108], there are certain limitations to the use of quasi-static mooring theory. These are mainly important when excitation of the system at wave-frequency takes place and the body is subject to relatively high accelerations. Moreover, difference-frequency response of the system occurs can not be accurately described by this approach. Spar-type floaters with very deep drafts are noted as possible victims to inappropriate modelling by quasi-static mooring approaches. This is different from traditional moored structures like floating production storage and offloading (FPSO) systems used in oil and gas exploitation, where the body mass is relatively large compared to that of the mooring lines.

Literature: Mooring line theory

Three models are used throughout literature to simulate mooring loads: a simple spring model, quasi-static mooring theory and dynamic mooring theory. The latter two are most sophisticated and are explained in section 2.4.2.

- In studies using a simple linear spring model, the mooring system is often represented by adding terms to the restoring coefficient matrix in the equations of motion. In the case of Li et al. [59], this resulted in inadequate representation of coupling effects in the response. Dunbar et al. [26] used a simplified restoring matrix too, which resulted in underprediction of the amplitude and natural periods of a heave and pitch decay test.
- Most other studies considered make use of either quasi-static or dynamic mooring theory. In short, nearly all studies that make use of quasi-static mooring theory obtain unsatisfactory results in the load analysis. In some cases, the horizontal motions are predicted correctly, though still the natural response is often simulated with large errors.
- Utsunomiya et al. [103] states that the use of quasi-static mooring theory gives results far off from the measurements at the case of an extreme wave event. Couling et al. [21] names the use of quasi-static mooring theory as one of the reasons for large errors in the predicted mooring line tensions at low frequencies. A direct comparison between dynamic and quasi-static mooring theory is seen in the OC5 project, where either one of the theories is used by participants [82]. It becomes clear that the mooring line tension RAO's are underpredicted by participants using quasi-static mooring theory. Therefore, the motions are predicted with relatively low errors, while the loads are significantly underpredicted. The ultimate and fatigue mooring line tensions are underpredicted by all participants, but the participants using mooring line tension are far off and therefore not considered in the mean loads of all participants.
- Matha et al. [66] obtains similar results for quasi-static and dynamic mooring theory. But here it is stated explicitly that this is due to the generally simplified set-up of their model.

2.5 Model validation methodology

The goal of numerical model validation is to increase the validity and reliability of the model's descriptions and predictions, and thereby its modelling performance. Applied to aero-hydro-servo-elastic codes, validation might provide FOWT designers with more confidence of having the information necessary for making decisions that influence the time, cost and risk associated with their product development. The aim of this section is to find trends in the methodology used for aero-hydro-servo-elastic model validation throughout literature. Here, methodology is defined as 'methods': specific procedures or techniques used to identify, select, process, and analyze information about a topic. A scheme of model validation methodology is described in figure 2.13. It is used as a basic model to classify approaches of validation of aero-hydro-servo-elastic models, and numerical models in general, found in literature for each validation step.

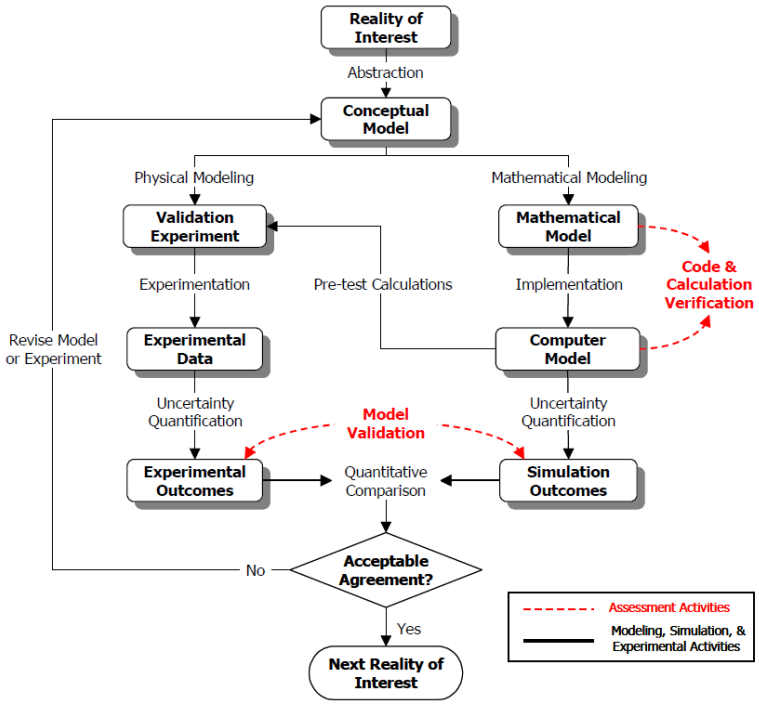

Figure 2.13: Model validation methodology. Adapted from [101].

The application of each step to aero-hydro-servo-elastic model validation is elaborated, as is applicable to this study. This is done made on a literature survey, of which main outcomes are compared in table A.1 in the Appendix.

Conceptual model

conceptual model involves identifying the computational objective, required level of predictive agreement of the model, the domain of interest, all physical processes and assumptions and the quantities that form the basis for comparison (validation metrics) [101]. The objectives for validation projects found vary widely within literature:

- Comparison of a different aero-hydro-servo-elastic codes on a range of validation metrics to gain a general overview of the state-of-the-art and identifying fields of code improvement ([48], [79], [82]);
- Comparison of different model set-ups in a single or multiple codes for capturing detailed physical phenomena ([21], [56], [8]);
- Validation of a newly developed code or a newly developed feature in a code ([60], [26], [59]);
- Showing the performance of a certain (newly developed) full-scale floating offshore wind turbine system ([88], [103], [15])

Modelling steps

Reality at first is modelled in terms of a physical and mathematical model, where the physical model refers to measurements of the that represent the environmental conditions and system behaviour of the real-world system, and the mathematical (or numerical) model refers to a FOWT model, to be translated into a computer model using an aero-hydro-servo-elastic code. All physical phenomena of interest are translated from their mathematical expression to a computer model. Here, assumptions are made regarding the structural dynamics, hydrodynamics, aerodynamics and mooring theory, as well as numerical discretization parameters used in predicting the dynamic system response. Sections 2.1 through 2.4.2 provide a broad analysis of types of mathematical modeling in the field of aero-hydro-servo-elastic code validation and considerations found in recent validation studies.

Three main types of physical models used to generate results used in comparison against aero-hydro-servo-elastic codes can be distinguished: results from numerical models of similar or higher accuracy ('code-to-code comparisons'), measurements from model-scale experiments and full-scale measurements on the real-world system ('one-to-one comparisons'). A measure of preference of type of physical model for different requirements is found in table 2.1. A detailed discussion on this is found in Appendix B.

Physical model requirements	**Aero-hydro-servo-elastic code**	**High-fidelity code**	**Model-scale experiment**	**Full-scale measurements**
Control over input conditions	++	+	+	-
Control over validation metrics	++	++	+	-
Capturing physical phenomena	-	+	+/-	++
Modeling of full system	+	-	+	++
Measurement repeatability speed	++	+	+/-	+/-

Table 2.1: An overview of the measure of preference of different type of physical models for different requirements.

Uncertainty

An uncertainty analysis can be made of the numerical and physical model to map the level of certainty of their results, which may give further insight in the importance of different error sources. In validation studies found in literature, however, quantitative assessment is often considered beyond the scope of validation studies, where sources of uncertainty are only addressed in a descriptive way. In recent studies, increasing attention to this subject is found ([78] and [78]), though this is mainly in the use of model-scale experiments.

Assessment activities

A distinction is generally made between code validation and verification. For the scope of this report, validation is defined as comparison an aero-hydro-servo-elastic code with full-scale measurements, where verification refers to code-to-code comparison, based on [76]. This general definition is due to the nature of each physical model: codes are useful in the generating controlled results from controlled inputs with high iterative ability, whereas full-scale measurements model the contain all detailed physical phenomena.

Quantitative comparison

Roughly three types of error sources may be defined in model validation:

1. from limitations in the model capacity
2. from errors in the model set-up
   - in the system model set-up
   - in the environmental conditions
3. from measurement errors

One may argue that only information to mitigate error source 1 is useful to achieve the goal of increased confidence in model predictions. Therefore a 'pure' comparison is desired, i.e. in which error sources 2 and 3 are minimized. Error source 2 could be sub-divided in set-up of the system model and the environmental conditions. As seen in Appendix A.1, both error sources are likely to occur in model validation. Full-scale measurements are considered the best to make a comparison of type 1 errors because all physical phenomena are captured. However, detailed information on the full-scale system is often limited, as well as correct environmental condition measurements. Moreover, the system is usually subjected to complex environmental conditions, i.e. a combination of wind, waves and currents each with their own intensity and direction,

which all give rise to type 2 and 3 errors. Therefore, model verification is often used as a step in the validation process with the aim of minimizing these error sources, as well as providing general insight in the behaviour of the modeled system.

Error analysis

Outcomes from physical modeling and numerical simulations are compared in terms of their validation metrics, after which a decision on the level of their agreement is made. In case discrepancies are observed, the model can be revised to improve agreement.
An analysis of errors found from validation can done on four levels:

1. Description of errors observed which are left to be explained in future research.
2. Explanation of these possible source(s) of errors observed and how they may be demonstrated or reduced.
3. Demonstration of errors to confirm they are caused by a certain source.
4. Mitigation of errors by removing the error source.

Each step can be performed in either a qualitative and quantitative fashion. Here, qualitative analysis of errors could be defined as an analysis of the occurrence of physical phenomena and possible reasons for their absence in simulation results. This can be substantiated in a quantitative way, e.g. providing a numerical error measure or rate of mitigation. Each comparison step further increases the level of confidence in simulation results. However, each step requires additional insight in the model, which may be limited e.g. by lack of theoretical background, access to the modeled or physical system or simply by lack of time. These may also limit the possibilities of providing numerical substantiation of qualitative errors.

In literature, comparisons are made using all four levels of analysis of errors. In much published work, conclusions are limited to description and explanation of validation errors. Moreover, any type of validation metrics found suitable for analysis is used interchangeably. Examples of frequently-occurring validation parameters are:

- Eigenmodes, static equilibrium position;
- Rigid body motions, velocities and accelerations timeseries.;
- Structural response, usually at tower bottom or tower top;
- Mooring lines tensions;
- Rotor thrust, torque, blade pitch angle or blade tip deflection;
- Generator active power or rotor (shaft) torque;
- Detailed system parameters, e.g. hydrodynamic coefficients.

Where validation metrics vary from: frequency domain analysis (PSDs, RAOs, TFs, 'effective' RAOs), direct timeseries comparison, statistics, scatter plots etc. Some validation metrics can be translated to prediction of the real-world system performance: equivalent fatigue damage (loads), ultimate design loads, annual energy production or even directly to costs.

No standardised approach using prescribed validation metrics are found across research project, let alone a total measure of a code's performance that can be used to compare different codes. Often, any metric that suits an analysis is seized. This is closely related to the wide variation of research objectives found earlier. One aiming to give an overview of detailed hydrodynamic phenomena may for example prefer comparison of spatial variation of Morison coefficients [8], whereas one aiming to show the performance of a new FOWT prototype is more interested in the generator power for varying waveheights [15]. On top of that, the availability or capacity of the physical model to a research project limits possibilities of validation metrics.

Conclusion for research approach set-up

For the purposes of this study, the performance of a code is defined as its validity: the level of agreement between the computational results from running the code (or simulation model) and from the measurements from a real-life system, that the code is compared to and might be based on.

The process of validation is defined as: establishing the level of agreement or validity level of a code. In this study this is operationalised by defining the number of modelling errors, their gravity and their (potential) effects in relation to pre-defined model parameters (e.g. load and motion simulations), and analysing sources of errors.

Increasing the performance of a code to a required level, by mitigating or avoiding errors, results in an increase in its explanatory and predictive capacity, and therefore in its validity.

2.6 Final research objective and questions

From this preliminary literature survey, the following main research objective has been established:

The purpose of this MSc. thesis project is to contribute to the validation of the performance of aero-hydro-servo-elastic software, by comparing the results of its theory-based simulations to the results of equivalent simulations, and to the results of measurements of a unique real-world floating offshore wind turbine, and by recommending what improvements could be integrated into simulation models.

The following main research question has been established:

How can load and motion simulations in BHawC/OrcaFlex aero-hydro-servo-elastic software be improved by using full-scale measurements of the Hywind Scotland floating offshore wind farm, leading to a higher performance level of the code?

The research question was decomposed into the following sub-questions:

- How do BHawC/OrcaFlex simulations perform in floating offshore wind turbine load and motion predictions compared to other aero-hydro-servo-elastic software codes?
- How do OrcaFlex simulations perform in load and motion predictions, compared to equivalent simulations by a variety of industry-standard aero-servo-hydro-elastic software codes on a floating offshore wind turbine model that resembles the Hywind Scotland system?
- How do BHawC/OrcaFlex simulations perform in floating offshore wind turbine load and motion predictions, compared to full-scale measurements of the Hywind Scotland floating offshore wind farm?
- How can the performance level of BHawC/OrcaFlex be increased, by using the results of the comparisons of its simulations to both the results of equivalent simulations and to the results of the measurements of the Hywind Scotland floating offshore wind farm?

2.7 Final research approach

In this section, the final research approached of this report is outlined. A visual outline is provided in figure 2.14 This is used to find an answer to the previously defined research questions.

Validation concept BHawC/OrcaFlex is validated using full-scale measurements as a physical model. The objective of this research can be categorized in 'validation of a newly developed aero-hydro-servo-elastic'. For this, measurements of the Hywind Scotland floating offshore wind farm are provided by Equinor, as well as an as-built full-scale system description. A wind turbine model and aerodynamic environment are provided in BHawC which were both separately validated. The wind turbine model contains all as-built system parameters, as well as the as-built control system of the Hywind wind turbine.

Modeling steps Mathematical and computer implementation take place in OrcaFlex. The BHawC turbine model is considered as pre-defined for the scope of this thesis and only modeling is done in definition of different inputs for load cases. An OrcaFlex model of the floater is not available and has to be set up for the purpose of this project, before it is coupled to BHawC to obtain a final BHawC/OrcaFlex model. Limited information on the as-built floater-mooring system is available from Equinor and SGRE, which requires several system parameters to be based on theory. The theoretical background modeling trade-offs from this chapter are used. The provided measurements on hydrodynamic environmental conditions are analysed thoroughly to support theoretical steps taken in the model set-up.

Assessment activities The combined description of the system, environmental conditions and measurements is very detailed but not exhaustive, which inherently leads to type 2 and 3 errors. Therefore, BHawC/OrcaFlex must be verified to mitigate error sources, as well as having them explained or demonstrated prior to this validation step. This is achieved by code-to-code comparison against OrcaFlex aero-hydro-servo-elastic code. The reason for this is two-fold: the floater-mooring system used in BHawC/OrcaFlex can be copied to the OrcaFlex-only model. Moreover, the hydrodynamic environment can be set up in an identical way, which reduced the possibility of type 2 errors in this verification step.

The Hywind turbine is not available in OrcaFlex and has to be set up for the purpose of this project. This is done using SGRE documentation on the BHaWC Hywind turbine model.

Due to its novelty, limited information is available on the OrcaFlex aero-hydro-servo-elastic code and its performance for spar-type FOWT. In order to gain sufficient confidence from the comparison to BHawC/OrcaFlex verification step, OrcaFlex in turn is verified against industry-standard aero-hydro-servo-elastic codes. The additional benefit of this is the separate verification of the OrcaFlex spar-type floater-mooring system and hydrodynamic environment used in the final BHawC/OrcaFlex model for comparison against measurements. For this, the Offshore Code Comparison Collaboration (OC3)-project is selected because of: 1) a publicly available system description, environmental conditions description and all results from participants in the project. 2) a stepwise verification procedure in which complexity of the system and environmental conditions are increased one step at a time. 3) use of a FOWT system that closely resembles Hywind Scotland in terms of floater type, geometry and hydrodynamic environment. All three steps allow for a pure comparison of codes with detailed analysis of type 1 errors and straightforward identification of type 2 and 3 errors. Unfortunately, the turbine model used in the OC3-project is not available in BHawC and set-up is too time-consuming for the scope of this thesis work. Therefore, the additional step of verification to OrcaFlex and its verification were required.

Each verification step builds towards the final BHawC/OrcaFlex model validation. However, lessons learned in the form of all four types of analysis of errors can be used to: 1) augment the BHawC/OrcaFlex final model set-up beforehand and 2) help in the analysis of errors observed from validation.

Quantitative comparison and error analysis The Equinor measurements consist of timeseries of six degree of freedom (DOF) rigid body motion, nacelle motions and tensions in each bridle line. Statistics of both motions and tensions are compared. This gives general insight in the predictive capacities of the model. Timeseries are long enough for a decent frequency-domain comparison. Therefore, a comparison of PSDs is made to give more detailed insight in the predictive capacities of the system response across a wide range of excitation frequencies. This also extends the possibilities of analysis of detailed physical phenomena. Where possible, explanation and demonstration of errors are used to augment the validation and thereby increase confidence in the model. Mitigated errors are detailed in the model set-up description.

No standardized approach for quantifying the performance of an aero-hydro-servo-elastic code is found from literature. Therefore, conclusions of each validation or verification step list an qualitative and (where feasible) quantitative analysis of errors and lessons learned from mitigation of error sources in early revisions.

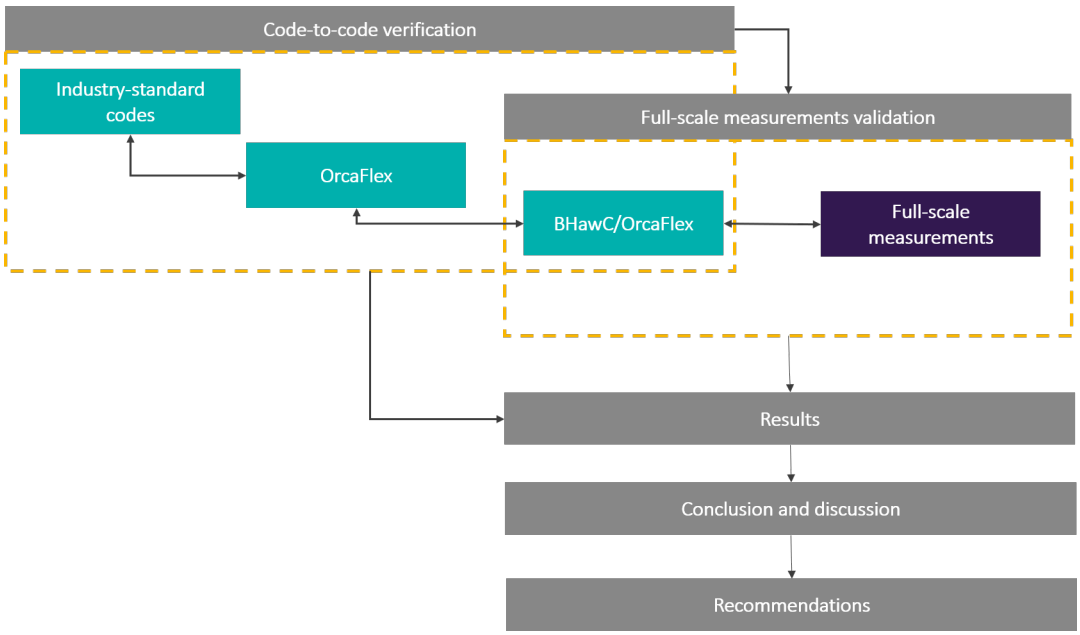

Figure 2.14: An outline of the research approach conducted in this report.

3

OrcaFlex verification to industry-standard codes

OrcaFlex aero-hydro-servo-elastic code is verified against industry-standard codes. This is done using a model set-up and results from the the Offshore Code Comparison Collaboration (OC3) project. The OC3-Hywind model is built in OrcaFlex and subjected to several load cases of increasing complexity. This is done in order to 1) gain confidence in the OrcaFlex hydro-elastic code, used later for validation of the coupled BHawC/OrcaFlex model with full-scale measurements and 2) gain confidence in the OrcaFlex hydro-aero-servo-elastic code, used later for preliminary verification of BHawC/OrcaFlex. In this chapter, an introduction to the OC3-project and relationship to this thesis work is given. Then, set-up of the model and decisions made are explained. In section 3.5, simulation results of all models is provided and errors are analysed.

3.1 Introduction to the OC3-project

The Offshore Code Comparison Collaboration (OC3), which operates under Subtask 2 of the International Energy Agency (IEA) Wind Task 23, was established to meet the worldwide need to verify the accuracy and correctness of aero-hydro-servo-elastic software codes [48]. Simulation of floating offshore wind turbines (FOWTs) under combined stochastic aerodynamic and hydrodynamic loading is complex. Comparison and verification, therefore, require a sophisticated approach that facilitates source identification of modeling discrepancies introduced by differing theories and model implementations in the various codes. This is possible only by (1) meticulously controlling all of the inputs to the codes and (2) carefully applying a stepwise verification procedure in which model complexity is increased one step at a time [48].

The OC3-project was performed among a group of international participants from universities, research institutions, and industry across various countries. The majority of FOWT-related aero-hydro-servo-elastic codes available at that time were tested within OC3. The project was executed using various load cases of increasing complexity, using prescribed environmental conditions as an input and a detailed prescribed model set-up. Furthermore, the turbulent full-field wind inflow and regular and irregular wave kinematics are model inputs controlled within OC3, which eliminates any differences caused by differences in turbulence models, wave theories, or stochastic realisations. This makes the results of this project highly suitable as a benchmark for aero-hydro-servo-elastic verification.

In Phase IV of the OC3-project, a FOWT model is verified. For this phase, an adaptation to the full-scale Hywind Demo system, the full-scale pilot preceding the Hywind Scotland wind farm, is made such that it can easily be implemented in various software codes. The original wind turbine was replaced by the publicly available NREL 5-MW turbine. This turbine is specified in detail w.r.t rotor aerodynamic properties, blade, drivetrain, nacelle, and tower structural properties and generator-torque and blade-pitch control system properties [49]. Some adaptations are made to the support structure and control system to prevent instability due to so-called 'negative damping' (Nielsen et al. [71], [87] and [57]). The adapted system is named the 'OC3-Hywind system' to distinguish from the original. The hydrodynamic and elastic properties of the varying offshore support structures used in the project are prescribed in detail by the OC3-Hywind definition ([47] and [48]).

The model input used in Chapter 5 all consist of stochastic environmental conditions with irregular waves and turbulent winds. Combined with an elastic structural wind turbine model, this causes a high level of complexity in the modeled system. Given the strong similarity between the widely tested and publicly available OC3-Hywind system and the later used Hywind Scotland model, the this project is selected to perform the first steps of this model verification approach. Orcina, the developer of the OrcaFlex software, previously compared OrcaFlex to OC3 participants results [72], but only considered the OC3 load case (LC)5.1 with deterministic wind and wave input. This is considered too limited to gain full confidence in the code.

3.2 Set-up of the general OC3-Hywind model in OrcaFlex

Orcina has built a publicly available OC3-Hywind model, the 'K01 Floating wind turbine' [73]. This model differs in several ways from the OC3-Hywind system prescribed by Jonkman [47]. The K01 turbine is mainly used to showcase OrcaFlex' latest features and modelling capacities of FOWT models. The OC3-project, however, took place in the years before 2010, when most aero-hydro-servo-elastic codes were less advanced than OrcaFlex is today. To make a pure code-to-code comparison, similar modeling theories should be used in each code. In this section, the model set-up is explained in terms of adaptations made to the publicly available K01 model instead of describing the model from scratch.

The K01 model uses a delta crow-foot connection, whereas the OC3-Hywind definition prescribes three single mooring lines, with equivalent properties to the delta connection. To compensate for the lost yaw-stiffness from the delta crow-foot connection, an artificial yaw stiffness should be included in the system. In OrcaFlex, mooring system is rebuilt according to the OC3-Hywind definition, by applying a yaw constraint with the appropriate rotational yaw stiffness to the floater centre line at fairlead depth. Next, the mooring line representation is changed from finite element method (FEM) to 'Analytic Catenary', which changes the mooring line theory from dynamic to quasi-static. The mooring line hydrodynamic drag and added mass, as well as seabed friction are therefore neglected (see section 2.4.2).

Wind loads on the tower and floater are disabled for consistency with other codes. In consultation with Orcina, some additional changes are made to the system, based on their experience in validating their wind turbine module.

- A generator mechanical to electrical conversion loss is of 94.4% is applied in the generator section. This is found to give a better approximation of the other codes.
- OrcaFlex does not automatically provides results for the tower shear. A Python script, provided by Orcina, is added to the model which externally calculates these values.
- A structural-damping ratio of 1% of the critical damping is prescribed by Jonkman [47] for all tower modes. This was not included in the original model nor recommended by Orcina. During verification it was discovered that tower damping is in fact necessary to obtain similar results as other codes, after which the model was updated and all load cases were re-run. Structural damping is realised in OrcaFlex by means of stiffness-proportional Rayleigh damping for the tower. Here, a response period at which the damping ratio will be achieved should be provided. For load cases in which OrcaFlex generates wave conditions, the wave period or peak period is used automatically. In LCs 4.2 and 5.3 in which externally defined wave conditions are used, the peak period is added manually to the system.

3.3 Load case table

The advantage of using the OC3-project as a benchmark for model verification is in its step-by-step increase of model complexity. New types of excitation are introduced in each load case, which helps to pin-point the influence of each of them on system response. Table 3.1 shows the load cases used in OC3 Phase IV. LCs 1.x are used to check structural properties of the system without external environmental conditions. LCs 4.x are wave-only cases using either regular or irregular waves. LCs 5.x are wind/wave cases using either steady or turbulent wind at below-rated, rated or above-rated regimes. LC 5.4 is used to create 'effective RAOs', i.e. to test the systems frequency response to wave excitation using nonlinear time-domain simulations. The word 'effective' distinguishes from typical RAOs that are found using linear frequency-domain techniques.

Load Case	Enabled DOFs	Wind conditions	Wave conditions	Analysis Type
1.2	Platform, tower, drivetrain, blades	None: air densitiy = 0	Still water	Eigenanalysis
1.3	Platform, tower, drivetrain, blades	None: air densitiy = 0	Still water	Static equilibrium solution
1.4	Platform	None: air densitiy = 0	Still water	Free-decay test time series
4.1	Platform, tower	None: air densitiy = 0	Regular Airy: H = 6 m, T = 10 s	Periodic time-series solution
4.2	Platform, tower	None: air densitiy = 0	Irregular Airy: H_s = 6 m, T_p = 10 s, JONSWAP wave spectrum	Time-series statistics, DELs, power spectra
5.1	Platform, tower, drivetrain, blades	Steady, uniform, no shear: V_{hub} = 8 m/s	Regular Airy: H = 6 m, T = 10 s	Periodic time-series solution
5.2	Platform, tower, drivetrain, blades	Turbulent: $V_{hub} = V_{rated}$(11.4 m/s), σ_1 = 1.981 m/s, Mann model	Irregular Airy: H_s = 6 m, T_p = 10 s, JONSWAP wave spectrum	Time-series statistics, DELs, power spectra
5.3	Platform, tower, drivetrain, blades	Turbulent: V_{hub} = 18 m/s, σ_1 = 2.674 m/s, Mann model	Irregular Airy: H_s = 6 m, T_p = 10 s, JONSWAP wave spectrum	Time-series statistics, DELs, power spectra
5.4	Platform, tower, drivetrain, blades	Steady, uniform, no shear: V_{hub} = 8 m/s	Regular Airy: H = 2 m, ω = 0.1, 0.2, ..., 3.5 rad/s	Time-series-generated "effective RAOs"

Table 3.1: Load-case table used in the OC3 Phase IV project.

For all cases, only selected output parameters are compared in the OC3 report that are considered useful in code comparison [48]. Only output parameters published in the OC3 report are considered for verification in this thesis work, as these are best available for comparison. LC 5.4 is considered beyond the scope of this thesis as LCs 4.x already showed good similarity and it is used in the report mainly to investigate the general capacity of codes, with less focus on comparison. After verification of LC 5.3 alone showed unexplained discrepancies, LC 5.2 is included in this comparison. Both LCs are analysed in terms of their turbulent wind only to gain additional insight in modeling errors.

3.4 Specific model set-up per load case

Next to the general model set-up described in section 3.2, each load case requires a specific additional set-up. This section shortly highlights additional modeling decisions made.

3.4.1 Load case 1.2: Eigenanalysis

First, a static equilibrium analysis is run, after which OrcaFlex provides a 'modal analysis' calculation of the first hundred system eigenmodes, ordered to increasing frequency. These modes are presented either as a visual animation or as a mode shape table for each system object. For this analysis, each natural frequency is identified manually by matching these animations to their corresponding mode shape descriptions found from [44].

3.4.2 Load case 1.4: Free decay tests

The tower, drivetrain and blades are made rigid. The tower's Young modulus is increased from $2.1{\cdot}10^8$ to $2.0{\cdot}10^{10}$ kPa. Here, a trade-off is made between sufficient stiffness to exclude tower bending response and numerical stability. Blades are be made rigid by an OrcaFlex option for 'fixed' blade DOFs.

Decay tests are executed using a winch object to impose an initial displacement to the system. The winch is released after reaching a new static position to perform a free-decay test. For pitch decay, two winches are assigned to the system in opposite direction about fairlead depth, with a distance in between to create a moment lever.

During decay tests an un-damped heave and nearly un-damped surge and pitch motion was observed. This is identified to the fact that no additional linear hydrodynamic damping had been defined. From development of the OC3-Hywind model Jonkman [47], it was found that the summed linear radiation damping (from potential flow theory) and the non-linear viscous drag (from the relative form of the Morison equation) were not matching that of the real Hywind Demo system. After consulting Orcina about this matter, they stated to have not used any additional linear hydrodynamic damping when performing their validation of LC5.1 [72].

Several decay tests are run with different ways of assigning the prescribed additional linear damping in OrcaFlex, as summarized below. Note, here, that the floating platform is made up of cylinder segments with varying diameter and length. The top 30 segments near SWL each have a length of 1 meter while the bottom 10 segments each have a length of 10 meters. OrcaFlex allows an axial and normal Unit damping force (kN/(m/s) and an axial and normal Unit damping moment (kN.m/(rad/s)) to be applied at each cylinder segment.

- First, assigning the OC3-Hywind prescribed damping was found to give good results in the surge and heave response, but a nearly un-damped pitch DOF.
- Next, the total prescribed surge, sway and yaw damping is divided by the number of 40 cylinder segments. Heave damping is applied only to the bottom cylinder. This results in slightly too much surge damping but perfectly matching pitch and surge decay motions, which indicates that unit damping in OrcaFlex is applied to cylinder segments independent of their length.
- Finally, the total prescribed surge, sway and yaw damping is divided by the total 130 m length of the floating platform. Next these damping values are assigned to the 1 meter cylinder segments and 10 times this value is assigned to the 10 meters cylinder segments. This results in perfectly matching surge and heave decay motion, but slightly too little pitch damping.

After consideration of these findings it is decided to continue with the final method of assigning additional linear hydrodynamic damping to the system. In the OC3 definition, no roll/pitch contribution is expected, while this is indirectly achieved by the division of surge and sway damping along the cylinder. The first method of damping was used on all load cases, but resulted in similar behaviour as described in section 3.5, with additional overprediction of the roll/pitch motion and too much surge damping in the wave-frequency region in cases with irregular waves.

3.4.3 Load case 4.1: Regular Airy waves

All blades are made rigid as described LC 1.4. Air density is set to 0. Regular Airy waves are generated by OrcaFlex with a height of 6 meters and a period of 10 seconds. Wheeler stretching is applied in order to give a more accurate representation of the wave kinematics. Waves ramp up for 100 seconds before results are recorded to prevent any initial transients.

3.4.4 Load case 4.2: Irregular Airy waves

Blades are made rigid as described for LC 1.4. Air density is set to 0. Irregular Airy waves are generated by OrcaFlex by means of a JONSWAP spectrum with a significant wave height of 6 meters and peak period of 10 seconds. Wheeler stretching is applied in order to give a more accurate representation of the wave kinematics. Waves ramp up for 30 seconds before results are recorded to prevent any initial transients, corresponding to other OC3 participants. The spectral density fundamental frequency is to 0.005 Hz, which is used to create power spectral density (PSD) graphs, which can be directly exported from OrcaFlex. This value is found to correspond with the fundamental frequency used by other OC3 participants from their results [44].

First, this method was used with 6 different seeds to reduce the statistical uncertainty of such a short stochastic wave realisation. However, this was found to give too high energy contents at high frequencies (see figure 3.1b). This is most likely due to the way the prescribed OC3 wave spectrum is cut-off at a frequency of 0.3 Hz. Lowering the wave high-cut frequency in OrcaFlex showed no improvement. Therefore, it was decided to redo these tests with the original surface elevation timeseries used by other OC3 participants (see figure 3.1a). This spectrum was made available along with the OC3 participants results [44].

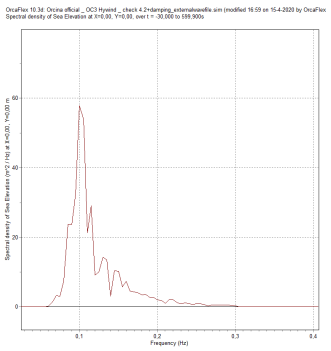

(a) A spectral density representation of the OC3 irregular wave spectrum.

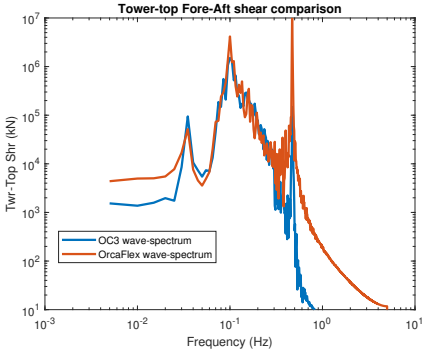

(b) Tower-top Fore-aft shear force comparison between a OrcaFlex-generated wave-spectrum and the OC3 wave-spectrum.

Figure 3.1: The effect of using the OC3 wave-spectrum instead of an OrcaFlex-generated wave-spectrum.

3.4.5 Load case 5.1: Regular Airy waves + steady wind

The tower and blades are made flexible for this and later load cases by resetting changes described in section 3.4.2. Air density is set to $1.225{\cdot}10^{-3}$ $\frac{kg}{m^3}$. A steady wind speed of 8 m/s is applied. Regular Airy waves are generated by OrcaFlex with a height of 6 meters and a period of 10 seconds. Wheeler stretching is applied in order to give a more accurate representation of the wave kinematics. The wind speed is built up for 100 seconds to prevent initial transients in the results.

3.4.6 Load case 5.3: Irregular Airy waves + turbulent wind

Air density is set to 1.225E-3 $\frac{kg}{m^3}$. The same prescribed irregular wave timeseries as detailed in section 3.4.4 is used. Both wind and waves are built up for 30 seconds to prevent any initial transients to the system, as prescribed in the load case definition.

The OC3-project prescribes a spatially varying wind field using a Mann turbulence model, generated by Risø [102]. Unfortunately, OrcaFlex only recognizes limited full wind field file types and the OC3 file type is not supported. On top of that, OrcaFlex is not capable of producing a spatially varying wind field. First, the load case is run with an OrcaFlex-generated wind 2D field. This uses a time-series realisation an API wind-spectrum, in a similar way to what is described in section 2.3.1.2. The results showed reasonable correspondence. However, a significant discrepancy was observed in low-frequency region, which made use of this turbulent wind model unsatisfactory.

In order to improve simulations, TurbSim [46] is used to calculate a 3D spatially varying full wind field that is accepted by OrcaFlex. For this, the IEC Kaimal model, defined in IEC61400-1 [45], is used as it is most similar to the Mann model. From this standard, the NTM turbulence class B definition is found to match most closely to the standard deviation from the OC3 prescribed wind field. The mean wind speed is set to 18 m/s at hub height. In correspondence with the OC3 wind field [102], the grid consists of 32 vertical and 32 horizontal grid points with an area of 150 m x 150 m and a generated time of 700 seconds. For most meteorological parameters, the default value of TurbSim is selected, meaning:

- An IEC type wind profile, meaning a power law profile on the rotor disc with a logarithmic profile elsewhere;
- A default surface roughness of 0.03 m;
- A power-law exponent of 0.2;
- An IEC coherence model used for the u-component wind speed and no coherence model used for the v- and w-component wind speed;

Figure 3.2 shows a PSD of wind speed generated by TurbSim compared to the wind speeds of the OC3 prescribed spectrum, as measured at hub height in both X, fore-aft(F-A) and Y, side-side(S-S), direction. The energy content at frequencies up to 1 Hz are are slightly higher for the OC3 spectrum, but this spectrum decreases more rapidly at higher frequencies. The theoretical API spectrum shows great resemblance to the TurbSim IEC-Kaimal wind field results. The OrcaFlex-generated API spectrum, however, shows results far off compared to the expected behaviour, with a jump in the spectral energy and smooth behaviour afterwards. No explanation for his behaviour is found.

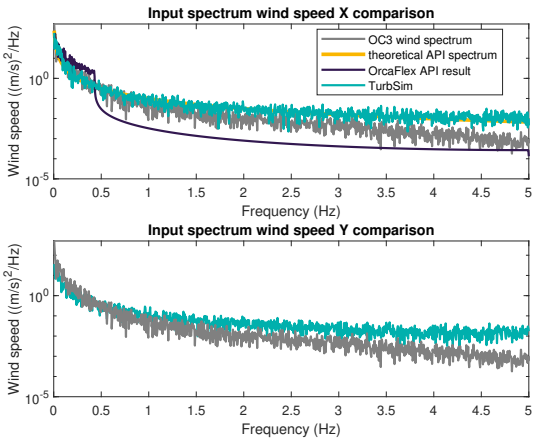

Figure 3.2: A comparison of the TurbSim-generated wind spectrum, compared to the prescribed OC3 wind velocity, a theoretical API spectrum and the OrcaFlex-generated API spectrum.

3.5 OrcaFlex verification results

Simulation results are extracted from OrcaFlex and compared to selected results from participants of the OC3 Phase IV project. Because this OrcaFlex model uses the Morison equation as a hydrodynamic model, only Morison-based participants are selected: 'FAST' by the National Renewable Energy Laboratory (NREL), 'ADAMS' by NREL, 'Bladed' by Garrad Hassan & Partners Limited (GH), 'HAWC2' by the Technical University of Denmark (Risø-DTU), 'SESAM' by Acciona Energia and '3Dfloat' by Institute for Energy Technology (IFE) and Norwegian University of Life Sciences (UMB). All participant results are publicly available [44]. Only a few participants manage to generate results for all load cases due to limited code capacities. Consequently, only limited results are available for comparison in complex environmental conditions, which increases the uncertainty of verification. In some cases, 'groups' of codes predict different outcomes. When OrcaFlex predictions match well to a single group, it is unknown what causes this match due to limited insight in the participant codes and model set-up. As a final remark, all OrcaFlex spectral densities have been obtained directly from the software. It is unknown what post-processing, if any, is performed by OrcaFlex when creating such a PSD.

3.5.1 Load Case 1.2: Eigenanalysis

The first 19 natural frequencies are calculated a the stationary system (see figure 3.3). Only a few OC3 participants manage to predict natural frequencies beyond rigid body motions and tower frequencies, as often the tower and RNA are modeled rigidly.

At first, some difficulties occurred in determining the 1st drivetrain torsion frequency and the 2nd tower bending frequencies. In order to capture the first drivetrain torsion frequency, the generator has to be locked in OrcaFlex. Secondary tower bending frequencies are hard to find because they are masked by severe blade motion arising in this eigenmode. However, two animations clearly stood out due to motion of the tower with a distinct secondary mode shape.

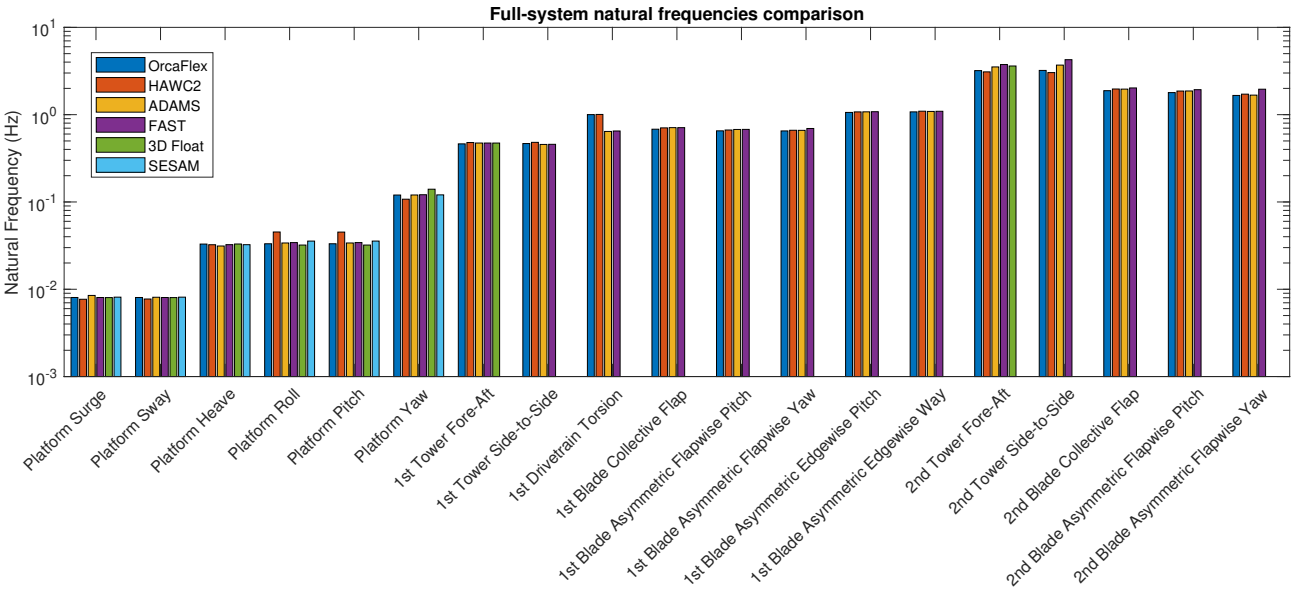

Figure 3.3: Full-system hydro-elastic prediction of first 19 natural frequencies from OC3 LC 1.2, comparison between OrcaFlex and selected participants.

OrcaFlex agrees well with the other codes in determining natural frequencies and most results are within the range of maximum and minimum predictions by the other participants. In all flexible blade natural frequencies, OrcaFlex predicts slightly lower values than the other participants. It is known that many codes at the time did not include blade axial, torsion, shear DOFs, which are included in OrcaFlex,. This may lower the expected natural frequency. Also, it can be observed that for the drivetrain torsion frequency OrcaFlex' prediction is closer to HAWC2 than to the two other codes. Due to limited insight in other codes no explanation can be found for this. As explained in [48], the discrepancy between participant results in the 2nd blade asymmetric flap-wise yaw frequency is likely due to modelling of the tower. Codes that include tower torsion (HAWC2 and ADAMS) show a lower natural frequency corresponding to more flexible compliance about the

tower centerline. OrcaFlex indeed includes tower torsion in its model and shows closer similarity to these two predictions than to FAST, which excludes tower torsion.

3.5.2 Load Case 1.4: Free-decay tests

Decay tests are performed in surge, heave and pitch. For each test, all other three DOFs are compared, to investigate coupling effects.

In general, OrcaFlex performs well on the motion prediction of all three decay tests. All decay frequencies, as well as most amplitudes and logarithmic decrement are corresponding well to the other participants. Some differences arise in the prediction of coupling motions. For the surge free-decay a difference exists between participants in their coupled surge-heave motion prediction (figure 3.4b). OrcaFlex' response corresponds best to HAWC2, but differs from FAST and ADAMS. Regarding coupled surge-pitch motion, OrcaFlex predicts correct behaviour, but lower amplitudes than the other codes (figure 3.4c). From [48] it is known that two other participants not included in this analysis (FAST by POSTECH and ADAMS by LUH) show rather similar results.

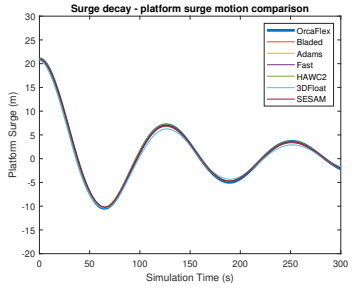

(a) Platform surge-surge motion.

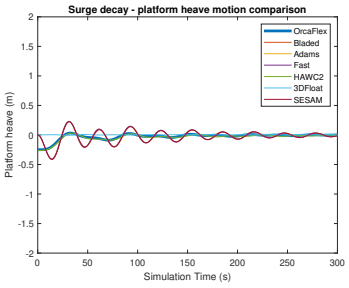

(b) Platform surge-heave motion.

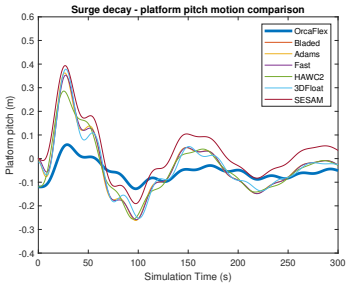

(c) Platform surge-pitch motion.

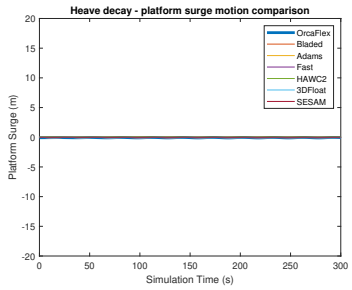

(d) Platform heave-surge motion.

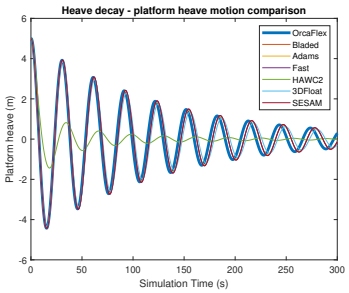

(e) Platform heave-heave motion.

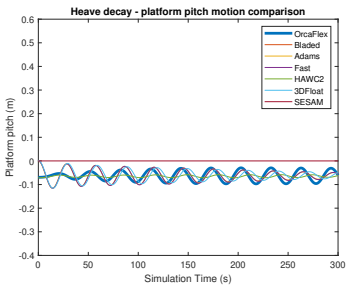

(f) Platform heave-pitch motion.

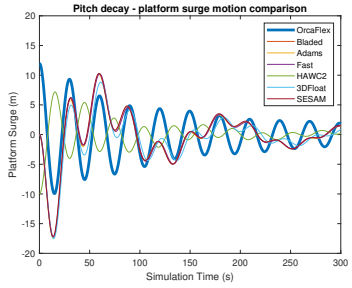

(g) Platform pitch-surge motion.

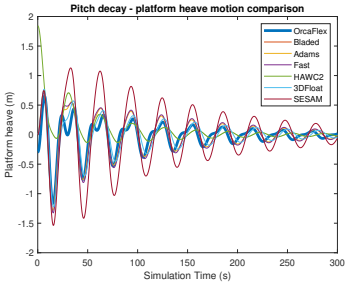

(h) Platform pitch-heave motion.

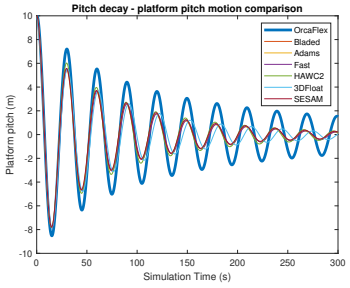

(i) Platform pitch-pitch motion.

Figure 3.4: Free decay in platform surge, heave and pitch from OC3 LC 1.4, rigid body motion comparison between OrcaFlex and selected participants.

All heave free-decay results match particularly well to the other codes. With the pitch free-decay, the pitch motion shows too little damping (figure 3.4i). This could be due to the way the hydrodynamic damping is distributed over the spar in the OrcaFlex model. Again, the pitch motion corresponds to that predicted by ADAMS by LUH, which is not shown in this figure [48]. The pitch-surge motion shows different behaviour,

but a correct amplitude, phase and rate of decay compared to the other codes (figure 3.4g). Most codes show an additional frequency in their response, whereas OrcaFlex shows a single-frequency response. The pitch-heave motion corresponds well with the other codes, except SESAM (figure 3.4h). Here, OrcaFlex shows a more distinct second frequency than the other codes, even though most of them do include a second frequency term.

As described in section 3.4.2 the method of damping set up were made whilst iterating between model set up and comparing preliminary results. With the 'official' method of assigning damping as a single surge/sway, heave and yaw value a larger overprediction of pitch-pitch decay motion was observed. The pitch-surge coupling effects shown currently were ameliorated.

3.5.3 Load Case 4.1: Regular Airy waves

Regular waves are included in the model. In all results, only the last two wave periods are shown.

In general, all predictions match well with the other codes. In almost all results, one or more of the participants show a significantly different behaviour than the other codes.

The only clear difference observed in the participant results is in the tower-top fore-aft (F-A) deflection and shear force. Here, HAWC2 and 3Dfloat predict a second frequency in the response. From a frequency-domain analysis of the results, it was observed that both models show a contribution of the first tower-bending mode in their response. Therefore, it seems as if their tower was not made sufficiently rigid.

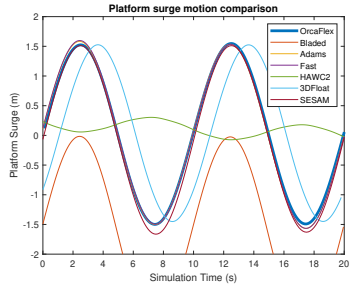

(a) Platform surge motion.

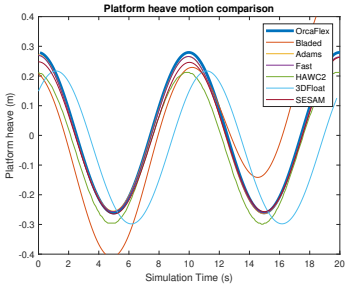

(b) Platform heave motion.

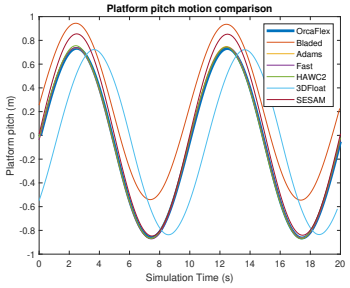

(c) Platform pitch motion.

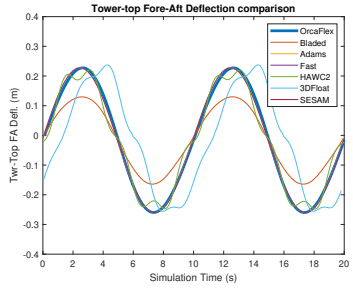

(d) Tower-top Fore-aft deflection.

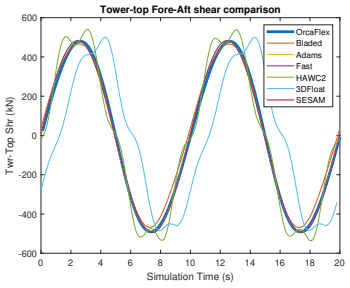

(e) Tower-top Fore-aft shear force.

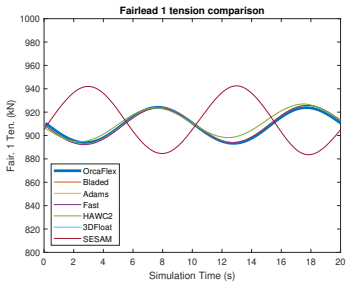

(f) Mooring line 1 tension.

Figure 3.5: Hydro-elastic response to regular waves from OC3 LC 4.1, comparison between OrcaFlex and selected participants.

3.5.4 Load Case 4.2: Irregular Airy waves

In considering the frequency response to irregular airy waves, a comparison of power spectral density (PSD) results is made. For OrcaFlex all spectral densities have been obtained directly from the software. It is unknown what post-processing, if any, is performed by OrcaFlex when obtaining such a PSD. Note that 3D-float and HAWC2 provide no results here.

In general all OrcaFlex spectra agree well with those of other codes. Important response peaks are found at similar frequencies. Results from all participants in the wave-frequency region correspond well. At lower frequencies, more variation in the results is found, because in the short simulation period of 600 seconds, high statistical uncertainty on low frequency response is expected.

The most relevant natural frequencies of the system are indicated with vertical gray dashed lines. These are the rigid surge/sway motion and heave/pitch motion natural frequency, wave peak period and first F-A

tower bending frequency. The system clearly shows relevant spectral energy peaks at these frequencies.

What mostly stands out is that OrcaFlex shows more energy at high frequencies in all three rigid body motion responses. At first, it was thought that this was due to the irregular wave spectrum used with a wrong cut-off frequency (see section 3.4.4). However, in all results shown in this chapter, the same irregular wave surface elevation is used in OrcaFlex as by other participants.

Also, OrcaFlex shows relatively higher energy in between peaks at tower-top deflection. This may be due to the way OrcaFlex creates the PSD when post-processing the results.

At first, the first tower-bending mode was excited by this extra amount of energy in several output signals. However, after assigning the correct definition of tower structural damping, this has been mitigated and the tower-bending response now matches well (see section 3.2). A slight low in tower-bending response may be the result of OrcaFlex assigning stiffness-proportional Rayleigh damping at the wave frequency by default, which gives increased damping at the tower-bending frequency.

Finally, at pitch natural frequency nearly all response peaks are slightly higher than other codes. This could be due to a lack of hydrodynamic damping for pitch motion, which is also shown in the pitch decay test (figure 3.4i). Little information on the behaviour at such low frequencies is available after only 600 seconds of simulation time. SESAM shows different behaviour in mooring line tension at higher frequencies, which is due to their FEM-based mooring line solution [48].

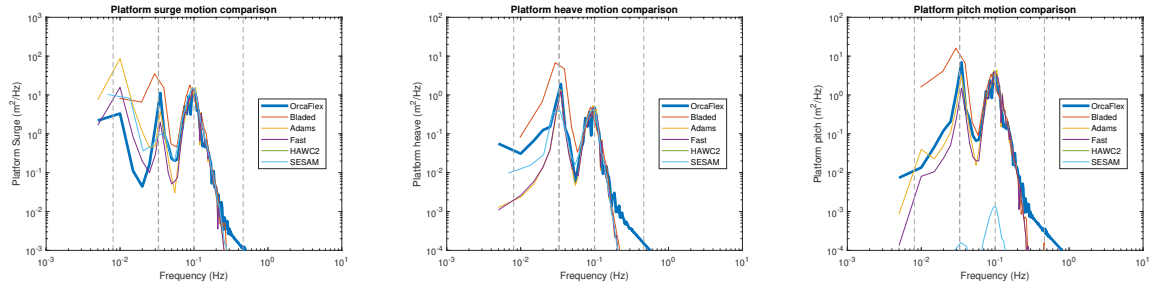

(a) Platform surge motion.

(b) Platform heave motion.

(c) Platform pitch motion.

(d) Tower-top Fore-aft deflection.

(e) Tower-top Fore-aft shear force.

(f) Mooring line 1 tension.

Figure 3.6: Hydro-elastic response to irregular waves from OC3 LC 4.2, comparison between OrcaFlex and selected participants.

3.5.5 Load Case 5.1: Regular Airy waves + steady wind

Several additional output parameters from both the turbine and the mooring system are included. As can be found in figures 3.7 and 3.8, all OrcaFlex load and motion predictions generally correspond well to those by other codes. Surge and pitch motions have moved to a non-zero mean due to the added wind thrust force. In some cases, some participants a different mean value for surge and pitch motion, which is likely due to a wrong result output location. The platform yaw motion shows most discrepancy between all codes, which is likely due to the difficulty of predicting the rotor gyroscopic yaw moment for aero-hydro-servo-elastic codes. A resulting difference in yaw position may be amplified by a different aerodynamic yaw moment. A slight negative mean is expected because of the gyroscopic yaw moment, which is correctly predicted by OrcaFlex. Some difference between codes in generator power predictions are found in figure 3.8d. Here, OrcaFlex' results are closer to FAST and ADAMS than to HAWC2 and Bladed.

A comparison of predicted blade tip deflections are not included in this report, as obtaining these from OrcaFlex requires considerable additional modeling effort and are therefore not considered in this time step.

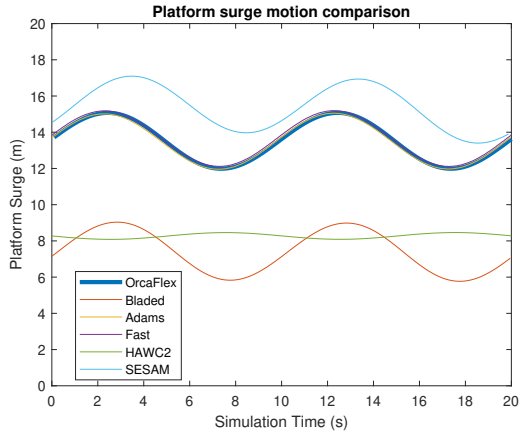

(a) Platform surge motion.

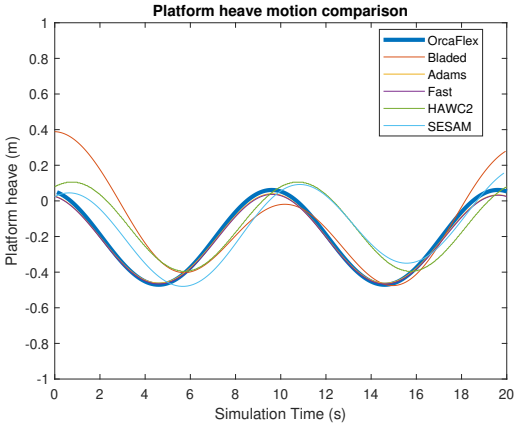

(b) Platform heave motion.

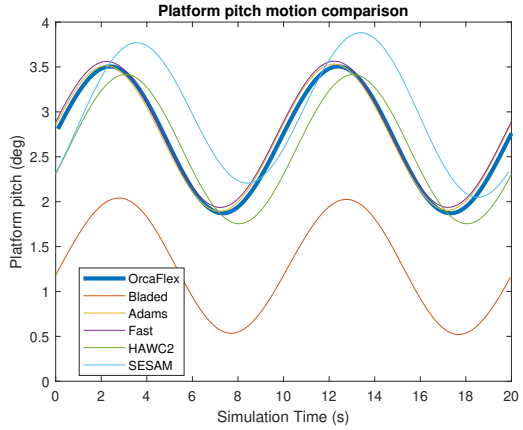

(c) Platform pitch motion.

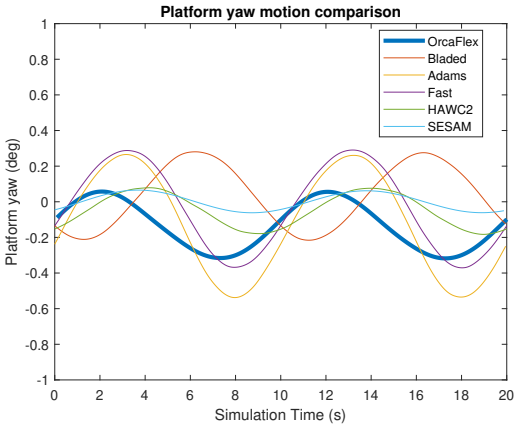

(d) Platform yaw motion.

Figure 3.7: Aero-hydro-servo-elastic response to steady wind + regular waves from OC3 LC 5.1, motion comparison between OrcaFlex and selected participants.

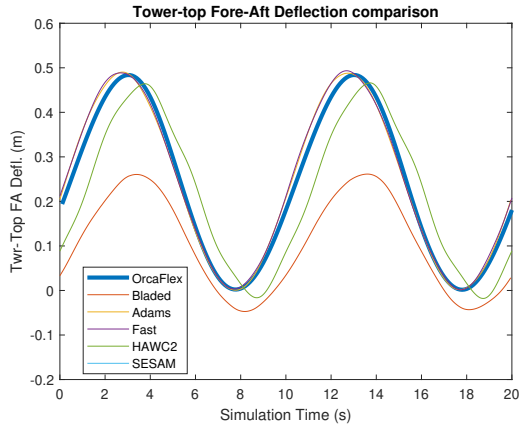

(a) Tower-top fore-aft deflection.

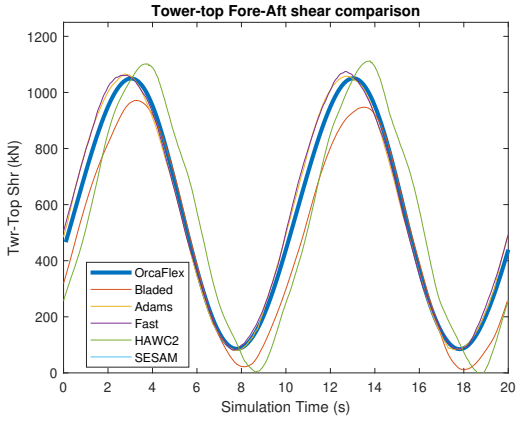

(b) Tower-top fore-aft shear.

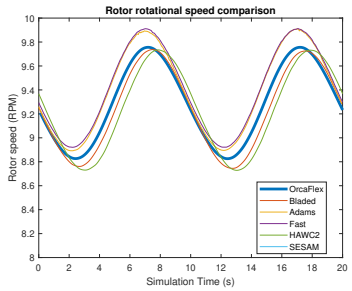

(c) RNA rotational speed.

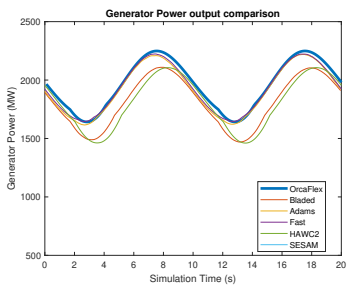

(d) Generator power production.

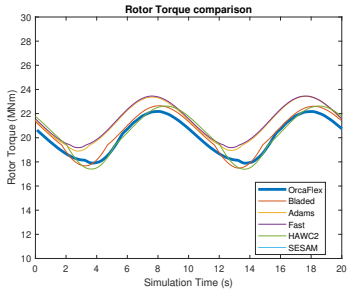

(e) RNA torque

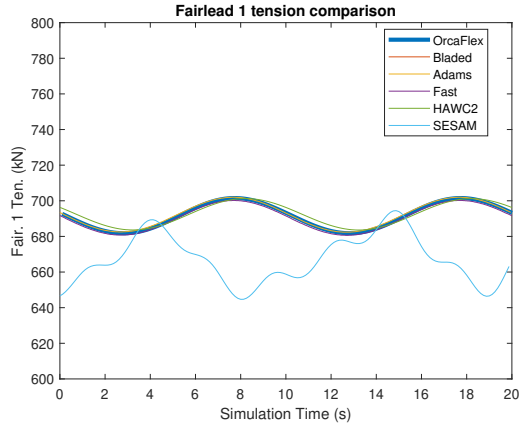

(f) Mooring line 1 tension.

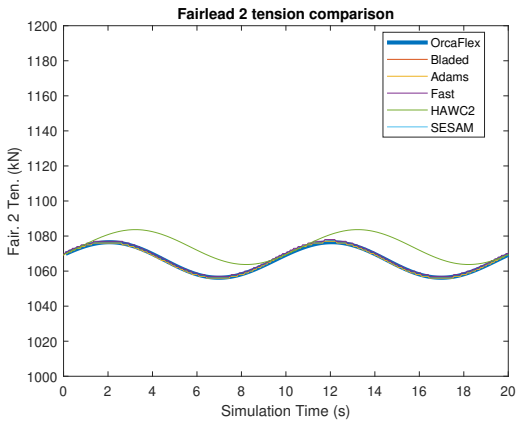

(g) Mooring line 2 tension.

Figure 3.8: Aero-hydro-servo-elastic response to steady wind + regular waves from OC3 LC 5.1, system behaviour comparison between OrcaFlex and selected participants.

3.5.6 Load Case 5.2: Irregular Airy waves + turbulent (rated) wind

From LC 5.3 discrepancies are observed in the rotor torque and generator power, that are attributed to a difference in the generator-torque control at above-rated wind speeds between OrcaFlex and OC3 participants. To limit errors from controller dissimilarities, load case 5.2 is used for verification.

At first, large discrepancy in the mooring line behaviour was observed with no distinct peaks at the surge, pitch and wave-frequency regions. After thorough revision of the results, it was noted that the spectral density results obtained directly from OrcaFlex show large overlapping of peaks. This may be due to their way of internal measurement post-processing to obtain PSD representation of results (see Appendix E). Time-domain results are now separately post-processed by normalizing, windowing and overlapping to obtain a PSD. Some results are improved by this, while others remain similar. None of the results are deteriorated by this approach. In this section, only results that show a significant upgrade from improved post-processing are

updated. In other cases, the OrcaFlex result is depicted for consistency with other load case results. At very low frequencies (<10^{-2}Hz), the statistical uncertainty in all results is significant, given the short time-domain realisation of only 600s, which would mean only a couple of response cycles occurring of these frequencies.

From external post-processing, the mooring line tensions are significantly improved, showing a clear match with other codes. It was observed that a high-frequency overprediction of rigid body motions (seen also in section 3.5.4 for irregular waves-only) is no longer present.

Most spectra agree well with those provided by the OC3 participants across all frequencies (figure 3.9). A larger pitch response in OrcaFlex can be observed at the pitch frequency, which translates to overprediction of the tower deflection and generator output at this frequency. Moreover, pitch-frequency response in surge motion is predicted lower by OrcaFlex compared to other participants. Both are due to the method of assigning hydrodynamic damping in this DOF observed from the decay tests.

Again, a slight low in tower-bending response in tower-deflection response at the first tower-bending frequency is observed, which may be due to definition of Rayleigh stiffness-proportional damping at the wave frequency by OrcaFlex. The generator power and torque show an higher response at the second tower bending frequency (highlighted here by an additional dashed grey line) predicted by OrcaFlex. It is expected that this is caused by the wind field generated by TurbSim, which contains more energy at higher frequencies than that prescribed by OC3 (see figure 3.2).

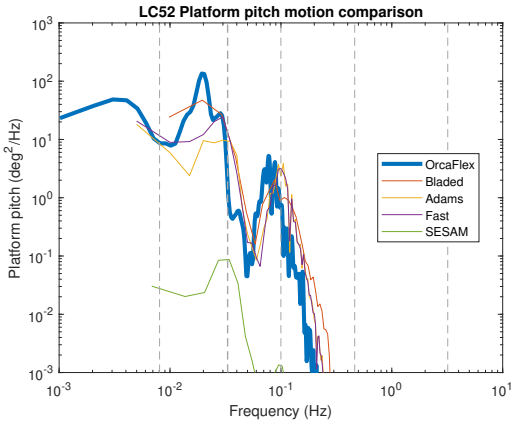

(a) RNA rotational speed.

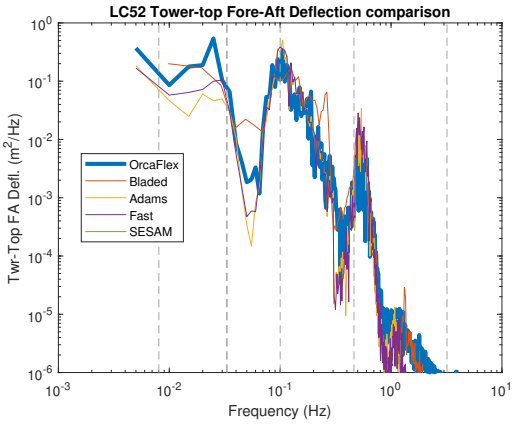

(b) Tower-top F-A deflection.

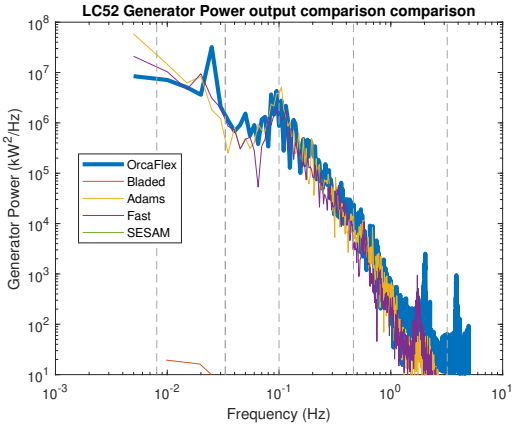

(c) Turbine generator power production.

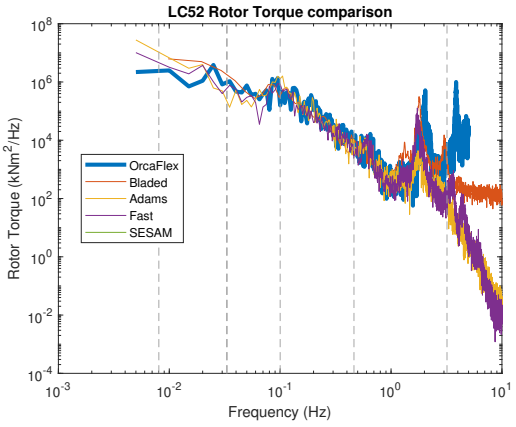

(d) Turbine rotor torque.

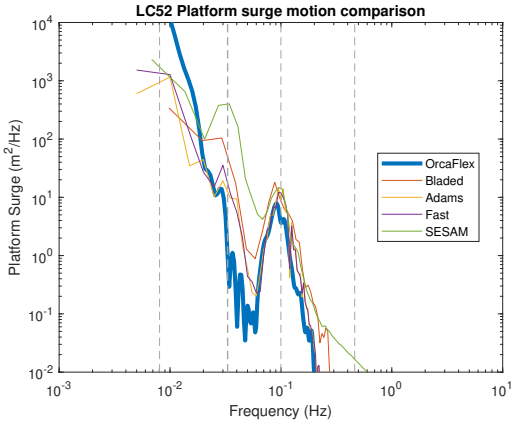

(e) Platform surge motion.

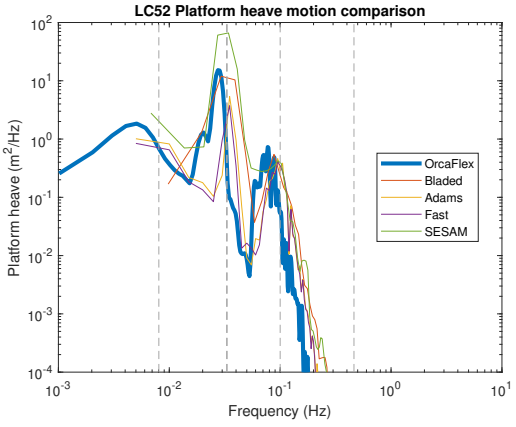

(f) Platform heave motion.

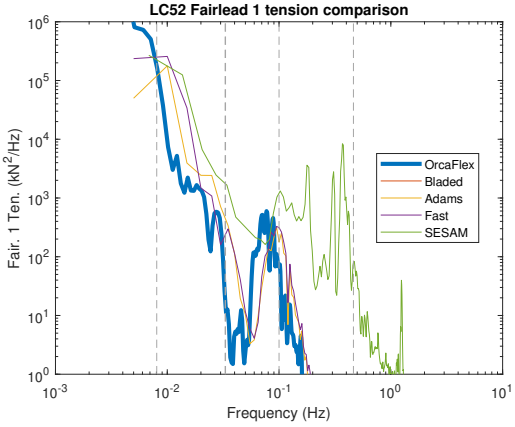

(g) Mooring line 1 tension.

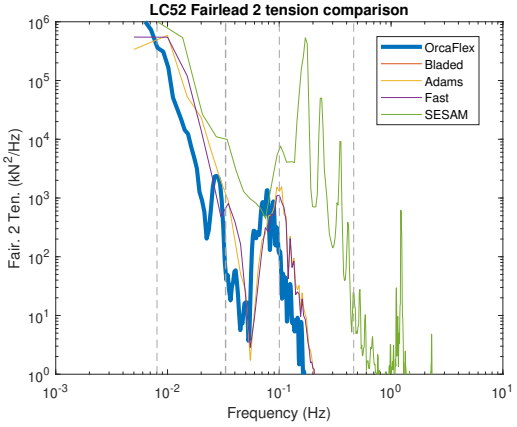

(h) Mooring line 2 tension.

Figure 3.9: Aero-hydro-servo-elastic response to irregular waves + turbulent (rated) wind, from OC3 LC 5.2, comparison between OrcaFlex and selected participants.

3.6 Conclusions: OrcaFlex verification against industry-standard codes

OrcaFlex aero-hydro-servo-elastic code was verified against results of participants of the OC3-project. In general, the OC3-Hywind model set-up in OrcaFlex described in section 3 matches well to that of the OC3 participants across load cases of increasing complexity. Hydro-elastic response to wave-only cases as well as full system response to regular waves and steady wind match particularly well. As described in section 2.5, three types of errors can be defined. These errors present in the are separately highlighted here. In addition, errors mitigated during model set-up are provided.

Type 1 (code capacity) errors identified are:

- Slight discrepancy is observed in the yaw motion results between all participants, this is explained from general difficulty of aero-servo-elastic codes to predict the turbine gyroscopic yaw moment [48]. OrcaFlex predicts a correct mean value, but also shows a shifted phase like each participant.
- Main differences in decay tests are surge-pitch coupling and pitch-pitch decay response. This could be due to the way linear hydrodynamic damping is defined in the system, which may provide correct total horizontal damping, but insufficient rotational damping in pitch direction. Additional linear hydrodynamic damping is needed to match free-decay and irregular waves results. The method proposed by the OC3-Hywind definition results in too little pitch response damping and too high surge motion response in the wave-frequency region. Distribution of the total additional hydrodynamic damping as 'unit damping' along cylinder segments of the floater improves results. A more refined distribution of unit damping across cylinders e.g. considering the cylinder segment diameter, wetted volume or expected wave velocity at the cylinder segment position may further reduce dissimilarities. The too low pitch damping shows in irregular wave response as overprediction of the pitch natural frequency.
- In OrcaFlex an equal energy distribution is used that generates a wide range of wave frequency components from a wave spectrum beyond the expected high-cut frequency. This overpredicts high-frequency response of the system. Therefore, to match the high-frequency wave-response, it is advised to use an externally defined surface elevation timeseries with the appropriate frequency range for this.

Type 2 and 3 (model set-up and physical model) errors identified are:

- TurbSim proves a useful tool in the generation of OrcaFlex spatially varying wind fields. Results match well with externally IEC turbulence simulated with a Mann model. It was found that the TurbSim spectrum contains more energy at high frequencies, which in some cases gives too much excitation of high-frequency results in generator power, rotor torque or tower bending.
- Natural frequencies match with a <1% percent error to the mean value of other participants. OrcaFlex includes blade axial, torsion and shear DOFs in the structural model. Moreover, tower torsion is included in its code. Both result in a <2 Hz reduction of natural frequency corresponding to blade natural frequencies.
- The OrcaFlex quasi-static 'analytic catenary' mooring representation matches well to that of other codes in all load cases. FEM mooring line representation used by some participants gives a more detailed high-frequency mooring response.
- Spectral density results directly obtained from OrcaFlex show significant errors for stochastic wind-wave input. Internal post-processing of the results in the software gives overlapping in peaks and overpredicted high-frequency response for rigid body motions. External post-processing by applying a Hann-window with window length ratio 0.5 and overlap ratio 0.6 and normalizing signals when performing an FFT gives similar results while removing the before-stated errors.
- A frequency domain analysis performed over 600s of time-domain realisation results in significant variation in the low-frequency response across participants, which does not allow for accurate prediction of the surge/sway natural frequency response.
- Constant generator-torque control in above-rated wind speeds in the OC3-project gave rise to errors in this load case, as it was not reported and therefore not modeled in OrcaFlex. Therefore, this load case was excluded from further analysis.

Here, it must be noted that OC3 participant models that gave clearly erroneous results for a specific load case were left out of the analysis in the OC3 project itself, which already limits type 3 errors. Errors mitigated during the model set-up are:

- Platform yaw stiffness is provided mainly by bridle lines in the Hywind crow-foot delta catenary mooring system. In case these are replaced by equivalent main lines, additional yaw stiffness is required.
- A generator mechanical to electrical conversion loss of 94.4% shows a better match with other codes results.
- Assigning the correct tower damping is essential to correctly capture the predict tower-bending re-

sponse peak energy. In OrcaFlex, stiffness-proportional Rayleigh damping proves a suitable way for this. However, stiffness-proportional damping is assigned at the wave peak period by default, gives too high damping at the tower-bending frequency observed in tower-deflection and tower shear response.

- The use of a 2D turbulence model to replace a 3D spatially varying wind fields provides unsatisfactory results, errors in the response energy levels across frequencies and output parameters.

From these results, it is concluded that no insurmountable errors in the OrcaFlex aero-hydro-servo-elastic code occur and it can be confidently used as a physical model in the verification against BHawC/OrcaFlex.

4

BHawC/OrcaFlex verification to OrcaFlex

In Chapter 3, the OrcaFlex hydro-elastic module and aero-hydro-servo-elastic module have been verified in load cases of increasing complexity against industry-standard aero-hydro-servo-elastic codes. This served two purposes: 1) Gaining confidence in the OrcaFlex hydro-elastic code with application to floating offshore wind turbine modeling, which is used in the BHawC/OrcaFlex coupled aero-hydro-servo-elastic code for validation against full-scale measurements in Chapter 5 and 2) Gaining confidence in the 'OrcaFlex-only' aero-hydro-servo-elastic code which is used in the verification of BHawC/OrcaFlex. A similar verification approach to the OC3-project is conducted, which means subjecting the system to several load cases of increasing complexity, hence isolating error sources in different modules of the code. Now, the verified OrcaFlex code serves to find errors in the BHawC/OrcaFlex before comparing this to full-scale measurements.

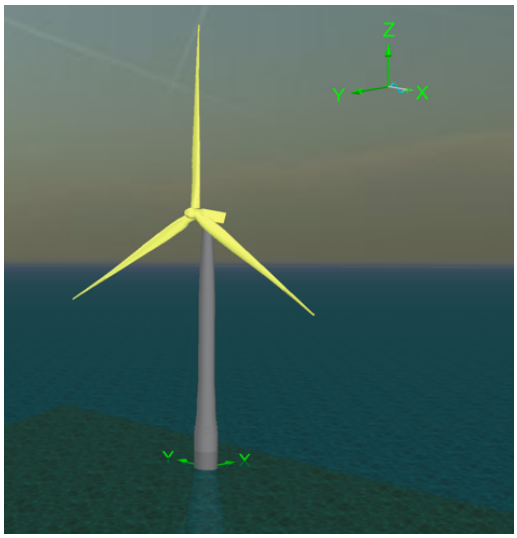

(a) OrcaFlex model of the Hywind Scotland floating offshore wind turbine in shaded graphics view.

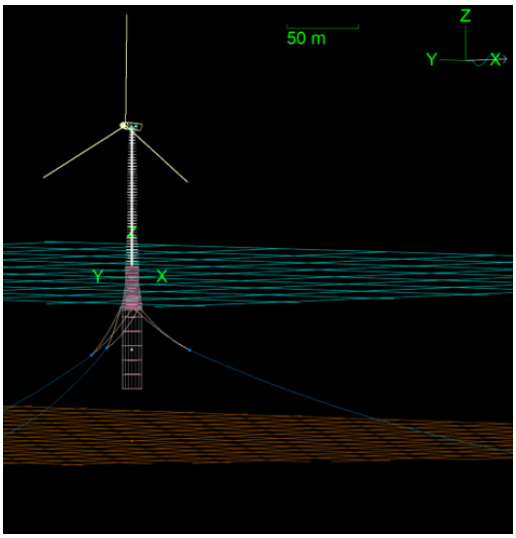

(b) OrcaFlex model of the Hywind Scotland floating offshore wind turbine in wired frame view.

Figure 4.1: An impression of the OrcaFlex aero-hydro-servo-elastic model of the Hywind Scotland floating offshore wind turbine used for this verification step.

Only the BHawC turbine model is provided for this project. Therefore, the OrcaFlex floater-mooring system, OrcaFlex Hywind turbine and OrcaFlex hydrodynamic environment need to be built for this verification step. In this chapter, the set-up of both the OrcaFlex (OF) and the BHawC/OrcaFlex (BH/OF) model of the Hywind Scotland floating offshore wind farm (Hywind) system are described. First, set-up of the floater, turbine and environmental conditions in OF are explained. Then, a general overview of the BHawC/OrcaFlex coupling and set-up of the BH/OF Hywind model are provided. A load case table and specific set-up of both models for each load case are detailed. In section 4.6, the simulation results of both models are provided and errors are analysed.

4.1 Set-up of the Hywind support structure model in OrcaFlex

The Hywind system consists of a spar-type floater [33] and the SWT-6.0-154 wind turbine developed by Siemens Gamesa Renewable Energy (SGRE) [30]. Several structural parameters from the OrcaFlex Hywind model are found in table 4.1, which were extended with theoretical parameter definitions. For development of the Hywind turbine, the tower and controller have been adapted from the original offshore turbine to match the requirements for a FOWT set-up. A tower design is always site-specific, whereas the controller update is necessary to prevent instability due to so-called 'negative damping' ([71], [87] and [57]).

Parameter	**Value**	**Parameter**	**Value**
Floater top geometry	Length: 12 m Diameter: 9.4 m	Mooring anchor radius	R = 640 m
Floater taper geometry	Length: 15 m	Mooring segment length	Bridle lines: 50 m Main lines: 609.7 m
Floater bottom geometry	Length: 58 m Diameter: 14.4 m	Mooring line coefficients	$C_{d,axial}$ = 2.4 $C_{d,normal}$ = 1.15 $C_{a,axial}$ = 1.0 $C_{a,normal}$ = 0.5 $C_{d,seabed}$ = 0.74
Floater Morison coefficients	C_a = 1.0 C_d = 1.0	Water depth	Floater: 113 m Anchors: [110 , 115] m

Table 4.1: An overview of selected parameters of the floater-mooring system of the OrcaFlex Hywind model.

4.1.1 OrcaFlex Hywind floater parameters

The floater is modeled as a spar buoy object in OrcaFlex [74], with a geometry obtained from [32]. As described in section 2.2.3.3, there are several ways of determining Morison drag and added mass coefficients. It is decided to assign constant estimates of coefficient values determined from literature which are independent of frequency and water depth (after consideration of [1], [16], [24], [36], [51] and [84]). This simplified method may differ from the real-world system, but still allows for 'pure comparison' in this code-to-code verification step. From a preliminary hydrodynamic analysis using Hywind measurements (see section 5.2 and Appendix D), typically occurring hydrodynamic regimes are identified with Reynolds numbers ($Re > 10^7$) and Keulegan-Carpenter numbers (KC<10), assuming a cylinder of low surface roughness ($k/D < 10^{-3}$). Marine growth is not included in this model, as the Hywind measurements used in the final model validation step are obtained within months after the full-scale system became operational. A detailed analysis of the development of marine growth at the given site is considered beyond the scope of this research.

The dry mass, displacement (weight based on the amount of water its hull displaces at varying loads), centre of gravity and centre of buoyancy are not provided in the by Equinor [32], but were obtained from SGRE internal documentation. This documentation also proposes values for an hydrodynamic added mass and hydrodynamic damping matrix, but after comparison of the resulting natural frequencies and response these values are considered erroneous.

4.1.2 OrcaFlex Hywind mooring system parameters

All Hywind floating offshore wind turbine (FOWT)s are held in position by a crow-foot delta-line catenary mooring system. The system consists of three main catenary lines, each connected by means of two bridle lines to the floater. A finite element method (FEM) representation is used to model all lines, which corresponds to the use of dynamic mooring line theory (see section 2.4.2). From Chapter 2, it is known that this is the desired method in the prediction of loads and motion of a FOWT and are later used in validation against measurements. Each line is rigidly connected to an anchor at a position of half the line diameter above seabed, to prevent undesired friction due to a simulated partly buried cable.

From [32], the nominal diameter, Young modulus, unit dry mass and unit weight in water per meter are provided for both main lines and bridle lines. With these properties, the outer diameter, equivalent drag diameter, contact diameter and axial stiffness are determined using general rules for mooring line geometries derived from the nominal diameter of a stud-less chain [106]. Morison added mass and drag coefficients provided in table 4.2 are found from DNV [109]. A detailed assessment of the line bending stiffness due to friction between mooring chains is considered beyond the scope of this verification step. The mooring chain seabed friction is typical for mega-rippled-silty sand and gravel [100], which occurs at the Hywind site [95].

4.1.3 OrcaFlex Hywind hydrodynamic environment parameters

The yearly variation in water temperature and salinity are obtained from [94] are used to calculate the water density and kinematic viscosity using [92]. A 3D surface for the seabed is specified in order to account for depth variation, which may influence hydrodynamic calculations. From the Hywind environmental report [95], the bathymetry of the site is found, which is used to determine anchor and floater coordinates and water depths at these positions. The mooring system is designed such that its anchors are only be subject to purely horizontal loading and can be considered fixed in these degrees of freedom. Therefore, soil-structure interaction at the anchors is considered beyond the scope of this thesis.

A wind-wave and swell-wave component are modeled separately by two different JONSWAP spectra. A description of the wave conditions for each load case can be found from table 4.2. Waves are Wheeler stretched and loads are calculated up to the exact instantaneous position of the floater, which may cause some second-order load effects.

4.2 Set-up of the Hywind turbine and aerodynamic model in OrcaFlex

Next, the SWT-6.0-154 wind turbine [30] (Hywind tubine) is designed in OrcaFlex, using SGRE internal documentation on the structural and aero-elastic parameters of the BHawC wind turbine model ([28], [29] and [27]). Here, the turbine set-up description is limited to additional calculation steps required to obtain parameters.

The tower is modeled as an homogeneous pipe with varying outer and inner diameters. The density is iteratively updated until the tower mass matches that of BHawC. The Young modulus is updated to include flanges and 'effective steel'. Structural damping is added to the tower by means of stiffness-proportional Rayleigh damping, which is applied to the tower-bending frequency as learned from the OrcaFlex verification step.

OrcaFlex allows a nacelle, hub and generator to be modeled with respect to its mass, centre of mass and inertia. This set-up is much simplified from that in BHawC, where each of these components and many more are modeled in terms of sub-components, each with their own mass, centre of mass and inertia. Therefore, these detailed descriptions of sub-components had to be lumped into pre-defined OrcaFlex components by combining structural parameters. Special attention was required as the both the global and local coordinate systems of BHawC and OrcaFlex are defined differently. The nacelle front and side drag coefficients and tilt angle are matched to BHawC. The generator gear ratio is updated to correspond to Direct Drive technology.

Blades are built in OrcaFlex using the SGRE aero-elastic model data documentation [27] for segments along the length of the blade. Many typical parameters for the definition of wind turbine blades, such as the chord, thickness percentage and aerodynamic twist of each blade segment are given directly from the documentation. The bend-, axial- and torsional stiffness are determined for each section by multiplying the given Young modulus and shear modulus to the corresponding moments of inertia and area. OrcaFlex demands the radii of gyration as a ratio of the flap-wise (r_y) and edge-wise (r_x) direction and the radius of gyration about the blades centre of mass as a percentage of the chord. The latter is determined using:

$$r_{i,z} = \left(\sqrt{r_{i,x}^2 + r_{i,y}^2}\right) / C \cdot 100\% \tag{4.1}$$

for each section. Where r_i is the radius of gyration about the given blade axis and C is the blade section chord.

Two sets of each 7 blade profiles (or 'wing types') are defined by SGRE. Each blade profile corresponds to a certain blade thickness percentage. However, many more thickness percentages occur in the blade than there are blade profiles. BHawC deals with this by interpolating all lift, drag and moment coefficients separately to correspond to each thickness percentage. One could argue that this operation is rather complex. In OrcaFlex, the blade profiles are defined to match its thickness percentage most closely. The steps for this operation can be found in Appendix C.2.

Finally, different coordinate systems to represent the centre of mass, neutral axis offset, aerodynamic centre, aerodynamic twist and structural pitch of each blade segment are used in BHawC and OrcaFlex. BHawC expresses all coordinates about a miscellaneous 'blade axis', whereas OrcaFlex expresses all coordinates about the leading edge, as a percentage of the chord. An overview of these coordinate systems can be found in figure 4.2. After careful consideration of both figures, all blade parameters translated from BHawC coordinates to OrcaFlex coordinates. The steps for this operation can be found in Appendix C.1.

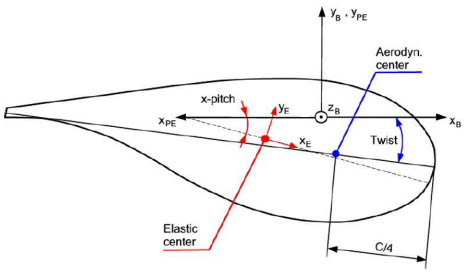

(a) BHawC aero-elastic blade coordinate system.

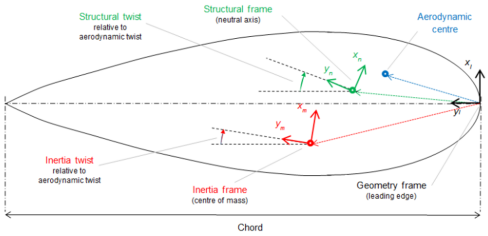

(b) OrcaFlex aero-elastic blade coordinate system.

Figure 4.2: Overview of the blade section coordinate systems used in BHawC and in OrcaFlex. The steps for rewriting BHawC coordinates to OrcaFlex coordinates can be found in C.1

Turbulent wind is generated separately by TurbSim [46]. A similar approach with similar assumptions as is described in section 3.4.6 is used. Here, only load case specific parameters are adapted to that from the load case table. Wind loads are included on the tower, floater and nacelle.

4.3 BHawC/OrcaFlex general Hywind model set-up

BHawC/OrcaFlex is a coupled dynamics software tool that uses the hydro-elastic code of OrcaFlex and the aero-servo-elastic code of BHawC. This coupling takes place through dynamic link libraries (DLLs). The coupled BHawC model is set-up and provided by SGRE for this thesis project. Therefore, only a generic overview of the set-up of the BHawC/OrcaFlex Hywind model is given in this section. A complete overview of the capacities of BHawC/OrcaFlex, as well as the mathematical background, can be found in [3] and [62].

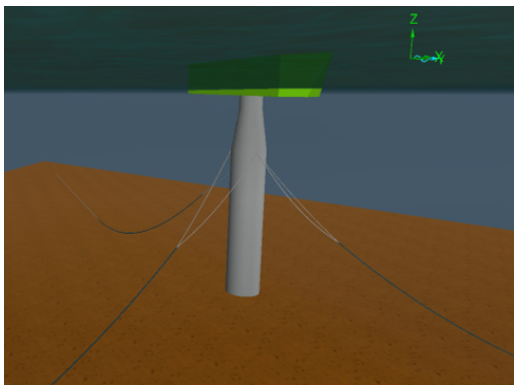

(a) BHawC/OrcaFlex model of the Hywind Scotland floating offshore wind turbine in shaded graphics view.

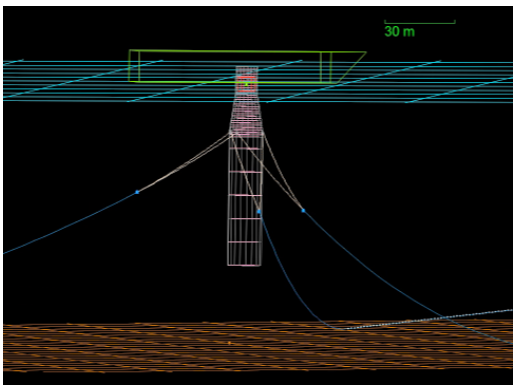

(b) BHawC/OrcaFlex model of the Hywind Scotland floating offshore wind turbine in wired frame view.

Figure 4.3: An impression of the BHawC/OrcaFlex aero-hydro-servo-elastic model of the Hywind Scotland floating offshore wind turbine used for this verification step. An interface vessel (with dummy shape) is used in the coupling between BHawC and OrcaFlex. No user interface is available for the wind turbine in BHawC.

BHawC/OrcaFlex simultaneously runs a dynamic analysis of the floater-mooring-system in OrcaFlex and the offshore wind turbine in BHawC. Here, BHawC communicates through the 'BHawCLink DLL' with an external 'OrcaFlex DLL', which in turn communicates with OrcaFlex (see figure 4.4). In each timestep:

- BHawC initiates a new iteration and calculates the aero-servo-elastic response.
- BHawCLink transfers the displacement, velocity and acceleration for given timestep to the external DLL.
- The external DLL uses OrcaFlex to calculate the hydro-elastic response of the floater-mooring-system to the pre-scribed motion. Next, it returns a mass matrix (**M**), tangent stiffness and damping matrices (**C**, **K**) and force vector ($\mathbf{F}_{ext}$) at the interface point (see section 2.1.1).
- BHawCLink uses these matrices to calculate the interface stiffness, as well as the interface forcing. This is included in the BHawC loads and motions solution at the affected interface degrees of freedom.
- The updated displacement, velocity and accelerations are calculated using the new load and motions solution.

- The process is repeated until the updated solution converges to a given tolerance. For the iteration process, the Newton-Raphson iteration scheme is used [90].

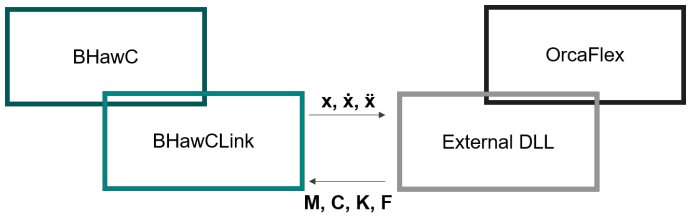

Figure 4.4: A schematic representation of the different software components of BHawC/OrcaFlex used in coupled dynamic analysis. Adapted from [62].

For the floater-mooring-system in BHawC/OrcaFlex, the same floater is used as described for the OrcaFlex-only model. The BHawC aero-servo-elastic wind turbine model is provided by SGRE. It contains an existing model of the SWT-6.0-154 Hywind wind turbine which was successfully validated using full-scale measurement data of the system prototype [75]. The system also contains the as-built Hywind turbine control system.

The aerodynamic environment is modeled completely in BHawC. Therefore, the air density is set to 0 in OrcaFlex for the coupled model. The hydrodynamic environment, however, is modeled completely in OrcaFlex. This environment is set up as described in section 4.1.3.

4.4 Load case table

Load Case	Wind Conditions	Wind-wave conditions	Swell-wave conditions	Initial Conditions	Analysis Type
1.1	None: air density = 0	Still water	Still water	All = 0	Static equilibrium solution
2.1	None: air density = 0	Still water	Still water	Platform surge = 21 m, Other = 0	Free-decay time series
2.2	None: air density = 0	Still water	Still water	Platform pitch = 10 deg, Other = 0	Free-decay time series
2.3	None: air density = 0	Still water	Still water	Platform yaw = 5 deg, Other = 0	Free-decay time series
3.1	NTM: $V_{hub} = 5m/s$, TI = 0.23(B)	Still water	Still water	Blade pitch = -3.5 deg, RPM = 6.2, Other = 0	Power spectra, Time-series statistics
3.2	NTM: $V_{hub} = 30m/s$, TI = 0.13(B)	Still water	Still water	Blade pitch = 88 deg, RPM = 0.1, Other = 0	Power spectra, Time-series statistics
4.1	None: air density = 0	Irregular Airy: H_s = 2.2 m, T_p = 8 s JONSWAP wave spectrum	Irregular Airy: H_s = 1.5 m, T_p = 10 s JONSWAP wave spectrum	All = 0	Power spectra, Time-series statistics
5.1	NTM: $V_{hub} = 5m/s$, TI= 0.23(B)	Irregular Airy: H_s = 2.2 m, T_p = 8 s JONSWAP wave spectrum	Irregular Airy: H_s = 1.5 m, T_p = 10 s JONSWAP wave spectrum	Blade pitch = -3.5 deg, RPM = 0.1, Other = 0	Power spectra, Time-series statistics
5.2	NTM: $V_{hub} = 30m/s$, TI = 0.13(B)	Irregular Airy: H_s = 2.2 m, T_p = 8 s JONSWAP wave spectrum	Irregular Airy: H_s = 1.5 m, T_p = 10 s JONSWAP wave spectrum	Blade pitch = 88 deg, RPM = 0.1, Other = 0	Power spectra, Time-series statistics

Table 4.2: Load-case table used in the comparison of BHawC/OrcaFlex to OrcaFlex.

A load case table is set up with load cases of increasing complexity to isolate possible dissimilarities. It is found that the blade pitch controllers in OrcaFlex and BHawC/OrcaFlex are insuperably different and can not be adapted to give a better match. Therefore, it was decided to leave out the controller in both models completely in this verification step. A constant pitch and RPM are assigned for load cases comprising wind. Two cases of very low and very high (idling) wind speeds are selected, as here a constant pitch angle best compares to as-built behaviour which minimises the risk of dynamic instability. All environmental conditions face the turbine head-on. Wave conditions are assigned that are typical for the Hywind site (see section 5).

4.5 Specific model set-up per load case

All cases are simulated for 1800 seconds to provide similar statistical properties for both models, which are comparable to the later used full-scale measurements. In load cases with environmental excitation, 100s of build-up time is included to prevent initial transients in the response. After several test simulations, the blades of the OrcaFlex model repetitively became unstable. No explanation for this could be found. There-

fore, it was decided to model the blades in both models rigidly. In OrcaFlex, 'blade DOFs' are set to 'fixed' and in BHawC/OrcaFlex, an 'infinitely' high stiffness is assigned to the blades.

4.5.1 Load Case 1: static analysis

Both OrcaFlex and BHawC/OrcaFlex results are obtained by running a dynamic analysis without any external excitation. Then, the results are visually inspected on any occurring transient events from either one of the models being accidentally in non-equilibrium conditions. For each parameter, the mean of dynamic results is taken and interpreted as being the static equilibrium result. This approach is chosen after it was found that not all static internal and external forces are incorporated in a 'static analysis' provided by both models.

4.5.2 Load Case 2: Free-decay tests

A similar approach as described in section 3.4.2 is taken. For both models, winches are defined in the OrcaFlex hydrodynamic environment of both models to give a static displacement of the system in the desired DOF. For rotational free-decay tests, two opposing winches are used at a different position on the floater to create a lever resulting in a static moment. Winches are released as results starts recording.

4.5.3 Load Cases 3 and 5: Turbulent wind

In BHawC/OrcaFlex and OrcaFlex, all blades are given a constant pitch angle to exclude comparison errors due to differences in the blade pitch control system. This constant pitch angle corresponds to the expected pitch angle at the given wind speed, based on SGRE internal documentation. No motion compensation takes place by the turbine from blade pitch.

In OrcaFlex, it was found that simulations with a constant blade pitch angle and generator torque controller are not possible. The only option to bypass this, is to assign a constant rotational velocity. This is done for both load cases, where the rotational velocity in load case 3.2 and 5.2 matches that of the idling turbine. For load case 3.1 and 5.1, a constant rotational velocity is assigned matching that of the expected RPM at 5 m/s incoming wind speed. This means comparison errors may arise due to the presence of generator torque control in the BHawC/OrcaFlex turbine.

The wind field used in OrcaFlex is simulated separately using TurbSim with similar assumptions as described in section 3.4.6, but updated turbine specifics to match the SWT6.0-154. In BHawC/OrcaFlex, wind is simulated using a Mann model. The resultant wind speeds at hub height in both models is normalised and a PSD is found in figure 4.5. Both spectra show similar energy content across all frequencies. A slight difference in the low-frequency energy at of the 5m/s wind field is observed, with OrcaFlex and BHawC/OrcaFlex giving different peaks around 10^{-2}Hz. Slightly higher energy is observed in BHawC/OrcaFlex at the 30m/s wind field around $2{\cdot}10^{-2}$Hz. Both differences may cause slight differences in the response of both models and are likely due to statistical variation in the low-frequent wind realisation.

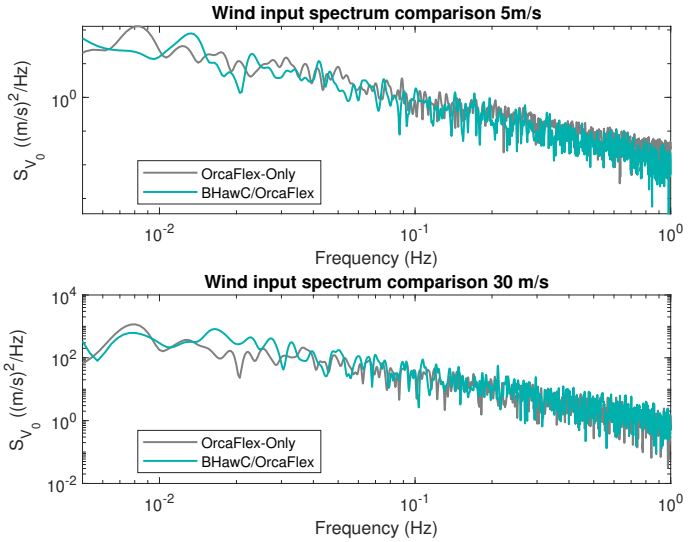

Figure 4.5: Wind field comparison of the spectrum used in OrcaFlex the spectrum used in BHawC/OrcaFlex.

4.5.4 Load Cases 4 and 5: Irregular waves

In the OrcaFlex hydrodynamic environment of both models, two JONSWAP wave spectra are defined using conditions from the load case table 4.2. Waves are generated from this spectrum using an equal energy distribution method. A similar wave seed is assigned to both models to create identical surface elevation timeseries and prevent differences in wave statistics. Wheeler stretching is applied in order to give a more accurate representation of the wave kinematics.

4.6 OrcaFlex vs BHawC/OrcaFlex verification results

In this section, BH/OF is verified against OF using load cases with environmental conditions of increasing complexity. Frequency response results of both models are obtained from a single 1800s time-domain simulation. More on the set-up of both models can be found in the previous sections. For the sake of compactness, only selected results that show clear dissimilarities are included in this chapter, where an attempt is made to minimise repetition of observed phenomena. In the BH/OF model, results from rigid body motion response could only be simulated on the tower at ~16m above SWL, which may cause overprediction of the response in the translation DOFs due to influence of the rotations. This is due to the identical BHawC wind turbine model used in later validation against full-scale measurements (see section 5.3), where these output positions match full-scale measurement sensors. Output locations were set accordingly in OF.

4.6.1 Load Case 1: Static analysis

An overview of the static analysis results is found in table 4.3. For both models, the heave position is slightly different from its expected position. This is due to differences in the total mass of the system, which is based on the summation of the masses of a large number of sub-components. Due to limited data available on the as-built system, no further improvement of the models could be made.

All static BLTs are either underpredicting or overpredicting values provided by Equinor [32]. A small difference is found in the static bridle line tension (BLT) of both models. OF predicts higher tensions in all bridle lines, which is found to be due to slightly lower tower mass in OF. Therefore, the system is at a higher vertical position in its equilibrium position, which causes an increase in BLTs.

The asymmetric errors in BLTs cause the surge position to be several meters from its expected equilibrium position. This error nearly equal for both models, though due to different tension distribution in the OF model this is slightly varied.

Parameter	**OF prediction**	**BH/OF prediction**	**Parameter**	**Equinor prediction**	**OF prediction**	**BH/OF prediction**
Surge (m)	+1.9	+2.1	**ml1b1 (kN)**	590	336	323
Sway (m)	-0.2	-0.2	**ml1b2 (kN)**	590	1112	1061
Heave (m)	0.8	-0.5	**ml2b1 (kN)**	590	713	693
Roll (deg)	6.2E-3	3.5E-3	**ml2b2 (kN)**	590	728	701
Pitch (deg)	0.1	0.5	**ml3b1 (kN)**	590	1107	1068
Yaw (deg)	6.0E-2	6.0E-2	**ml3b2 (kN)**	590	342	322

Table 4.3: A comparison of the static analysis results of OrcaFlex, BHawC/OrcaFlex and Equinor provided values.

4.6.2 Load Case 2: Free-decay tests

DOF	**Equinor prediction (s)**	**OF prediction (s)**	**BH/OF prediction (s)**	**Relative error OF**	**Relative error BH/OF**
Surge	96.2	84.0	84.7	-13 %	-12 %
Sway	96.2	84.0	84.7	-13 %	-12 %
Heave	25.8	24.8	25.2	-3.9 %	-2.3 %
Roll	33.7	35.1	32.3	+4.2 %	-4.2 %
Pitch	33.7	35.1	32.3	+4.2 %	+4.2 %
Yaw	13.0	14.7	15.1	+13 %	+16 %

Table 4.4: Comparison of rigid body motions natural periods of the Hywind Scotland system predicted by OF and BH/OF.

A free-decay test is performed in surge, heave and yaw. For most degrees of freedom DOFs, the natural frequencies are predicted well by BH/OF and OF. In both models, the surge/sway frequency is overpredicted and yaw is significantly underpredicted. Both DOFs natural frequencies are strongly influenced by the mooring restoring stiffness. As described in section 4.2, the total system roll and pitch inertia of the OF model were tuned to match that of the BH/OF model. A small difference in the yaw inertia may cause the difference in natural frequency here. This significantly reduced the error between the natural frequency prediction of both models. Note that the over- or underprediction here is based on the natural period in seconds.

4.6.3 Load Case 3.1: Turbulent below-rated wind-only

A comparison of the frequency-domain responses can be found in figure 4.6. In general, a good match between OF and BH/OF is observed. Main differences are the shift in surge/sway and roll/pitch peak frequencies, which are expected from decay tests. The energy level natural frequency response peaks is similar in both models.

The first tower bending peak is located at a similar frequency in both models (see figure 4.6c). The energy at tower bending is similar, meaning the level of tower damping is comparable. A slightly larger tower-bending response is predicted in BH/OF. This could be be due to the fact that a more sophisticated method for defining the tower bending is in this model, with separated Rayleigh damping coefficients for the axial, bending and torsional DOF, instead of a single coefficient for stiffness and mass proportional damping from classical Rayleigh damping definition. Moreover, BH/OF does not support a constant rotational velocity as this is not a physical operational condition. In this code, a constant RPM is pursued by means of active blade pitch control. This causes the rotor speed to vary about a constant RPM (see figure 4.6f), which may give dynamic thrust variations and therefore excite tower bending.

The bridle line response shows much similarity at all frequencies (see figure 4.6d). Both floater-mooring systems are modeled in OrcaFlex, but the coupling to BHawC in the BHawC/OrcaFlex does not significantly impact the response predicted. The yaw response is predicted with great similarity here. From the OC3-project results, it was found that different aero-hydro-servo-elastic codes often predict different yaw response due to a yaw gyroscopic moment that is difficult to simulate. Apparently, the advanced aero-servo-elastic code from BH/OF performs similar to that of OF, here. It must be noted that this load case and assumptions made in both model set-ups provide a simplification of the comparison.

4.6.4 Load Case 3.2: Turbulent above cut-out wind-only

A comparison of the FD response is depicted in figure 4.7. Much of the phenomena observed for LC 3.1 are repeated in this load case. Selected results showing additional phenomena are included here. The surge response peak in BH/OF is has shifted to a lower frequency compared to LC3.1. This due to a different mean surge position in this idling load case from the previous LC3.1. As the mooring system behaves highly non-linear, bridle stiffness and therefore surge frequency varies with floater position variations.

The overall response contains higher energy in BH/OF compared to OF. It is expected that this is due to the rotor efficiency of both models. As described in section 4.2, blade profiles had to be assigned in the OF Hywind turbine model in a simplified way. This reduced efficiency may cause a lower thrust force in OF which becomes more visible for high wind speeds of this case.

Now, the first tower bending peak is not captured in OF for the idling load cases, while it is apparent in the BH/OF case. This too may be due to excitation of the tower bending mode due to variations in rotor torque in the BH/OF model. Also, it is known that no rotor mass-imbalance is modeled in OF while it is in BH/OF. This, too may excite tower bending, where its contribution may be more apparent for an idling load case than seen in LC3.1.

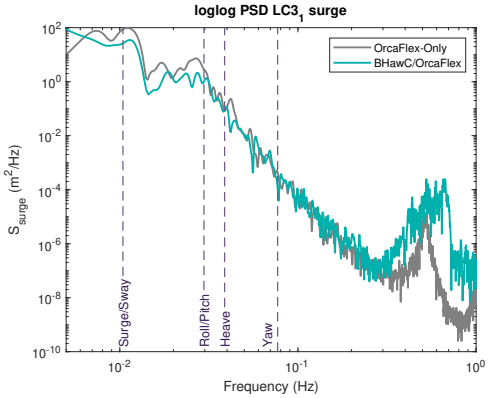

(a) Comparison of surge response of load case 3.1 predicted by OrcaFlex and BHawC/OrcaFlex.

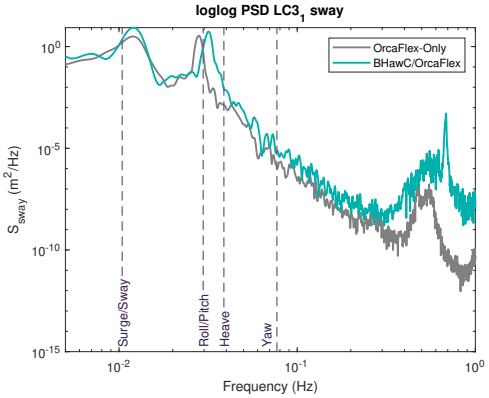

(b) Comparison of sway response of load case 3.1 predicted by OrcaFlex and BHawC/OrcaFlex.

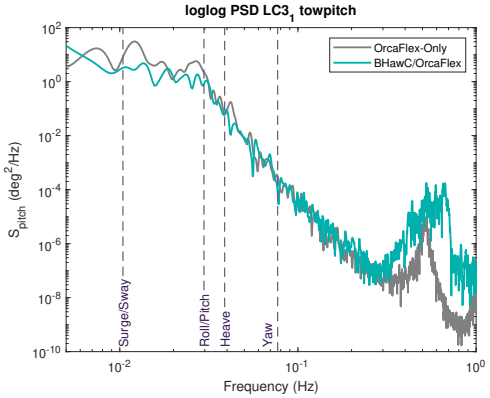

(c) Comparison of tower pitch response of load case 3.1 predicted by OrcaFlex and BHawC/OrcaFlex.

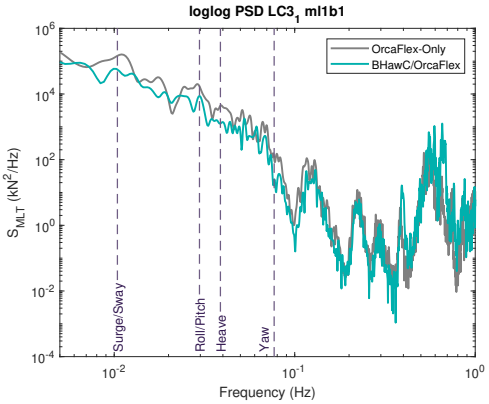

(d) Comparison of tower roll response of load case 3.1 predicted by OrcaFlex and BHawC/OrcaFlex.

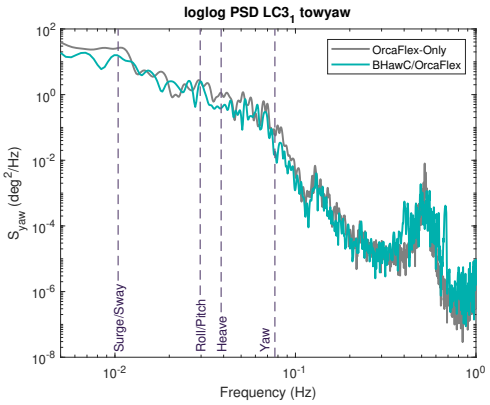

(e) Comparison of tower yaw response of load case 3.1 predicted by OrcaFlex and BHawC/OrcaFlex.

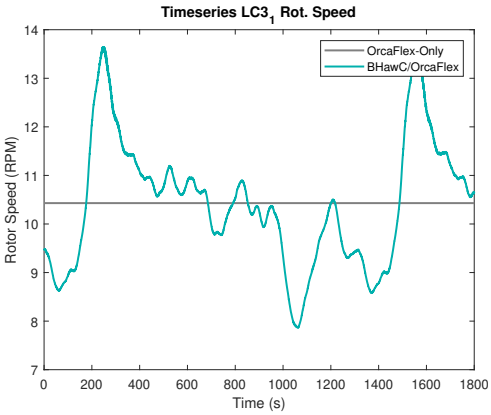

(f) Comparison of ml1b1 response to the below-rated turbulent wind-only of load case 3.1 predicted by OrcaFlex and BHawC/OrcaFlex.

Figure 4.6: Aero-hydro-elastic response to load case 3.1 comparison between OF and BH/OF.

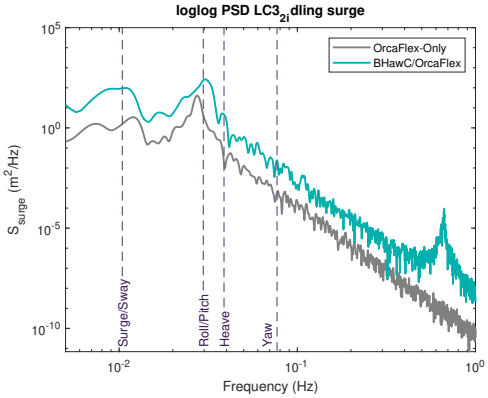

(a) Comparison of surge response of load case 3.2 predicted by OrcaFlex and BHawC/OrcaFlex.

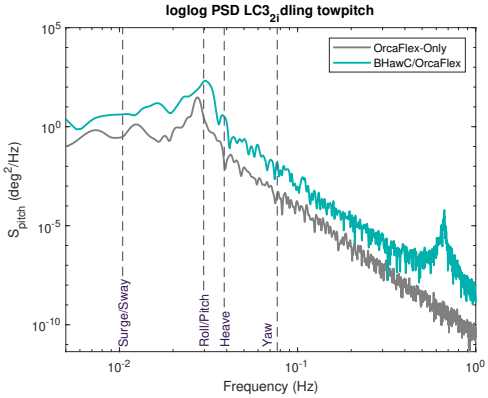

(b) Comparison of pitch response of load case 3.2 predicted by OrcaFlex and BHawC/OrcaFlex.

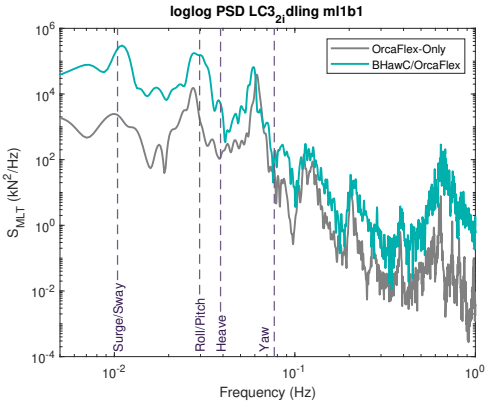

(c) Comparison of ml1b1 response of load case 3.2 predicted by OrcaFlex and BHawC/OrcaFlex.

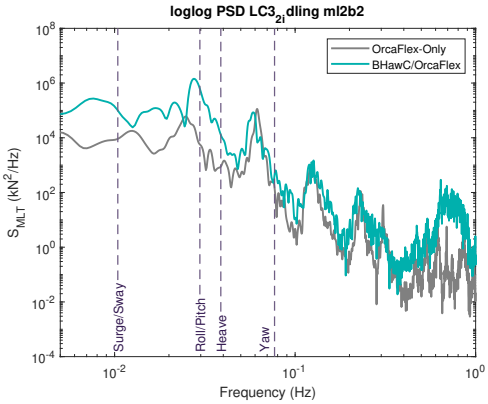

(d) Comparison of ml2b2 response of load case 3.2 predicted by OrcaFlex and BHawC/OrcaFlex.

Figure 4.7: Aero-hydro-elastic response to load case 3.2 comparison between OF and BH/OF.

4.6.5 Load Case 4: Irregular Airy waves

In this load case an irregular wave spectrum containing both a wind-wave and swell component is applied to the system. The general response matches well between both codes. The roll and sway response are predicted higher in BH/OF than OF (figure 4.8b). After closer inspection, it is found that the rotor in BH/OF is spinning at about 3.5 RPM, compared to no rotor speed in OF (figure 4.8f). This constant rotation causes excitation of the sway and roll motion, due to additional aerodynamic torque. Moreover, the tower-bending frequency is excited, likely due to rotor mass-imbalance modeled in BH/OF. The exact reason for the non-zero rotor speed remains unknown. No air density is present in both models. It is therefore expected that response is due to wave-induced excitation, which is translated by the turbine in a constant rotor speed. This would suggest that the multi-body-dynamics representation in BH/OF is more advanced than in OF, where this phenomenon is not captured. For surge and pitch, the pitch-frequency response, is smaller in BH/OF, which may be caused by additional aerodynamic damping due to the spinning rotor.

The surge response is significant in both cases, which may be due to hydrodynamic difference-frequency effects causing slow-drift of the system. Given that Morison model is used here with integration of the loads up to the instantaneous surface, this may be a small source of excitation of the system. This response is predicted equally well in both codes.

In yaw, the response is overpredicted over a range of frequencies BH/OF. It is expected that due to the non-zero rotor speed, a gyroscopic moment moment is exerted to the system that excite yaw motion and coupled dynamic response in other DOFs.

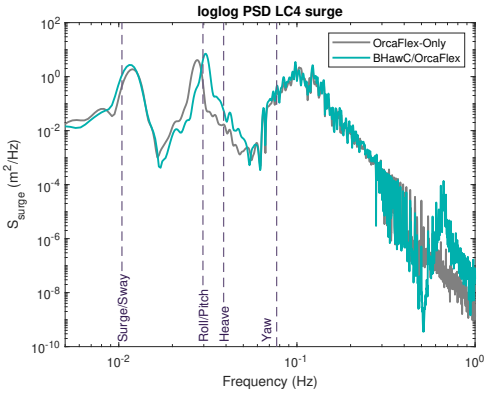

(a) Comparison of surge response of load case 4 predicted by OrcaFlex and BHawC/OrcaFlex.

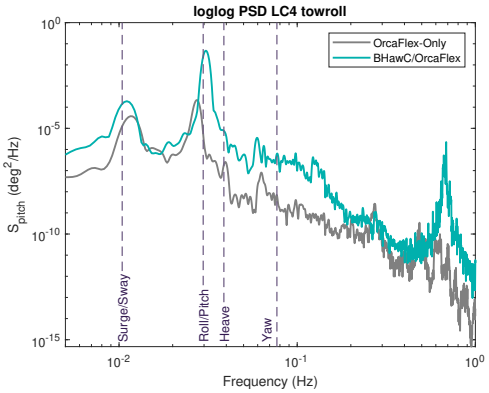

(b) Comparison of tower pitch response of load case 4 predicted by OrcaFlex and BHawC/OrcaFlex.

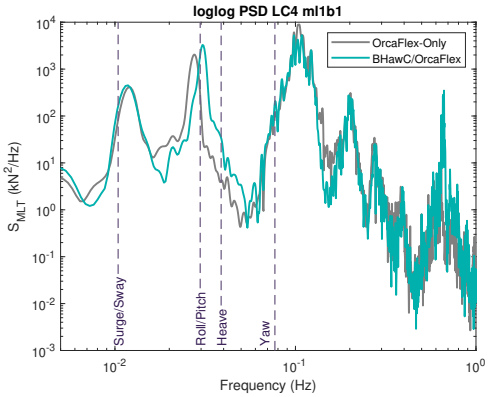

(c) Comparison of ml1b1 response of load case 4 predicted by OrcaFlex and BHawC/OrcaFlex.

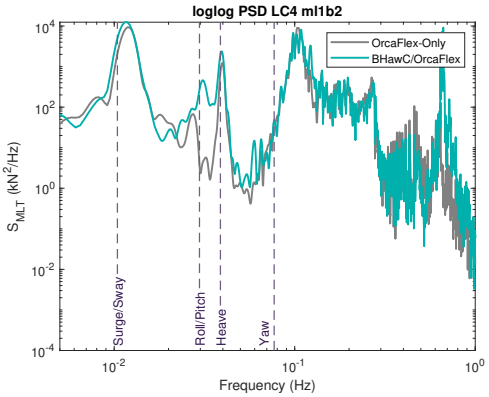

(d) Comparison of ml1b2 response to load case 4 predicted by OrcaFlex and BHawC/OrcaFlex.

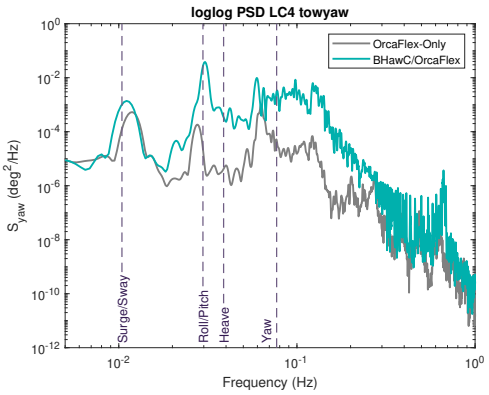

(e) Comparison of tower yaw response of load case 4 predicted by OrcaFlex and BHawC/OrcaFlex.

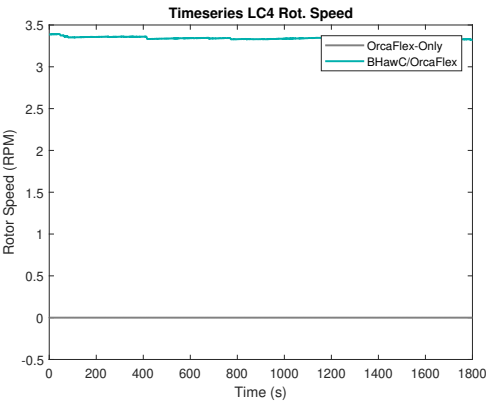

(f) Comparison of rotor speed of load case 4 predicted by OrcaFlex and BHawC/OrcaFlex.

Figure 4.8: Hydro-elastic response to load case 4 comparison between OF and BH/OF.

4.6.6 Load Case 5.1 and 5.2: Irregular Airy waves + turbulent wind

Two cases are presented together due to limited additionally observed discrepancies. The general response between BH/OF and OF of LC5.1 matches well (figure 4.9). Some differences are noticed in the low-frequency response for surge and pitch (figure 4.9a), where BH/OF predicts a larger response than OF. It is expected that this is due a more efficient rotor model in BH/OF. The heave response matches well (figure 4.9d), except for a larger roll/pitch response in BH/OF, which may be caused by the larger wind-induced excitation. The bridle line response matches well, for the combined stochastic wind and wave loads.

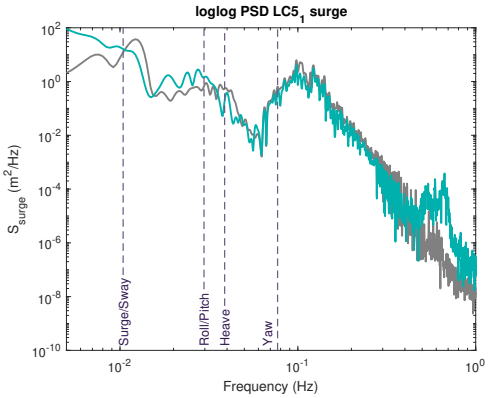

(a) Comparison of surge response of load case 5.1 predicted by OrcaFlex and BHawC/OrcaFlex.

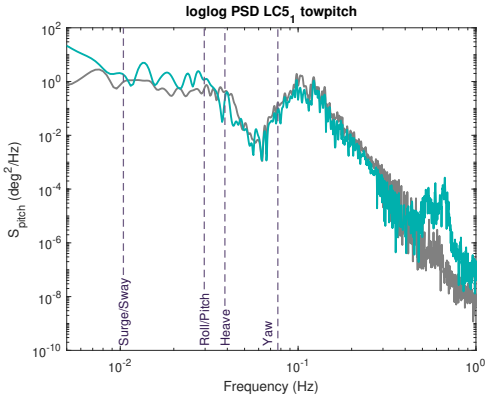

(b) Comparison of sway response of load case 5.1 predicted by OrcaFlex and BHawC/OrcaFlex.

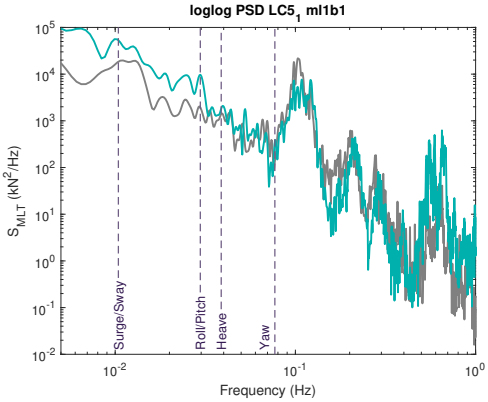

(c) Comparison of tower pitch response of load case 5.1 predicted by OrcaFlex and BHawC/OrcaFlex.

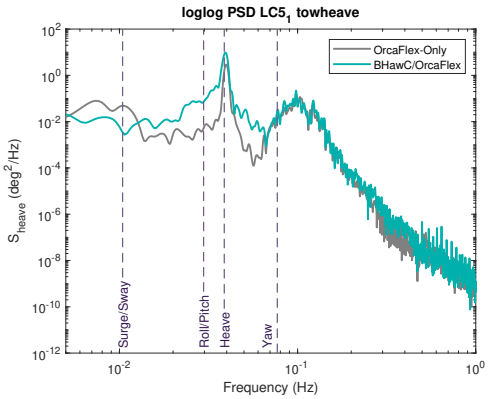

(d) Comparison of tower heave response of load case 5.1 predicted by OrcaFlex and BHawC/OrcaFlex.

Figure 4.9: Aero-hydro-elastic response to load case 5.1 comparison between OF and BH/OF.

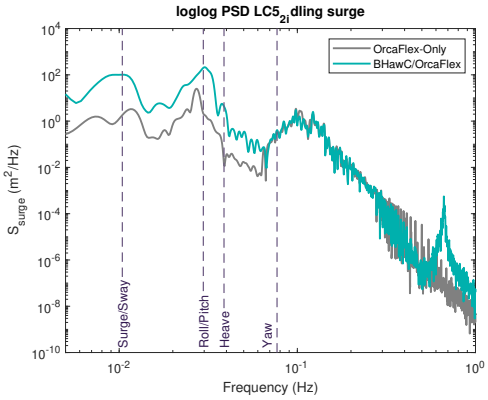

(a) Comparison of surge response of load case 5.2 predicted by OrcaFlex and BHawC/OrcaFlex.

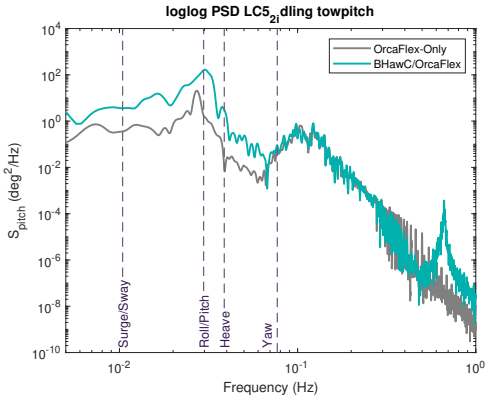

(b) Comparison of tower pitch response of load case 5.2 predicted by OrcaFlex and BHawC/OrcaFlex.

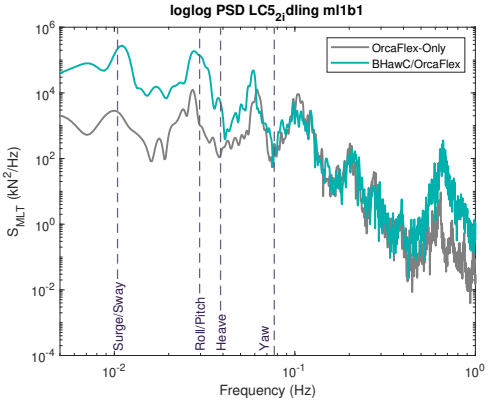

(c) Comparison of ml1b1 response of load case 5.2 predicted by OrcaFlex and BHawC/OrcaFlex.

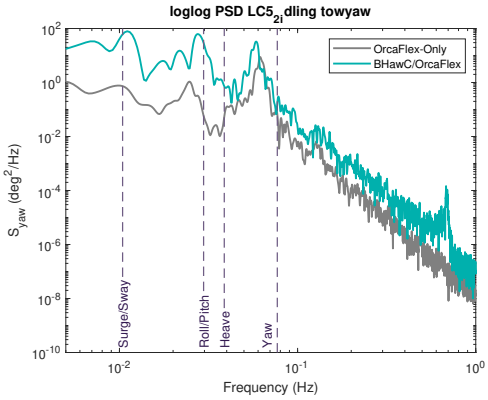

(d) Comparison of tower yaw response of load case 5.2 predicted by OrcaFlex and BHawC/OrcaFlex.

Figure 4.10: Aero-hydro-elastic response to load case 5.2 comparison between OF and BH/OF.

In LC5.2 again larger low-frequency response is observed, similar to the wind-only case. This may be due to 1) higher rotor efficiency in BH/OF, 2) small RPM variations in BH/OF. The wind fields used in both models are different, which may cause additional wind-induced excitation. However, the wind spectra of both cases depicted in figure 4.5 show no clear obvious energy differences that may give rise to discrepancies.

4.7 Conclusions: BHawC/OrcaFlex verification against OrcaFlex

In general, OrcaFlex and BHawC/OrcaFlex match well in their response to environmental conditions of increasing complexity. The bridle line response matches well in both systems, and give similar differences from the Equinor expected values of static BLTs. As described in section 2.5, three types of errors can be defined. These errors present in the are separately highlighted here. In addition, errors mitigated during model set-up are provided. Type 1 (code capacity) errors identified are: Type 1 (capacity) errors between from comparison are:

- In the irregular wave-only case, a constant rotor speed is observed in BHawC/OrcaFlex, compared to zero RPM in OrcaFlex. No air density is modeled, so this can only be due to wave excitation. Given an identical surface elevation timeseries, floater-mooring system model and hydrodynamic environment, this would imply that the multi-body-dynamics representation of BHawC/OrcaFlex is more advanced than that of OrcaFlex because it includes better coupling between response in different DOFs. However, further analysis of this error is required.
- Non-linearity of the mooring system causes shifts in the surge/sway response peaks at large mean horizontal displacement of the floater. This is due to a change in bridle stiffness inherent to the non-linear behaviour of a catenary mooring system.
- Differences in the low-frequency region are partly attributed to differences in rotor efficiency of both codes. BHawC directly interpolates aerodynamic coefficients along the blade for each time step, whereas in OrcaFlex fixed blade profiles must be assigned to each blade segment. This results in a lower thrust force from the OrcaFlex model, resulting in reduced wind-induced surge and pitch motion.
- OrcaFlex defines structural tower damping using classical Rayleigh coefficients, whereas BHawC/OrcaFlex uses separated stiffness and mass-proportional coefficients, which is more sophisticated. This results in a lower predicted wind-induced tower bending response in OrcaFlex.
- No rotor mass imbalance is modeled in OrcaFlex, which results in absence of the tower-bending frequency in most idling cases.

Type 2 and 3 (model set-up and physical model) errors are:

- Despite careful set-up of the OrcaFlex Hywind turbine, no numerically stable model could be created. This instability was mainly observed from the blade structural parameters. The only way simulations were possible was to assign fixed blades in both codes in all load cases.
- An insuperable difference in the control system capacities of BHawC and OrcaFlex limit a direct comparison of the aero-servo-elastic codes at their full performance. Therefore, load cases are adapted to very high and very low wind speeds to minimize the effect of control impact on the response.
- In OrcaFlex, no generator torque control is allowed when assigning a constant blade pitch angle. Therefore, a constant rotational velocity had to be assigned. In the BH/OF, a constant RPM is pursued by an active control system. Minor variations in RPM cause additional excitation of the surge/sway, roll/pitch and tower bending response peaks.
- Large differences in the static tensions of the mooring system are observed between both codes and expected values provided by Equinor. Set-up had to be done using limited information on the as-built mooring system, which required parameters to be decided based on literature. This causes a ~13-16% error in the surge, sway and yaw natural frequency predictions in both models. Also, a non-zero static surge position is observed due to asymmetrical static bridle line tensions. Finally, non-diagonal terms in the mooring response matrix are likely caused by a modeled 3D seabed in OrcaFlex. In both models, the bridle line response is very similar.

Errors mitigated during the model set-up are:

- Adding artificial roll/pitch inertia by means of a 'vessel object' [74] at SWL in OrcaFlex helps to match in the inertia to another model of interest.

It should be noted that the model set-up in both codes had to be simplified from the final BHawC/OrcaFlex model used in validation, due to numerical instability of the OrcaFlex model.. By either creating a representative controller of the SWT6.0-154 Hywind turbine in OrcaFlex or creating a model of the publicly available NREL5MW in BHawC, both software codes could be tested to their full performance.

5

BHawC/OrcaFlex validation with full-scale measurements

In this final validation step, aero-hydro-servo-elastic simulations in BHawC/OrcaFlex (BH/OF) are compared with full-scale measurements on the Hywind Scotland floating offshore wind farm (Hywind), which are provided by Equinor together with a description of the as-built system. In previous chapters, BHawC/OrcaFlex was verified to OrcaFlex (OF), which in turn was verified using industry-standard aero-hydro-servo-elastic software codes. Hywind measurements consist of 11 'load cases' each containing 30-minute-averaged statistics of the environmental conditions and 30-minute timeseries of load and motion measurements on the full-scale system. In this chapter, the set-up of the BH/OF model used in this final comparison step is explained. Next, available data and post-processing methods are explained. Also, a detailed description of expected hydrodynamic phenomena are given. Then, a load case table of each of the simulations used in this validation step is provided and a specific model set-up for each load case is explained. In section 5.5, simulation results are compared to measurements. In section 5.6, a detailed analysis of selected error is made to increase confidence in the validation results and hence the code capacity.

5.1 Set-up of the Hywind Scotland model in BHawC/OrcaFlex

For the final validation step in this research, an aero-servo-hydro-elastic floating offshore wind turbine model is set-up in BHawC/OrcaFlex. A similar BHawC/OrcaFlex model is as used for verification against OrcaFlex. A detailed description of this model, including any modeling decisions can be found in Chapter 4 (sections 4.1 and 4.3). Preliminary verification results of this BHawC/OrcaFlex model against an OrcaFlex-only model can be found in section 4.6.

Several revisions of the model were made after it was compared against OrcaFlex. In the most revisions, obvious errors in the model set-up, environmental conditions definitions and results post-processing were solved. In the final revision, improvements to the mooring system were made, as large discrepancy from Equinor was observed from the previous verification step.

5.1.1 Tuning of the mooring system to match static tensions

In the Hywind Scotland system description [32], static pre-tensions in the upper end of all lines are provided. According to Equinor, the static tensions in main lines are given as ~ 760 kN and in the bridle lines as ~ 590 kN. Equinor states that the prescribed system parameters may give higher tensions in ML1 bridle 1 and ML3 bridle 2 compared to measurements due to differences with the as-built system. In addition, an (idealized) mooring restoring matrix is provided by Equinor.

After building the floater and mooring system in OrcaFlex and the turbine in BHawC, as described in section 4.1, large discrepancies in the static pre-tensions are found. Therefore, it was decided to adapt the mooring system to better match the prescribed tensions. This was done in several steps:

- First, a comparison was made between the mooring restoring matrix provided by Equinor and one generated by OrcaFlex. OrcaFlex allows to calculate a separate mooring restoring matrix, including all stiffness effects except hydrostatic stiffness (see equation 2.72). It was found that OrcaFlex showed large non-diagonal coupling terms at nearly all matrix element. An explanation was found by the 3D

seabed that was used to describe the original system environment. Mooring chains in OrcaFlex are modeled as continuous lines instead of actual chain links. The system is more sensitive to changes in the seabed bathymetry than may be the case in reality, as these may cause unwanted normal and shear forces components on the lines, which in turn may cause undesired coupling terms. It was found that by simplifying the environment to a flat seabed, most of the unwanted coupling terms were removed. Therefore, these setting were used for further analysis of the model.

- The anchor depth variation around -113 m was found to cause generally too high tensions in all lines. This value was originally found from a Hywind Scotland technical report on the bathymetry (see section 4.1). From the Hywind data description [32] a generic estimated value of -100 m is prescribed. Therefore, this assumption was taken over in further analysis of the system.
- Finally, the lengths of all lines were varied manually until a general match was found between the prescribed and simulated static tensions. It may be worth noting that only small length variations sufficed in tuning the system.

The results of tuning can be found in table 5.1. The length of each line influences tensions in all other lines. Therefore, accurate tuning is a cumbersome process. In the final chosen lay-out a non-negligible error in static bridle line tensions (~15%) was accepted. This is still much improved to the original errors. Priority here, was given to making sure each line type has a similar error, instead of values differing per line as in the original system.

Mooring line	Tension (kN) expected	Tension (kN) before tuning	Tension (kN) after tuning	Relative error before tuning	Relative error after tuning
Main line 1	~ 760	1490	785	96 %	3.3 %
Main line 2	~ 760	1250	785	64 %	3.3 %
Main line 3	~ 760	1540	785	103 %	3.3 %
ML1 bridle 1	~ 590	350	500	-41 %	-15 %
ML1 bridle 2	~ 590	1340	500	127 %	-15 %
ML2 bridle 1	~ 590	720	500	22 %	-15 %
ML2 bridle 2	~ 590	720	500	22 %	-15 %
ML3 bridle 1	~ 590	1340	500	127 %	-15 %
ML3 bridle 2	~ 590	350	500	-40 %	-15 %

Table 5.1: Mooring line tensions and their corresponding relative error to prescribed values from Equinor [32], before and after tuning.

5.2 Overview of environmental conditions measurements

An extensive set of measurement data is made publicly available through a data sharing agreement between ORE Catapult and Equinor ASA. Measurements are taken from a single turbine of the Hywind Scotland floating offshore wind farm, 25 kilometers off the East-coast of Scotland. The site consists of 5 floating wind turbines each moored by three catenary lines. The turbine location and position in the wind farm lay-out are depicted in figure 5.1. Measurements are provided for Turbine #4 from this overview.

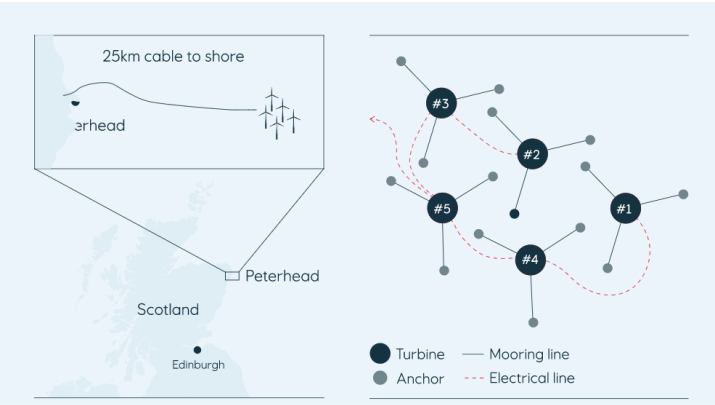

Figure 5.1: An overview of the location and lay-out of the Hywind Scotland floating offshore wind farm. Adapted from [33].

The data consists of 11 'data intervals' or 'load cases', which are selected based upon finding stationary conditions that makes them relevant for doing simulations of the same events [14]. Each of the 11 load cases contains 30 minutes of measurements in varying conditions. During cases 1-9 the system is operational and during cases 10-11 the system is idling due to extreme wind speeds. Each load case consists of a combination of environmental conditions and system load and motion measurements. The environmental conditions comprise:

- Wind speed, wind standard deviation, wind direction;
- Total significant wave height, total wave period and total wave direction;
- Wind sea significant wave height, wind sea period and wind sea direction;
- Swell significant wave height, swell period and swell direction;
- Total current speed and total current direction;
- Current speed and current direction at 4 different water depths.

Here, the 'total' conditions in some cases are suggested by Equinor to represent the detailed conditions in a fair way. For example, the current speed is provided at 4 different water depths, where the total conditions translate this to a single speed by weighting out the detailed conditions.

All environmental conditions are given as 30-minute statistics per load case. Note that the wind speed is given both as a system measurement (timeseries) and environmental conditions measurement (30-minute statistics). All load cases are provided by Equinor in a 'random' order regarding their severity. In this report, all load cases are re-defined such that they are ordered to increasing wind speed, with load case 1 having the lowest wind speed and load case 11 the highest.

It should be noted that the wave buoy measuring wave and current conditions is located 2.5 km away from the turbine, South-East of the wind farm site. Throughout this report, all measured environmental conditions values are considered to be constant over the entire site. Therefore, wave scattering or radiation effects are neglected and no additional extrapolation to turbine location are made (e.g. as performed by Skaare et al. [88]). This can be justified by the relatively remote nature of the site and therefore unlikely disturbance of these conditions due to external factors. Wind is measured from the turbine anemometer, where statistics are corrected for the turbine motion.

5.2.1 Wind conditions

An overview of the wind speeds and variation is found in figure 5.2a. Here, the turbulence intensity (TI) is obtained from the standard deviation using equation 2.59. The cut-in, rated and cut-out velocities of the SWT6.0-154 turbine are shown as horizontal dashed lines [29]. It can be seen that cases 1 and 2 are in the below-rated regime, with a relatively constant blade pitch angle. Cases 4 through 7 are around rated wind speed. Case 8 and 9 are in the above-rated regime. This means that cases 4 through 9 expect active blade pitch control influence in their response. Cases 10 and 11 can be considered above cut-out and therefore the turbine is idling, with no active control. It can be observed that as the wind speed increases, turbulence intensity increases with it, showing highly fluctuating wind speeds with gusts at 'storm' conditions in cases 10 and 11. Wind conditions are estimated based upon the turbines wind anemometer. For the idling cases, moments when the blade was covering the anemometer where removed from these statistics calculations.

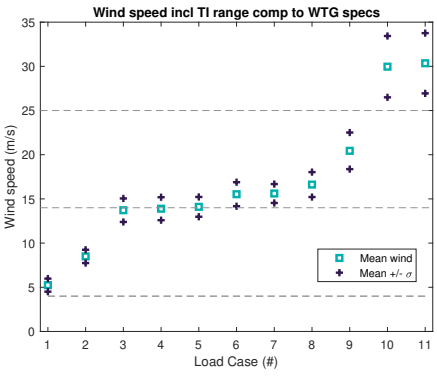

(a) Wind conditions.

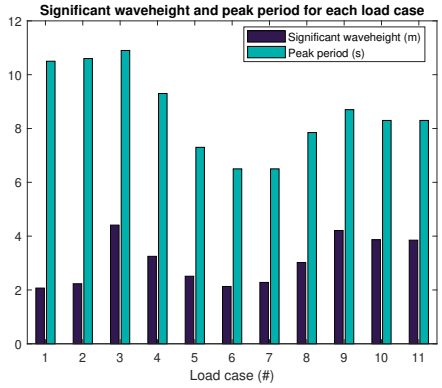

(b) Spectral peak period.

Figure 5.2: An overview wind and wave conditions per load case.

5.2.2 Wave conditions

An overview of the total wave conditions per case can be found in figure 5.2. It can be seen that the significant wave height roughly varies between 2 and 4.5 meters, which can be considered normal sea state (NSS) conditions. From a Hywind MetOcean design basis [94], it can be observed that waves in all cases are well below design conditions.

There is no clear trend in the relationship between the wind speed and wave conditions. The lowest wave heights, however, do occur in combination with the lowest wind speeds. Furthermore, an increase in wave height with respect to the peak period can be observed for an increase in wind speed.

Next, the 'total wave height' is compared to the individual wind and swell component heights. The relative importance of wind and swell waves can then be found in figure 5.3a, by dividing each component by the sum of both components. Cases 1-4, of low wind speed, and cases 9-11 of high wind speed have an equal wind sea and swell contribution. The 'middle' cases, however, are mostly dominated by wind waves. A look at the wind- and swell wave periods (figure 5.3b) shows that these are roughly equal for each case. It can also be seen that, as found in theory, swell waves in general have a longer wave period as they have developed over a longer fetch.

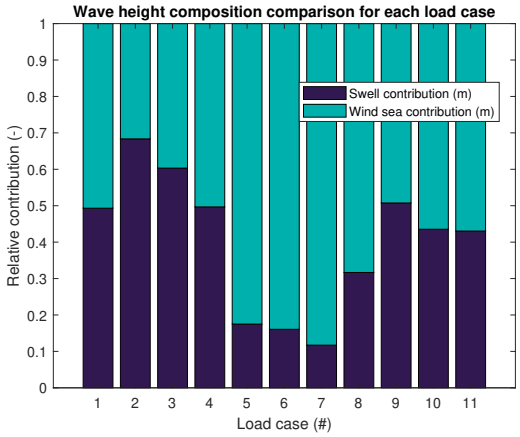

(a) An overview of the wind speed and range of turbulence intensity per load case.

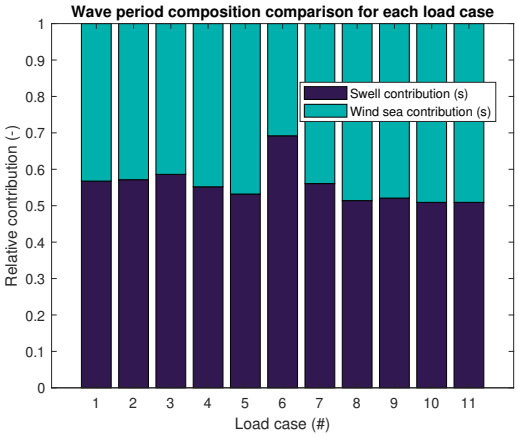

(b) An overview of the significant wave height and spectral peak period per load case.

Figure 5.3: An overview of the wind and wave conditions per load case. Ordered with respect to increasing wind speed.

5.2.3 Current conditions

The current profile distribution over height for each case is depicted in figure 5.4a. It can be seen that the current velocity profile shape varies significantly with each case and can not always be identified as constant, linear or logarithmic (see section 2.2.2). At low current speeds, however, the profile is more or less constant.

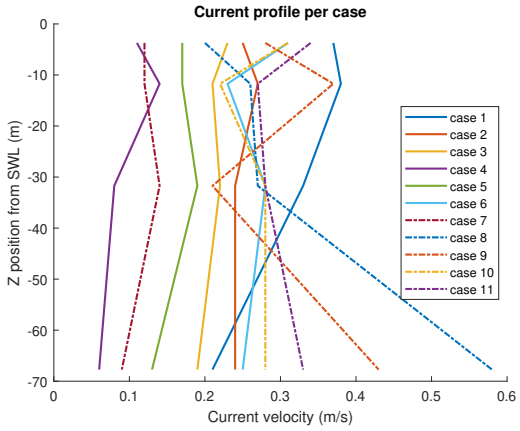

(a) Current profile for each load case.

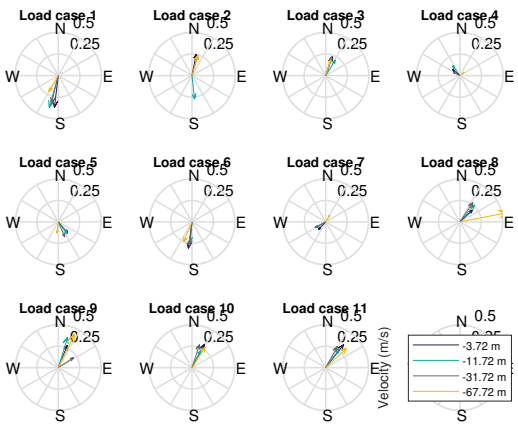

(b) Current direction over its depth for each load case.

Figure 5.4: An overview of the current conditions per load case.

What also stands out is that some current velocities are rather high for North-Sea circumstances, with a maximum of 0.6 m/s near floater bottom dept. This can be explained by the high water depth, as well as relatively 'oceanic' location in the North of the United Kingdom, with little shelter from the Atlantic Ocean. This sharp increase of speed in deeper waters indicates deep water currents that are not directly caused by local winds. There appears to be no direct relationship between the wind speed and total current velocity. However, for cases 10 and 11 with high wind speeds a sharp increase of current velocity near the free surface is observed.

Next, the current directions are included in the analysis. The current velocity and direction component at each measurement depth can be found in figure 5.4b. Here, it can be seen that next to the current velocity, the direction in some cases varies greatly over the depth as well. In some cases the current direction at one depth may oppose those of all the others. This shows that it is of major importance to include this directionality in simulations, as these this depth variation could cause an overturning moment or influence VIM behaviour.

5.2.4 Total sea state

An overview of the directions of all 'total' environmental conditions are given in figure 5.5b. Total conditions in this case are conditions with a single direction to represent distributions of conditions from multiple direction, e.g. current directions at different water depths. Here, the size of each vector is constant and not related to the velocity or height. It can be observed that for most cases, the wind and wave directions are well-aligned. A clear dominant North-South wind direction can be identified, which equals cross-shore wind for the given location. In a few cases, however, significant wind/wave misalignment can be observed. The current direction, on the other hand, is more often misaligned than aligned to the wind and wave directions. This can be explained by the relatively deep water conditions at the Hywind Scotland location, with currents being able to develop far away from the site and left relatively undisturbed by local wind and seabed conditions.

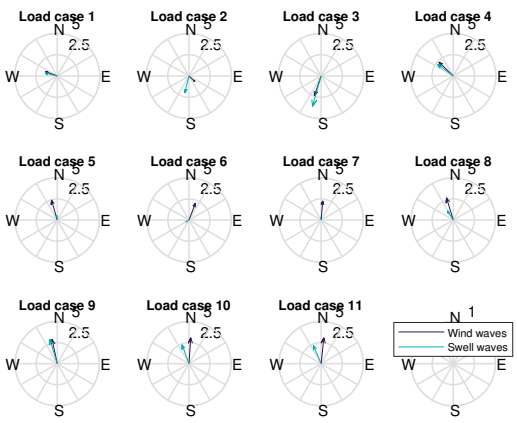

(a) Direction of the wind-wave and swell components per load case. The arrow direction indicates the direction in which the wave train propagates and the arrow magnitude indicates the significant waveheight.

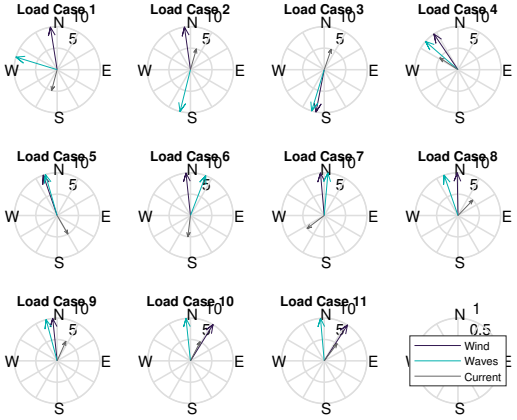

(b) Direction of the 'total' wind, waves and current conditions per load case. The arrow direction indicates the direction in which the environmental condition is measured. The arrow magnitude is independent of the magnitude of the considered environmental condition.

Figure 5.5: An overview of the directions of environmental conditions per load case.

From figure 5.5a it is noted that the wind and swell directions conditions are mostly equal, with some exemptions being load case 2 and 6. Here, wind waves are found to correspond well to the wind direction. In some cases (e.g. load case 2), this is not true, which could be explained by a sudden shift in wind direction just before the start of these measurements. That would allow a wind sea to develop, but not yet to be blown away by the new wind direction.

One can observe from the farm lay-out in figure 5.1, that for 'Northerly winds' the incoming wind flow is disturbed by the other wind turbines. This may cause increased turbulence and reduced wind speeds for these conditions. It is important to keep this in mind for further measurement observations. The wave conditions, on the other hand, are not expected to be disturbed severely by the other turbines. Due to the mooring system, the distance between floaters is more than 640 meters (the anchor radius) at all times.

5.2.5 Hydrodynamic analysis

Despite a detailed description of the as-built system and environmental condition measurements, the floating support structure and hydrodynamic environment must be set up based on theoretical assumptions. In order to minimize errors made in this step, a thorough hydrodynamic analysis is performed which can be found in Appendix D. The outcomes are used to 1) determine model parameters based on literature and 2) help in the analysis of validation errors. Several conclusions can be drawn from the hydrodynamic analysis:

- LC 5-11 could may include mildly non-linear wave effects. The probability of waves with these properties, however, is small.;
- In all LCs, the wave response is inertia-dominated, meaning both Morison equation and potential flow theory apply here;
- In LC 6-7, diffraction effects may occur, meaning caution should be taken with the use of Morison equation without any diffraction correction;
- In all LCs, highly turbulent flow is observed (Re>10^7) near SWL, below the floater taper a varying reduction of the Re-number is observed per load case O(10^4 - 10^6). This would theoretically result in a variation of the drag coefficient along the floater.
- This analysis provides insight in the expected flow regimes when the floater is not moving. In (resonant) dynamic conditions, the floater velocity is expected to increase, thereby increasing the Re and KC number and consequently the possibilities of flow separation. This may increase the drag contribution to the total loads and hereby the contribution of viscous damping.

5.3 Overview of full-scale load and motion measurements

Next to the environmental conditions statistics, 30-minute timeseries are given of full-scale measurements on the Hywind system [32]. These measurements consist of:

- Wind speed, measured by the turbine's anemometer;
- Nacelle yaw direction in cardinal coordinates;
- Nacelle roll and pitch orientation in local coordinates, based on the nacelle direction. Measured by a motion reference unit (MRU) (+99 m above SWL);
- Tower roll, pitch and yaw orientation in local coordinates, based on the nacelle direction. Measured by a MRU (+16.9 m above SWL);
- Floater surge and sway position, in cardinal coordinates. This means a positive displacement in the North and East direction, respectively. Measured by a GPS antenna (+15.3 m above SWL);
- Bridle line tension, measured by a load cell in the upper end of each bridle line.

Next to the Hywind measurements available from Equinor, access was given by SGRE to supervisory control and data acquisition (SCADA) data. This data consists of 10-minute-averaged statistics of the year 2018 during which all Equinor measurements took place. SCADA data is used in this thesis purely to provide additional insights in the behaviour of the system or as a back-up check of the Equinor measurements and is not the main focus of this research. Nacelle motions are more strongly influenced by the tower and blade flexible body dynamic response, which add complexity to the analysis. Therefore, it is decided to use these signals only as a back-up check of the tower motion response and focus on comparison of the other signals.

Several relevant frequencies are identified and included in the comparison figures of section 5.5. These consists of:

- The wind and swell wave spectrum peak frequency, determined from the environmental data of the corresponding measurement load case;
- The rigid body motion natural frequencies, obtained from the Hywind data description [32];
- rotational speed frequency (1P) and blade-passing frequency (3P) are determined from available SGRE SCADA data. Here, rotational velocity at the time of available Equinor measurements is determined using the previously described serial date number. For each load case, timeslots are matched to those of the measurement data. Three 10-minute-averaged statistics are obtained (corresponding to 30 minutes of measurements) from the SCADA data. The mean of these three data points is used to create 30-minute-averaged statistics, which are added to the figure as the final rotational velocity (1P and 3P) for the given load case.
- An estimation of the 1st tower-bending frequency is available in the SGRE SCADA data. A similar method is used to match the SCADA data timeslot to that of the Equinor measurements. Which provides a 30-minute-averaged first tower bending frequency at the time of the measurement. The tower-

bending frequency estimation provided in the SCADA data is made based on the measured tower-top acceleration in the turbine.
- The second tower bending frequency is visually identified from the measurement signal peaks.

5.3.1 Post-processing of full-scale measurement and simulation results

In order to be able to use the provided full-scale measurement data timeseries from Equinor, several post-processing steps had to be taken. A detailed explanation of post-processing of results throughout this report is provided in Appendix E. Post-processing of simulation results is performed in a similar way as for the measurements. First, all measurements were interpolated to get rid of discontinuous sampling frequencies and assign an identical timestep to each signal. Power spectral density (PSD) representation of the frequency domain (FD) response of all signals is obtained by applying a fast Fourier transform (FFT) to each timeseries signal. First, each signal is normalised and a Hann window with a window length ratio of 0.4 and an overlap ratio of 0.5 is applied. On BHawC/OrcaFlex simulation data, a window length ratio of 0.7 and a overlap ratio of 0.5 is applied.

Here, the PSD results of simulations are obtained by taking the mean value of 24 seeds for the stochastic wind and wave realisations of 1800 s. The timeseries shown for BH/OF results is that of a single seed, which gives an impression of the order of magnitude and general behaviour of the load and motion predictions. All results are obtained from output channels that match in location on the turbine with the measurement devices of the full-scale system (see section 5.3). For statistics results a box plot visualisation is selected to give a compact, comprehensive overview. The central mark indicates the median, the bottom and top edges indicate the 25th and 75th percentiles and the wiskers show the most extreme data points corresponding to approximately +/- 2.7σ. Outliers are plotted with a red '+'.

5.4 Load case table

All load cases available from the Hywind measurement data are summarized in the load case table below in terms of their wind, wind-wave, swell and current conditions. Note that the load cases are ordered to increasing wind speed. This order differs from the load case definition originally provided by Equinor. The total current conditions are provided instead of a speed and direction distribution per water depth (see figure 5.4b) for compactness.

Finally, note that the definition of the environmental conditions directions is followed from Equinor [32]. Here, the wind and waves directions are defined as 'coming from', with 0 degrees meaning wind coming from North. However, the current direction is defined as 'going towards', with 0 degrees meaning current coming from South. In all figures from section 5.2 this difference is accounted for and all conditions are translated to the same global coordinate system with the arrow pointing in the 'going towards' direction. Similarly, this difference in definition is accounted for in the simulations set-up.

A spatially varying wind field is generated in BHawC/OrcaFlex using a Mann turbulence model with the provided wind speed and turbulence intensity. Use of this model was validated by SGRE for their turbine prototype [75]. For load cases 10 and 11 it is known that the turbine is idling, which had to be separately imposed on the BHawC wind turbine model.

Load Case	Wind Conditions	Wind-wave conditions	Swell-wave conditions	Current conditions
1	NTM: V_{hub} = 5.25 m/s Direction: 171 deg	H_s = 1.5 m, T_p = 8.0 s, Direction: 111 deg	H_s = 1.4 m, T_p = 11 s, Direction: 103 deg	U_{cur} = 0.32 m/s. Direction = 195 deg.
2	NTM: V_{hub} = 8.49 m/s Direction: 172 deg	H_s = 0.9 m, T_p = 8.0 s, Direction: 313 deg	H_s = 2.0 m, T_p = 11 s, Direction: 14 deg	U_{cur} = 0.24 m/s. Direction = 16 deg.
3	NTM: V_{hub} = 13.7 m/s Direction: 11 deg	H_s = 2.4 m, T_p = 7.7 s, Direction: 19 deg	H_s = 3.7 m, T_p = 11 s, Direction: 16 deg	U_{cur} = 0.21 m/s. Direction = 19 deg.
4	NTM: V_{hub} = 13.9 m/s Direction: 146 deg	H_s = 2.3 m, T_p = 7.6 s, Direction: 134 deg	H_s = 2.3 m, T_p = 9.3 s, Direction: 127 deg	U_{cur} = 0.09 m/s. Direction = 303 deg.
5	NTM: V_{hub} = 14.1 m/s Direction: 161 deg	H_s = 2.5 m, T_p = 7.3 s, Direction: 164 deg	H_s = 0.5 m, T_p = 8.3 s, Direction: 174 deg	U_{cur} = 0.17 m/s. Direction = 150 deg.
6	NTM: V_{hub} = 15.5 m/s Direction: 174 deg	H_s = 2.1 m, T_p = 6.5 s, Direction: 201 deg	H_s = 0.4 m, T_p = 15 s, Direction: 61 deg	U_{cur} = 0.27 m/s. Direction = 187 deg.
7	NTM: V_{hub} = 15.6 m/s Direction: 174 deg	H_s = 2.3 m, T_p = 6.5 s, Direction: 185 deg	H_s = 0.3 m, T_p = 8.3 s, Direction: 170 deg	U_{cur} = 0.12 m/s. Direction = 233 deg.
8	NTM: V_{hub} = 16.6 m/s Direction: 179 deg	H_s = 2.7 m, T_p = 7.9 s, Direction: 163 deg	H_s = 1.3 m, T_p = 8.3 s, Direction: 148 deg	U_{cur} = 0.33 m/s. Direction = 44 deg.
9	NTM: V_{hub} = 20.4 m/s Direction: 174 deg	H_s = 2.9 m, T_p = 8.0 s, Direction: 168 deg	H_s = 3.0 m, T_p = 8.7 s, Direction: 163 deg	U_{cur} = 0.32 m/s. Direction = 24 deg.
10	ETM: V_{hub} = 30.0 m/s Direction: 212 deg	H_s = 3.1 m, T_p = 8.0 s, Direction: 184 deg	H_s = 2.4 m, T_p = 8.3 s, Direction: 160 deg	U_{cur} = 0.27 m/s. Direction = 27 deg.
11	ETM: V_{hub} = 30.3 m/s Direction: 213 deg	H_s = 3.1 m, T_p = 8.0 s, Direction: 186 deg	H_s = 2.3 m, T_p = 8.3 s, Direction:157 deg	U_{cur} = 0.30 m/s. Direction = 37 deg.

Table 5.2: Load-case table used in the comparison of BHawC/OrcaFlex to full-scale Hywind measurements.

5.5 Hywind Scotland validation results

The results of BH/OF aero-hydro-sevo-elastic load and motion simulations are validated against measurements from the Hywind Scotland floating offshore wind farm Hywind. More on the model set-up can be found in section 5.1. First, response statistics are compared for this load case to get a general impression of the prediction accuracy. Then, frequency domain response is compared to get a more detailed insight in the physical phenomena observed.

Simulations of load case 4 through 9 (rated or above-rated wind speed) showed severe oscillation in the results due to absence of motion compensation from the control system. This is likely due to varying pitch natural frequency of the system in each load case, causing the notch filter in the controller to be tuned to the wrong frequency.Therefore, only load cases 1, 2, 3, 10 and 11 are available for proper comparison and are included here.

Figure 5.6: Schematic overview of the floater and bridle lines lay-out.

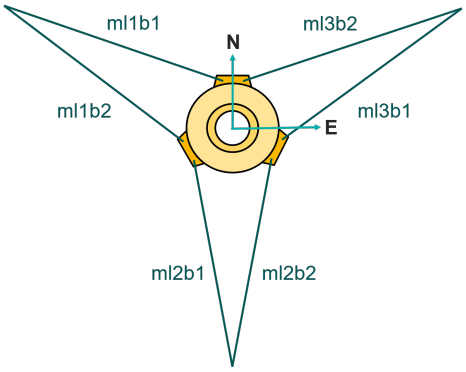

5.5.1 General observations

Several general observations are made, which do not depend on the model set-up.

- First, it was discovered that all wind measurements are influenced by turbine motions. The incoming wind speed is measured by Equinor using the turbines anemometer, which is located on the nacelle. This means the measured wind speed is the sum of the incoming wind speed and nacelle velocity in downstream direction, defined as the relative incoming wind speed. The environmental conditions 30-minute-averaged statistics provided by, however, are corrected from turbine motion influence [32]. Discrepancies in operational cases are mainly observed in the standard deviations (figure 5.8a). In the software, a fixed output coordinate is used for the wind speed timeseries, excluding all turbine motions. Measuring the relative wind speed, however, results in lower wind speeds when the turbine moves downstream and vice versa. This gives a larger oscillation in wind speed and therefore larger standard deviation. The main difference is observed for load cases 10 and 11, which are idling cases. Here, it is known that the rotor speed and pitch angle are constant and no motion compensation is provided by the turbine control system.
- Secondly, it is found that the measurements from load case 1 contain a clear transient in the surge/sway/roll motions and bridle line tensions (see figure 5.7). As the wind speed in this case is only slightly above the cut-in wind speed from the turbine (figure 5.2a), it is likely that the turbine cut in only moments before these measurements were recorded. Such an event causes a sudden increase in (mean) rotor thrust force, moving the turbine to a new mean position. This is confirmed by a relatively high energy peak in the surge/sway frequency (see figure 5.7) compared to BHawC/OrcaFlex, where steady-state conditions are assumed.
- Thirdly, it is observed that for nearly all load cases, the low-frequency response is predicted with less accuracy than the other two regions due to statistical uncertainty (see section 5.6.2).
- The general energy level in the region above 1Hz is usually underpredicted. High-frequent measurement noise is suspected to add energy in this region, which is not due to physical response. The dynamic GPS sensor has a sampling rate of 1Hz. According to Equinor, data was up-sampled to better match the other measurements. Therefore, all surge and sway results are cut-off at 0.5 Hz, an upper limit of the frequencies that the sensor can still capture.
- It was stated by Equinor [32] that in main line 1, bridle line 1 (ml1b1) and main line 3, bridle line 2 (ml3b2), tensions could be lower in the measurements than predicted from the prescribed system, due deviation in the as-built system from provided values. Possible dissimilarities are due to non-identical mooring lines or a non-uniform seabed.
- Finally, in some load cases a mean platform yaw of 9 degrees is reported from the measurements. This is acknowledged by Equinor [32] to be incorrect and has been updated to a 0 degree mean.

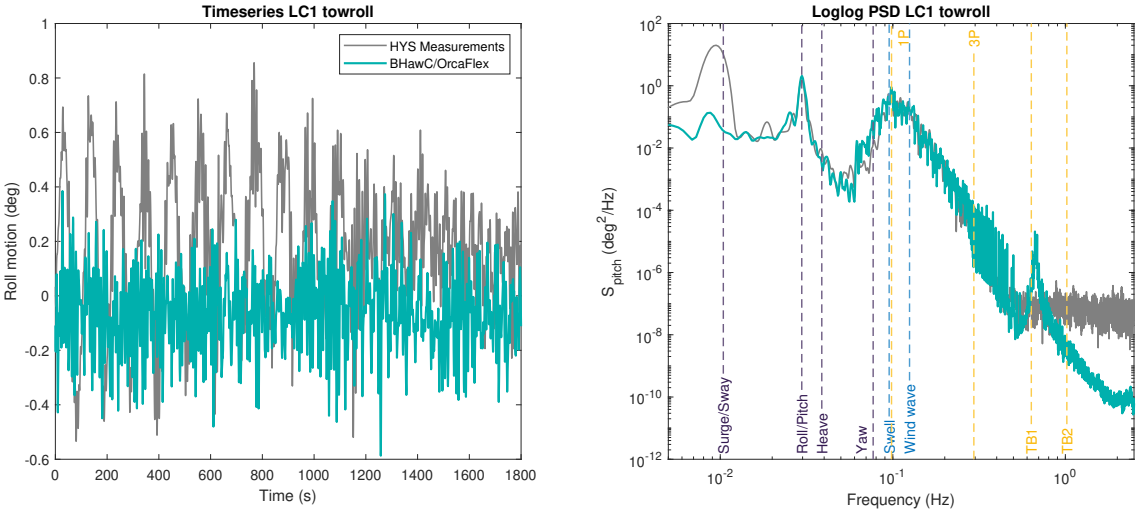

Figure 5.7: Comparison of tower roll response of load case 1 predicted by BH/OF and full-scale measurements.

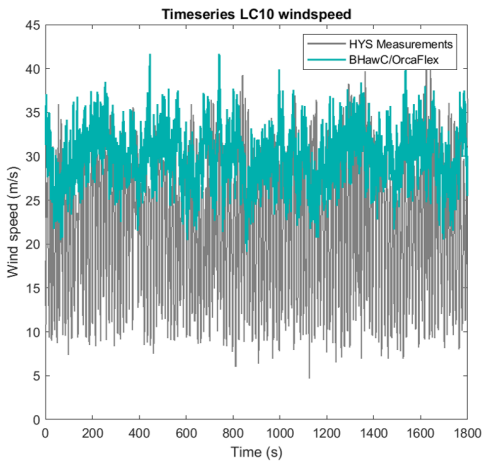

(a) Wind speed timeseries comparison in BHawC/OrcaFlex and from measurements of load case 10.

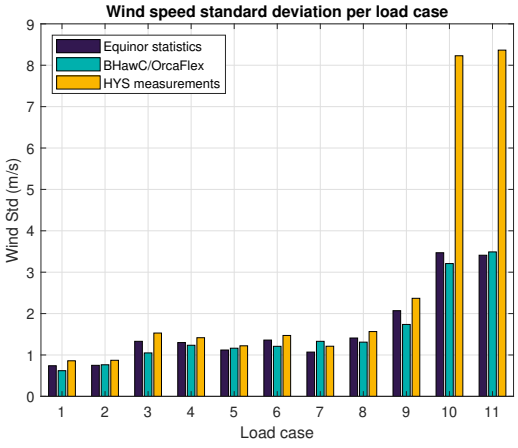

(b) Wind speed standard deviation per load case according to direct measurements, processed Equinor statistics and BHawC/OrcaFlex simulations.

Figure 5.8: Wind conditions per load case according to different sources.

5.5.2 Free-decay tests

Free-decay tests in surge, heave and yaw are performed. Values of identified natural frequencies compared to those provided by Equinor are given in table 5.3. The heave and roll/pitch natural frequency match well with the Equinor provided values. The surge and yaw natural frequency response are significantly underpredicted. Given that the roll, pitch and heave response show correct values, no errors in the mass or inertia are expected. The tuned mooring system is known to provide too low static tensions in all bridle lines (see section 5.1.1). The crow-foot delta lines provide yaw-stiffness of the mooring system, as seen in section 3.2. The surge/sway response is influenced by combined main line and bridle line characteristics, whereas the yaw response is mainly due to the bridle lines, hence the higher error. An additional response peak was observed in the bridle line tensions at 0.0175 Hz. This could be a response from double the surge motion.

DOF	Equinor prediction (Hz)	BH/OF prediction (Hz)	Relative error
Surge	96.2	113	-15 %
Sway	96.2	113	-15 %
Heave	25.7	25.5	+1 %
Roll	33.7	33.7	+0 %
Pitch	33.7	33.7	+0 %
Yaw	13.0	20.5	-37 %

Table 5.3: Comparison of rigid body motions natural periods of the Hywind Scotland system predicted by BH/OF and values provided by Equinor.

5.5.3 Load Case 3: rated wind speed

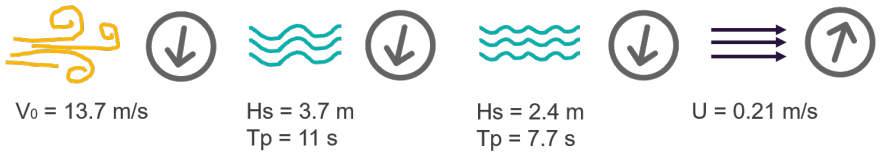

Figure 5.9: A schematic overview of the wind, swell, wind-wave and current conditions of load case 3.

figure 5.9 shows the environmental conditions of load case 3. In this section, selected simulation results are provided and compared against measurements. Most phenomena observed in this section are similar to other load cases. Therefore, results are elaborated in more detail for this load case to minimize repetition.

A comparison of the motions of load case 3 is provided in figure 5.10a. In general, the motions are predicted well by BHawC/OrcaFlex. The variation in signal is correct for most of the motion predictions. What stands out is significant overprediction of the mean surge motion. As seen from figure 5.9, all environmental conditions are in the same direction of application or 180 degrees turned for the current motion, showing a horizontal displacement mainly in surge. The mean surge and mean sway are overpredicted, which is due to too little stiffness of the bridle line tensions. For similar reasons, the yaw variation is overpredicted.

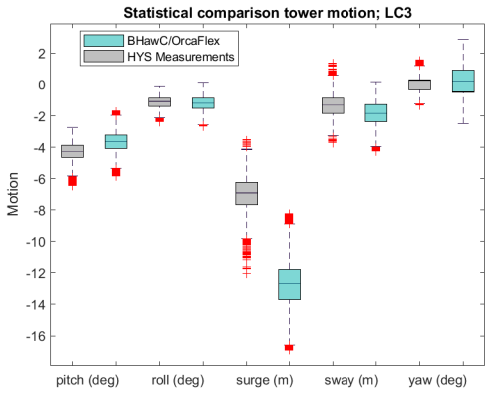

(a) Statistical comparison of tower roll response of load case 3 predicted by BH/OF and full-scale measurements.

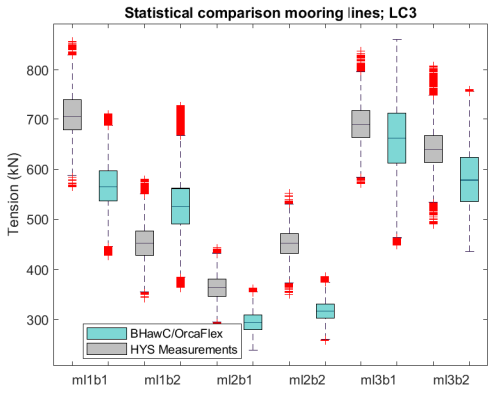

(b) Statistical comparison of bridle line response of load case 3 predicted by BH/OF and full-scale measurements.

Figure 5.10: Statistical comparison of motion and bridle line response of load case 3. The layout of the bridle lines is found in figure 5.6.

Next, the frequency domain response is compared. In general, BHawC/OrcaFlex predicts the motion response well in all DOFs. The wave-frequency region is captured correctly in all signals and most important peaks frequencies are correctly predicted with varying discrepancy in the energy levels.

Figure 5.11 shows the tower pitch response. At lower frequencies, the surge-frequency peak is shifted from the expected value in the measurements, which occurs at most load cases. One cause for shifts in the surge/sway natural frequency is variation in the bridle lines stiffness when the system moves from its original position. The bridle system behaves highly non-linear, so the further the line is stretched the more the stiffness increases. Note, again, the statistical uncertainty in the results. More on the mooring stiffness is found in section 5.6.

The roll and pitch tower bending response is overpredicted. This may be due to too little tower structural damping or too high modeled wave energy in this region, as seen in the OrcaFlex verification step (section 3.5). Structural tower damping is analysed in more detail in section 5.6.

The sway motion (see figure 5.14) is captured well by BH/OF. The two simulated wind/wave and swell spectrum peaks in the the wave-frequency response are more distinct than the measurements. BH/OF applies two long-crested wave trains with a fixed direction. In reality, wave spreading results in less distinct wave component peaks, which results in larger excitation perpendicular to the wave direction. Also, it should be noted that the wave buoy measurements on which the simulated wave conditions are based is located at 2.5 km distance from the turbine. The wave conditions at the turbine location may differ in direction or period.

What stands out is a significant $\sim O(10^1)$ overprediction of the roll/pitch-frequency response energy peak. This peak is overpredicted in most of the pitch, roll, surge and sway results of all load cases. This could be due to too much energy in the wind spectrum in BH/OF around this frequency, resulting in overprediction of wind-induced response. As other regions of the response match well and the low-frequent response is underpredicted, it is unlikely that large errors in the wind occur. Unfortunately, no direct comparison between wind signals can be made due to errors in the measurements. Another cause of this peak could be a source of system damping that has not been modeled correctly. Aerodynamic damping directly affects the pitch response. This damping results indirectly from aero-servo-elastic load calculations in the BHawC code and can not be influenced. Damping has been validated for the onshore prototype [75], but increased motions for floating platforms compared to bottom-fixed may introduce errors in this calculation. Hydrodynamic damping could also reduce the roll/pitch frequency response. It is known from the OC3-project that additional linear hydrodynamic damping was needed to match the simulated roll/pitch decay responses with those of the full-scale Hywind demo system. In the current model set-up, no additional linear hydrodynamic damping has been added to the system. A detailed analysis of hydrodynamic damping effects is found in section 5.6.

The yaw response generally matches well to the measurements. The yaw natural frequency peak is underpredicted due to a shift in the frequency found from the decay response. The 1P response peak is clearly overpredicted, which may be due to the modelling of rotor mass imbalance. A default rotor mass imbalance in BHawC is based on design values, which are generally conservative. This may become visible in the yaw motion due to a periodic variation in the yaw gyroscopic moment caused by the imbalance. What stands out is the clear match at higher frequencies, where also the second tower bending mode is predicted correctly. Predictions in the yaw response are often difficult to make, as was seen in the OrcaFlex verification step (section 3.5).

The bridle line tensions of LC3 are investigated. A comparison of bridle response statistics can be found in figure 5.10. All mean values of the bridle line tensions are underpredicted, except for ml1b2. The variation in bridle line response is either over- or underpredicted in most cases. Globally, the direction of environmental loading and resulting horizontal motion is reflected in the bridle lines. An overview of the bridle lay-out can be found in figure 5.6.

General trends in bridle response are covered by BH/OF. An example is given for ml1b1 in figure 5.15. Overpredictions in the roll/pitch response peak in system motion response are translated to the bridle system. The surge response seems to be predicted at the right frequency and contains the correct amount of energy. However, the surge/sway frequency differs between ml1b1 and ml1b2 results, which suggests this shift mainly due to statistical variation. For the ml2b2 signal, the general behaviour is predicted incorrectly by BH/OF (see figure 5.16). The energy level is in underpredicted at nearly all frequencies, with a significant overprediction at roll/pitch frequency. Some important peaks are still at the expected frequency, such as the 1P and 3P response and tower bending and both wave peaks. It is unclear why this specific mooring line shows such different behaviour from the others.

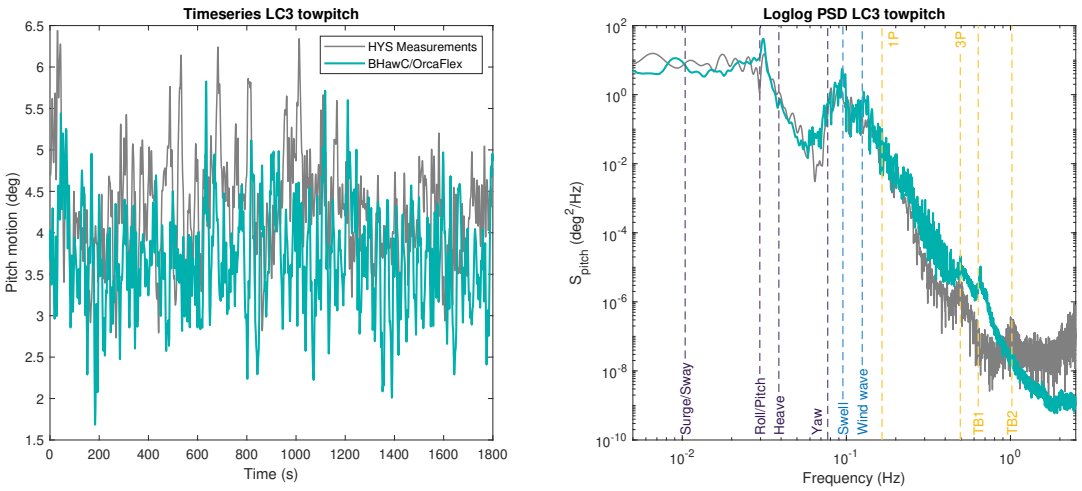

Figure 5.11: Comparison of tower pitch response of load case 3 predicted by BH/OF and full-scale measurements.

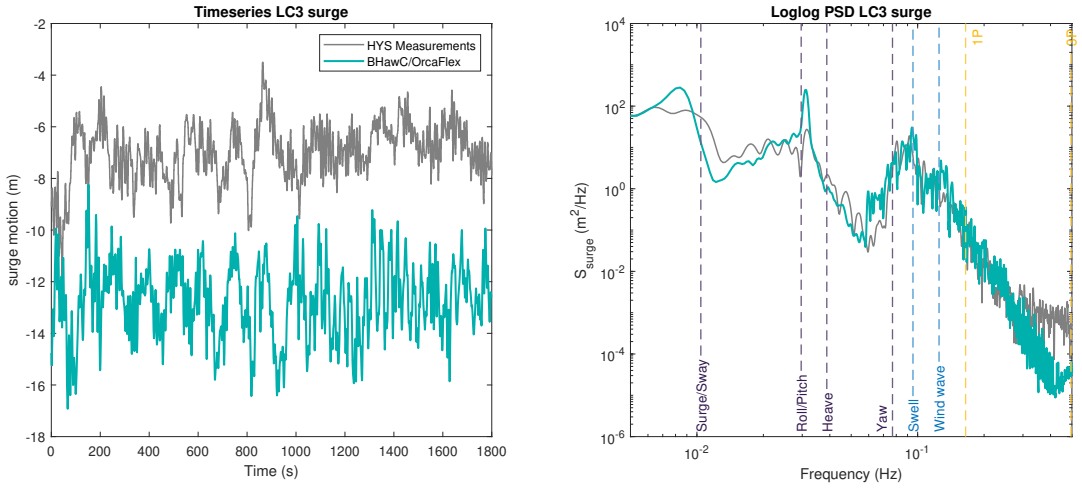

Figure 5.12: Comparison of platform surge response of load case 3 predicted by BH/OF and full-scale measurements.

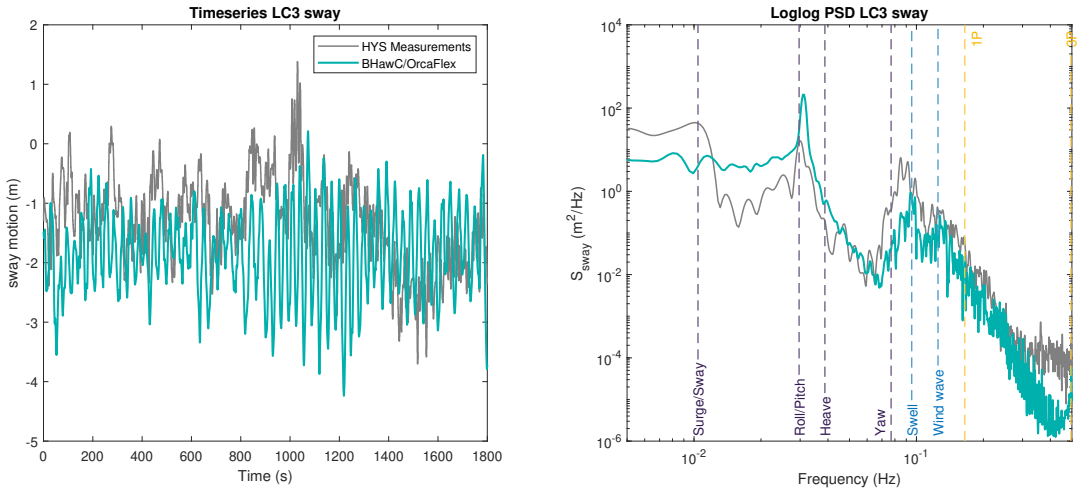

Figure 5.13: Comparison of platform sway response of load case 3 predicted by BH/OF and full-scale measurements.

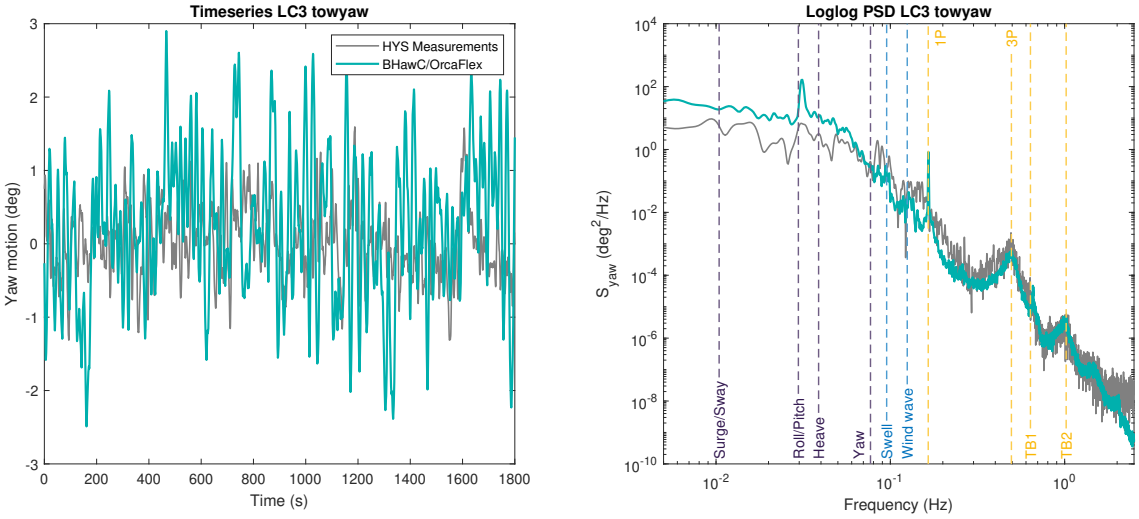

Figure 5.14: Comparison of platform yaw response of load case 3 predicted by BH/OF and full-scale measurements.

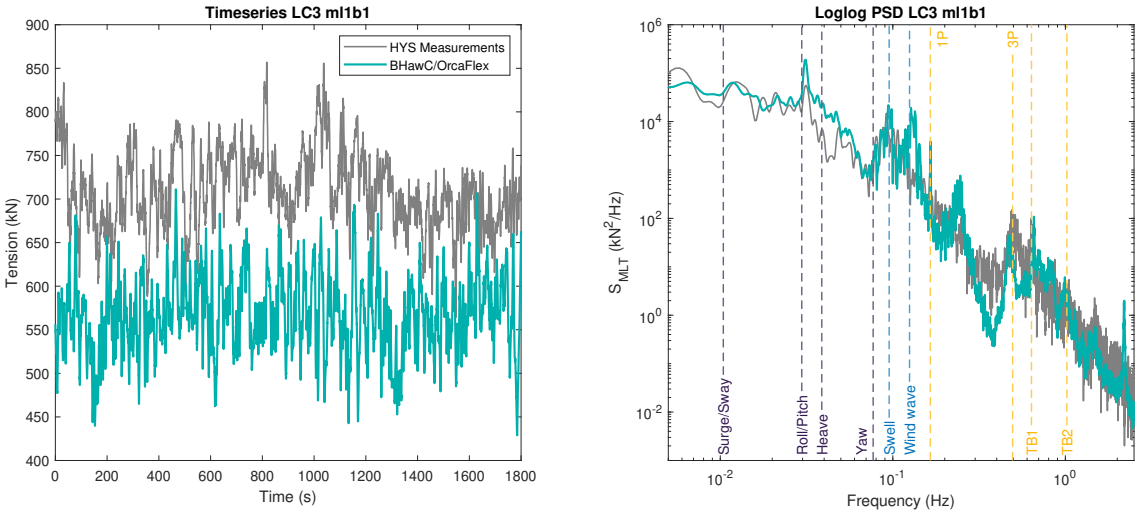

Figure 5.15: Comparison of main line 1, bridle line 1 response of load case 3 predicted by BH/OF and full-scale measurements.

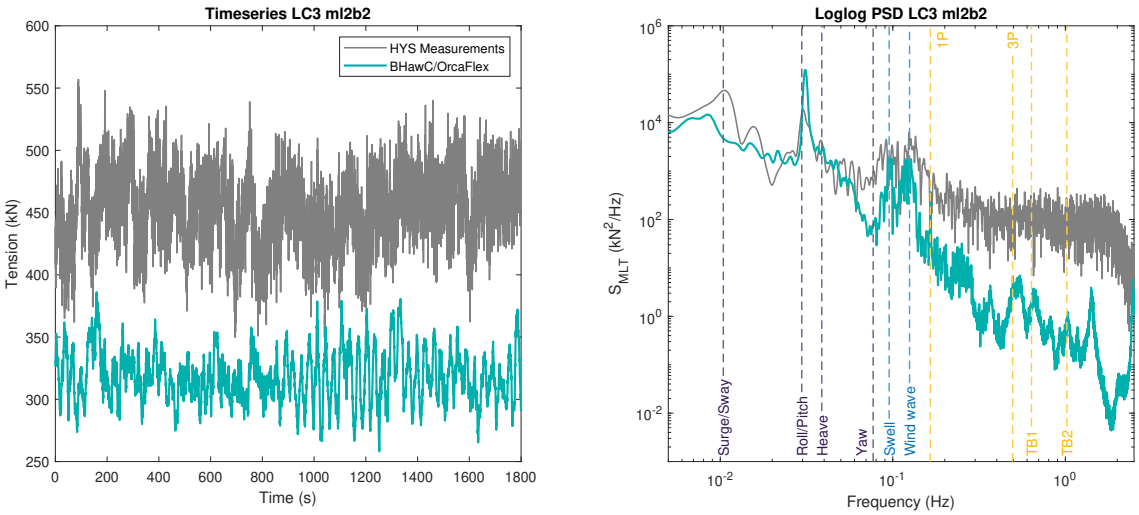

Figure 5.16: Comparison of main line 2, bridle line 2 response of load case 3 predicted by BH/OF and full-scale measurements.

5.5.4 Load Case 2: below-rated wind speed

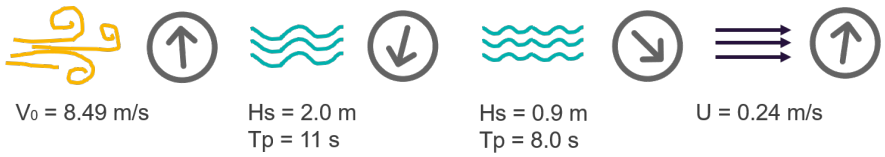

Figure 5.17: A schematic overview of the wind, swell, wind-wave and current conditions of load case 2.

The environmental conditions of LC 2 can be found in figure 5.17. Statistics are compared in figure 5.18a. The sway motion in load case 2 is far off from the measurements. BH/OF predicts a mean displacement of 6 meters, whereas the full-scale system oscillates around 0 mean. After re-running the simulations with turbulent wind only, the resulting sway motion is still similar. The wind in this case is coming almost directly from the South, so only a positive surge motion is expected here. After a double-check it is found that environmental conditions in simulations are correctly assigned. An exact explanation remains unknown. It could be that the rotor causes an undesired coupled moment that gives a mean displacement of the sway direction. Combined with the low mooring stiffness, this may result in significant overprediction. The mean surge motion is underpredicted by OrcaFlex, which may be due to the overpredicted sway motion that changes the bridle line tensions, giving a net different surge displacement.

In all signals, the surge/sway frequency peak is overpredicted. This may be due to lack of modeled damping in the mooring system. In reality, mooring chains links experience friction forces from neighbouring links due to bending or rotation of the mooring lines. In OrcaFlex this was not included due to limited of data on the as-built system. Also, hydrodynamic viscous damping from the mooring lines and floater could be under-predicted. More on this can be found in section 5.6. At even lower frequencies, an additional peak is observed which is slightly broader. This may be due to difference-frequency effects from different wave trains. Morison equation is modeled up to the instantaneous surface with wave stretching, which may capture some difference-frequency effects.

The surge and sway motion show a clear peak around 0.06 Hz, between the heave and yaw natural frequencies, which is not captured by BH/OF. It could be that this response is due to an additional low-frequent swell component which was not documented by Equinor. Also, it could be that some coupled response in rigid body motions gives resonance at a frequency beyond these original frequencies. This response would then not be captured by BH/OF at all, which would be unlikely given the detailed finite-element representation of the system containing advanced multi-body dynamics which for BHawC and OrcaFlex have been validated extensively separately.

A comparison of the bridle response statistics is found in figure 5.18b. Ml1b1 and ml3b2 overpredict mean tensions and all other signals underpredict means. For these signals it is known from Equinor [32] that tensions may be lower than the idealized system due to differences from the as-built mooring system. More on this is found in section 5.6. Similar to load case 3, some bridle line response matches well, whilst some others do not.

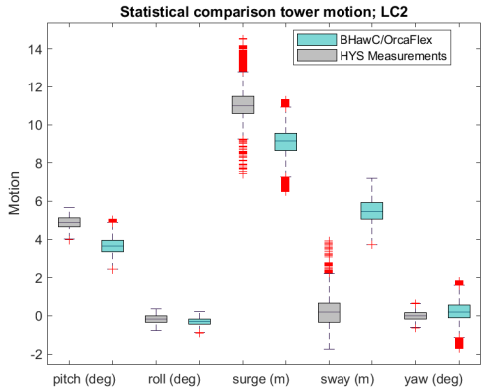

(a) Statistical comparison of tower roll response of load case 2 predicted by BH/OF and full-scale measurements.

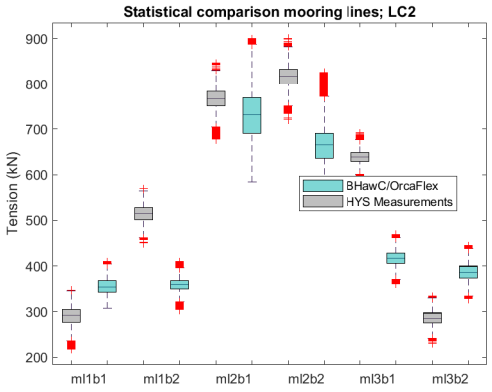

(b) Statistical comparison of bridle line response of load case 2 predicted by BH/OF and full-scale measurements.

Figure 5.18: Statistical comparison of motion and bridle line response of load case 2. The layout of the bridle lines is found in figure 5.6.

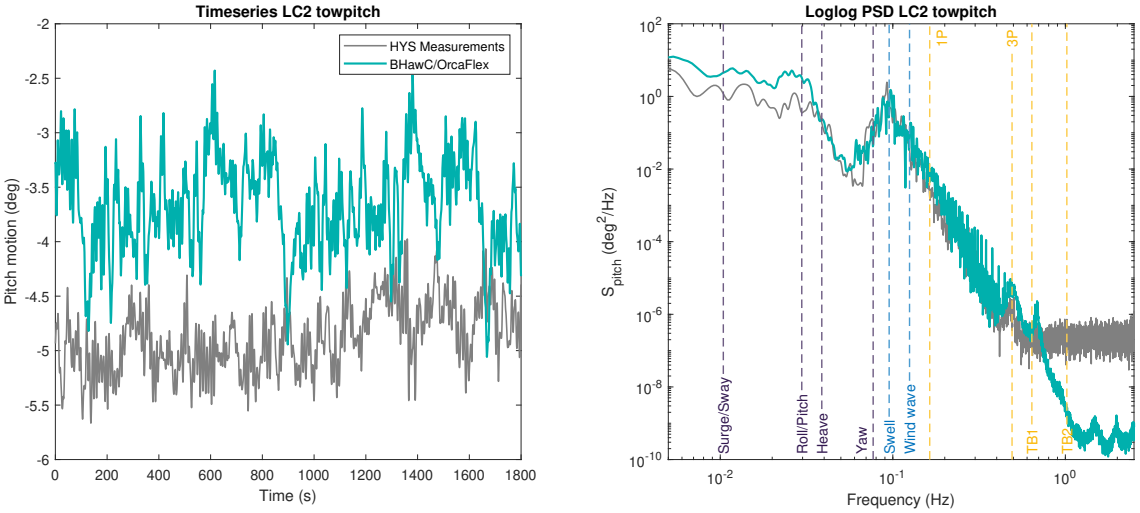

Figure 5.19: Comparison of tower pitch response of load case 2 predicted by BH/OF and full-scale measurements.

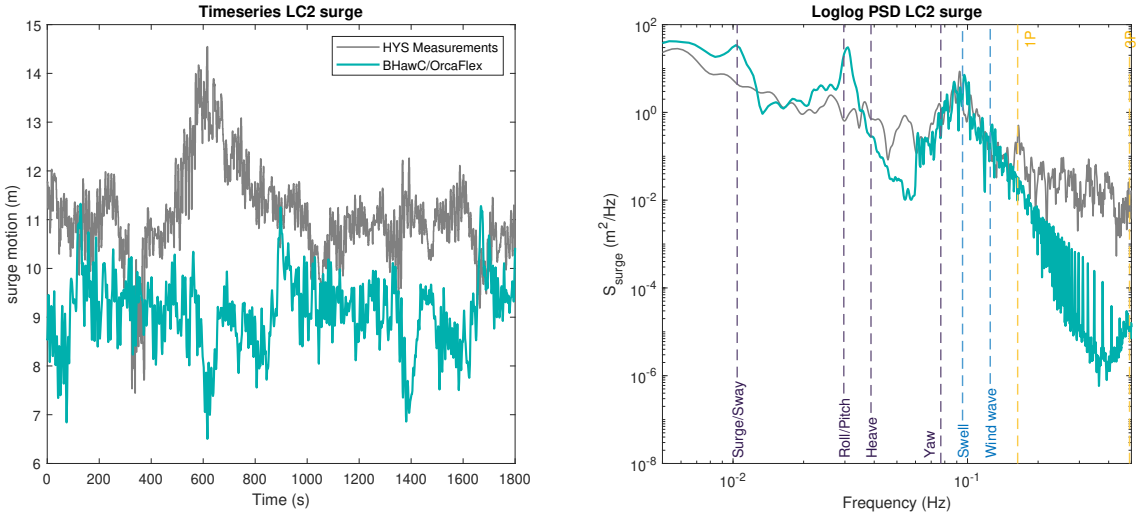

Figure 5.20: Comparison of platform surge response of load case 2 predicted by BH/OF and full-scale measurements.

5.5.5 Load cases 10 and 11: above cut-out wind speed

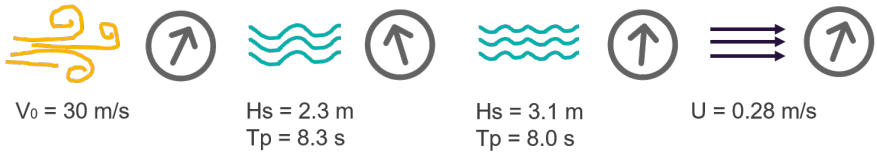

Figure 5.21: A schematic overview of the wind, swell, wind-wave and current conditions of load cases 10 and 11.

The environmental conditions of load cases 10 and 11 are depicted in figure 5.21. The analysis of both load cases is combined as they are subjected to similar environmental conditions. In fact, these measurements were recorded during the same extreme wind speed event [32]. In general, predictions are improved from the operational cases. Interaction with the control system generally adds a lot of complexity to the system, which is excluded for idling cases. This gives a simplification of the turbine behaviour which improves the performance of BH/OF.

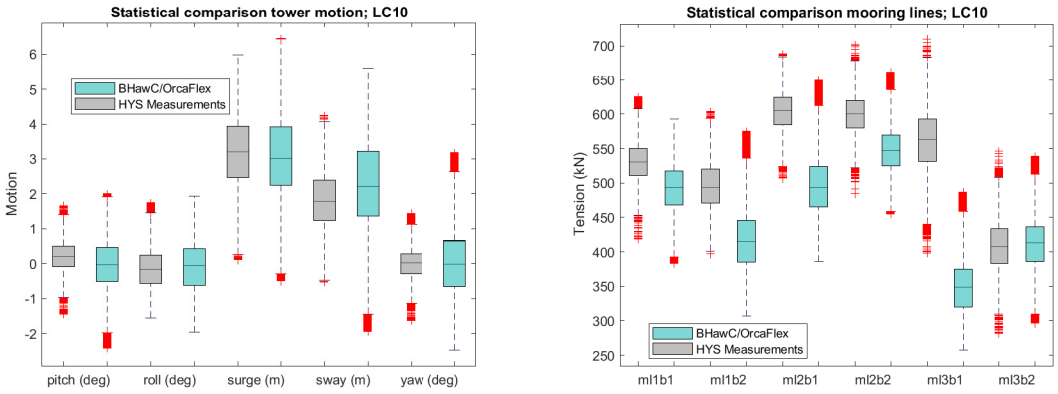

(a) Statistical comparison of system dynamics response of load case 10 predicted by BH/OF and full-scale measurements.

(b) Statistical comparison of bridle line response of load case 10 predicted by BH/OF and full-scale measurements.

Figure 5.22: Statistical comparison of system dynamics and bridle tension response of load case 10. For load case 11, equivalent values are observed.

In figure 5.22 the surge, sway, roll and pitch motion of the system are depicted. It can be observed that BH/OF means of all signals match well to the measurements. Both pitch and roll now show a zero-mean value as no overturning thrust moment is present. Most variations, however, are slightly higher in BH/OF than in measurements. Motions of an idling turbine load case will show a more clear effect of the hydrodynamic response. As seen in previous load cases, the BH/OF model probably lacks hydrodynamic damping at the surge/sway and pitch/roll frequencies.

Surge, pitch and yaw motion frequency domain responses match well to measurements. A significant overprediction of the low-frequency response is observed, though the distribution of energy is correct. This may be due to lack of hydrodynamic damping, with the hydrodynamic excitation being more dominant in idling cases. Also, it could be that the wind field has too high modeled energy. The Equinor wind speed and turbulence statistics used to generate the simulated wind field are corrected for the turbine motion, but may still be erroneous. This shows specifically in the yaw motion, where large lack of bridle stiffness amplified with wind-induced yaw moment causes severe overpredictions. From the OrcaFlex verification step it is known that yaw hydrodynamic damping is required for the OC3-Hywind model. More on this is found in section 5.6.

Statistics of the mooring system response is provided in figure 5.22b. Similar to load cases 2 and 3, significant differences between the bridle line responses is observed. The overall impression of the error in mean values and signal distributions, however, is much improved compared to the operational case. Most mean

tensions are within the range of offset in static bridle tensions (see figure 5.1) and most distributions match well to the measurements. The mean tension of ml3b1 is far off similar to load case 2. This could be due to the similarity of the wind direction in both load cases. The idling system has lower horizontal motion variation, which may improve the comparison due to limited mooring stiffness variations.

Bridle line ml1b1 frequency domain response is shown in figure 5.25. Both signals match at the most important peaks. The wave-frequency response is predicted correctly for most lines. The yaw frequency is shifted, but also clearly overpredicted. Contributions from aerodynamic damping are limited for both the modeled and the full-scale system. From the OC3-Hywind definition, additional yaw hydrodynamic damping was required. No viscous drag or radiation damping contribution is modeled in BHawC/OrcaFlex, which may give rise to requirement of additional linear hydrodynamic damping.

A clear peak is observed at approximately 0.25 Hz. The yaw frequency in measurements is at approximately 0.07-0.09 Hz, which could mean this is a double of the yaw response. However, BH/OF correctly predicts this peak, while it underpredicts the yaw natural frequency. One option could be the occurrence of mooring line vibrations. From a mooring system modal analysis, this may be from the 2nd in-line bending frequency. Peaks between 0.4 and 0.5 are expected to be due to the rotor flapwise yaw and tilt natural frequencies, which may be more distinct for an idling turbine than for operational cases.

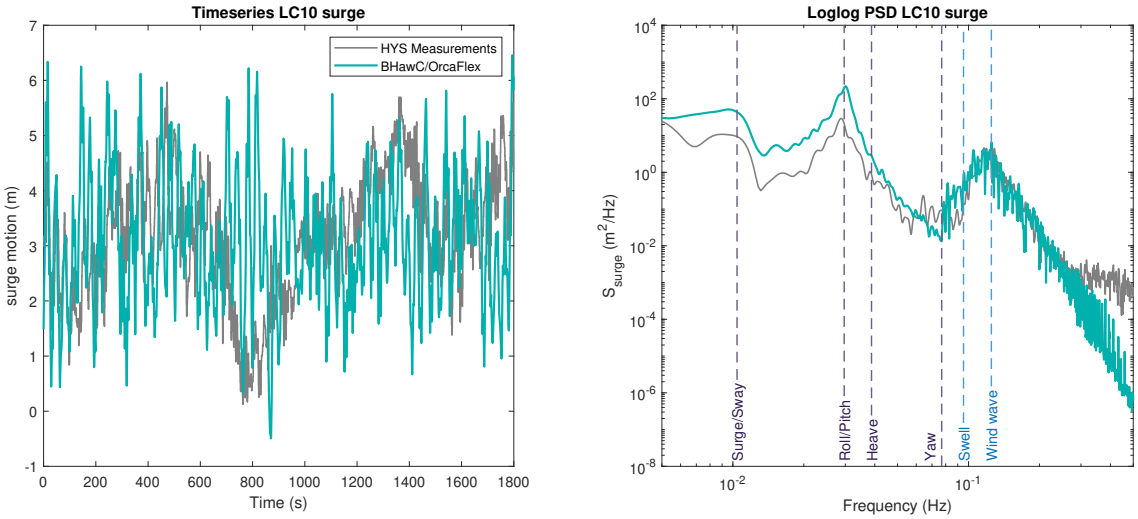

Figure 5.23: Comparison of platform surge response of load case 10 predicted by BH/OF and full-scale measurements.

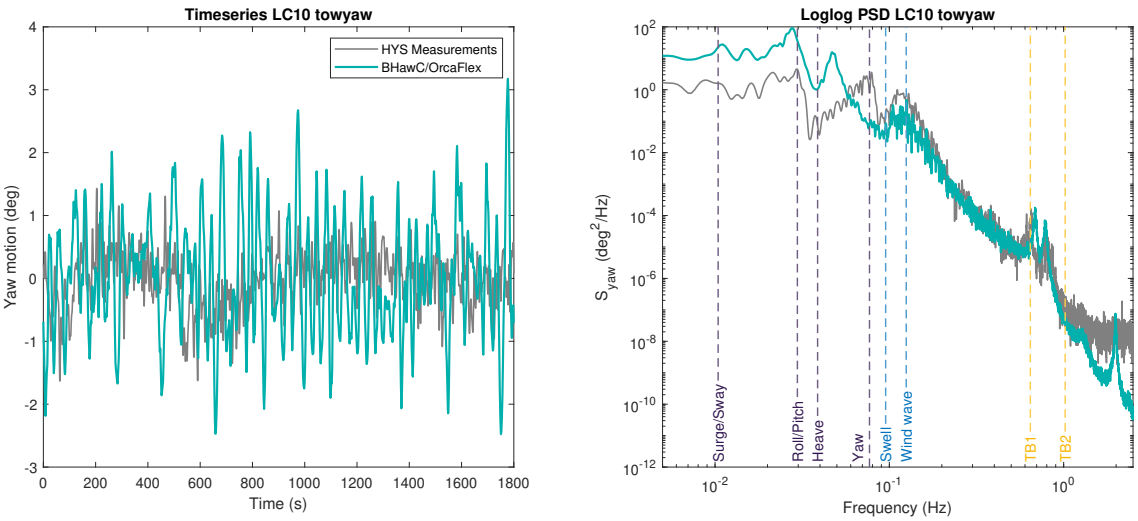

Figure 5.24: Comparison of platform yaw response of load case 10 predicted by BH/OF and full-scale measurements.

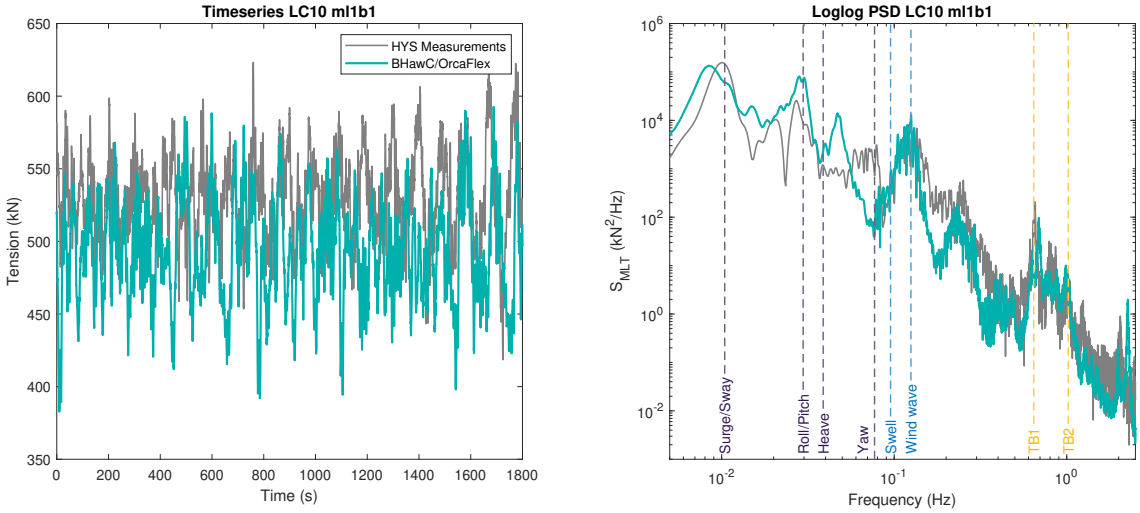

Figure 5.25: Comparison of main line 1, bridle line 1 response of load case 10 predicted by BH/OF and full-scale measurements.

5.6 Detailed analysis of selected errors

In this section, error sources that were described and explained in the previous sections are analysed in more detail. This helps to increase confidence in the validation results and errors explained, which could be used in a future model revision to mitigate these errors. For most analyses, a sensitivity study is performed, meaning variation of a single parameter to separately investigate its impact on the results. For each sensitivity study, all simulations of load case 3 are redone by varying only a single parameter, after which the 'original results', i.e. those provided in the previous results section are plotted with results with the parameter variation. Only results of the signal in which the error is observed are provided and a detailed depiction on the specific frequency region is added. As described in section 2.5, no standardized approach exist for the quantitative comparison of performance or mitigation. In this section, relative error reduction in maximum energy level prediction of frequency domain response peaks of interest is used to indicate the mitigation performance of parameter variations.

5.6.1 Mooring system tuning effects

A mooring force-displacement diagram is made comparing the surge, sway and displacement to the total horizontal force and the yaw rotation to the total yaw moment the floater, before and after tuning (figure 5.26a). In addition, the effective tension in each bridle line is compared to displacement for these three DOFs (figure 5.26b) of the tuned mooring system only.

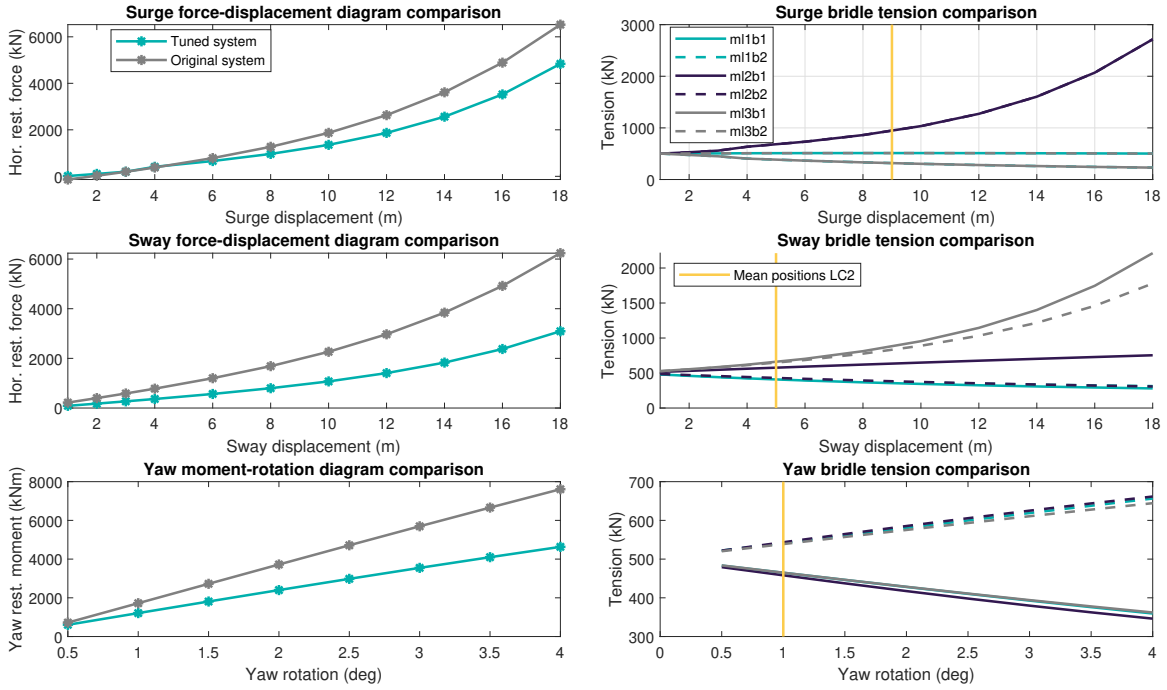

(a) Force-displacement diagram for surge and sway and moment-rotation diagram for yaw DOF of the tuned and un-tuned mooring system.

(b) Bridle line tension for given surge, sway and yaw displacement of the tuned mooring system.

Figure 5.26: Comparison of restoring properties of the tuned and un-tuned mooring system.

Figure 5.26a shows the expected non-linear restoring properties from theory, with varying stiffness mainly in the surge and sway DOFs. One can observe a decrease in total mooring stiffness in all three DOFs for the tuned and original system. Figure 5.26b shows that for surge motion, symmetrical loads are exerted by 'pairs' ml2b1 & ml2b2, ml1b2 & ml3b1 and ml1b1 & ml3b2. For yaw motion, lines 'mlxb2' show increasing tension while lines 'mlxb1' show decreasing tension. For sway motion, less symmetry in the bridle line tensions is observed. Behaviour in all three DOFs is inherent to the bridle system geometry (see figure 5.6). These 'pairs' providing similar tension in a given DOF are clearly reflected in the bridle tension statistics.

A comparison is made to the mean surge, sway and yaw motion and resulting bridle line tensions of LC2 shown in yellow. The dynamic bridle line tension results (5.18a and 5.18b) show a clear relationship with the expected tensions from the diagram. For example, the bridles of main line 2 show high tensions due to the large mean surge displacement, where bridle 2 shows slightly lower tensions due to the significant sway

displacement. It should be noted, here, that the tension-displacement diagrams were made for a pure displacement in each DOF. In dynamic simulations, coupled rotations from e.g. surge and sway displacements will slightly reduce these tensions.

It is observed that the of natural frequency response of the untuned system compared to the tuned system is worsened (tables 4.4 and 5.3), which corresponds to a lower overall restoring stiffness in the tuned system. This means that tuning for increased mooring stiffness from the original system will likely solve these errors.

5.6.2 Statistical uncertainty

Irregular surface elevation or turbulent wind fields provide stochastic input to a model, i.e. the input is randomly determined based on a probability distribution. The dynamic response is therefore varying for each simulation. This influences the comparison between measurements and simulation results. The measurement timeslot could be considered a single stochastic realisation, which may fall within the range of statistical response predicted for different environmental realisations. Figure 5.27 shows the results of the tower pitch and ml3b2 response from the same model to the 12 realisations of environmental input with similar statistical properties. Increasing variation is observed below ~0.07Hz. This is due to the fact that for a 1800s time-domain realisation, only few cycles of these frequencies are in the results, which makes it prone to statistical variation. Increasing variation is again observed above ~0.3Hz. Here, the response is of high frequency as well. Given a limited sampling frequency from simulations, less accuracy is available on the response here.

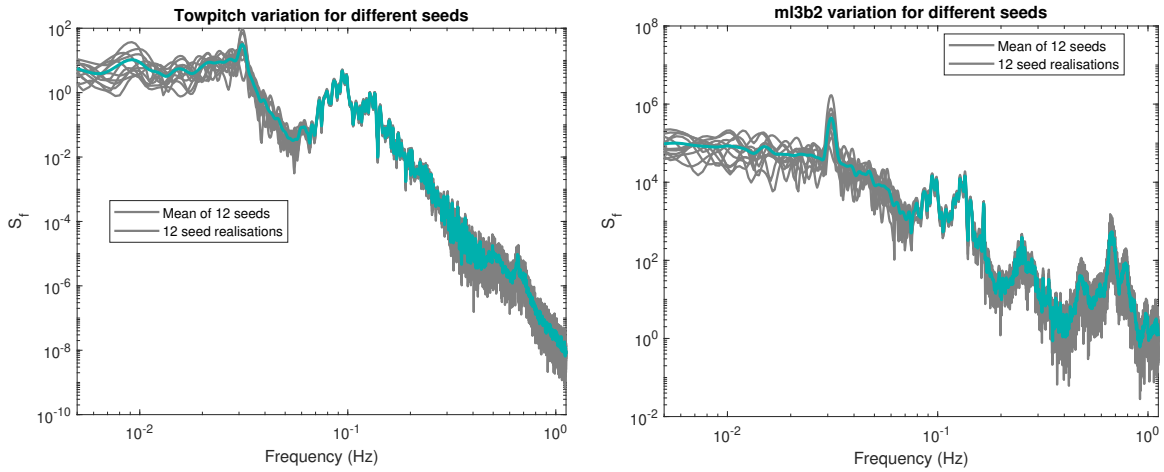

(a) Statistical variation of tower pitch motion response.

(b) Statistical variation of ml3b2 response.

Figure 5.27: Statistical variation of simulations with stochastic environmental input for different seed realisations.

5.6.3 Mooring line vibrations

All load cases include multi-directional steady current. From theory, it is known this that a line placed in a steady in-line flow may be subject to transverse motions from vortex shedding (see section 2.2.3). When the vortex shedding frequency gets near to the line natural frequency, VIV resonance may occur, which would be visible through a response peak in the bridle line tensions from the measurements and simulations. Therefore, it may be of interest to know the mooring system natural frequencies. In OrcaFlex, a modal analysis is performed to determine occurring mooring line modes and their frequency (see table 5.4). A visual impression of these modes is given by figure 5.28. The coupled lines, main lines and bridle lines each have their own frequencies. Most mooring line natural frequencies are in the wave-frequency and high-frequency region. The first in-line bending mode, which may occur in at lower frequencies, is not captured by OrcaFlex.

From the BHawC/OrcaFlex simulation results, a clear peak is observed between 1.9 and 2.2 Hz in most of the MLT responses. There may be a contribution here from the 2nd in-line bending mode of the combined lines. It should be noted that from changing positions of the floater, the bridle tensions and its resulting stiffness vary from its equilibrium position at which the modal analysis was made. Consequently, these mooring eigenfrequencies are shifting as well. OrcaFlex allows a VIV analysis to capture VIV effects occurring in time-domain simulations. However, these depend on external software and are therefore considered beyond the scope of this report.

Natural frequencies (Hz)	Combined main + bridle lines	main lines	bridle lines
1st Transverse bending	$1.3{\cdot}10^{-1}$	$1.4{\cdot}10^{-1}$	$3.4{\cdot}10^{-1}$
2nd In-line bending	$1.9{\cdot}10^{-1}$	$2.7{\cdot}10^{-1}$	$6.8{\cdot}10^{-1}$
2nd Transverse bending	$2.2{\cdot}10^{-1}$	$2.8{\cdot}10^{-1}$	$6.9{\cdot}10^{-1}$
3rd In-line bending	$2.8{\cdot}10^{-1}$	$4.0{\cdot}10^{-1}$	$9.5{\cdot}10^{-1}$

Table 5.4: An overview of the occurring eigenmodes of the mooring system and its natural frequency per component.

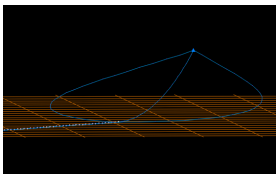

(a) In-line vibration.

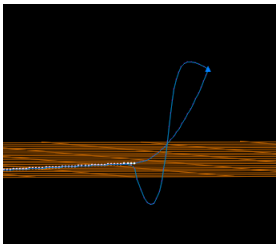

(b) Transverse vibration.

Figure 5.28: A visual impression of mooring line eigenmodes.

5.6.4 Tower-bending response

From a comparison of tower pitch and roll motion an overprediction of the first tower-bending mode is observed across load cases. One explanation for this is too low modeled tower structural damping. The original Rayleigh damping ratio is estimated for a linearised floater, 0 deg blade pitch with rotor standstill and 12m/s wind speed facing the turbine head-on. This shows a damping of ~3% LogDec on the first tower-bending mode. For idling cases the blade pitch is adapted, which reduced the total damping to ~2% LogDec at a nearly similar tower-bending frequency. These are expected values for modeling tower structural damping from SGRE common practice. The effect of variation of tower damping is demonstrated by varying Rayleigh stiffness-proportional coefficients from between 50% and 500% its original value. The results are found in figure 5.29a. Five times the expected tower damping hardly influences the response gives an 80% error reduction of the response. However, from comparison of the resulting tower-bending response limited effect is observed. Moreover, these structural damping are not physically expected from a wind turbine tower. It is therefore concluded that another explanation is needed to explain this error. From the OC3 project, it is known that OrcaFlex equal energy distribution wave discretization method causes overprediction of the high-frequency response, as wave components occur at too high frequencies. The effect of different high-cut frequencies are demonstrated in figure 5.29b. A relative error reduction of 163% is achieved. This shows increased effect from the tower damping variation.

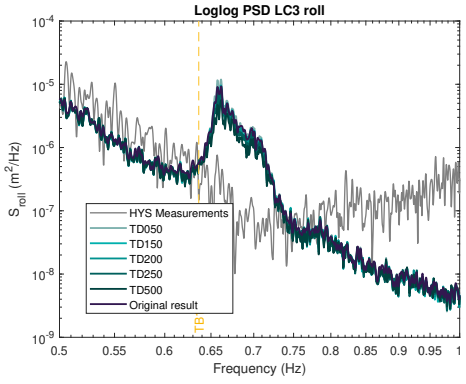

(a) A demonstration of the improvement of tower-bending frequency response predictions for an increased structural tower damping percentage.

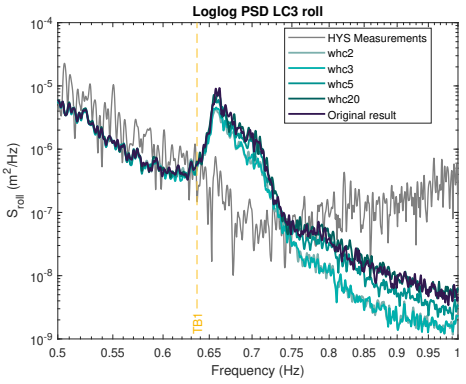

(b) A demonstration of the improvement of tower-bending frequency response predictions for a reduced high-cut frequency of the wave spectrum.

Figure 5.29: A demonstration of the improvement of tower-bending frequency response predictions for an increased structural tower damping percentage from different sources.

5.6.5 Hydrodynamic damping

To improve the response energy level at surge/sway and roll/pitch natural frequencies, the effect of hydrodynamic damping is demonstrated. Sources of hydrodynamic damping and their effects are discussed in section 2.2.4. A preliminary hydrodynamic analysis (section D) showed that for a fixed floater low viscous effects are expected, but increased floater velocity may increase the KC number thus increasing the importance of viscous damping effects. Both linear and quadratic damping effects are separately demonstrated to isolate their importance. For demonstration of linear damping 1) the OC3 required additional linear damping is added to the floater and varied between 10% and 200% of its original value and 2) separate pitch/roll damping based on an expected percentage of the critical damping is added to the floater and varied between 10% and 500%. For demonstration of quadratic damping 1) the floater drag coefficient is varied between 50% and 200% its original value and 2) the mooring drag coefficient is varied between 50% and 200% its original value.

Linear hydrodynamic damping

As explained in section 3.4.2, additional linear hydrodynamic damping is necessary in matching decay tests from aero-hydro-servo-elastic codes to the response of the Hywind Demo system. The required additional linear damping could be different for the Hywind Scotland system as the floater has a different geometry. In the original model set-up, no clear overprediction is observed in yaw and heave degrees of freedom. The influence of linear hydrodynamic damping is investigated by adding the linear damping from the Hywind Demo system in surge/sway and roll/pitch degrees of freedom. Values are varied between 20% and 200% of the OC3 damping. From set-up of the OC3-Hywind system (section 3.4.2) damping in one of these DOFs does not affect the response in the other DOFs, hence they are all varied simultaneously.

Figure 5.30a shows the demonstrates the variation of surge, sway, heave and yaw linear hydrodynamic damping. Differences observed from the original results are only in the low-frequency region. For 150% the OC3 damping an error reduction of 390% in surge, 247% in roll/pitch and 56% in yaw are observed. Next to the surge/sway frequency, the roll/pitch frequency is clearly damped, even though no damping is added to this specific DOF.

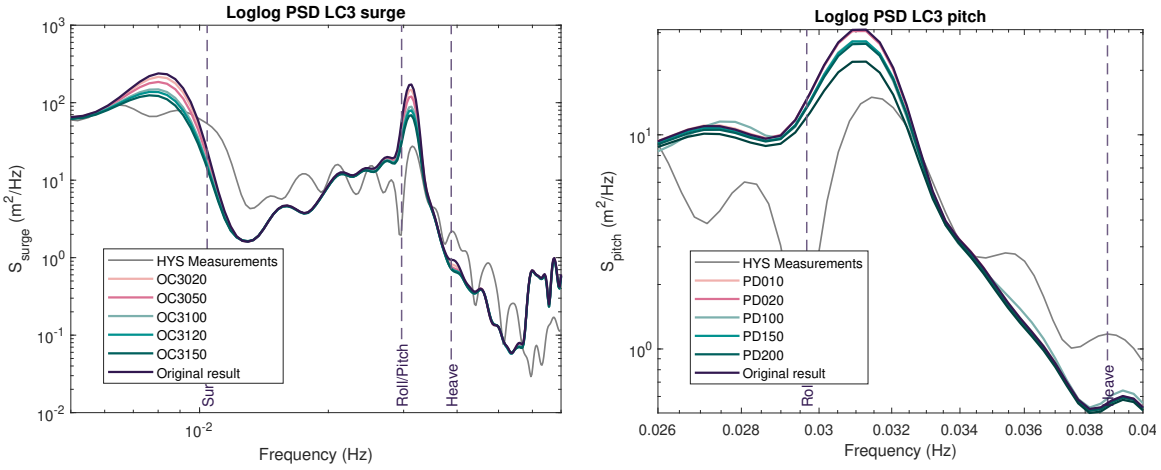

(a) A demonstration of the improvement of surge/sway and roll/pitch frequency response predictions for an increased linear hydrodynamic damping percentage from the OC3-Hywind definition.

(b) A demonstration of the improvement of roll/pitch frequency response predictions for increased estimated critical damping percentage of linear hydrodynamic pitch/roll damping.

Figure 5.30: A demonstration of the effect of varying linear hydrodynamic damping.

In the OC3-Hywind definition, no linear hydrodynamic damping in the roll/pitch DOF is prescribed. To get an impression of the effect on the overprediction of the roll/pitch frequency, a separate analysis is made. Roll/pitch linear hydrodynamic damping is added and varied between 0.1% and 50% of the critical damping. Here, a simplified estimate of the damping coefficient needed for to determine the level of critical damping is obtained from basic 1-DOF vibration mechanics as:

$$\xi_i = \frac{C_{ii}}{2I_{ii}\omega_{n,i}} \qquad i = 4,5 \tag{5.1}$$

Where I is the inertia of the total system obtained from [32] and ω the natural frequency obtained from decay tests and the set up model. Damping is defined as 'unit damping' in OrcaFlex at the centre of rotation of the total system, similar to what is described in section 3.4.2. Figure 5.30b demonstrates the effect of varying percentages of linear hydrodynamic roll/pitch damping on the response. A 127.9% error reduction is measured, but hardly any absolute improvement is observed in the response. Even the overprediction of the pitch response at pitch-frequency is only slightly improved. It could be that the level of critical damping identified is insufficient to have any significant effect.

Quadratic viscous hydrodynamic damping

In the original model set-up from section 4.3, a constant drag coefficient is estimated based on theory. It is known that for Re-numbers O(>10^7), limited experimental data is available from literature on suitable drag coefficients. Increased surface roughness could increase the expected drag coefficient by up to 60% for a very rough cylinder [24]. Also, (mildly) increased KC number could increase the drag coefficient by 20% [51]. It should be noted that the drag coefficient is used directly by OrcaFlex to determine hydrodynamic loads. Therefore, variation of this coefficient may also affect prediction outside of the frequency response region at which damping is achieved.

From the sensitivity analysis, a significant error reduction of the surge/sway (280%) and roll/pitch (149%) energy overprediction is observed across motion response. No other frequencies seem affected. Figure 5.31a demonstrates the results of variation of the floater constant drag coefficient. The improvement is larger at the surge/sway frequency, as this most affected by viscous damping due to its low-frequent horizontal motions. In the bridle line response, the same trend is observed. However, some BLT's are overpredicted and some underpredicted in LC3. Therefore, no clear conclusion on the level of improvement can be made.

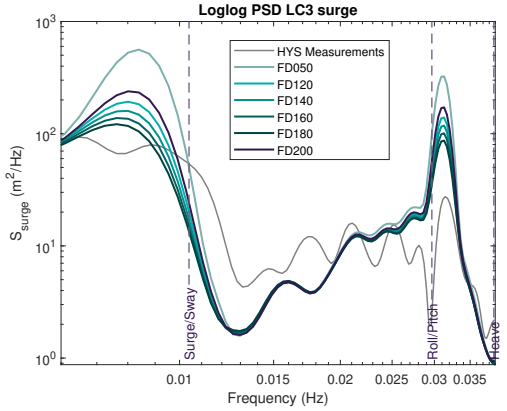

(a) A demonstration of the improvement of surge/sway and roll/pitch frequency response predictions for increased floater drag coefficients.

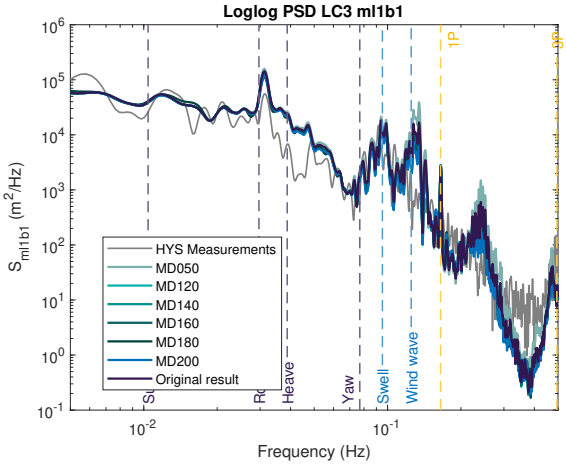

(b) A demonstration of the improvement of surge/sway and roll/pitch frequency response predictions for increased mooring drag coefficients.

Figure 5.31: A demonstration of the improvement of surge/sway and roll/pitch frequency response predictions for increased drag coefficients.

The mooring system fixed drag coefficients used in the original model set-up from section 4.3 are obtained from DNV [109]. They state that values 'are specified as lower bound, to avoid unconservative overestimate of damping effects' for design purposes. The effect of mooring viscous damping is investigated by varying the normal and longitudinal drag coefficients between 50% and 250% of their original value in both the main lines and bridle lines. The demonstration is found in figure 5.31b. Hardly any variation mitigation of the surge/sway and roll/pitch response overprediction is observed in bridle line tensions or in the motion response, in contrary to what is expected from literature. On the other hand, several high-frequency peaks vary with 2.4e3% due to varying mooring drag. Moreover, the wind-wave frequency response energies varies with 1.2e3% .

5.7 Conclusions: Hywind Scotland validation

A model is set up using an Equinor description and SGRE internal documentation on the as-built system. In operational cases, BHawC/OrcaFlex (BH/OF) performs well in the prediction of motions with regard to both their statistics and frequency domain response. For the bridle line tensions, however, most response statistics are off, though trends in the frequency domain response are captured correctly. In idling cases, BH/OF matches very well to the measurements, with seemingly increased performance compared to operational cases. This may be due to the reduced complexity of the total system as impact of the control system on the response is limited. As described in section 2.5, three types of errors can be defined. These errors present in the are separately highlighted here. In addition, errors mitigated during model set-up are provided. An attempt is made to quantify errors by using the relative error percentage (and percentage error reduction) as validation metrics.

Type 1 (code capacity) errors identified are:

- Across load cases, the roll/pitch response peak is clearly overpredicted. This could be due to discrepancies in the modeled aerodynamic damping. This damping is simulated in BHawC and is previously validated to perform well for offshore conditions. Errors could arise due to the severe motions of a FOWT compared to a bottom-fixed turbine. On top of that, hydrodynamic damping is likely underpredicted by BH/OF. Several sources of hydrodynamic damping are analysed in detail in section 5.6. Both added linear damping and viscous damping show significant error reduction of the response. From literature, however, no linear hydrodynamic damping term is expected, which gives the preference of mitigation by means of variation of the hydrodynamic drag coefficient.
- From the measurements, clear variation in the surge/sway response frequency can be observed across load cases. One cause of this is the non-linear bridle stiffness which changes with floater displacements. This is captured by BH/OF, despite values being off due to underprediction of the mean bridle line tensions.
- In load case 2, the mean sway motion is significantly overpredicted by BH/OF. After rerunning simulations with separate environmental conditions it is found that wind is the main cause of this displacement. No explanation could be found for this discrepancy.
- For surge and sway in load case 2, an additional peak is observed between the heave and yaw frequency at approximately 0.06 Hz, which is not captured in simulations. This may be caused by a coupled motion which is not correctly included by BH/OF, or due to an additional low-frequency swell component which was not reported by Equinor.
- Additional peaks in the surge and pitch motion at very low frequencies may be caused by difference-frequency effects, which are captured to a reduced degree by Morison model with integration up to the instantaneous surface elevation used here (compared to second order potential flow theory).

Type 2 and 3 (model set-up and physical model) errors are:

- Errors in the BH/OF control system set-up cause an unstable system in load cases 4-9. Therefore, only load cases 2, 3, 10 and 11 are considered here.
- Statistical uncertainty due to a limited time-domain realisation limits comparison of the results in the low-frequency region (see figure 5.27a). Both shifts in peak frequencies as well as energy levels are observed. At high frequencies, the statistical uncertainty increases again due to limited sampling frequencies. Here, only the energy level and not the response frequencies vary.
- bridle line tensions are either overpredicted or underpredicted by 5 to 40 % in BH/OF at all load cases. This causes a 200 to 600 % error of the mean surge and sway motion of operational load cases and a 10 to 50 % error for idling cases. Also, the yaw variation is overpredicted between 20 and 120 % due to too little restoring stiffness. Rotations show a less than 80% error. From comparison of a tension-displacement diagram of all bridle lines, it was observed that the mean bridle tensions correspond well to the expected values for the modeled mooring system. Therefore, further tuning of the mooring system is expected to improve the overall prediction performance. Still, individual lines throughout load cases show large errors, for which no clear trend is observed. Too low mean static bridle line tensions cause a shift of 15% surge/sway and 37% in yaw natural frequency, which is an error increase from the un-tuned system. This is because the system was tuned to match individual bridle tensions instead of overall restoring tension. This means natural frequency predictions are certainly caused by mooring restoring errors. In other degrees of freedom, the natural frequencies are predicted well by BH/OF with <1% error. The bridle line frequency domain response captures most physical phenomena. However, some lines in some load cases show significant errors in their response prediction in some load cases. No trends for these seemingly random occurring discrepancies could be found.

- The fist tower-bending response is overpredicted in tower roll and pitch results in multiple load cases, despite expected structural tower-damping being present in the model. From detailed analysis of the structural tower-damping a 5 times increase of tower damping shows an 80% error reduction, but limited effect on the absolute tower bending response. Moreover, these structural damping levels are not physically expected from a wind turbine tower. Therefore, over-excitation of the tower bending mode due to too much wave energy at these frequencies is expected, as this is also observed in the OrcaFlex verification results. Setting the high-cut frequency to 1 Hz instead of 10 Hz reduces the error by 163%, whilst showing hardly any variation in the wave-frequency response.
- In all load cases, the sway and roll wave-frequency response are underpredicted. This is is explained from long-crested wave assumptions in BH/OF. Wave spreading in the real-world system causes additional wave-induced excitation perpendicular to the wave direction. Also, it must be noted that the wave buoy is located at a distance 2.5 km from the Hywind system, which may result in different wave conditions modeled from those experienced by the full-scale system.
- In most load cases, the surge/sway response peak is clearly overpredicted, which may be due to lack of mooring line structural damping, mooring line viscous damping or floater hydrodynamic damping. Each effect is analysed in more detail, showing significant mitigation of both added linear hydrodynamic damping and increased viscous damping. Both can be justified by literature and show equal importance. Therefore, it is expected that a combined lack of both sources of damping causes the underprediction.
- A rotor mass imbalance in BHawC based on conservative design values likely causes overprediction of the yaw 1P response. This is explained from a periodic variation in the yaw gyroscopic moment caused by the imbalance.
- In idling cases, an overprediction of the low-frequency response is observed. This may be due to too much energy in the simulated wind field. The aerodynamic environment is modeled based on wind measurements from the turbine anemometer, which were corrected for the turbine motion. This correction could be flawed.

Errors mitigated during the model set-up are:

- Tuning of the mooring system has unexpected coupling motion terms observed in the original system due to simplification from a 3D to a 2D seabed representation. Furthermore, the static bridle line tensions were significantly improved.

6

Conclusions

The following main research question was established for this research: *How can load and motion simulations in BHawC/OrcaFlex aero-hydro-servo-elastic software be improved by using full-scale measurements of the Hywind Scotland floating offshore wind farm, leading to a higher performance level of the code?*

First the main conclusion to this answer is presented. Later, answers to each sub-question are formulated in the order of occurrence in the report.

Main conclusion No standardized approach for quantifying the performance of an aero-hydro-servo-elastic code is found from literature. A qualitative performance measure is provided by comparison of response statistics and frequency domain response. Natural frequencies are predicted correctly except for those influenced by errors in the mooring system. This shows a general capacity of modelling a complete system including sub-components mass and inertia. In the frequency domain response, most response peaks are at the correct frequencies with energy levels in the correct order of magnitude. A quantitative comparison shows correct prediction of the rotations, but significant errors in mean and variation of motions in the horizontal plane, as well as the mooring line tensions show an are observed. Within the scope of this report, most error sources could be either explained or mitigation methods could be successfully demonstrated.

The model validation study performed in this work can be further extended by increasing the level of error analysis from description to explanation to demonstration and mitigation. Several demonstrated error sources that could be mitigated are: limited viscous- and absent linear hydrodynamic damping, the likely occurrence of mooring VIV and further tuning of the mooring system. Further analysis of these errors will further improve (confidence in) the code performance level.

1) *How do OrcaFlex simulations perform in load and motion predictions, compared to equivalent simulations by a variety of industry-standard aero-servo-hydro-elastic software codes on a floating offshore wind turbine model that resembles the Hywind Scotland system?*

OrcaFlex was verified against a wide range of industry-standard aero-hydro-servo-elastic codes in load cases of step-wise increasing complexity. Here, the general performance in response prediction over a wide range of validation metrics was very well. Two significant code capacity errors were found. The first is in the definition of prescribed linear hydrodynamic damping. An alternative way of distributing the total damping level over floater was required to match the general response of other participants. This resulted in too high pitch response in all load cases. The second in the use of the equal energy distribution to generate wave trains from a wave spectrum predicts too high wave-induced response at high frequencies. Most errors in the model set-up were due to simplifications in the other codes. Improvements on the model set-up used in other validation steps were the inclusion of appropriate Rayleigh structural tower damping, use of TurbSim 3D spatially varying wind fields instead of a 2D turbulence model and separate post-processing of OrcaFlex results. A detailed overview of this errors and phenomena observed in this verification step is found in section 3.6.

2) *How do BHawC/OrcaFlex simulations perform in floating offshore wind turbine load and motion predictions compared to other aero-hydro-servo-elastic software codes?*

BHawC/OrcaFlex was verified against the previously verified OrcaFlex aero-hydro-servo-elastic codes in load cases of step-wise increasing complexity. Simplifications to both model set-ups had to be made in order to overcome insurmountable differences between both codes with limited possibilities of adaptation of the BHawC/OrcaFlex model. This comprised rigid blades, a constant rotor velocity and constant blade pitch angle. The predicted response between both codes agreed well across all load cases. No errors in the code capacity of BHawC/OrcaFlex were identified at this step. Errors were only observed in the OrcaFlex model set-up, which is in many aspects simplified compared to that of BHawC/OrcaFlex. Main differences arose from a reduced efficiency of the simplified OrcaFlex rotor model, absence of rotor mass imbalance in OrcaFlex and a different inertia of the total modeled system due to the simplified OrcaFlex structural tower model. A detailed overview on the errors and phenomena observed is found in section 4.7.

3) *How do BHawC/OrcaFlex simulations perform in floating offshore wind turbine load and motion predictions, compared to full-scale measurements of the Hywind Scotland floating offshore wind farm?*

No standardized approach for quantifying the performance of an aero-hydro-servo-elastic code is found from literature. A qualitative performance measure is provided by comparison of response statistics and frequency domain response. Natural frequencies are predicted correctly except for those influenced by errors in the mooring system. This shows a general capacity of modelling a complete system including subcomponents mass and inertia. In the frequency domain response, most response peaks are at the correct frequencies with energy levels in the correct order of magnitude. A quantitative comparison shows correct prediction of the rotations, but significant $O(10^2)$% errors in mean and variation of motions in the horizontal plane. The mooring line tensions show an $O(10^1)$% error in all load cases. Both are found to be due to too low mooring restoring stiffness due to errors in the mooring system set-up from limited information of the as-built system. Tuning of the mooring system improved the overall performance. Also, it should be noted that due to insuperable errors in the control system, only load cases in the below-rated and above cut-out regime gave stable results and could be used for validation. Within the scope of this report, most errors could be either explained or mitigation could be successfully demonstrated. A detailed overview on the errors and phenomena observed is found in section 4.7.

4) *How can the performance level of BHawC/OrcaFlex be increased, by using the results of the comparisons of its simulations to both the results of equivalent simulations and to the results of the measurements of the Hywind Scotland floating offshore wind farm?*

The model validation study performed in this work can be further extended by increasing the level of error analysis from description to explanation to demonstration and mitigation. This further increases the confidence in of BHawC/OrcaFlex performance and likely the performance level itself. Several responses could not be explained within the scope of this report. These include surge and pitch response peaks in the low-frequency region, sway response peaks between the heave and yaw natural frequency which were not captured by BHawC/OrcaFlex and a mean surge motion in load case 2 that was severely overpredicted. Selected explained results that could be demonstrated are: shifts in the surge/sway response frequency due to changes in bridle line stiffness from floater displacement, the underprediction of sway and roll response due to simplification of wave spreading and overprediction of the 1P response due to a conservative modeled rotor-mass imbalance. Several demonstrated error sources that could be mitigated are: limited viscous- and absent linear hydrodynamic damping, the likely occurrence of mooring VIV and further tuning of the mooring system. Further analysis of these errors will further improve (confidence in) the code performance level.

More concretely, the most basic errors observed from the results are the motions and mooring line statistics. These should be matching correctly to gain a basic level of confidence in the code. It is expected that further tuning of the mooring and hydrodynamic parameters will significantly improve this.

Only a few errors were captured across all load cases. This comprised the statistical of low-frequency frequency domain response analysis with a structure that has large natural periods, the overprediction of the high-frequency (tower-bending) response due to an equal energy wave generation method with too high

cut-off frequency and ways of modelling hydrodynamic damping.

7

Discussion and recommendations

Without doubt it can be established that the full potential of this research set-up has not yet been achieved. Given the unique set-up with detailed information of the as-built wind turbine and control system, as well as the availability of full-scale measurements, many more detailed comparisons could be made.

From the conclusions drawn of this project, it can be observed that despite careful model set-up most discrepancies are due to modelling errors. First of all, the control system should be repaired in BHawC in order to obtain simulation results for load cases 4-9. This gives a much broader possibility for analysis, as now clear trends across load cases that are can be linked to environmental conditions can be identified. To continue, future research could further analyse each error type that is observed in the results of this report. This starts with mitigation of demonstrated errors. Some examples are 1) careful tuning of the Morison drag coefficients of the floater and mooring lines to provide better matching hydrodynamic damping results. 2) careful tuning of the mooring system either such that is matches the prescribed properties or such that it matches the mooring response observed. 3) improve the wave train discretization model used for generating irregular waves from a spectrum in OrcaFlex. In addition, explained phenomena e.g. too high 1P modeled in BHawC or absence wave spreading effects could be analysed to find how they affect the response. Finally, an attempt could be made to further investigate unexplained phenomena and types of response. Undoubtedly, successful execution of the further analysis and mitigation of errors observed will increase the model performance and confidence.

From this, new types of (more detailed) analyses can be executed. Not all 'modelling trade-offs' discussed in Chapter 2 have been included in the final model validation. Comparison of the effect of non-linear (irregular) waves, modeling with and without current and types of modeling flow separation and VIM in OrcaFlex can be executed using the current model set-up. A comparison could be made with the performance of a potential-flow theory based model with the same turbine and mooring system. This could give a clear overview of the accuracy of second-order load effects predicted by both models. A deepened understanding of the mysterious additional required linear hydrodynamic damping and its importance compared to full-scale measurements could be achieved. The methodology could be extended by including a dedicated high-fidelity hydrodynamic model to separately substantiate these phenomena.

Additional and improved physical model could be pursued by obtaining better measurements. This regards more measured parameters on more locations. Or longer timeseries to further reduce statistical uncertainty. Furthermore, detailed measurements on the wind and wave conditions could certainly enhance this model set-up, in particular by eliminating turbine motion effects on wind statistics. In general, more and improved information on the as-built system would always result in a better model. Think of a more detailed representation of the mooring system, containing the exact anchor positions and their water depths or catenary chain geometry.

As described in section 2.6, validation metrics of this study were mainly based on the available measurements and relative novelty of the validation campaign, attempting to get a basic insight of the performance. Improved validation metrics could comprise fatigue damage calculation or scattered plots of comparisons

of interest when more load cases are available to identify trends. When more measurement parameters, e.g. tower-bottom or top -shear and bending are made available, a translation could be made from these validation metrics to cost effects. This could more directly provide a performance measure of the code.

As described in section 2.5, no standardized approach for aero-hydro-servo-elastic model validation was found from literature. This leaves each research project to compare their own validation metrics on their desired level of error analysis. A standardized approach for validation would 1) provide a starting point for new model validation campaigns on how to set up a model and compare it, 2) allow more easy continuation of validation projects, given that improvement of the performance would more easily be measured, 3) allow for inter-project comparison, which could give an overall 'ranking' of aero-hydro-servo-elastic software codes for a standardized set of validation metrics, perhaps even summarized in a single grade. This could help gain insight in the reason why some codes perform better than others. 4) help companies that develop codes to gain external parties' trust in their codes by being able to clearly communicate performance levels. The closest realisation of this standardisation is observed from the OC projects. Here, still, a wide variety of validation metrics for varying input is used for comparison throughout different projects.

Appendices

A

Literature survey compact overview

Legend

Measurement type:
- HDL = Hydrodynamic loading
- FS = full-scale measurements
- MS = model-scale experiments
- CFD = Computational Fluid Dynamics model
- NM = other numerical model

General:
- vs. = comparison between
- + = combination
- various = various types compared

Model definition:
- S = Scaled
- DeepC. = Floating DeepCwind semi-submersible
- Spar = Floating spar
- S-Spar = Floating Stepped-spar
- C-Spar = Floating concrete spar
- WindFl. = WindFloat semi-submersible concept
- F-BFC = Flexible Botton-Fixed Cylinder
- R-BFC = Rigid Bottom-Fixed Cylinder
- BFJ = Bottom-Fixed Jacket

Theories:
- IRT = Impulse Response Theory
- ME = Morison's equation
- PF = Potential Flow Theory
- PF + MD = Potential Flow Theory + Morison's drag component
- BEM = Blade Element Momentum theory
- BEM+ = Blade Element Momentum theory augmented with (combination of) skewed inflow, unsteady airfoil, dynamic wake theory and/or shear correction
- STF = Static Thrust Force applied at hub height
- SW = steady wind
- RB = Rigidy body dynamics
- BT = Beam Theory
- D = Dynamic mooring theory
- Q-S = Quasi-Static mooring theory
- K = Kaimal turbulence spectrum
- K+ = Kaimal turbulence spectrum including 3D-effects
- NPD = Norwegian Petroleum Directorate turbulence spectrum
- IW = irregular wave spectrum applied
- RW = Regular wave applied
- BM = Bretschneider-Mitsuyasu wave spectrum
- JS = JONSWAP wave spectrum
- N-L = Non-Linear wave theory
- L = Linear (Airy) wave theory
- WC = Wind-generated current
- SC = Steady uniform current

Analysis:
- L-F = Low-frequency region
- W-F = Wave-frequency region
- WTD = Wind Tower Drag
- TBM = Tower Bending Moment
- HDL = Hydrodynamic loads
- TV-HDL = Transverse hydrodynamic loads
- TBL = Tower Base Loads
- TTL = Tower Top Loads
- UL = Ultimate Loads
- FL = Fatigue Loads
- acc = acceleration

Comparison:
- $\uparrow$ = Overpredicted w.r.t. measurements
- $\downarrow$ = Underpredicted w.r.t. measurements
- $\updownarrow$ = Difference w.r.t. measurements
- $\varnothing$ = Phenomenon not captured by numerical simulation

Causes:
- Experimental error = various types of experimental (measurement) errors, exact cause not stated in this compact overview due to irrelevance for this thesis.
- $\diagdown$ = excluded from compact overview due to irrelevance for thesis
- ? = reason for difference not explained by authors
- unknown = reason for difference unknown to authors
- Simulation error = Error in simulation due to impossibility of making correct numerical model due to incompleteness or confidentiality of full-scale model characteristics
- QS-mooring = error caused by simplifications in use of quasi-static mooring theory in simulations
- LWT = error caused by simplifications in use of linear wave theory

Table A.1: A compact overview of recent numerical model validation studies in the field of (floating) offshore wind energy. For the full legend explaining abbreviations see 'Legend'.

Author	Year	Meas. type	Meas. location	Software Hydro	Software Aero	Turbine Size	Substruct. Type	Hydro. load. Theory	Aero. load. Theory	Struc. theory	Mooring theory	Wind input	Wave input	Current input	Differences loads	Differences motions	Differences other	Causes
Kvittem et al. [56]	12	NM	NO	SIMO /RIFLEX	FAST /AeroDyn + TurbSim	5MW	WindFl.	ME (4 types) vs. PF vs. PF+MD	BEM	RB + FEM	D	NTM	R vs IR	-	-	RW: 0) breakdown PF model L-F 1) Heave and pitch ME ↑ vs PF. 2) surge motion L-F ↓ ME vs PF. IW: 3) ME ↑ surge vs PF	turbwind +IW: 4) slight increase torque and power production variation ME vs PF	RW: 0) PF breakdown without drag, incl drag good results. 1) ME with forces calculated to mean water level. Up to wave elevation better agreement. 2) ME including dynamic pressure only, may be due to surge/pitch coupling. 3) extra drift force caused by inertia forces above the mean water level acting on a symmetrical structure. 4) increased pitch motion both wind and wave frequencies. statistics insufficient .
Utsunomiya et al. [103]	13	FS	JP	SparDyn (set of equations solved)	Fast+MSC Adams	100 kW	Spar	-	-	RB	QS	K	BM	WC	1) wind/wave coupling. 2) Bending moments ↑ for calm conditions.	3) Mean sway motion . Yaw motion . 4) Low-frequency surge&sway ↑. 5) Roll&pitch response peak ↑.	-	Sub-surface currents neglected. Current same direction as wind. Wind collinear assumed. Varying Cd and mooring theory. Quasi-static theory far-off. More damping in system than simulations.
Robertson et al. [81]	16	MS	DK	Various	Various	-	F - BFC	ME vs. PF vs. PF-MD	-	FEM	-	-	var N-L vs L, R vs IR	-	1) first round, all HDL off. NL-RW: 4)force maxima ↓. 5) Differences loads ME en PF. 6) response to higher-order harmonics. NL-IW: 10) loads/motions distribution match better for CFD/FNPF-kinematics	2) additional natural frequency, excited by N-L waves. 7) in max acc NL-RW. 8) acc response L-IW. 9) acc response NL-IW	3) in N-L surface elevation	1,2,8) experimental errors4) NL-wave peaks/thoughs ↓ by linear models 5) ME allowed tuning Ca to include wave basin reflection effects & PF assumes body rigid, body acceleration contribution. 6) LWT higher order harmonics. 7) unknown. 9) wave breaking . 10) LWT &NLWT wave development over slope, CFD can.
Robertson et al. [79]	15	MS	NO	Various	Various	-	R - BFC	F-ME vs. PF	-	RB	-	-	var N-L vs L, R vs IR	-	1/2) Higher order harmonic response peak . 3) second order stokes force 4) 2nd response peaks ↑ and 3rd order response peaks ↓. 5) Force ↓ L-F IW. 6) Steep wave event well predicted, decay freq ↓.	-	-	1) Linear wave theory used by those. 2) Non-linear drag coefficient in Morison neglected by those. 3) lack of stretching above MSL. Those with stretching capture phenomena. 4) non-slender diffraction not included in the model. 5)?. 6) ?.
Skaare et al. [88]	14	FS	NO	SIMA	SIMA	2.3 MW	Spar	ME	BEM	FEM	D	-	R	-	5) PSD peak amplitude at 1st TBM mode ↑. PSD 1st TBM mode Std ↑6) MLT wave-freq ↑ 7) MLT L-F ↓.	3) mean roll and pitch for operational cases. Below rated: 4) std roll ↓.above rated: 8) std roll ↓, pitch ↑ 9) std yaw motion ↑	1) general differences. 2) All results high-pass filtered.	1) long crested wave assumption. 2) LF motions due to currents neglected. 3) experimental errors 4) ?. 5) load case has high thrust force with small waves (wind dominated), wind fields stochastics. 7) VIV not included in the model OR difference in the wind fields, hightrustlowwaves - wind dominated OR low tensions compared to pretension. 8) waves spreading neglected 9) difference wind field simulations and measurement.
Popko et al. [77]	18	FS	GE	Various	Various	5 MW	BFJ	ME	BEM vs BEM+	var	-	K+	var N-L vs L, R vs IR	-	1) 2) 4) strain amplitude 1P	5) reponse 1st global bending mode ↓, 2nd global mode ↑. H-F amplitude increase .	3) Generator power std ↓. 6) shutdown: pitch angle . Generator speed ↓. 7) structural damping std	1) 2) 3,4,6,7) simulation error 5) underpredictions: wrong system damping in simulations. Overpredictions: simulation error
Robertson et al. [82]	17	MS	NL	Various	Various	5MW (scaled)	DeepC.	ME vs. PF vs. PF-MD	BEM vs BEM+	var	D vs QS	-	var N-L vs L, R vs IR	-	1) WTD . 2) Wind-Only: excitations ↓. 4) MLT RAO ↓. 5) avg UL and FL ↓ at TBL and TTL 6) avg UL and FL ↓ upwind MLT. wind+waves: 7) FL ↓↓, UL . 8) TBL ↓ PF. 9) TBL ↑ ME. 10) IW+steadywind: ULS ↓. 11) IW+unsteadywind: FL ↓ PF, some ME ↑. 12) IW: upwind MLT UL ↓ FL ↓.	3) Heave RAO ↓	-	1) experimental error 2) damping calibration off BEM+ OR experimental error 3) ME models neglect dynamic pressure on top and bottom of base collumns OR need to include relative fluid velocity in viscous drag calculations OR neglect axial drag loads on heave plates. 4) QS-mooring 5) ?. 6)?. 7)?. 8) Pitch response at nat freq ↓ all tools incl PF. pitch nat freq excited by N-L such as 2nd order effects, NL-W, stretching, hydo loads at instantaneous position. Damping. PF rest PSD good results. 9) Tower bending frequency ME far off. Related to added-mass dependency on frequency but taken constant. Pitch RAO overpredicted for high frequencies. 10) wind damped out pitch & tower bending response, so above results less off. 11) increased turbulence. 12) QS-mooring

Author	Year	Meas. type	Meas. location	Software Hydro	Software Aero	Turbine Size	Substruct. Type	Hydro. load. Theory	Aero. load. Theory	Struc. theory	Mooring theory	Wind input	Wave input	Current input	Differences loads	Differences motions	Differences other	Causes
Cermelli et al. [15]	18	FS	PT	OrcaFlex + WAMIT	FAST + TurbSim	2 MW	WindFl.	PF-MD + ME	BEM	FEM	?	K	JS	-	1) S-S TBM ↓, F-A TBM ↑. 2) FL correct but vary with turbulent wind spectrum.	-	-	1)?. 2)
Couling et al. [21]	13	MS	NL	FAST + WAMIT	FAST	5 MW (S)	DeepC.	PF	BEM	FEM	QS	NPD	JS	-	WAVE ONLY 5) Poor statistics obtained. 6) MLT L-F response .	WAVE ONLY 1) Surge response ↓. 2) Surge response ↓ using difference-frequency wave loads. 3) 4) Surge response phase .	-	1) Linear wave-diffraction forcing model severely ↓ L-F response of the system. L-F dominated response spectrum measured. 2) damping coefficient off. 3) 4) Newman's approximation TF off. 5) First order wave case only. 6) First order wave case only AND QS mooring
Liu et al. [60]	18	MS	CH	FAST + WAMIT	FAST	5MW (S)	?	?	BEM	?	QS	SW	JS	-	2) MLT PSD far ↓ for L-F 4) TBM PSD strong response at 1P	1) Surge, pitch, heave response PSD for L-F ↓. 3) yaw PSD strong response at 1P	-	1) second-order difference-frequency effects not well captures. 2) Surge response at nat freq not wel captured. 3)/4) gyroscopic moment caused at 1P not included in models OR experimental error
Sethuraman and Venugopal [86]	12	MS	SC	OrcaFlex	-	2MW (S)	S-Spar	ME	-	RB	QS	-	JS	-	-	1) All motions phase 2) oscillations scale model around theoretical mean	3) I-W heave/pitch natural response peak ↑.	1,2,3) experimental errors
Matha et al. [66]	15	MS	ES	HydroDyn + SIMPACK	SIMPACK	5MW - pulley system	C-Spar	PF	STF	RB	QS	-	IR - ?spec	-	-	1) pitch and roll decay tests amplitude ↓ after some time. 2) 3) limited responses found wrt wind loads and coupled effects	-	1,3) experimental errors. 2)
Dunbar et al. [26]	15	CFD	US	FAST + vs. OpenFOAM	-	-	DeepC.	PF	-	RB	-	-	-	-	-	1) heave decay: amplitude ↓ at first periods . 2) heave small decay: period ↓. 3) pitch decay: amplitudes ↓, periods ↓.	-	1 & 2) reynolds-dependent viscous effects such as flow separation off. 3) viscous effects, physics for pitch motion hard with semi-sub, shadowing effects. 1,2,3) linear restoring matrix off. Drag coefficients off.
Li et al. [59]	15	MS + NM	CH	Wind-SKLOE	Wind-SKLOE	5MW (S)	DeepC.	PF+MD + IRT	BEM+	RB	QS	-	JS	-	4) Thrust force ↑ comp to FAST.	1) surge/pitch coupling RAO 2) Heave RAO L-F ↑. 3) pitch RAO peak ↑. 5) 3DOF (pitch, heave, surge) motions RW mean ↑. 6) FAST 3DOF motions RW mean ↓. 7) FAST PSD surge ↓ L-F. 8) Surge peak ↓. 9) pitch peak ↑ CFD AND ↑ FAST. 10) extreme conditions all ↓ outside W-F region.	-	1) QS-mooring 2)?. 3,8) experimental errors 4) ?. 5) QS-mooring AND experimental errors 6,7,9) mean and slow drift . 10) N-L hydrodynamic effects.
Benitz et al. [8]	14	CFD	US	FAST + WAMIT vs. OpenFOAM	-	-	DeepC.	PF + MD	-	-	-	-	R	SC	Current only: 1) FAST ↑ HDL compared to CFD. 2&8) FAST TV-HDL . 3) FAST ↑ total HDL. 4) FAST constant HDL, CFD varying. 5) FAST total HDL is sum of components, CFD not. Wave only: 7) FAST larger HDL loads than CFD. 9) FAST slightly ↑ heave HDL. 10) TV-HDL increases with wave height for CFD, stays zero for FAST.	-	6) Current-only case motions FAST vs CFD. Wave-only case excellent agreements.	1,3) ME Shadowing effects 1,7) drag coefficients diff between FAST and CFD OR constant FAST drag coefficient off. 2,8,10) ME, PF vortex shedding. 3) Small components more viscous dominated so ME better approximation. 4) FAST ME definition constant force for constant flow. 5) 3D flow 6) PF accounts for shadowing effects. 9) ?.
Benitz et al. [9]	15	CFD	US	FAST + WAMIT vs. OpenFOAM	-	-	DeepC.	ME	-	-	-	-	-	SC	1) FAST ↑ HDL to CFD. 2) FAST assumes constant HDL. 3) FAST upstream HDL equals downstream members.	-	-	1) Drag coefficient 2)ME vortex shedding. 3) ME Shadowing effects

B

Discussion of types of physical models

Firstly, model scale experiments (abbreviated to MS in the compact overview) are a common way of generating measurement data. The advantage of model scale experiments is the ability to select desired environmental conditions and subject the model to each of them separately, without any undesired disturbance. This allows e.g. for separate testing of hydrodynamics of regular waves and irregular waves, or linear and non-linear (steep) waves [80]. Another advantage is the ability to extensively control and vary the input. One can vary the waveheight or wind speed to which the model is subjected to what is most interesting to the researcher, compared to full-scale measurements where the environmental conditions are stochastic input. Thirdly, MS allows to have measurements of the environment at any location that is practically achievable, compared to limited placement possibilities and measurement noise in full-scale measurements.

The main disadvantage, however, is that proper scaling of a wind turbine is very hard to achieve. Two laws can are often used: Froude and Reynolds scaling. Both laws are contradictory in the case of a wind turbine. This is a widely occurring issue in the case of floating wind turbine experiments, despite efforts of creating an optimized geometry of blades and thrust curves [82]. Additionally, experimental errors are likely to occur in the case of scale experiments. In the compact overview, these are summarized as 'experimental errors' without stating individual reasons. Some errors of frequent occurrence are:

- **Wave basin reflection** ([86], [66] and [80]). Waves generated in a basin of finite size are likely to reflect off the basin walls, while waves in real seas will propagate to 'infinity' after interacting with the structure. Reflected waves may interact with the structure and cause response peaks in addition to waves generated by the original wave source. The exact contribution of these reflected waves is often unknown. Therefore, this category is not necessarily an error and could also be described as an uncertainty.
- **Wind/wave simulations** ([66], [59] and [82]). Several difficulties occur in the production of an accurate wind/wave climate. Many wave basins are used for testing hydrodynamic loading only. Therefore, additional efforts may be required in creating an experimental set-up that includes a wind generation source. Still, some wave basins are simply not suitable for generation of a (uniform) wind field. This causes discrepancies in the comparison of simulated and measured wind fields. In one case, a pulley system is used to mimic a steady thrust force, which is found to underpredict wind-induced motions. In another case, 6 DOF motions of a scale model cause too much misalignment between the incoming wind and RNA. In some cases, this is not included in simulations or not corrected for in measurements, which in turn causes difficulties in the comparison.
- **Experimental set-up** ([82], [86] and [60]). Errors in experimental set-up are inevitable, despite significant efforts of researchers. Some errors are due to data-processing, such as manual synchronisation of measurements and response motions. Others are due to general scaling difficulties, such as achieving the right level of tower stiffness whilst keeping other parameters correct. Some are due to the general experimental set-up, such as the presence of a cable bundle at the scale model turbine which could cause additional loads not accounted for in simulations.

The uncertainty of experiments can be assessed by cumulatively assessing the each source of uncertainty [82]. A first assessment on the uncertainty of wave-basin experiments shows that wave-making in a basin can be done with low uncertainty, but selection of measurement tools could still be a source of increased uncertainty [83]. Large ongoing research campaigns, such as the OC6 project, focus on assessing the uncertainty of

model validation.

The use of more detailed numerical models is becoming more and more popular, due to the development of computational fluid dynamics software. The main advantage is that these numerical models can give detailed insight in the flow patterns around floating structures [9], which are often simplified in 'engineering codes'. This could provide insight in specific fluid dynamics phenomena, such as hydrodynamic flow separation or aerodynamic wake development. The main disadvantage, is the computational efforts required by these tools. Therefore, floating wind comparison studies are often limited to simplified hydrodynamic cases using regular waves only, neglecting structural flexibility and validating rigid body motions only [26]. Developments in this field are ongoing and the results so far are promising for future applications.

Finally, the use of full-scale data is a widely accepted way of validating numerical models. The main advantage is that one can be sure all physical phenomena are included in the full-scale model. Scaling errors and simplified computations are no longer an issue. On the other hand, new challenges arise here. In the compact overview these are stated as 'simulation errors'. A selection of simulation errors are:

- **Confidentiality** ([77] and [15]). In most cases, full-scale system properties such as blade aerodynamic properties, blade pitch control system, or mooring system details are kept (partially) confidential by wind turbine suppliers and wind farm developers. Consequently, researchers have to make assumptions regarding the behaviour of the full-scale system, which inherently lead to simulation errors. A common approach is extensive calibration and tuning of a numerical model set-up that uses publicly available system properties, such as the OC3-Hywind system [47] with the NREL-5MW turbine [49], before using it for validation [76]. Despite efforts of researchers to mimic the as-built system as closely as possible, sometimes inexplicable phenomena, like specific behaviour of the RNA active pitch system, occur that have not been included in numerical simulations.
- **Data selection** ([88], [77] and [15]). Most wind farms are equipped with basic loads and motions measurement tools. On top of that, prototype farms such as the Hywind Demo project and the WindFloat1 project are heavily equipped with measurement tools that can be used for system analysis. Such large amounts of data need careful processing and selection before they can be used in model validation. Data sets need to be selected with representative environmental conditions, minimizing possible farm effects like wake interaction for a sufficiently long period. Still, however, perfect 'wind-only' or 'wave-only' cases hardly occur in nature due to wind/wave interaction. Therefore, detailed analysis of certain phenomena observed in these cases is harder for full-scale data compared to model scale experiments.
- **Measurement data availability** ([103], [77] and [15]). Full-scale measurement systems on offshore (floating) wind turbines are subject to the harsh offshore climate. Therefore, proper maintenance of the measurement system is vital to keep secure data availability. This limits the simultaneous availability of loads, motions and environmental conditions measurements required for proper validation. Moreover, in the case of extreme weather conditions like typhoons, which are of particular interest to researchers due to the unique system response, data availability is even more limited as power losses or sensor failure may occur. In some cases, measurement data (like current velocity or tower shear force) is simply not available due to absence of appropriate measurement systems. In the case of environmental conditions measurements, this makes it harder to simulate reality. In the case of system response measurements, it may reduce the possibilities of proper analysis.

C

Additional information on OrcaFlex Hywind turbine model set-up

C.1 Method structural parameters from BHawC to OrcaFlex

Method for translating blade structural parameters from BHawC to OrcaFlex coordinate system. Please not that the minus sign is depicted as '_' here due to errors in the text compiler to distinguish from namegiving variables.

```
%% COORDINATE SYSTEMS REWRITE
% AERODYNAMIC CENTRE IN ORCAFLEX COORDINATES
% express coordinates relative to aerodynamic centre
X_ac_1 = BladeAeroFile.ac_x '_' BladeAeroFile.ac_x;
Y_ac_1 = BladeAeroFile.ac_y '_' BladeAeroFile.ac_y;

% rotate coordinates with aerodynamic twist
X_ac_2 = X_ac_1 .* cosd( '_' BladeAeroFile.Twist) '_' Y_ac_1 .* sind(  '_'  ...
    BladeAeroFile.Twist);
Y_ac_2 = X_ac_1 .* sind( '_' BladeAeroFile.Twist) + Y_ac_1 .* cosd( '_' ...
    BladeAeroFile.Twist);

% shift with C/4 to express coordinates relative to OrcaFlex 'geometry frame'
X_ac_3 = X_ac_2 + BladeAeroFile.Chord/4;
Y_ac_3 = Y_ac_2;

% express coordinates in OrcaFlex geometry frame, as a percentage of the chord
BladeStructFile.X_ac_of = Y_ac_3 ./ BladeAeroFile.Chord *100;
BladeStructFile.Y_ac_of = X_ac_3 ./ BladeAeroFile.Chord *100;

% NEUTRAL AXIS CENTRE IN ORCAFLEX COODRINATES
% express coordinates relative to aerodynamic centre
X_ec_1 = BladeStructFile.x_ea_PE '_' BladeAeroFile.ac_x;
Y_ec_1 = BladeStructFile.y_ea_PE '_' BladeAeroFile.ac_y;

% rotate coordinates with aerodynamic twist
X_ec_2 = X_ec_1 .* cosd( '_' BladeAeroFile.Twist) '_' Y_ec_1 .* sind( '_' ...
    BladeAeroFile.Twist);
Y_ec_2 = X_ec_1 .* sind( '_' BladeAeroFile.Twist) + Y_ec_1 .* cosd( '_' ...
    BladeAeroFile.Twist);

% shift with C/4 to express coordinates relative to OrcaFlex 'geometry frame'
X_ec_3 = X_ec_2 + BladeAeroFile.Chord/4;
Y_ec_3 = Y_ec_2;

% express coordinates in OrcaFlex geometry frame, as a percentage of the chord
BladeStructFile.X_ec_of = Y_ec_3 ./ BladeAeroFile.Chord *100;
BladeStructFile.Y_ec_of = X_ec_3 ./ BladeAeroFile.Chord *100;

% CENTRE OF GRAVITY IN ORCAFLEX COORDINATES
```

```
% express coordinates relative blade coordinate system
X_cg_0a = BladeStructFile.x_cg_EA '_' BladeStructFile.x_ea_PE;
Y_cg_0a = BladeStructFile.y_cg_EA '_' BladeStructFile.y_ea_PE;

% rotate coordinates with structural pitch
X_cg_0b = X_cg_0a .* cosd(BladeStructFile.StrPitch) '_' Y_cg_0a .* ...
    sind(BladeStructFile.StrPitch);
Y_cg_0b = X_cg_0a .* sind(BladeStructFile.StrPitch) + Y_cg_0a .* ...
    cosd(BladeStructFile.StrPitch);

% express coordinates relative to aerodynamic centre
X_cg_1 = '_' X_cg_0b '_' BladeAeroFile.ac_x;  % x axis changes sign
Y_cg_1 =   Y_cg_0b '_' BladeAeroFile.ac_y;

% rotate coordinates with aerodynamic twist
X_cg_2 = X_cg_1 .* cosd( '_' BladeAeroFile.Twist) '_' Y_cg_1 .* sind( '_'  ...
    BladeAeroFile.Twist);
Y_cg_2 = X_cg_1 .* sind( '_' BladeAeroFile.Twist) + Y_cg_1 .* cosd( '_' ...
    BladeAeroFile.Twist);

% shift with C/4 to express coordinates relative to OrcaFlex 'geometry frame'
X_cg_3 = X_cg_2 + BladeAeroFile.Chord/4;
Y_cg_3 = Y_cg_2;

% express coordinates in OrcaFlex geometry frame, as a percentage of the chord
BladeStructFile.X_cg_of = Y_cg_3 ./ BladeAeroFile.Chord *100;
BladeStructFile.Y_cg_of = X_cg_3 ./ BladeAeroFile.Chord *100;

% Angles
BladeStructFile.StrPitchOF = BladeAeroFile.Twist '_' BladeStructFile.StrPitch;

% Calculate radii of gyration in OrcaFlex definitions
BladeStructFile.Ry_Rx = BladeStructFile.ri_y ./ BladeStructFile.ri_x;
BladeStructFile.Rz = sqrt(BladeStructFile.ri_y.^2 + BladeStructFile.ri_x.^2) ./ ...
    BladeAeroFile.Chord *100;
```

C.2 Method blade profile from BHawC to OrcaFlex

Method for assigning the correct blade profiles from BHawC to OrcaFlex coordinate depending on the blade thickness percentage.

```
%% Assign correct blade wing to corresponding blade section
for i = 1:length(BladeAeroFile.Blades)
    if BladeAeroFile.Blades(i) ≤ ...; % values are left out for confidentiality
        BladeAeroFile.Profileset(i) = 1;
    elseif BladeAeroFile.Blades(i) ≤ .. && BladeAeroFile.Blades(i)> ...
        BladeAeroFile.Profileset(i) = 2;
    elseif BladeAeroFile.Blades(i) > ...
        BladeAeroFile.Profileset(i) = 1;
    else
        BladeAeroFile.Profileset(i) = NaN;
    end

end

% Define positions on blade on which each blade profile applies
Bench17 = ...; % values are left out for confidentiality
Bench16 = ...;
Bench15 = ...;
Bench14 = ...;
Bench13 = ...;
Bench12 = ...;
Bench11 = ...;

Bench26 = ...;
Bench25 = ...;
Bench24 = ...;
Bench23 = ...;
```

```
Bench22 = ...;
Bench21 = ...;

% Assign correct profile set to blade position, based on blade thickness
for i = 2:length(BladeAeroFile.Profileset)

    if BladeAeroFile.Profileset(i) == 1
        if BladeAeroFile.Thick(i) ≤ 100 &&  BladeAeroFile.Thick(i) > Bench17
           BladeAeroFile.set(i) = 1.7;  %Profile set 1, blade profile 7
        elseif BladeAeroFile.Thick(i) ≤ Bench17 &&  BladeAeroFile.Thick(i) > Bench16
           BladeAeroFile.set(i) = 1.6;
        elseif BladeAeroFile.Thick(i) ≤ Bench16 &&  BladeAeroFile.Thick(i) > Bench15
           BladeAeroFile.set(i) = 1.5;
        elseif BladeAeroFile.Thick(i) ≤ Bench15 &&  BladeAeroFile.Thick(i) > Bench14
           BladeAeroFile.set(i) = 1.4;
        elseif BladeAeroFile.Thick(i) ≤ Bench14 &&  BladeAeroFile.Thick(i) > Bench13
           BladeAeroFile.set(i) = 1.3;
        elseif BladeAeroFile.Thick(i) ≤ Bench13 &&  BladeAeroFile.Thick(i) > Bench12
           BladeAeroFile.set(i) = 1.2;
        elseif BladeAeroFile.Thick(i) ≤ Bench12 &&  BladeAeroFile.Thick(i) > Bench11
           BladeAeroFile.set(i) = 1.1;
        else
            BladeAeroFile.set(i) = NaN;
        end
    elseif BladeAeroFile.Profileset(i) == 2
        if BladeAeroFile.Thick(i) ≤ 100 &&  BladeAeroFile.Thick(i) > Bench26
           BladeAeroFile.set(i) = 2.6; % Profile set 2, blade profile 7
        elseif BladeAeroFile.Thick(i) ≤ Bench26 &&  BladeAeroFile.Thick(i) > Bench25
           BladeAeroFile.set(i) = 2.5;
        elseif BladeAeroFile.Thick(i) ≤ Bench25 &&  BladeAeroFile.Thick(i) > Bench24
           BladeAeroFile.set(i) = 2.4;
        elseif BladeAeroFile.Thick(i) ≤ Bench24 &&  BladeAeroFile.Thick(i) > Bench23
           BladeAeroFile.set(i) = 2.3;
        elseif BladeAeroFile.Thick(i) ≤ Bench23 &&  BladeAeroFile.Thick(i) > Bench22
           BladeAeroFile.set(i) = 2.2;
        elseif BladeAeroFile.Thick(i) ≤ Bench22 &&  BladeAeroFile.Thick(i) > Bench21
           BladeAeroFile.set(i) = 2.1;
        else
            BladeAeroFile.set(i) = NaN;
        end
    else
        BladeAeroFile.set(i) = NaN;
    end
end
```

D

Hydrodynamic analysis of full-scale measurements

Using the environmental conditions measurements for each load case described in Chapter 5, an analysis is made of the expected flow regime. The variation of diameter of the Hywind Scotland floater below water level is depicted in figure D.1a. The maximum horizontal wave velocity for each load case is calculated in accordance with first order potential flow theory and simultaneously the dispersion relation (equation 2.16) is solved. Next, the final result is obtained by first calculating the undisturbed wave velocity of the total wave conditions over the entire floater depth and later taking the maximum at each water depth. The results can be found in figure D.1b. It can be clearly observed that the maximum undisturbed horizontal velocity occurs at the free surface. Note that the unstretched wave velocity profile is used in the analysis. In all analyses, the maximum occurring wave height is determined from the significant wave height using $H_{max} = 1.86 H_s$ as explained in [51]. Current effects are neglected in these analyses.

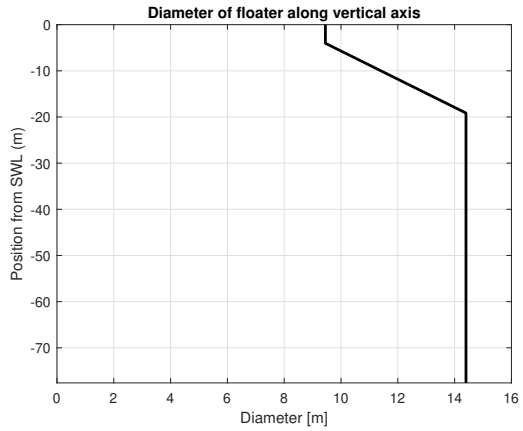

(a) Diameter of the Hywind spar-type floater along its draught, below SWL.

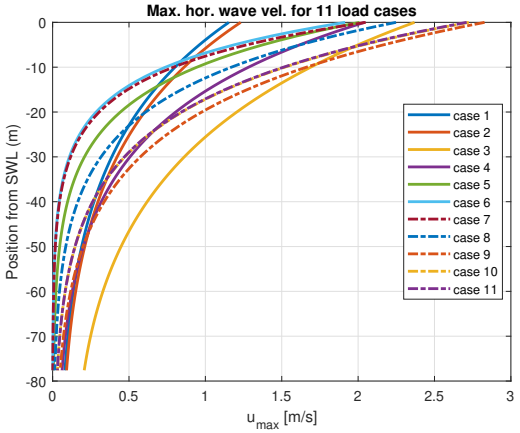

(b) Overview of the maximum horizontal wave velocity along the floater per load case.

Figure D.1: Basic properties of the Hywind Scotland system used in the hydrodynamic analysis.

D.1 Diffraction significance

As explained in section 2.2.3.3, the main limitation in the use of Morison's equation is the occurrence of wave diffraction effects. As a rule of thumb, wave diffraction effects can be considered negligible for large wave lengths compared to the structure. More concretely, in conditions with a ratio of $\frac{\lambda}{D} < 5$ or $\frac{D}{\lambda} > 0.2$ diffraction effects become significant.

For each load case, this condition is investigated. The wave length is determined here by solving the finite-depth dispersion relation for given total wave peak period, total wave height and water depth (equation

2.16). Note that for irregular waves, many wave components will have a period lower than this. However, the energy related to these periods is relatively small. The results can be found in figure D.2a. The diffraction limit is depicted by a dashed vertical line. As the wavelength is considered constant for each load case in this analysis, the ratio clearly follows the shape of the taper.

The maximum occurring ratio along the floater is depicted in figure D.2b. It can be observed that the ratio is only exceeded in load cases 6 and 7. From figure 5.3b it is known that these sea state in these cases are dominated by wind waves, hence the short wave length. This means that for these two sea states, Morison's equation may give slightly erroneous results. As these sea states involve only small wave heights, however, absolute differences may be small. Moreover, one could consider a diffraction correction or using a combined potential-flow with Morison's drag model for this load case.

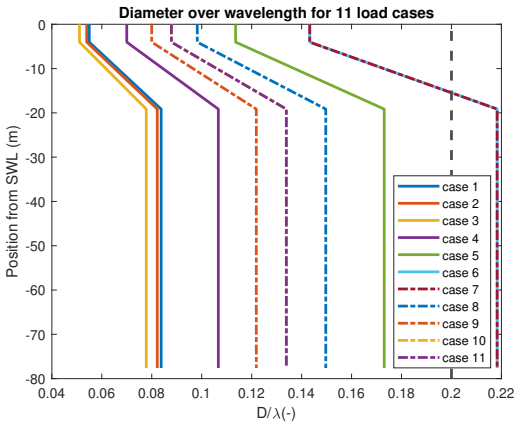

(a) Distribution of ratio of diameter over wavelength along the floater per load case.

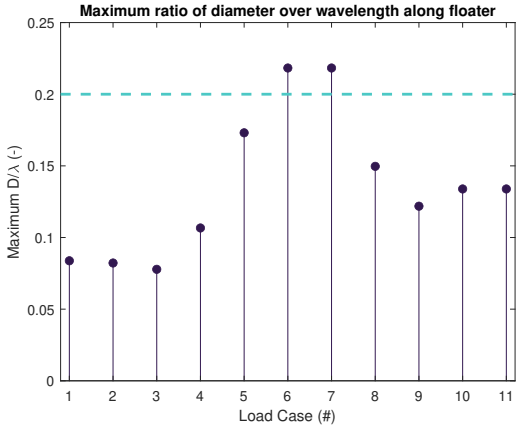

(b) Maximum occurring ratio of diameter over wavelength at peak period along the floater per load case. The horizontal line indicates the value at which diffraction becomes important.

Figure D.2: Analysis of the diffraction significance per load case.

D.2 Dominant hydrodynamic loading

In order to determine the importance of either drag or inertia loads, the Keulegan-Carpenter number (KC-number) can be determined as explained in 2.2.3.3. For load cases that are clearly drag-dominated potential flow theory can not be applied without adding an additional (Morison) drag component.

The KC-number along the floater is calculated for each load case using equation 2.52 and the velocities found in figure D.1b. The results can be found in figure D.3a. It can be observed that all load cases stay well below the KC limit of three. Also, the effect of the tapered section can clearly be observed, giving an extra increase in KC-number near the free surface.

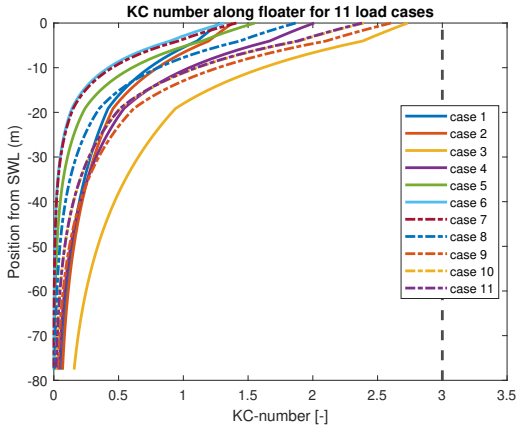

(a) Distribution of KC-number along the floater per load case. The vertical line indicates the value at which drag becomes important.

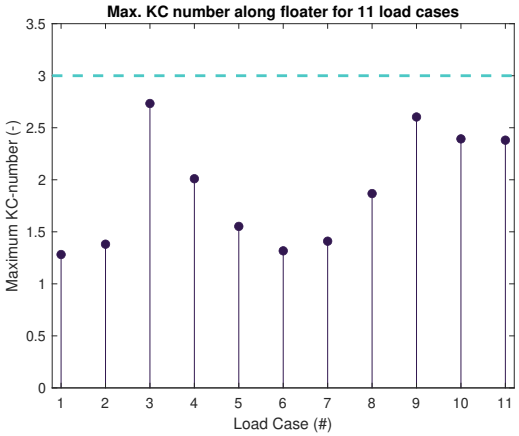

(b) Maximum occurring KC-number along the floater per load case. The horizontal line indicates the value at which drag becomes important.

Figure D.3: Analysis of the dominant type of hydrodynamic loading per load case.

For the sake of clarity, an additional overview giving the maximum occurring KC-number over the entire floater for each sea state is provided in figure D.3b. A comparison to the sea state composition of figure 5.2b shows a clear relationship to the significant waveheight and thus the expected maximum waveheight. In order to look at this in more detail, a ratio of the wave height over diameter for each of case is calculated along the floater, as can be found in figure D.4a. The maximum occurring wave height over diameter for each sea state is given in figure D.4b. The results are compared to figure 2.7. Here, the horizontal lines are interpreted to represent an H/D value of 10.6, 1.8 and 0.15 from the top down, which are included in the results by means of horizontal dashed lines. It can be clearly observed that all load cases lie in the 'negligible drag region'.

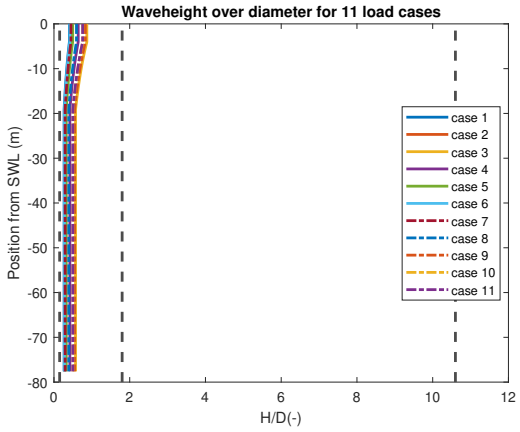

(a) Distribution of ratio of wave height over diameter along the floater per load case. The vertical lines indicate the values of increasing drag importance.

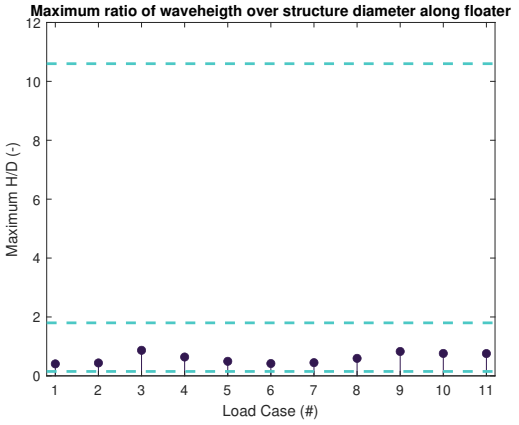

(b) Maximum occurring ratio of wave height over diameter along the floater per load case. The horizontal lines indicate the values of increasing drag importance.

Figure D.4: Analysis of the dominant type of hydrodynamic loading per load case.

D.3 Wave steepness

An analysis of the wave steepness is included. Based on figure 2.4, the appropriate (non-linear) wave model can be selected based on the dimensionless water depth and waveheight (see figure D.5). Non-linear waves could in higher-order harmonics in the system response, as well as increased peak loads near the sea surface, which is wrongly predicted by a linear waves assumption [12].

All load cases are in very deep water. From this analysis it would be suggested that the LCs 1 through 4 are in the Stokes 2^{nd} order regime and LCs 5 through 11 are in the Stokes 3^{rd} order regime. It should be noted, here, that the maximum occurring waveheight is considered in this analysis, in combination with the peak

period. This is not a very common combination of waves to occur. Moreover, the rule of thumb used to give a maximum wave elevation assumes a sea state of at least 1000 waves, which is not the case for this 30-minute statistic representation. For given peak periods, less than less than 250 'significant' waves are expected to pass in 1800 s. Therefore, the occurrence of non-linear waves is considered beyond the scope of this analysis.

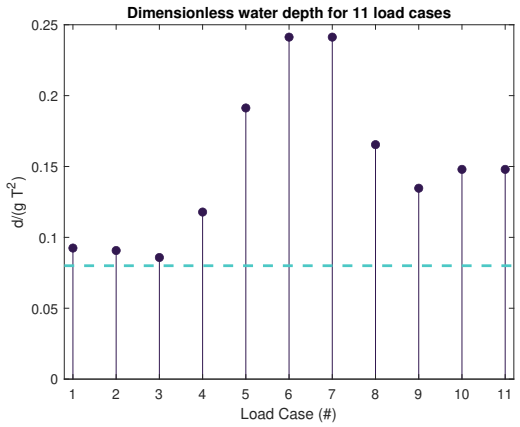

(a) Maximum dimensionless water depth per load case. The horizontal line indicates the value at which the water can be considered deep.

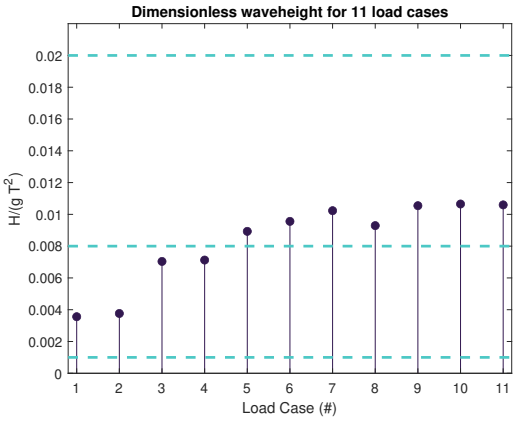

(b) Maximum dimensionless waveheight per load case. The horizontal lines indicate the values at which (from bottom to top) the Stokes 2nd, 3rd and 5th regimes should be considered.

Figure D.5: Analysis of the wave steepness per load case.

D.4 Turbulence

Finally, the maximum occurring Reynolds number is calculated along the floater, using equation 2.43. Here, the maximum flow velocity is determined from the maximum occurring wave height. This gives an impression of the expected flow regime for each sea state, which could be used to determine hydrodynamic coefficients such as the normal drag coefficient. The distribution of the Reynolds number over the floater is found in figure D.6a. A logarithmic scale is used for improved clarity. The highest and lowest values of the maximum occurring Reynolds number along the floater are depicted in figure D.6b. It can be observed that the maximum occurring Reynolds number is relatively constant for each load case being well above 10^7. However, a closer observation shows a relations to the significant waveheight in figure 5.2b. This is intuitively explained by higher waveheights giving higher horizontal wave velocities and therefore more turbulence.

The lowest maximum Reynolds number along the floater, however, varies significantly between order 10^4 and 10^6. A clear relationship between the maximum wave length and lowest maximum Re-number is observed, with lower Re-numbers for larger wave lengths and vice-versa. These, in turn, relate strongly to the relative sea state composition observed in figure 5.3a.

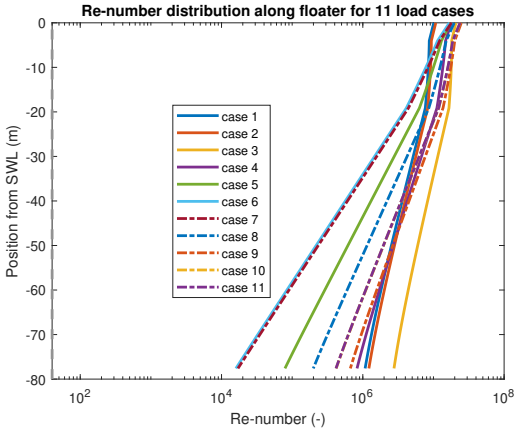

(a) Distribution of the maximum occurring Reynolds number per load case.

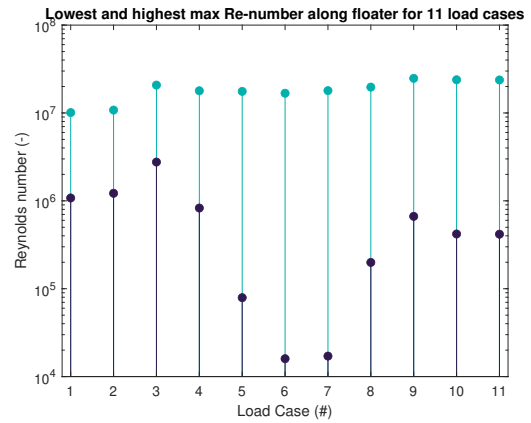

(b) Lowest and highest occurring Reynolds number per load case.

Figure D.6: Analysis of the flow regime per load case.

E

Measurements and simulation results post-processing

In order to be able to use the provided full-scale measurement data timeseries, several post-processing steps had to be taken. Here, post-processing of full-scale measurements is explained. A similar approach is taken for the simulation measurements.

E.0.1 Full-scale measurements post-processing

Most measurement signals use a different sampling frequency, as devices used to record the signals are also different of nature. This influences the possibilities of describing the data in frequency domain (FD), as higher frequencies require a higher time domain sampling rate to be able to include them in the analysis. Moreover, most of the measurement signals were created using discontinuous sampling frequencies, meaning the timestep at which data was recorded varies along the timeseries. This complicates the direct comparison of time-domain signals. From this combination of factors, it was decided to interpolate all data to the lowest occurring (continuous) sampling frequency. The signals identified with lowest measurement frequency are the bridle line tensions, each sampled at 5 Hz. Here, the fact is considered that interpolation removes frequency-domain information from the measurements at frequencies above the Nyquist frequency of 2.5 Hz. However, as most relevant (natural) frequency energy of a floating offshore wind system are well below 2.5 Hz, this is considered acceptable for later frequency-domain analysis. It should be noted, here, that to accurately identify occurring frequencies, a higher sampling rate than the Nyquist frequency is desired. An example of the effect of interpolation is found in figure (E.1b), where high-frequency oscillations are observed around the interpolated signal.

All measurements consist of a data number, a measurement time and the measured value. In order to execute interpolation, all signal time vectors are transferred to a serial date number and added to the data set. Serial date numbers are counted from January 0, 2000, where each number represent a consecutive timestep. Due to the discontinuous sampling rates, some signals contained more data points than others. Therefore, each signal's starting time and ending time were identified manually.

MATLAB R2019b allows several methods for 1-D data interpolation of signals. All methods were tested and analyzed in terms of their resulting Root Mean Square Error (RMSE) (see figure E.1a). Mooring line tension signals are used for investigation errors, as their original sampling rate is used for interpolation. This means interpolated values should be identical to original values. A 'piecewise cubic hermite interpolating polynomial' (PCHIP) is found to give the best result [67]. Here, 'next-neighbor' and 'nearest-neighbour' methods are neglected as these methods do not interpolate between values but directly assume the original value. As the original and interpolated signal are exactly similar for mooring line tensions but not for other signals, this gives a distorted impression of the true expected error.

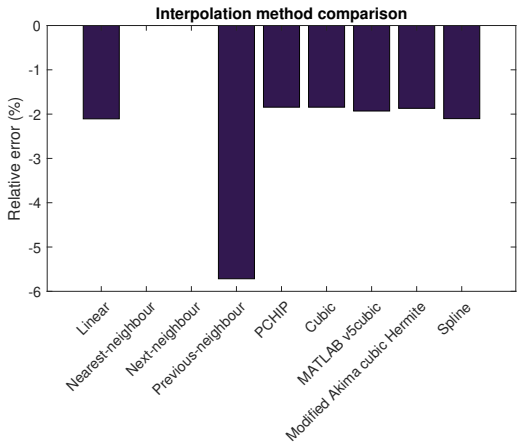

(a) Relative errors between original and interpolated signal for different interpolation methods, for mooring line 1, bridle line 1 in load case 1.

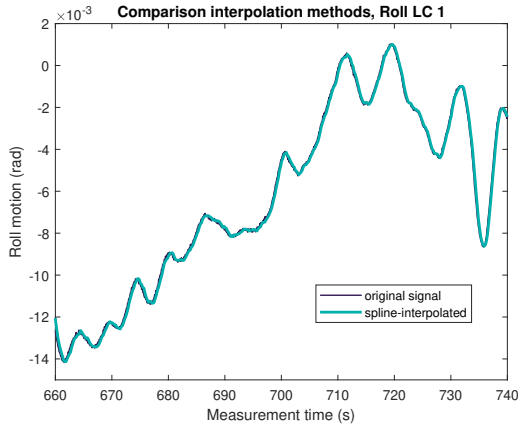

(b) Original signal and 'spline' interpolated signal of platform roll motion in load case 1.

Figure E.1: An example of the effect of interpolation on the Hywind measurement signals.

Next, a Fast Fourier Transform (FFT) (equation E.1) is applied to transform discrete time domain data to discrete FD data, used to obtain power spectral density (PSD) representations. The FD representation now has a frequency resolution given by the sampling frequency divided by the number of samples.

$$F[k] = \sum_{n=0}^{N-1} f[n] e^{-i2\pi k \frac{n}{N}} \tag{E.1}$$

When the input frequency is not an exact multiple of the sampling frequency, spectral leakage will occur. As a result, FD peaks at similar frequency can become hard to recognize. In full-scale measurements measurement, noise may be present in the signal causing additional spectral energy peaks. This augments the indistinctness of FD peaks. In order to cope with both phenomena, time-domain windowing can be applied to the signal before applying a FFT. A discrete-time window function, w[n], is multiplied by the signal, f[n]. Windows are often bell-shaped making the signal beyond the window length zero-valued. This allows only a small part of the signal to be transformed, which results in less spectral leakage.

After windowing, however, peaks in FD get wider. The downside of this is that when the signal contains multiple peaks at almost the same frequency, this widening will make the peaks harder to distinguish. The smaller the window length, the more each peak gets smeared out. Overlapping can be applied for time-domain signals that are longer than needed to show its frequency content. The signal is then cut into segments which are windowed individually.

For windowing, two parameters are of importance: the window length ratio and overlap ratio. The smaller the window length ratio and overlap ratio, the smoother the signal will become, but the more information on local extrema is lost (see figure E.2a). For this thesis, a Hann Window [91] is applied according to SGRE common practice. The Hann window is defined as

$$w[n] = \begin{cases} 0.5 - 0.5\cos(2\pi n/M), & 0 \leq n \leq M \\ 0, & else \end{cases} \tag{E.2}$$

where the length of the window is given as M+1. Manually, different ratios are tested to find a signal that contains all relevant information of the measurements, whilst significantly improving distinctness in the PSD plots. A window length ratio of 0.4 with an overlap ratio of 0.5 is selected, as shown in figure E.2b.

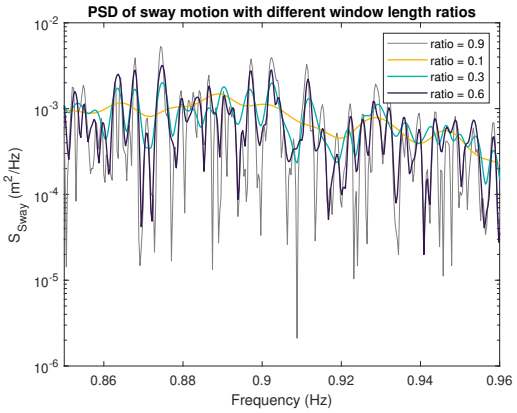

(a) Zoom-in on the effect of different Hann window length ratio's on a FD signal.

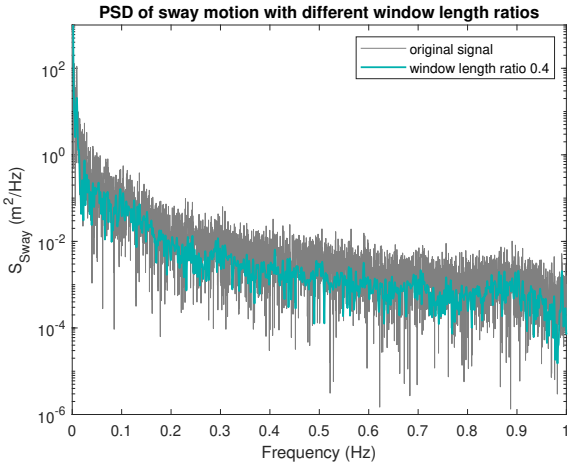

(b) An example of the effect of applying a Hann window with windowlength ratio of 0.4 on the PSD of the sway motion of load case 1.

Figure E.2: An example of the effect of windowing on the Hywind Scotland measurement signals.

Finally, all signals are normalised before constructing a PSD. As defining a time-domain non-zero mean value requires high energy at around 0 Hz frequencies, leaving the mean value before applying a FFT results in a high peak around 0 Hz. This is not improving identification of system behaviour.

E.0.2 Post-processing of BHawC/OrcaFlex simulation data

Post-processing of simulation results is performed in a similar way as for the measurements. FD results are obtained by applying a FFT to each timeseries signal. First, each signal is normalised PSD and a Hann window with window length ratio of 0.7 and a overlap ratio of 0.5 is applied. This higher window length ratio is found to fit better to the higher sampling rate of BH/OF simulations.

Bibliography

[1] E. Achenbach. Influence of surface roughness on the cross-flow around a circular cylinder. *Journal of fluid mechanics*, 46(2):321–335, 1971.

[2] International Energy Agency. Offshore wind outlook 2019. Technical report, International Energy Agency, 2019.

[3] V. Arramounet, C. E. de Winter, N. Maljaars, S. Girardin, and H. Robic. Development of coupling module between bhawc aeroelastic software and orcaflex for coupled dynamic analysis of floating wind turbines. In *Journal of Physics: Conference Series*, volume 1356, page 012007. IOP Publishing, 2019.

[4] B. Balodis. Imsouane (the bay), 2018. URL `https://magicseaweed.com/photo/381263/album/a9d5cdced077e918cd3ab840137d4846/`. [Online; accessed November 11, 2019].

[5] Erin E Bachynski, Trygve Kristiansen, and Maxime Thys. Experimental and numerical investigations of monopile ringing in irregular finite-depth water waves. *Applied Ocean Research*, 68:154–170, 2017.

[6] C. K. Batchelor and G. K. Batchelor. *An introduction to fluid dynamics*. Cambridge university press, 2000.

[7] I. Bayati, J. Jonkman, A. Robertson, and A. Platt. The effects of second-order hydrodynamics on a semisubmersible floating offshore wind turbine. In *Journal of Physics: Conference Series*, volume 524, page 012094. IOP Publishing, 2014.

[8] M. A. Benitz, D. P. Schmidt, M. A. Lackner, G. M. Stewart, J. Jonkman, and A. Robertson. Comparison of hydrodynamic load predictions between engineering models and computational fluid dynamics for the oc4-deepcwind semi-submersible. Technical report, National Renewable Energy Lab.(NREL), Golden, CO (United States), 2014.

[9] M. A. Benitz, D. P. Schmidt, M. A. Lackner, G. M. Stewart, J. Jonkman, and A. Robertson. Validation of hydrodynamic load models using cfd for the oc4-deepcwind semisubmersible. Technical report, National Renewable Energy Lab.(NREL), Golden, CO (United States), 2015.

[10] W. Bierbooms. Offshore wind climate (*Lecture Slides*). 2018.

[11] M. Borg and M. Collu. A comparison between the dynamics of horizontal and vertical axis offshore floating wind turbines. *Philosophical Transactions of the Royal Society A: Mathematical, Physical and Engineering Sciences*, 373(2035):20140076, 2015.

[12] P. J. M. Bussemakers. Validation of numerical hydrodynamic load and motion simulations in BHawC/OrcaFlex with full-scale measurements on the Hywind Scotland floating wind farm - Literature report, 2019. [Not published].

[13] L. Castro-Santos and V. Diaz-Casas. *Floating offshore wind farms*. Springer, 2016.

[14] Offshore Renewable Energy Catapult. Floating turbine design cases, 2020. URL `https://pod.ore.catapult.org.uk/data-collection/floating-turbine-design-cases`. [Online; accessed March 19, 2020].

[15] C. Cermelli, C. Leroux, Sandra Díaz D., and A. Peiffer. Experimental measurements of windfloat 1 prototype responses and comparison with numerical model. In *ASME 2018 37th International Conference on Ocean, Offshore and Arctic Engineering*. American Society of Mechanical Engineers Digital Collection, 2018.

[16] S. Chakrabarti. *Handbook of offshore engineering*. Elsevier ocean engineering series, 2005.

[17] A. Chougule, J. Mann, M. Kelly, and G. C. Larsen. Simplification and validation of a spectral-tensor model for turbulence including atmospheric stability. *Boundary-layer meteorology*, 167(3):371–397, 2018.

[18] European Comission. A clean planet for all: A european strategic long-term vision for a prosperous, modern, competitive and climate neutral economy. Technical report, European Commission, 2018.

[19] European Commission. COMMUNICATION FROM THE COMMISSION The European Green Deal; COM/2019/640 final. Technical report, European Commission, 2019.

[20] International Electrotechnical Commission. Iec 61400-1: Wind turbines part 1: Design requirements. 2005.

[21] A. J. Couling, A. J. Goupee, A. N. Robertson, and J. M. Jonkman. Importance of second-order difference-frequency wave-diffraction forces in the validation of a fast semi-submersible floating wind turbine model. Technical report, National Renewable Energy Lab.(NREL), Golden, CO (United States), 2013.

[22] J. Cruz and M. Atcheson. *Floating offshore wind energy: the next generation of wind energy*. Springer, 2016.

[23] R. G. Dean. Stream function representation of nonlinear ocean waves. *Journal of Geophysical Research*, 70(18):4561–4572, 1965.

[24] DNV. Environmental conditions and environmental loads. Technical report, 2014.

[25] T. M. Duarte, A. J. Sarmento, and J. M. Jonkman. Effects of second-order hydrodynamic forces on floating offshore wind turbines. In *32nd ASME Wind Energy Symposium*, page 0361, 2014.

[26] A. J. Dunbar, B. A. Craven, and E. G. Paterson. Development and validation of a tightly coupled cfd/6-dof solver for simulating floating offshore wind turbine platforms. *Ocean Engineering*, 110:98–105, 2015.

[27] Siemens Gamesa Renewable Energy. Swt-6.0-154, aeroelastic model data, aerodynamic layout. Technical report, Siemens Gamesa Renewable Energy, 2014. [Classification: Confidential].

[28] Siemens Gamesa Renewable Energy. Swt-6.0-154, aeroelastic model data, main document. Technical report, Siemens Gamesa Renewable Energy, 2014. [Classification: Confidential].

[29] Siemens Gamesa Renewable Energy. Swt-6.0-154, aeroelastic model data, structural and mechanical data. Technical report, Siemens Gamesa Renewable Energy, 2014. Project: Type Certification. [Classification: Confidential].

[30] Siemens Gamesa Renewable Energy. SWT-6.0-154 Offshore wind turbine, 2020. URL `https://www.siemensgamesa.com/en-int/products-and-services/offshore/wind-turbine-swt-6-0-154`. [Online; accessed May 5, 2020].

[31] Equinor. Equinor has installed batwind - the world's first battery for offshore wind, 2018. URL `https://www.equinor.com/en/news/26june2018-equinor-has-installed-batwind.html`. [Online; accessed December 11, 2019].

[32] Equinor. Hywind scotland measurement data description. Technical report, Equinor ASA, 2019. [Classification: Restricted].

[33] Equinor. Equinor — the world's leading floating offshore wind developer, 2019. URL `https://www.equinor.com/en/what-we-do/hywind-where-the-wind-takes-us.html`. [Online; accessed September 25, 2019].

[34] Equinor. The future of offshore wind is afloat, 2020. URL `https://www.equinor.com/en/what-we-do/floating-wind.html`. [Online; accessed July 5, 2020].

[35] Equinor and Masdar. Hywind scotland - the world's first commercial floating wind farm. Technical report, 2015. URL `https://www.equinor.com/content/dam/statoil/documents/newsroom-additional-documents/news-attachments/brochure-hywind-a4.pdf`. [Online; accessed November 26, 2019].

[36] O. M. Faltinsen. *Sea Loads on Ships and Offshore Structures*. Cambridge University Press, 1999. ISBN 0521458706.

[37] J. D. Fenton. A fifth-order stokes theory for steady waves. *Journal of waterway, port, coastal, and ocean engineering*, 111(2):216–234, 1985.

[38] J. Fredsøe. *Hydrodynamics*. Danmarks Tekniske Universitet, 2008. ISBN Unpublished Book.

[39] M. Greco. *TMR 4215: Sea Loads Lecture Notes*. Department of Marine Technology, Norwegian University of Science and Technology, 2018. ISBN Unpublished Book.

[40] M. O. L. Hansen. *Aerodynamics of Wind Turbines*. Earthscan from Routledge, 3 edition, 2015. ISBN 978-1-138-77507-1.

[41] K. Hasselmann, T. P. Barnett, E. Bouws, H. Carlson, D. E. Cartwright, K. Enke, J. A. Ewing, H. Gienapp, D. E. Hasselmann, P. Kruseman, et al. Measurements of wind-wave growth and swell decay during the joint north sea wave project (jonswap). *Ergänzungsheft 8-12*, 1973.

[42] L. H. Holthuijsen. *Waves in oceanic and coastal waters*. Cambridge university press, 2010.

[43] E. Huse, K. Matsumoto, et al. Mooring line damping due to first-and second-order vessel motion. In *Offshore Technology Conference*. Offshore Technology Conference, 1989.

[44] IEAWind. Task 30 Research Results - OC3 Simulation Results, 2018. URL `https://community.ieawind.org/task30/ourlibrary`. [Online; accessed March 27, 2020].

[45] International Electrotechnical Commission IEC. Iec 61400-1. wind energy generation systems - part 1: Design requirements. 2019.

[46] B. J. Jonkman. Turbsim user's guide v2. 00.00. *Natl. Renew. Energy Lab*, 2014.

[47] J. Jonkman. Definition of the Floating System for Phase IV of OC3. Technical report, National Renewable Energy Lab.(NREL), Golden, CO (United States), 2010.

[48] J Jonkman and W Musial. Offshore code comparison collaboration (oc3) for iea task 23 offshore wind technology and deployment. *Contract*, 303(December):1–70, 2010.

[49] J. Jonkman, S. Butterfield, W. Musial, and G. Scott. Definition of a 5-mw reference wind turbine for offshore system development. Technical report, National Renewable Energy Lab.(NREL), Golden, CO (United States), 2009.

[50] J. M. Jonkman. Dynamics modeling and loads analysis of an offshore floating wind turbine. Technical report, National Renewable Energy Lab.(NREL), Golden, CO (United States), 2007.

[51] J. M. J. Journée and W. W. Massie. *Offshore Hydromechanics, First Edition*. Delft University of Technology, 2001. ISBN Unpublished Book.

[52] J. C. Kaimal, J. C. J. Wyngaard, Y. Izumi, and O. R. Coté. Spectral characteristics of surface-layer turbulence. *Quarterly Journal of the Royal Meteorological Society*, 98(417):563–589, 1972.

[53] J. C. Kaimal, J. C. J. Wyngaard, Y. Izumi, and O. R. Coté. Spectral characteristics of surface-layer turbulence. *Quarterly Journal of the Royal Meteorological Society*, 98(417):563–589, 1972.

[54] Madjid Karimirad and Torgeir Moan. Effect of aerodynamic and hydrodynamic damping on dynamic response of a spar type floating wind turbine. *development*, 2:3, 2010.

[55] G. H. Keulegan and L. H. Carpenter. Forces on cylinders and plates in an oscillating fluid. *J. Research of the National Bureau of Standards Research Paper*, 2857:423–440, 1958.

[56] M. I. Kvittem, E. E. Bachynski, and T. Moan. Effects of hydrodynamic modelling in fully coupled simulations of a semi-submersible wind turbine. *Energy Procedia*, 24:351–362, 2012.

[57] T. J. Larsen and T. D. Hanson. A method to avoid negative damped low frequent tower vibrations for a floating, pitch controlled wind turbine. In *Journal of Physics: Conference Series*, volume 75, page 012073. IOP Publishing, 2007.

[58] B. Le Méhauté. *An introduction to hydrodynamics and water waves*. Springer Science & Business Media, 1976.

[59] L. Li, Z. Hu, J. Wang, and Y. Ma. Development and validation of an aero-hydro simulation code for offshore floating wind turbine. *J Ocean Wind Energ*, 2(1):1–11, 2015.

[60] H. B. Liu, F. Duan, F. Yu, and B. Yuan. Validation of a fast spar-type floating wind turbine numerical model with basin test data. In *IOP Conference Series: Earth and Environmental Science*, volume 188, page 012096. IOP Publishing, 2018.

[61] P. A. Madsen. Generation and analysis of linear random waves(*Lecture Slides*), 2017.

[62] N. Maljaars and C. E. De Winter. Bhawclink functionality and requirements - version 8.2.0. Technical report, Siemens Gamesa Renewable Energy, 2019. [Classification: Confidential].

[63] J. Mann. The spatial structure of neutral atmospheric surface-layer turbulence. *Journal of fluid mechanics*, 273:141–168, 1994.

[64] J. Mann. Wind field simulation. *Probabilistic engineering mechanics*, 13(4):269–282, 1998.

[65] V. Masson-Delmotte, P. Zhai, H. O. Pörtner, D. Roberts, J. Skea, P. R. Shukla, A. Pirani, W. Moufouma-Okia, R. Péan, C.and Pidcock, S. Connors, J. B. R. Matthews, Y. Chen, X. Zhou, M. I. Gomis, E. Lonnoy, T. Maycock, M. Tignor, and T. Waterfield. Global Warming of 1.5°C. An IPCC Special Report on the impacts of global warming of 1.5°C above pre-industrial levels and related global greenhouse gas emission pathways, in the context of strengthening the global response to the threat of climate change, sustainable development, and efforts to eradicate poverty. Technical report, IPCC, 2018.

[66] D. Matha, F. Sandner, C. Molins, A. Campos, and P. W. Cheng. Efficient preliminary floating offshore wind turbine design and testing methodologies and application to a concrete spar design. *Philosophical Transactions of the Royal Society A: Mathematical, Physical and Engineering Sciences*, 373(2035): 20140350, 2015.

[67] MathWorks. Help Center - pchip, 2020. URL `https://nl.mathworks.com/help/matlab/ref/pchip.html#References`. [Online; accessed April 21, 2020].

[68] D. H. Meadows, D. L. Meadows, J. Randers, and W. W. Behrens. The limits to growth. Technical report, The Club of Rome, 1972.

[69] A. V. Metrikine. *Dynamics, Slender Structures and an Introduction to Continuum Mechanics*. Delft University of Technoloy, 2018. ISBN Unpublished Book.

[70] J. R. Morison, J. W. Johnson, S. A. Schaaf, et al. The force exerted by surface waves on piles. *Journal of Petroleum Technology*, 2(05):149–154, 1950.

[71] F. G. Nielsen, T. D. Hanson, and B. Skaare. Integrated dynamic analysis of floating offshore wind turbines. In *25th international conference on offshore mechanics and arctic engineering*, pages 671–679. American Society of Mechanical Engineers Digital Collection, 2006.

[72] Orcina. Orcina project 1405 - wind turbine validation report. Technical report, 2018. URL `https://www.orcina.com/wp-content/uploads/resources/validation/R14050101-Wind-Turbine-Validation-Report.pdf`. [Online; accessed March 25, 2020].

[73] Orcina. K01 floating wind turbine. Technical report, 2019. URL `https://www.orcina.com/resources/examples/?key=k`. [Online; accessed November 26, 2019].

[74] Orcina. Orcaflex manual - version 10.3d. Technical report, 2019.

[75] M. S. Pedersen. One2one comparison with bhawc 7.0 swt-6.0-154 direct drive in østerild, denmark. Technical report, Siemens Gamesa Renewable Energy, 2014. [Classification: Confidential].

[76] W. Popko, M. L. Huhn, A. Robertson, J. Jonkman, F. Wendt, K. Müller, M. Kretschmer, F. Vorpahl, T. R. Hagen, C. Galinos, et al. Verification of a numerical model of the offshore wind turbine from the alpha ventus wind farm within oc5 phase iii. In *ASME 2018 37th International Conference on Ocean, Offshore and Arctic Engineering*. American Society of Mechanical Engineers Digital Collection, 2018.

[77] W. Popko, A. N. Robertson, J. Jonkman, F. F. Wendt, P. Thomas, K. Muller, M. Kretschmer, T. R. Hagen, C. Galinos, L. Dreff, et al. Validation of numerical models of the offshore wind turbine from the alpha ventus wind farm against full-scale measurements within oc5 phase iii. Technical report, National Renewable Energy Lab.(NREL), Golden, CO (United States), 2019.

[78] A. N. Robertson. Uncertainty analysis of oc5-deepcwind floating semisubmersible offshore wind test campaign. Technical report, National Renewable Energy Lab.(NREL), Golden, CO (United States), 2017.

[79] A. N. Robertson, F. F. Wendt, J. M. Jonkman, W. Popko, F. Vorpahl, C. T. Stansberg, E. E. Bachynski, I. Bayati, F. Beyer, J. B. de Vaal, et al. Oc5 project phase i: Validation of hydrodynamic loading on a fixed cylinder. Technical report, National Renewable Energy Lab.(NREL), Golden, CO (United States), 2015.

[80] A. N. Robertson, F. Wendt, J. M. Jonkman, W. Popko, M. Borg, H. Bredmose, F. Schlutter, J. Qvist, R. Bergua, R. Harries, et al. Oc5 project phase ib: validation of hydrodynamic loading on a fixed, flexible cylinder for offshore wind applications. *Energy Procedia*, 94:82–101, 2016.

[81] A. N. Robertson, F. Wendt, J. M. Jonkman, W. Popko, M. Borg, H. Bredmose, F. Schlutter, J. Qvist, R. Bergua, R. Harries, et al. Oc5 project phase ib: validation of hydrodynamic loading on a fixed, flexible cylinder for offshore wind applications. *Energy Procedia*, 94:82–101, 2016.

[82] A. N. Robertson, F Wendt, J. M. Jonkman, W. Popko, H. Dagher, S. Gueydon, J. Qvist, F. Vittori, J. Azcona, E. Uzunoglu, et al. Oc5 project phase ii: validation of global loads of the deepcwind floating semisubmersible wind turbine. *Energy Procedia*, 137:38–57, 2017.

[83] A. N. Robertson, E. E. Bachynski, S. Gueydon, F. Wendt, P. Schünemann, and J. Jonkman. Assessment of experimental uncertainty for a floating wind semisubmersible under hydrodynamic loading. In *ASME 2018 37th International Conference on Ocean, Offshore and Arctic Engineering*. American Society of Mechanical Engineers Digital Collection, 2018.

[84] T. Sarpkaya. Fluid forces on oscillating cylinders. *Nasa Sti/recon Technical Report A*, 78:275–290, 1978.

[85] T. Sarpkaya. *Wave forces on offshore structures*. Cambridge university press, 2010.

[86] L. Sethuraman and V. Venugopal. Hydrodynamic response of a stepped-spar floating wind turbine: Numerical modelling and tank testing. *Renewable Energy*, 52:160–174, 2013.

[87] B. Skaare, T. D. Hanson, and F. G. Nielsen. Importance of control strategies on fatigue life of floating wind turbines. In *ASME 2007 26th International Conference on Offshore Mechanics and Arctic Engineering*, pages 493–500. American Society of Mechanical Engineers Digital Collection, 2007.

[88] B. Skaare, F. G. Nielsen, T. D. Hanson, R. Yttervik, O. Havmøller, and A. Rekdal. Analysis of measurements and simulations from the hywind demo floating wind turbine. *Wind Energy*, 18(6):1105–1122, 2015.

[89] L. Skjelbreia and J. Hendrickson. Fifth order gravity wave theory. *Coastal Engineering Proceedings*, 1(7): 10, 1960.

[90] M. D. Smith. Newton-Raphson Technique, 1998. URL `https://web.mit.edu/10.001/Web/Course_Notes/NLAE/node6.html`. MIT - Massachusetts Institute of Technology. [Online; accessed May 10, 2020].

[91] S. W. Smith et al. The scientist and engineer's guide to digital signal processing, 1997.

[92] ITTC Specialist Committee et al. Ittc–recommended procedures (7.5-02-01-03) fresh water and seawater properties. Technical report, 2011.

[93] J. M. J. Spijkers, A. W. C. M. Vrouwenvelder, and E. C. Klaver. *Structural Dynamics CT4140, Part 1 - Strucural Vibrations*. Delft University of Technoloy, 2005. ISBN Unpublished Book.

[94] Statoil. Hywind buchan deep metocean design basis re2014-002. Technical report, Statoil, 2014.

[95] Statoil. Hywind scotland pilot park project - environmental statement. Technical report, 2015.

[96] G. G. Stokes. On the theory of oscillatory waves. (8):441–473, 1847.

[97] G. G. Stokes. Mathematical and physical papers. 1, 1880.

[98] I. A. Svendsen. *Introduction to nearshore hydrodynamics*, volume 24. World Scientific, 2006. ISBN 981-256-142-0.

[99] I. A. Svendsen and P. Justesen. Forces on slender cylinders from very high and spilling breakers. In *Symposium on description and modelling of directional seas*, pages 18–20, 1984.

[100] R. Taylor and P. Valent. Design guide for drag embedment anchors. Technical report, Naval Civil Engineering Lab Port Hueneme CA, 1984.

[101] Ben H Thacker, Scott W Doebling, Francois M Hemez, Mark C Anderson, Jason E Pepin, and Edward A Rodriguez. Concepts of model verification and validation. Technical report, Los Alamos National Lab., 2004.

[102] K. Thomson. Mann turbulence for the IEA Code Comparison Collaborative (OC3), 2006.

[103] T. Utsunomiya, I. Sato, S. Yoshida, H. Ookubo, and S. Ishida. Dynamic response analysis of a floating offshore wind turbine during severe typhoon event. In *ASME 2013 32nd International Conference on Ocean, Offshore and Arctic Engineering*, pages V008T09A032–V008T09A032. Citeseer, 2013.

[104] H. J. J. Van den Boom. Dynamic behaviour of mooring lines. *BOSS'85 Behavior of Offshore Structures*, pages 359–368, 1985.

[105] P. Van der Male. Basis of Design - Offshore Wind Support Structures (*Lecture Slides*). 2018.

[106] R. Van 't Veer. OE44100 Floating Structures & Offshore Moorings (*Lecture Slides*). 2018.

[107] P. S. Veers. Three-dimensional wind simulation. Technical report, Sandia National Labs., Albuquerque, NM (USA), 1988.

[108] Bureau Veritas. Classification of mooring systems for permanent and mobile offshore units. *NR 493DTR03E*, 2015.

[109] Det Norske Veritas. Offshore standard dnv-os-e301 position mooring. *Det Norske Veritas: Høvik, Norway*, 2015.

[110] J. D. Wheeler et al. Methods for calculating forces produced by irregular waves. In *Offshore technology conference*. Offshore Technology Conference, 1969.

[111] WindEurope. Floating offshore wind vision statement. Technical report, WindEurope, 2017.

[112] K. J. Åström and R. M. Murray. *Feedback Systems, An Introduction for Scientists and Engineers*. Princeton University, 2009. ISBN 978-0-691-13576-2.

NTNU

SG

TU Delft